IntechOpen

Emerging Solar Energy Materials

Edited by Sadia Ameen,
M. Shaheer Akhtar and Hyung-Shik Shin

EMERGING SOLAR ENERGY MATERIALS

Edited by **Sadia Ameen, M. Shaheer Akhtar**
and **Hyung-Shik Shin**

Emerging Solar Energy Materials
http://dx.doi.org/10.5772/intechopen.71145
Edited by Sadia Ameen, M. Shaheer Akhtar and Hyung-Shik Shin

Contributors

Ersan Yudhapratama Muslih, Badrul Munir, Xun Cao, Ping Jin, Nilesh Kumar Pathak, R P Sharma, Weidong Zhu, Jingjing Chang, Chunfu Zhang, Jincheng Zhang, Yue Hao, Adel Najar, Amine El Moutaouakil, Ahmed Mourtada Elseman, Sajid Sajid, Ahmed Esmail Shalan, Mohamed M. Rashad, Meicheng Li, Dong Wei, Huey-laing Hwang, Yijian Liu, Dazheng Chen, Shanzheng Pang, Hwan Kyu Kim, Mohammad Aftabuzzaman, Renat Salikhov, Yuliya Biglova, Akhat Mustafin, Amalraj Peter Amalathas, Maan Alkaisi, Zhao Xu

© The Editor(s) and the Author(s) 2018
The rights of the editor(s) and the author(s) have been asserted in accordance with the Copyright, Designs and Patents Act 1988. All rights to the book as a whole are reserved by INTECHOPEN LIMITED. The book as a whole (compilation) cannot be reproduced, distributed or used for commercial or non-commercial purposes without INTECHOPEN LIMITED's written permission. Enquiries concerning the use of the book should be directed to INTECHOPEN LIMITED rights and permissions department (permissions@intechopen.com).
Violations are liable to prosecution under the governing Copyright Law.

Individual chapters of this publication are distributed under the terms of the Creative Commons Attribution 3.0 Unported License which permits commercial use, distribution and reproduction of the individual chapters, provided the original author(s) and source publication are appropriately acknowledged. If so indicated, certain images may not be included under the Creative Commons license. In such cases users will need to obtain permission from the license holder to reproduce the material. More details and guidelines concerning content reuse and adaptation can be foundat http://www.intechopen.com/copyright-policy.html.

Notice

Statements and opinions expressed in the chapters are these of the individual contributors and not necessarily those of the editors or publisher. No responsibility is accepted for the accuracy of information contained in the published chapters. The publisher assumes no responsibility for any damage or injury to persons or property arising out of the use of any materials, instructions, methods or ideas contained in the book.

First published in London, United Kingdom, 2018 by IntechOpen
eBook (PDF) Published by IntechOpen, 2019
IntechOpen is the global imprint of INTECHOPEN LIMITED, registered in England and Wales, registration number: 11086078, The Shard, 25th floor, 32 London Bridge Street
London, SE19SG – United Kingdom
Printed in Croatia

British Library Cataloguing-in-Publication Data
A catalogue record for this book is available from the British Library

Additional hard and PDF copies can be obtained from orders@intechopen.com

Emerging Solar Energy Materials
Edited by Sadia Ameen, M. Shaheer Akhtar and Hyung-Shik Shin

p. cm.

Print ISBN 978-1-78923-582-1

Online ISBN 978-1-78923-583-8

eBook (PDF) ISBN 978-1-83881-518-9

Meet the editors

Dr. Sadia Ameen obtained her PhD degree in Chemistry (2008) and then moved to Chonbuk National University. Presently, she is working as an assistant research professor at the School of Chemical Engineering, Chonbuk National University. Her current research focuses on dye-sensitized solar cells, perovskite solar cells, organic solar cells, chemical sensors, photocatalytic degradation, and optoelectronic devices. She received a gold medal in academics and is a holder of merit scholarship for the best academic performances. She is a recipient of a Best Researcher Award (2016). She has published more than 95 peer-reviewed papers in the field of solar cells, photocatalytic degradation, and sensors, contributed to book chapters, and edited books. She is an inventor and a coinventor of patents.

Professor M. Shaheer Akhtar received his PhD degree in Chemical Engineering (2008) from the Chonbuk National University, South Korea. Presently, he is working as a full-time associate professor at the Chonbuk National University, South Korea. His research interest constitutes the photoelectrochemical characterizations of thin-film semiconductor nanomaterials, composite materials, polymer-based solid-state films, solid polymer electrolytes and electrode materials for dye-sensitized solar cells (DSSCs), hybrid organic-inorganic solar cells, small molecule-based organic solar cells, and photocatalytic reactions.

Professor Hyung-Shik Shin received his PhD degree in the kinetics of initial oxidation Al (111) surface from the Cornell University, USA, in 1984. Presently, he is a professor at the School of Chemical Engineering, Chonbuk National University, South Korea. He is a promising researcher and visited several universities as a visiting professor/an invited speaker worldwide. He is an active executive member of various renowned scientific committees such as KiChE, copyright protection, and KAERI. He has an extensive experience in electrochemistry, renewable energy sources, solar cells, organic solar cells, charge transport properties of organic semiconductors, inorganic-organic solar cells, biosensors, chemical sensors, nano-patterning of thin-film materials, photocatalytic degradation, and so on.

Contents

Preface

The demand for clean environment in our current society has increased with large-scale economic developments and population growth. The standard energy sources based on fossil fuels are limited and pollute the environment, leading to climatic change on a global scale. Taking care of the environment today is a sustainable act for the generations of tomorrow. The process of developing new techniques and improving older types of technologies is still ongoing. The most important thing is to understand that remediation actions need to be justified and optimize the adopted actions and must do more good than harm. The end results should always be a balance between risks, costs, benefits, and remediation viability. Solar energy and other renewable sources enable us to meet the demand for energy while offering a cleaner and greener footprint.

Based on the developments in the field of solar technology, we decided to compose a book based on materials and concepts in solar cells. In parallel with the growth rate of renewable energy, essential attention is being paid to the development of advanced techniques and materials for the effective utilization of energy resources. An attempt has also been made to provide the fundamental understanding of the functioning of solar cells. The main objective of writing this book is to create a comprehensive and easy-to-understand source of information on the advances in this rapidly growing research area. This book includes enough information on the basics to be used as a textbook undergraduate coursework in engineering and the sciences. The inclusion of advanced concepts and research trends will also make it useful as a reference for scientists and professionals. We hope that the book can serve its function to draw attention to this emerging solar cell field with a great potential.

Emerging Solar Energy Materials is divided into 2 parts comprising 12 chapters written by leading experts in the solar cell field and is organized with the intention to provide a big picture of the latest progress in the solar cell field and at the same time give an in-depth discussion on fundamentals of solar cells for interested audiences. In this book, each part opens with a new author's essay highlighting their work for contribution toward solar energy. To help the reader evaluate progress and recognize how difficult some problems are, the chapters present charts, graphs, and figures to help illustrate the scope of environmental issues; the text's main focus is on identifying major issues and giving appropriate examples to illustrate the complex interactions that are characteristic of renewable energy.

Preparing such a book is not possible without the support from others. We want to express our special thanks to the authors' hard work and contributions, copyright owners, and reviewer's comments and suggestions. Without all these support, it would not have been possible for us to publish this book. We wish to express our gratitude to the staff of IntechOpen for their patience during the development of this project and for encouraging us during the various stages of preparation.

Sadia Ameen
School of Chemical Engineering
Chonbuk National University
Jeonju, Republic of Korea

M. Shaheer Akhtar
New & Renewable Energy Material Development Center (NewREC),
Chonbuk National University
Jeonbuk, Republic of Korea

Hyung-Shik Shin
School of Chemical Engineering
Chonbuk National University
Jeonju, Republic of Korea

Section 1

Functional Solar Energy Materials

Solar Modulation Utilizing VO_2-Based Thermochromic Coatings for Energy-Saving Applications

Xun Cao and Ping Jin

Additional information is available at the end of the chapter

http://dx.doi.org/10.5772/intechopen.75584

Abstract

Energy consumption has become an urgent issue not only for the global environment, but also for people's lives. Among total energy consumption, buildings take nearly 40%. For buildings, energy exchange through windows accounts for over 50% by means of conduction, convection, and radiation. To reduce energy consumption, new structures should be developed for glass surfaces to enhance their thermal insulation properties. Vanadium dioxide (VO_2) is the most well-known thermochromic material, which exhibits a notable optical change from transparent to reflecting in the infrared upon a semiconductor-to-metal phase-transition. In this chapter, we provide a comprehensive summary of advances on the VO_2-based thermochromic coatings. Although the research on VO_2 smart window has been carried on for several decades, the real commercial use of it has not yet been achieved. The hindrance factors against commercial use are conventionally known as the unsatisfactory intrinsic properties of VO_2 material and have recently emerged as new challenges.

Keywords: solar modulation, vanadium dioxide, optical design, multilayer structures, energy-saving

1. Introduction

Nowadays, for environmental deterioration and energy shortage in modern human society, people are paying more attention to finding energy-efficient materials to reduce the energy consumption and greenhouse gas emission. According to the survey, buildings are responsible for about 40% of the energy consumption and almost 30% of the anthropogenic greenhouse gas emissions owing to the use of lighting, air-conditioning, and heating [1–5]. Energy exchange through windows accounts for over 50% of energy consumed through a building's envelope by means of conduction, convection and radiation, as shown in **Figure 1(a)**. Therefore, energy saving of windows contributes the critical and important roles in building energy-efficient projects. Managing heat exchange through windows is a feasible approach to reduce the building energy consumptions. In summer, solar radiation entering buildings should be controlled to reduce the air-conditioning energy consumption. On the contrary, thermal radiation from the buildings must be limited to consume lesser energy for heating.

An effective route to achieve this goal would be using smart coatings on building windows to control the solar radiation. Therefore, smart coatings based on electrochromism [6–10], thermochromism [11–19], gasochromism [20–22] and photochromism [23–26] have been widely investigated for energy-efficient coatings. Thermochromic-coated window can modulate near-infrared radiation (NIR) from transmissive to opaque in response to the environmental temperature from low to high, which does not require extra stimuli and can save more energy consumption. It has two states: a transparent state with a higher solar transmittance and an opaque state with a lower solar transmittance. The thermochromic window [27–29], whose transition depends on the temperature, is widely investigated type of chromogenic window.

Vanadium dioxide (VO_2) is one of the most promising thermochromic materials, which has been widely studied. VO_2 exhibits an automatic reversible semiconductor–metal phase transition (SMT) at a critical transition temperature (T_c) at 68°C [30], which has been widely investigated as smart coatings for building fenestrations [31–35]. As shown in **Figure 1(b)**, for temperatures below the T_c, VO_2 is monoclinic ($P2_1/c$, M1) phase with the transmittance of NIR. On the contrary, the material is a tetragonal structure ($P4_2/mnm$, R), which is reflective for NIR [36, 37]. This feature makes VO_2 an amazing material for thermochromic smart coatings [37–45]. Based on VO_2-thermochromic coatings, smart windows can let the solar energy (mainly caused by NIR) in and out during the cold and hot days, respectively, which are shown in **Figure 1(c)**.

VO_2 smart coatings are usually used in two forms including flexible foils based on VO_2 nanoparticles [34, 46–52] and VO_2-based multilayer films [11, 12, 33, 53–55]. However, for commercial application as smart coatings on windows, there are still many obstacles severely limiting the relative applicability of VO_2 smart coatings. (I) The phase-transition temperature (T_c) for pure bulk VO_2 (68°C) is too high to be applied on building windows, while T_c around 40°C is acceptable. (II) For conventional VO_2 coatings, relative modulation abilities are not efficient enough for energy saving. That can be explained by the fact that the modulation of VO_2 for solar radiation is most attributed to the transmittance switch in the near-infrared region, which only accounts for 43% of solar energy in the solar spectrum [23]. (III) The luminous transmittance (T_{lum}) for single layer VO_2 with desirable solar modulation (ΔT_{sol}) is usually less than 40% (even 30%) due to the absorption in the short-wavelength range in both the semiconducting and metallic states of VO_2, which should be larger than 50% at least for daily applications. (IV) For practical applications as smart coatings, VO_2 must maintain excellent thermochromic performances during a long-time period-at least 10 years. However, VO_2 can easily transform into the V_2O_5 phase in the real environment,

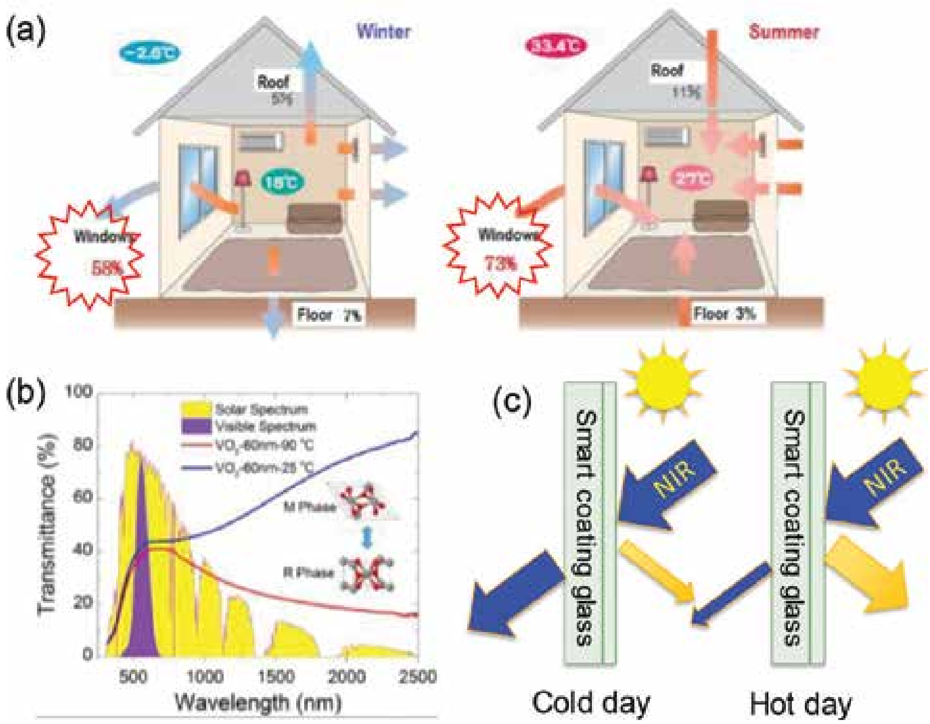

Figure 1. (a) Schematic of energy exchange in winter and summer days. (b) Typical optical properties of thermochromic coatings before and after phase-transition temperature. Inset is the crystallographic structure of VO_2 (monoclinic phase) and VO_2 (rutile phase). (c) Schematic of energy-efficiency based on thermochromic smart coatings.

which is the most thermodynamically stable phase of vanadium oxide but does not possess the thermochromic property [56]. Therefore, environmental stability of VO_2 is a great challenge for practical applications as smart coatings.

These obstacles have to be overcome for practical applications, and many efforts have been made to achieve this goal. Doping of proper ions can effectively reduce the phase transition temperature of VO_2: cations larger than V^{4+}, such as W^{6+} [57], Mo^{6+} [58] and Nb^{5+} [59], and anions larger than O^{2-}, such as F^- [60], have been utilized to reduce the T_c. However, obstacles in (II)–(IV) mentioned above have not yet been solved. Although several reviews about VO_2 coatings have been reported [35, 36, 61, 62], most of them are still in lab scale and few prospects of commercial applications are available.

In this chapter, we will review strategies of thermochromic VO_2 smart coatings for improved thermochromic performance, environmental stability, and large-scale production for commercial applications on building fenestrations. Firstly, strategies to enhance thermochromic performance (T_{lum} and ΔT_{sol}) of VO_2 coatings have been introduced as well as the balance between T_{lum} and ΔT_{sol} (Section 2). Then, methods to improve the durability of VO_2 coatings, including protective layers for multilayer films, will be summarized in Section 3. Meanwhile, multi-functional design of VO_2 smart coatings such as photocatalysis and self-cleaning function has been discussed in Section 4. Recent progress for large-scale production of VO_2 smart coatings has been surveyed in Section 5. Finally, future development trends of VO_2 coatings have prospected for large-scale production as practical and commercial applications.

2. Improvements of optical properties of VO_2

Luminous transmittances (T_{lum}) and solar modulation ability (ΔT_{sol}) are the most important indexes of thermochromic properties for VO_2 smart coatings. The integral luminous transmittances (T_{lum}) and solar transmittances (T_{sol}) of the samples can be obtained by the following equations:

$$T_{\text{lum, sol}} = \int \Phi_{\text{lum, sol}}(\lambda)\mathrm{T}(\lambda)\mathrm{d}\lambda \Big/ \int \Phi_{\text{lum, sol}}(\lambda)\mathrm{d}\lambda \tag{1}$$

where $T(\lambda)$ represents the transmittance at wavelength λ; Φ_{lum} is the standard efficiency function for photopic vision; and Φ_{sol} is the solar irradiance spectrum for an air mass of 1.5, which corresponds to the sun standing 37° above the horizon. The solar modulation ability (ΔT_{sol}) of the films was calculated by $\Delta T_{sol} = T_{\text{sol, lt}} - T_{\text{sol, ht}}$, where *lt* and *ht* represent low temperature and high temperature, respectively.

VO_2 smart coatings always suffer from the problem of low luminous transmittance due to the absorption in the short-wavelength range in both the semiconducting and the metallic states [63]. The luminous transmittance of VO_2 coatings is largely dependent on relative thicknesses. Based on optical calculation, a single layer VO_2 film (80 nm), for example, exhibits an integrated luminous transmittance (T_{lum}) of 30.2% and 25.1% for semiconducting and metallic VO_2 (see **Figure 2(a)**). As for solar modulation ability, the majority of reported modulation abilities are less than 10%, which are not efficient enough for energy-saving function [64–67]. For VO_2 coatings before and after the phase-transition, the contrast of relative optical transmittance is mainly in the near-infrared region (780–2500 nm), which only account for 43%.

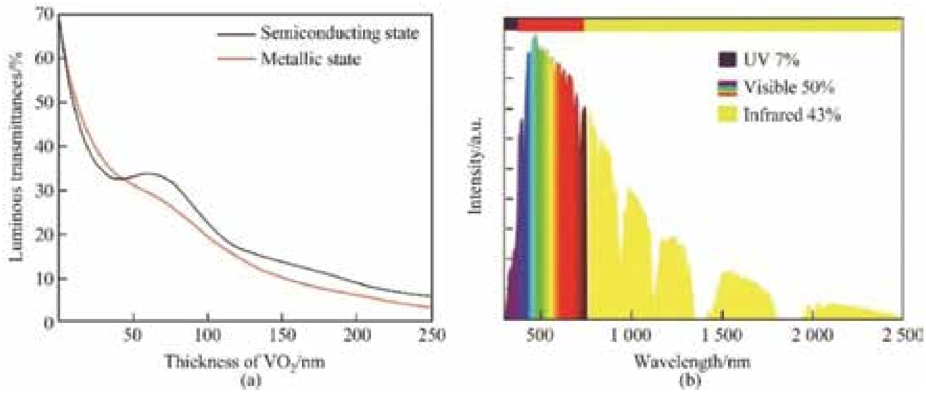

Figure 2. (a) Calculated luminous transmittance for single-layer VO_2 films with various thickness at semiconducting state (black line) and metallic state (red line) and (b) the solar spectrum and relative energy distribution.

2.1. Strategies for enhanced luminous transmittance and solar modulation ability

Many efforts have been made to improve the luminous transmittance and solar modulation ability of VO_2-based smart coatings. For VO_2 films fabricated by deposition, the design of multilayer structures is an effective way to improve the optical properties [11, 55, 68]. Thermochromic smart coatings incorporating VO_2 films with additional layers have been fabricated for improved thermochromic performances including desirable luminous transmittance and effective solar modulation ability. Schematic illustration of additional layers such as antireflection layers and buffer layers has been shown in **Figure 3** with three typical structures for VO_2 thin films and relative SEM images.

An effective way to improve the luminous transmittance of VO_2 coatings is to employ an antireflection (AR) layer, such as SiO_2 [69–72], TiO_2 [73], ZrO_2 [74], etc. Lee et al. [70, 71] reported that SiO_2 antireflection layer successfully increased the luminous transmittance of the VO_2 films. However, the luminous transmittance is still not sufficient. TiO_2 was selected as AR layer for VO_2 films [73] because TiO_2 has a higher refractive index and is a more effective antireflection material for VO_2 than the reported SiO_2. The optimized VO_2/TiO_2 structure has been fabricated and demonstrated the highest T_{lum} improvement among the reported at that time. The optical calculation was performed upon a basic structure of a VO_2 layer with an AR layer of refractive index n and thickness d [74]. Optimization was carried out on n and d for a maximum integrated luminous transmittance (T_{lum}). The calculation demonstrates that the optimal n value changes with the thickness of VO_2, and at $n \approx 2.2$ it gives the highest T_{lum} enhancement from 32 (without AR coating) to 55% for 50 nm VO_2. They deposited an optimized structure of VO_2/ZrO_2, and an improvement from 32.3 to 50.5% in T_{lum} was confirmed for the semiconductor phase of VO_2, which was in good agreement with the calculations.

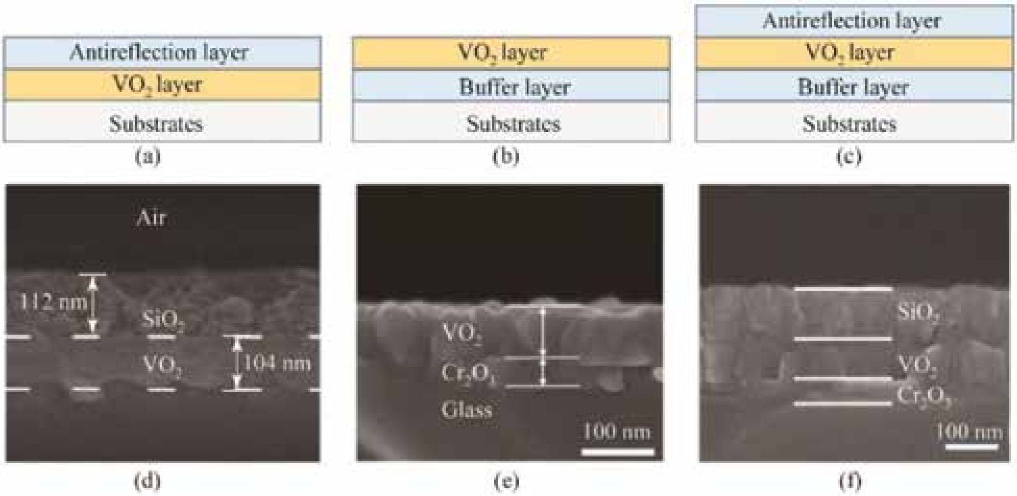

Figure 3. Schematic illustration of VO_2-based films with (a) antireflection layer, (b) buffer layer, and (c) both of antireflection layer and buffer, respectively. Relative SEM images of three typical structures have been shown in figures. (d)–(f) corresponding to figures. (a)–(c) [12, 33, 72], respectively.

Besides the antireflection layers on the top of VO_2 films, buffer layers between the substrates and VO_2 films also play important roles in the optical performances of integrated coatings. Some buffer layers as SiO_2, TiO_2, SnO_2, ZnO, CeO_2, and SiN_x have been investigated in reported work [64, 75–77]. Nevertheless, thermochromic performances of VO_2 coatings obtained based on above buffer layers were fair, which still cannot match the requirements for practical applications.

In our recent work, Cr_2O_3 has been selected to act as a structural template for the growth of VO_2 films as well as the AR layer for improving the luminous transmittance [12]. The suitable refractive index (2.2–2.3) is predicted to be beneficial for the optical performance of VO_2 thin films. Refractive index of Cr_2O_3 is between the glass and the VO_2, which is considered to enhance the luminous transmittance. Meanwhile, Cr_2O_3 has similar lattice parameters with VO_2(R), which can act as the structural template layer to lower the lattice mismatch between VO_2 thin films and glass substrates and to reduce the deposition temperature of VO_2 thin films (see **Figure 4(a)**, **(b)**). Different crystallization of VO_2 films can be obtained by introducing Cr_2O_3 layers with various thicknesses at a competitive temperature range from 250 to 350°C, where different thermochromic performance can be obtained (see **Figure 4(c)**). The Cr_2O_3/VO_2 bilayer film deposited 350°C with optimal thickness shows an excellent ΔT_{sol} = 12.2% with an enhanced $T_{lum, lt}$ = 46.0% (see **Figure 4(d)**), while the value of ΔT_{sol} and $T_{lum, lt}$ for the single-layer VO_2 film deposited high temperature at 450°C is 7.8 and 36.4%, respectively. The Cr_2O_3 insertion layer dramatically increased the visible light transmission as well as improved the solar modulation of the original films, which arose from the structural template effect and antireflection function of Cr_2O_3 to VO_2.

For better thermochromic performance, sandwich structures based on VO_2 films have been fabricated. Double-layer antireflection incorporating TiO_2 and VO_2 ($TiO_2/VO_2/TiO_2$) has been proposed [63], and a maximum increase in T_{lum} by 86% (from 30.9 to 57.6%) has been obtained, which is better than the sample with single-layer antireflection (49.1%) [73].The same structure of $TiO_2/VO_2/TiO_2$ has also been investigated by Zheng et al. [11] and Sun et al. [38] for improved thermochromic performance and skin comfort design. A novel sandwich structure of $VO_2/SiO_2/TiO_2$ has been described by Powell et al. [68], where the SiO_2 layers act as ion-barrier interlayers to prevent diffusion of Ti ions into the VO_2 lattice. The best-performing multilayer film obtained in this work showed excellent solar modulation ability (15.29%), which was very close to the maximum possible solar modulation for VO_2 thin films. Unfortunately, the corresponding luminous transmittance is weak around 18% for both semiconducting and metallic states.

A novel $Cr_2O_3/VO_2/SiO_2$ (CVS) sandwich structure has been proposed and fabricated based on optical design and calculations [33]. The bottom Cr_2O_3 layer provides a structural template for improving the crystallinity of VO_2 and increasing the luminous transmittance of the structure. Then, the VO_2 layer with a monoclinic (M) phase at low temperature undergoes a reversible phase transition to rutile (R) phase at high temperature for solar modulation. The top SiO_2 layer not only acts as an antireflection layer but also greatly enhances the environmental stability of the multilayer structures as well as providing a self-cleaning layer for the versatility of smart coatings. Optical simulation of luminous transmittances (semiconducting state) for the CVS

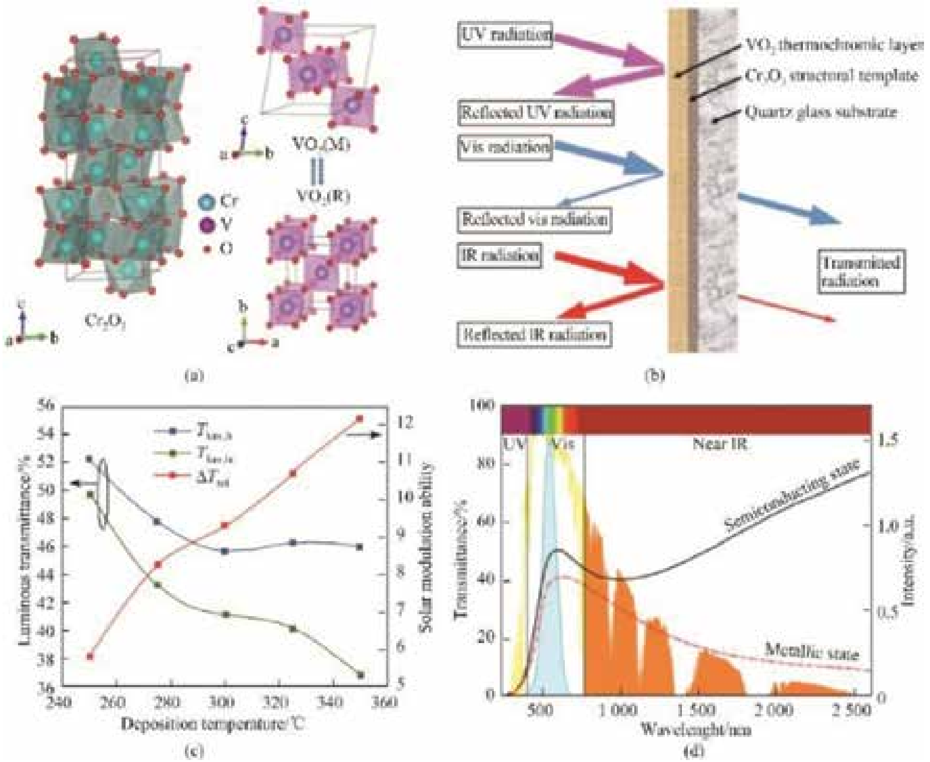

Figure 4. (a) Crystal structure of hexagonal Cr_2O_3, monoclinic VO_2, and rutile VO_2, respectively, (b) schematic illustration of Cr_2O_3/VO_2 bilayer thermochromic film, (c) variation curve of $T_{\text{lum, lt}}$, $T_{\text{lum, ht}}$ and ΔT_{sol} for VO_2 films deposited with 40 nm Cr_2O_3 structural template layer at different temperatures, (d) transmittance spectra (250–2600 nm) at 25 and 90°C for VO_2 films deposited with 40 nm Cr_2O_3 structural template layer at 350°C and standard solar spectra [12].

structure has been shown in **Figure 5(a)** (three-dimensional image). The thickness of the VO_2 layer was fixed at 80 nm to demonstrate significant thermochromic performance while varying thicknesses of Cr_2O_3 and SiO_2 were investigated for optimized optical properties. Four clear peaks are observed in the luminous transmittance simulations, which can be attributed to the interference effect of the multilayer structure. The highest value of $T_{\text{lum, lt}}$ is about 44.0% at approximately 40 and 90 nm of Cr_2O_3 and SiO_2, respectively. In this work, the proposed CVS multilayer thermochromic film shows an ultrahigh ΔT_{sol} = 16.1% with an excellent $T_{\text{lum, lt}}$ = 54.0%, which gives a commendable balance between ΔT_{sol} and $T_{\text{lum, lt}}$ (see **Figure 5(b)**, **(c)**). The demonstrated structure shows the best optical performance in the reported structures grown by magnetron sputtering and even better than most of the structures fabricated by solution methods. To date, the proposed CVS structure exhibits the most recommendable balance between the solar modulation ability and the luminous transmittance to reported VO_2 multilayer films (see **Figure 5(d)**).

There is some work focus on multilayer films with more layers for enhanced thermochromic performances. A five-layer thermochromic coating based on $TiO_2/VO_2/TiO_2/VO_2/TiO_2$ has been studied [52]. A featured wave-like optical transmittance curve has been measured by the five-layer coating companying an improved luminous transmittance (45.0% at semiconducting

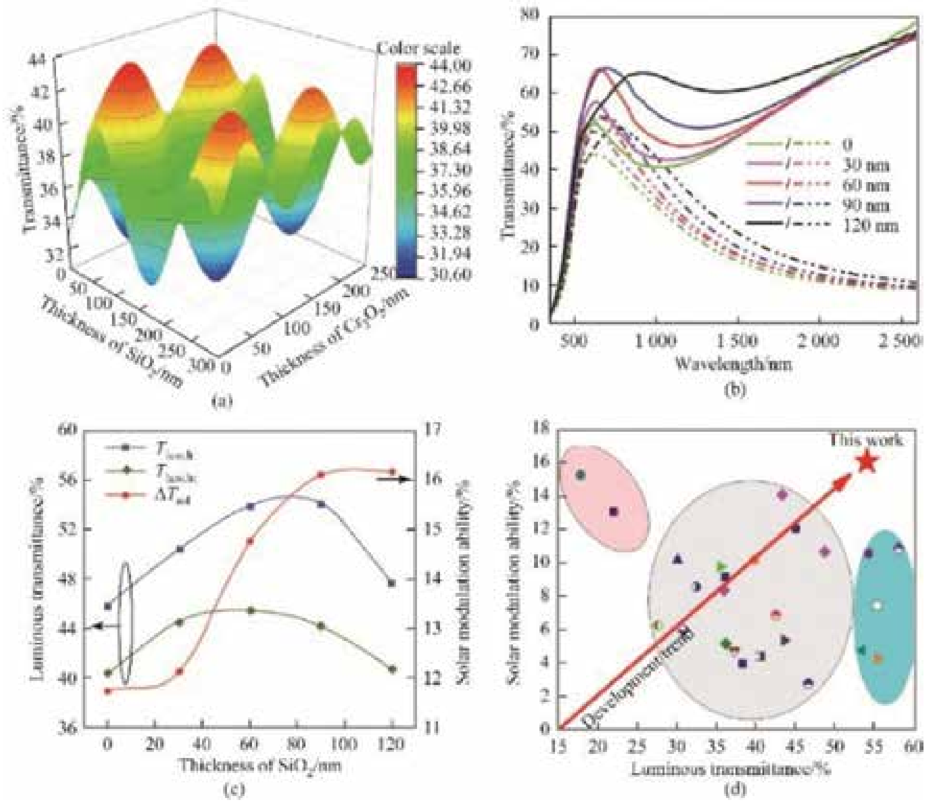

Figure 5. (a) 3D surface image of the luminous transmittance ($T_{\text{lum, lt}}$) calculation of the Cr_2O_3/VO_2 (80 nm)/SiO_2 multilayer structure on the thickness design of Cr_2O_3 (bottom layer) and SiO_2 (top layer), (b) transmittance spectra (350–2600 nm) at 25 (solid lines) and 90°C (dashed lines) for the CVS structures with various thickness of SiO_2 layers, (c) corresponding variation curves of $T_{\text{lum, lt}}$, $T_{\text{lum, ht}}$, and ΔT_{sol} for (b), (d) comparison of this work with recently reported VO_2-based thermochromic films.

state) and a competitive solar modulation ability (12.1%). Multilayer structure like SiN_x/$NiCrO_x$/SiN_x/VO_x/SiN_x/$NiCrO_x$/SiN_x exhibits superior solar modulation ability of 18.0%, but the luminous transmittance (32.7%) and the complicated structure pose an enormous obstacle for practical application of this structure.

2.2. Balance between luminous transmittances and solar modulation ability

Regarding practical application of VO_2-based thermochromic smart coatings, high solar modulation ability (ΔT_{sol}) accompanied by high luminous transmittance (T_{lum}) is required. Nevertheless, we can find that it is tough to make a good balance between luminous transmittance (T_{lum}) and solar modulation ability (ΔT_{sol}). A unilateral pursuit of distinguished solar modulation ability or ultrahigh luminous transmittances is meaningless.

Most work on VO_2-based smart coatings pursue large contrast of optical transmittance in the near-infrared region (780–2500 nm), while inconspicuous contrast in the visible light region

(380–780 nm) is desirable for both semiconducting and metallic states. In the solar spectrum, ultraviolet light, visible light, and infrared light is responsible for about 7, 50, 43% of solar energy, respectively [23]. Therefore, if there is an increased contrast in the visible light region for VO_2-based smart coatings between the semiconducting and the metallic state, relative solar modulation ability can be robustly enhanced due to the contribution from the visible light region. That means that the transmittance in the visible light region for VO_2 smart coating of metallic state should be maintained at least 50%, while the coating shows higher luminous transmittance of semiconducting state. Some works have been reported to increase ΔT_{sol} of VO_2 by mixing with specific materials, which shows a robust contrast in the visible light region in different temperatures [48, 78]. However, more investigations are required for a facile and low-cost method to achieve the balance between luminous transmittances and solar modulation ability of VO_2-based smart coatings.

3. Methods to improve the stability of VO_2 for long-time use

In previous work, researchers usually focus on the thermochromic properties of VO_2 to improve the luminous transmittances and solar modulation ability. However, environmental stability is another great challenge for VO_2 coatings from lab to industrial production. Vanadium is a multivalent element and there are several kinds of vanadium oxide, such as VO, V_2O_3, VO_2, V_6O_{13}, V_4O_9, V_3O_7, and V_2O_5. Among them, V_2O_5 is the most thermodynamically stable phase and VO_2 will gradually transform into the intermediate phases of V_6O_{13} and V_3O_7 and finally into V_2O_5 [57]. However, unlike VO_2, V_2O_5 does not possess thermochromic optical change properties near the room temperature. Therefore, how to maintain the thermochromic performance of VO_2 coatings during a long-time period is an inevitable problem that must be overcome.

To prevent VO_2 films from degradation, introduction of protective layers above VO_2 is an effective way that has been widely used. Chemically stable oxide films such as Al_2O_3 [56, 79], CeO_2 [80, 81], WO_3 [66], etc. have been studied to keep VO_2 away from oxidant like water and O_2 in air. It should be noted that the selected materials to be used as protective layers might affect the optical properties of VO_2, where dual enhancement in the optical properties and the stability is preferred.

Al oxide is a typical material that has been investigated as a protection layer for VO_2 coatings. In work reported by Ji [56], different thicknesses of Al oxide protective layers have been deposited for VO_2 by DC magnetron sputtering. The durability of the samples was evaluated at a high temperature around 300°C in dry air and highly humid environment. They found that the Al oxide protective layers provided good protection and delayed the degradation process of VO_2 in dry air at 300°C and humid environment. The similar structure was also investigated [79], while the Al_2O_3 protective layers were fabricated by atomic layer deposition (ALD). The Al_2O_3 films can protect the VO_2 from oxidation in the heating test but not sufficient in the damp environment, which can be attributed to the corrosion of water to Al_2O_3. It is worthy to mention that in above cases, the test period of the samples is less than 1 week (168 h), which is far from the request for practical applications.

Long et al. [66] proposed a novel sandwich structure of $WO_3/VO_2/WO_3$, where WO_3 not only functions as an AR layer to enhance the luminous transmittance (T_{lum}) of VO_2 but also performs as a good protective layer for thermochromic VO_2. The stability of samples was investigated in a constant-temperature humid environment with 90% relative humidity at 60°C. For the single-layer VO_2, the thermochromism nearly vanishes after 20 day's treatment in the tough environment. On the contrary, there shows almost no change in the optical transmittance of $WO_3/VO_2/WO_3$ multilayer films with the same treatment. However, though protection is provided by WO_3, the solar modulation ability of the sample is weakly reduced due to the diffusion of W^{6+} to VO_2.

In the works above, the protective layers are usually single-layer films. To enhance the durability of thermochromic VO_2 films, bilayer coatings such as $VO_2/TiO_2/ZnO$, $VO_2/SiO_2/ZnO$, and VO_2/SiO_2 /TiO_2 have been studied [82]. In this study, VO_2 films with TiO_2/ZnO protective coatings have demonstrated higher antioxidant activity under aging tests, which can be attributed to the different oxygen permeability through different inorganic films [83].

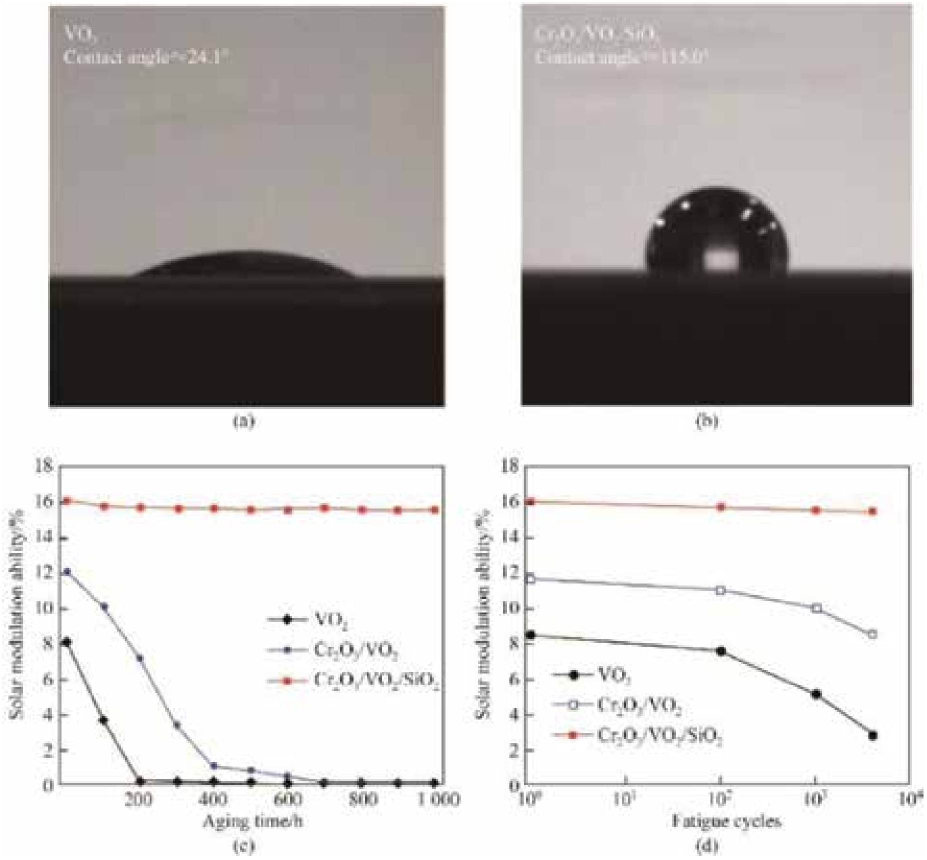

Figure 6. Images of contact angle measurement of (a) the single-layer VO_2 and (b) the proposed $Cr_2O_3/VO_2/SiO_2$ structure. Variation curves of ΔT_{sol} for VO_2, Cr_2O_3/VO_2, and $Cr_2O_3/VO_2/SiO_2$ with different duration time (c) and different fatigue cycles (d).

Zhan et al. [84] fabricated a complicated multilayer structure of $SiN_x/NiCrO_x/SiN_x/VO_x/SiN_x/NiCrO_x/SiN_x$, which exhibits enhanced thermal stability up to 375°C. However, aging test in a humid environment is not applied to the samples.

The $Cr_2O_3/VO_2/SiO_2$ structure proposed by our lab shows robust environmental stability for long-time use [33]. The top SiO_2 layer is chemically stable and makes the static water contact angle of the films change abruptly from 24.1° (hydrophilicity) to 115.0° (hydrophobicity) (see **Figure 6(a)**, **(b)**). Hydrophilicity of the single-layer VO_2 indicates contact with water, which will accelerate the degradation process of relative thermochromic performance. On the contrary, the hydrophobicity exhibited by the CVS structure is helpful to keep the VO_2 isolated from the water, which can protect the coatings against oxidation. Wettability is dependent on the chemical composition and structure of the surface. The surface of silicon is normally hydrophilic without additional treatments, but previous studies have demonstrated that the wettability of the silicon surface can be significantly changed by structuring the surfaces. So, fabrication of SiO_2 top coatings in this work has been deliberately optimized with enhanced roughness for hydrophobic surfaces (see **Figure 6(b)**). The double protection from Cr_2O_3 and SiO_2 makes an excellent promotion for the environmental stability of the CVS coatings, which is desirable for long-time use. The proposed CVS structure shows remarkable environmental stability due to the dual protection from the Cr_2O_3 and the SiO_2 layer, which shows negligible deterioration even after accelerated aging (60°C and 90% relative humidity) of 10^3 h and 4×10^3 fatigue cycles, while VO_2 single-layer samples almost become invalid (see **Figure 6(c)**, **(d)**).

4. Multifunctional design and construction

Nowadays, multifunctional fenestrations of the buildings are favored by customers. As is known to all, the fenestrations of the buildings and vehicles always need to be cleaned, which would lead to additional pollutants from the use of detergents and wasting a mass of labors. Semiconductor photocatalysts like TiO_2 are widely and frequently employed to decompose pollutants. There are three different polymorphs of crystalline TiO_2: rutile (tetragonal), anatase (tetragonal) and brookite (orthorhombic). Rutile TiO_2 (TiO_2 (R)) is a thermodynamically stable phase at all temperatures and the most common natural form of TiO_2. Due to similar lattice parameters, TiO_2 (R) films are acted as buffer layer and growth template of VO_2 (M) films. However, TiO_2 (R) films are less efficient photocatalysts than anatase TiO_2 (TiO_2 (A)) films, which occupy an important position in the studies of photocatalytic active materials. Zheng et al. [11] constructed a $TiO_2(R)/VO_2(M)/TiO_2(A)$ multilayer film, while the photocatalytic and photo-induced hydrophilic properties from the top $TiO_2(A)$ layer were studied for self-cleaning effects (see **Figure 7(a)**).

Self-cleaning property of the $TiO_2(R)/VO_2(M)/TiO_2(A)$ multilayer film was evaluated by the decomposition of stearic acid under UV radiation. The degradation of stearic acid was related to the decrease in IR absorption of the C—H stretches, which has been summarized in **Figure 7(b)**. Before UV light irradiation, the characteristic alkyl C—H bond stretching

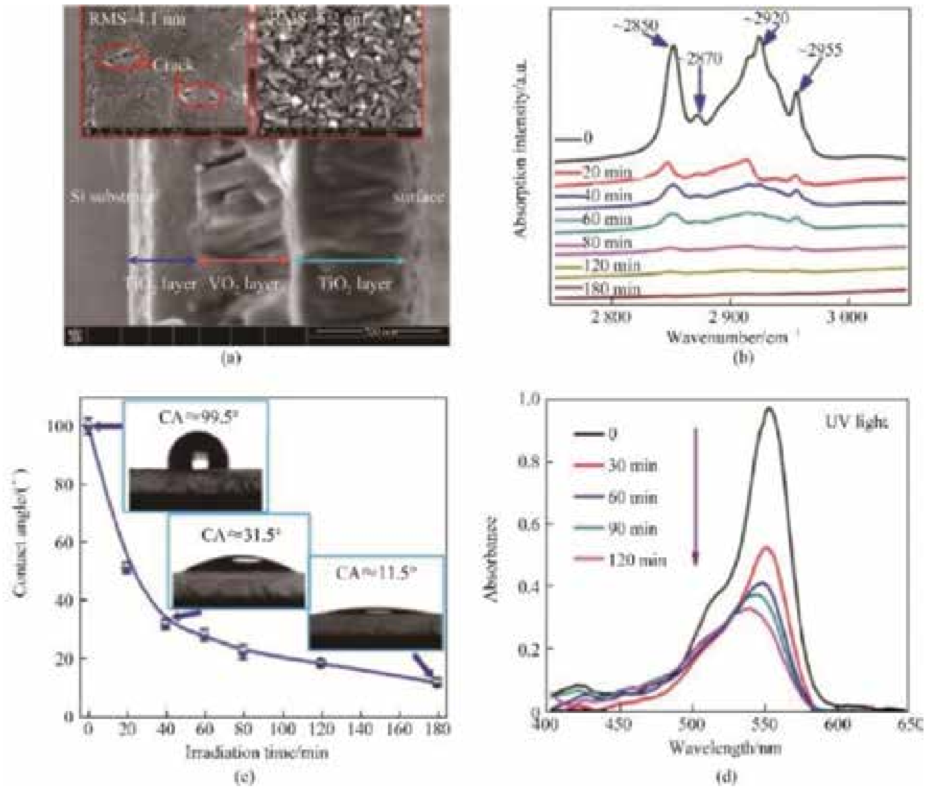

Figure 7. (a) FESEM image of a fractured cross section of the multilayer film (the insets are surface morphology of VO_2(M) (left) and TiO_2(A) layers (right), respectively), (b) IR absorbance spectra of TiO_2(R)/VO_2(M)/TiO_2(A) multilayer film with stearic acid overlayer at various irradiation time under UV light, (c) CAs of the multilayer film with stearic acid overlayer dependence on irradiation time (the insets correspond to water droplet shapes on the surface), (d) variation of absorption spectra of RhB aqueous solution degraded by the multilayer film.

vibrations of CH_2 and CH_3 groups (3000–2800 cm^{-1}) can be distinctly detected. After UV light irradiation of 20 min, the absorbance of C—H bond stretching vibrations decreased drastically, which means that a considerable proportion of stearic acid was decomposed. The IR absorbance slowly became weak with the increase of irradiation time, and finally almost faded away after 180 min irradiation time. In addition, the degradation of stearic acid also can be confirmed by the changes of the contact angle of the multilayer film. The contact angles of the surface transform from 99.5° (hydrophobic) to 11.5° (hydrophilic) (see **Figure 7(c)**), which can be ascribed to the degradation of stearic acid and the photoinduced hydrophilicity of multilayer film. The photocatalytic activity of TiO_2(R)/VO_2(M)/TiO_2(A) multilayer film also has been demonstrated by the decomposition rate of RhB under UV light irradiation. **Figure 7(d)** shows that the absorption spectra of RhB aqueous solution degraded by the multilayer film under UV light irradiation. Thermochromic smart coatings with self-cleaning function have also been achieved by the $VO_2/SiO_2/TiO_2$ structure where the SiO_2 layer acts as the ion-barrier interlayer [68]. The proposed VST structure shows a significant degradation rate of stearic acid and is comparable to that of a standard Pilkington Activ glass, which is a commercially available self-cleaning glass, which contains a thin TiO_2 layer (15 nm) deposited by CVD methods.

For self-cleaning function and improved stability, VO_2 thermochromic smart coatings with hydrophobic surface have been favored and studied by researchers. VO_2 films with moth-eye

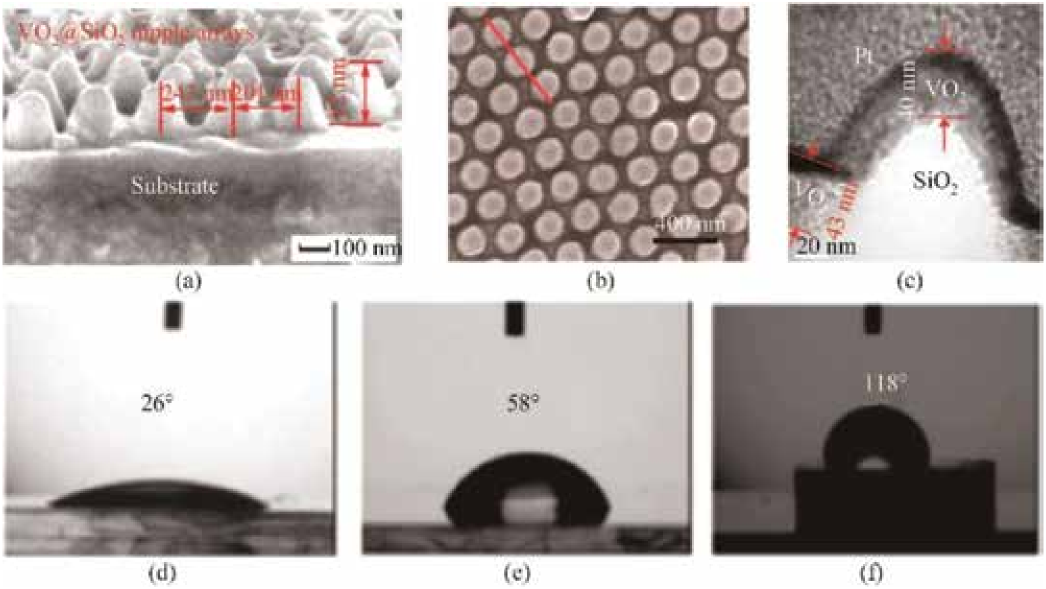

Figure 8. (a) SEM cross-sectional profile of the sample with 210 nm period, (b) top-view SEM image of the sample with 440 nm period, (c) TEM cross-sectional image to show the thickness of VO_2 coatings on SiO_2, (d) planar VO_2, 210 nm patterned VO_2 with 40 nm thickness, and 210 nm patterned VO_2 with fluorooctyl triethoxysilane (FOS) overcoat.

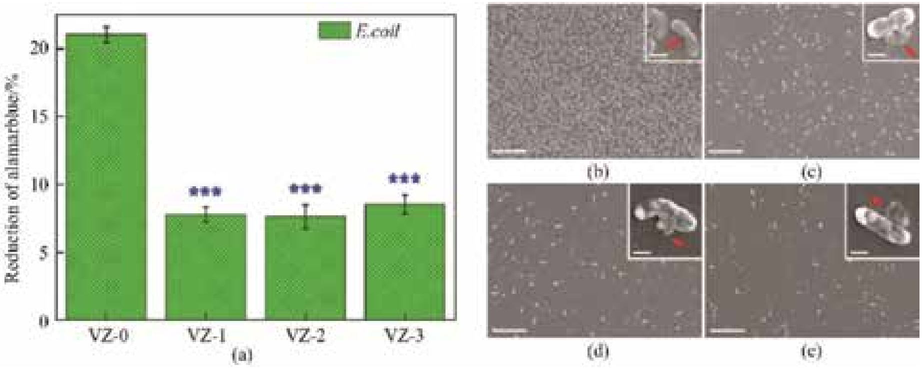

Figure 9. (a) Proliferation viability of *Escherichia coli* after culture of 24 h on samples VZ-0, VZ-1, VZ-2 and VZ-3, accompanied by the SEM morphology of *E. coli* after culture of 24 h on surfaces of (b) VZ-0, (c) VZ-1, (d) VZ-2 and (e) VZ-3 (the scale bar is 20 μm. The insets show the corresponding partially enlarged SEM images and the scale bar is 1 μm).

nanostructures have been fabricated to enhance the thermochromic properties, and the hydrophobic surface (contact angle 120°) can be achieved with additional overcoat [85]. Fused silica substrates with AR patterns of different periods (0, 210, 440, 580, and 1000 nm) were prepared by reactive ion etching using 2D polystyrene colloidal crystals as a mask. Nipple arrays based on VO_2/SiO_2 have been realized and the additional fluorooctyl triethoxysilane (FOS) overcoat provides hydrophobicity of the surface (see **Figure 8**).

The biosafety of VO_2 is also under consideration, while the ZnO layer has been used to provide the antibacterial property [86]. ZnO-coated VO_2 thin films exhibited excellent antibacterial property proved by SEM observation results that ZnO-coated samples cause the membrane disruption and cytoplasm leakage of *E. coli* cells and fluorescence staining results that the amounts of viable bacteria are evidently lower on the surface of ZnO-coated films than that of uncoated films (see **Figure 9**). The sterilization mechanism of ZnO films is believed to be attributed to the synergistic effect of released zinc ions and ZnO nanoparticles by elaborately designing a verification experiment. More importantly, the ZnO layer with an appropriate thickness can significantly reduce the cytotoxicity of VO_2 and thus promote the VO_2 biosafety.

5. Large-scale production of VO_2 smart coatings

For commercial applications on building fenestrations in our daily life, large-scale production of VO_2-based smart coatings is a great challenge that must be developed. For VO_2-based films, magnetron sputtering is the most commonly used method and several works about large-scale production of VO_2-based films by magnetron sputtering have been reported. A large-scale TiO_2(R)/VO_2 (M)/TiO_2 (A) multilayer film was prepared on a glass with the area of 400 × 400 mm^2 using magnetron sputtering method by Zheng et al. [11], where a combination of energy-saving, antifogging, and self-cleaning functions has been achieved (see **Figure 10(a)**). TiO_2(R)/VO_2 (M)/TiO_2 (A) multilayer film was deposited using medium frequency reactive magnetron sputtering (MFRMS, see **Figure 10(b)**) system to sputter planar rectangular metal targets in a suitable atmosphere. The proposed structure shows excellent ability to block out infrared irradiation, which causes a temperature reduction of 12°C compared with the blank glass (see **Figure 10(c)**).

The magnetron sputtering coating system could be applied in architecture commercial glasses, and the designed large area sputtering cathode can make the coating on large area glass substrates. The optimized design and precise manufacturing can guarantee to get a higher vacuum and a shorter cycle time by using a smaller pumping system. Sputtering is a vacuum process used to deposit thin films on substrates. It is performed by applying a high voltage across a low-pressure gas (usually argon) to create a “plasma,” which consists of electrons and gas ions in a high-energy state. During sputtering, energized plasma ions strike the target, which is composed of the desired coating material, and causes atoms from that target to be ejected with enough energy to travel to and bond with the substrate (see **Figure 10(d)**).

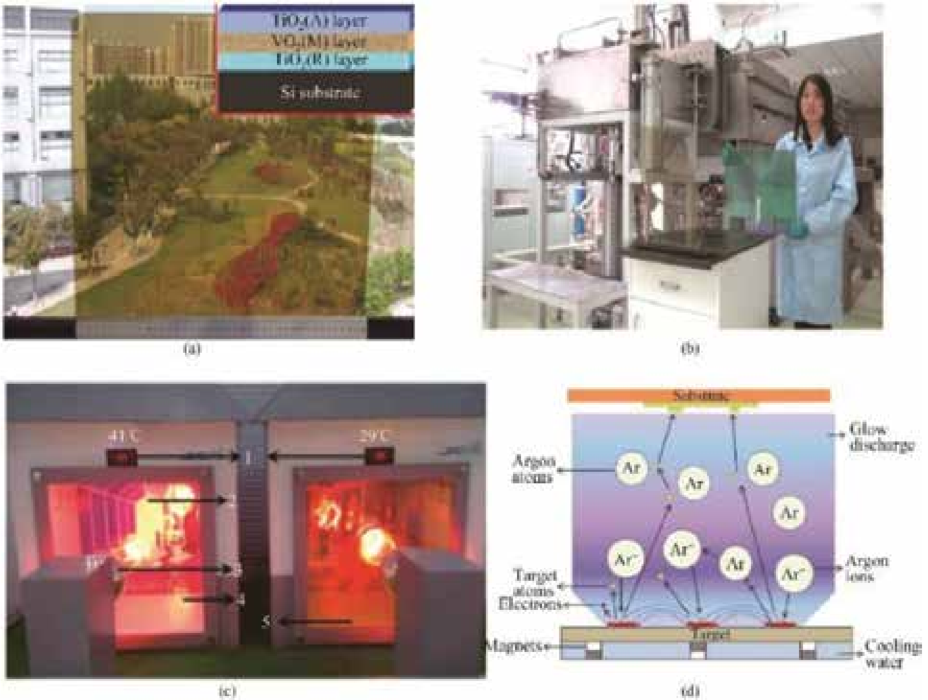

Figure 10. (a) Photograph of large-scale (400 × 400 mm) multilayer film at room temperature (the inset is corresponding structure diagram of the multilayer film), (b) photograph of the magnetron sputtering system, (c) photographic illustration of the testing system, 1: Temperature monitor, 2: Temperature probe, 3: Infrared lamps, 4: Blank glass, 5: Glass with TiO_2(R)/VO_2(M)/TiO_2(a) multilayer film, (d) schematic diagram illustrating the basic components of a magnetron sputtering system.

6. Conclusion and prospects

As the most attractive thermochromic technology, VO_2-based smart coatings have gained great attention by researchers and many efforts have been made to promote the real commercialization. Method of multilayer structures has been carried out to improve thermochromic performance with enhanced luminous transmittance, solar modulation ability, and environmental stability. However, more efforts are still needed to make this technology into our daily lives.

I. Optical performances of VO_2 thermochromic smart coatings can be improved by methods, such as element doping, fabricating multilayer structures, and designing nanostructures. For practical applications, VO_2-based smart coatings should have 50% luminous transmittance and 15% solar modulation ability for sufficient energy-saving effect. Optical properties of VO_2 smart coatings can be further improved by computational calculations and simulations for better luminous transmittance and solar modulation ability.

II. Environmental stability of VO_2 coatings is a great challenge for long-time use. Protective layers for VO_2 films can effectively improve the environmental stability of VO_2 coatings.

Future work can be carried out by choosing materials with versatility for protective, antireflection, and self-cleaning functions.

III. Large-scale production of VO_2 smart coatings is necessary to turn this technology from the lab into the industrial and commercial application. Traditional methods, such as hydrothermal synthesis, spray pyrolysis, and sol–gel, etc., are limited due to their low production and complicated process. An effective way to solve this problem is fabricating VO_2-based smart coatings during the production of glasses, just like the deposition of low-emissivity (low-E) coatings on the glass production lines.

Acknowledgements

We want to thank Tianci Chang for discussion about the VO_2 materials. This chapter was financially supported by the National Natural Science Foundation of China (Grant No. 51572284) and the "Youth Innovation Promotion Association, Chinese Academy of Sciences" (Grant No.2018288).

Conflict of interest

There is no conflict of interest to declare.

Author details

Xun Cao* and Ping Jin

*Address all correspondence to: caoxun2015@gmail.com

State Key Laboratory of High Performance Ceramics and Superfine Microstructure,
Shanghai Institute of Ceramics, Chinese Academy of Sciences, Shanghai, China

References

[1] Omer AM. Energy, environment and sustainable development. Renewable and Sustainable Energy Reviews. 2008;**12**:2265-2300

[2] Granqvist CG, Lansåker PC, Mlyuka NR, et al. Progress in chromogenics: New results for electrochromic and thermochromic materials and devices. Solar Energy Materials and Solar Cells. 2009;**93**(12):2032-2039

[3] Granqvist CG. Electrochromics and thermochromics: Towards a new paradigm for energy efficient buildings. Materials Today: Proceedings. 2016;**3**:S2-S11

[4] Granqvist CG. Recent progress in thermochromics and electrochromics: A brief survey. Thin Solid Films. 2016;**614**:90-96

[5] Granqvist CG, Green S, Niklasson GA, et al. Advances in chromogenic materials and devices. Thin Solid Films. 2010;**518**(11):3046-3053

[6] Granqvist CG, Pehlivan IB, Ji YX, et al. Electrochromics and thermochromics for energy efficient fenestration: Functionalities based on nanoparticles of In_2O_3: Sn and VO_2. Thin Solid Films. 2014;**559**:2-8

[7] Deb SK. Opportunities and challenges in science and technology of WO_3 for electrochromic and related applications. Solar Energy Materials and Solar Cells. 2008;**92**(2):245-258

[8] Granqvist CG. Oxide-based chromogenic coatings and devices for energy efficient fenestration: brief survey and update on thermochromics and electrochromics. Journal of Vacuum Science & Technology B. 2014;**32**(6), 060801:1-13

[9] Wang J, Zhang L, Yu L, et al. A bi-functional device for self-powered electrochromic window and self-rechargeable transparent battery applications. Nature Communications. 2014;**5**(4921):1-7

[10] Granqvist CG. Oxide electrochromics: An introduction to devices and materials. Solar Energy Materials and Solar Cells. 2012;**99**:1-13

[11] Zheng J, Bao S, Jin P. TiO_2(R)/VO_2(M)/TiO_2(A) multilayer film as smart window: Combination of energy-saving, antifogging and self-cleaning functions. Nano Energy. 2015;**11**:136-145

[12] Chang T, Cao X, Li N, et al. Facile and low-temperature fabrication of thermochromic Cr_2O_3/VO_2smart coatings: Enhanced solar modulation ability, high luminous transmittance and UV-shielding function. ACS Applied Materials & Interfaces. 2017;**9**(31):26029-26037

[13] Babulanam SM, Eriksson TS, Niklasson GA, et al. Thermochromic VO_2 films for energy-efficient windows. Solar Energy Materials. 1987;**16**(5):347-363

[14] Sobhan MA, Kivaisi RT, Stjerna B, et al. Thermochromism of sputter deposited $W_xV_{1-x}O_2$ films. Solar Energy Materials and Solar Cells. 1996;**44**(4):451-455

[15] Shen N, Li Y, Yi XJ. Preparation of VO_2 films with nanostructure and improvement on its visible transmittance. Journal of Infrared and Millimeter Waves. 2006;**25**(3):199-202

[16] Soltani M, Chaker M, Haddad E, et al. Thermochromic vanadium dioxide smart coatings grown on Kapton substrates by reactive pulsed laser deposition. Journal of Vacuum Science & Technology A: Vacuum, Surfaces, and Films. 2006;**24**(3):612-617

[17] Binions R, Hyett G, Piccirillo C, et al. Doped and un-doped vanadium dioxide thin films prepared by atmospheric pressure chemical vapour deposition from vanadyl acetylacetonate and tungsten hexachloride: The effects of thickness and crystallographic orientation on thermochromic properties. Journal of Materials Chemistry. 2007;**17**(44):4652-4660

[18] Evans P, Pemble ME, Sheel DW, et al. Multi-functional self-cleaning thermochromic films by atmospheric pressure chemical vapour deposition. Journal of Photochemistry and Photobiology A: Chemistry. 2007;**189**(2-3):387-397

[19] Shi JQ, Zhou SX, You B, et al. Preparation and thermochromic property of tungsten-doped vanadium dioxide particles. Solar Energy Materials and Solar Cells. 2007;**91**(19):1856-1862

[20] La M, Zhou H, Li N, et al. Improved performance of Mg-Y alloy thin film switchable mirrors after coating with a superhydrophobic surface. Applied Surface Science. 2017;**403**:23-28

[21] Jang WL, Lu YM, Chen CL, et al. Local geometric and electronic structures of gasochromic VO(x) films. Physical Chemistry Chemical Physics. 2014;**16**(10):4699-4708

[22] Wittwer V, Datz M, Ell J, et al. Gasochromic windows. Solar Energy Materials and Solar Cells. 2004;**84**(1-4):305-314

[23] Li N, Li Y, Sun G, et al. Selective and tunable near-infrared and visible light transmittance of MoO_{3-x} nanocomposites with different crystallinity. Chemistry, an Asian Journal. 2017;**12**(14):1709-1714

[24] Li N, Li Y, Li W, et al. One-step hydrothermal synthesis of TiO_2@MoO_3 core-shell nanomaterial: Microstructure, growth mechanism, and improved photochromic property. The Journal of Physical Chemistry C. 2016;**120**(6):3341-3349

[25] Li N, Li Y, Zhou Y, et al. Interfacial-charge-transfer-induced photochromism of MoO_3@ TiO_2 crystalline-core amorphous-shell nanorods. Solar Energy Materials and Solar Cells. 2017;**160**:116-125

[26] Li N, Li Y, Sun G, et al. Enhanced photochromic modulation efficiency: A novel plasmonic molybdenum oxide hybrid. Nanoscale. 2017;**9**(24):8298-8304

[27] Kamalisarvestani M, Saidur R, et al. Materials and coatings technologies of thermochromic thin films on smart windows. Renewable and Sustainable Energy Reviews. 2013;**26**:353-354

[28] Hoffmann S, Lee E, et al. Examination of the technical potential of near-infrared switching thermochormic windows for commercial building applications. Solar Energy Materials & Solar Cells. 2014;**123**:65-80

[29] Lee E, Pang X, et al. An empirical study of a full-scale polymer thermochromic window and its implications on material science development objective. Solar Energy Materials & Solar Cells. 2013;**116**:14-26

[30] Morin FJ. Oxides which show a metal-to-insulator transition at the Neel temperature. Physical Review Letters. 1959;**3**(1):34-36

[31] Zhang Z, Gao Y, Luo H, et al. Solution-based fabrication of vanadium dioxide on F: SnO_2 substrates with largely enhanced thermochromism and low-emissivity for energy-saving applications. Energy & Environmental Science. 2011;**4**(10):4290-4297

[32] Gao Y, Wang S, Luo H, et al. Enhanced chemical stability of VO_2 nanoparticles by the formation of SiO_2/VO_2 core/shell structures and the application to transparent and flexible VO_2-based composite foils with excellent thermochromic properties for solar heat control. Energy & Environmental Science. 2012;**5**(3):6104-6110

[33] Chang T, Cao X, Dedon LR, et al. Optical design and stability study for ultrahigh-performance and long-lived vanadium dioxide-based thermochromic coatings. Nano Energy. 2018;**44**:256-264

[34] Gao Y, Wang S, Kang L, et al. VO_2-Sb: SnO_2 composite thermochromic smart glass foil. Energy & Environmental Science. 2012;**5**(8):8234-8237

[35] Gao Y, Luo H, Zhang Z, et al. Nanoceramic VO_2 thermochromic smart glass: A review on progress in solution processing. Nano Energy. 2012;**1**(2):221-246

[36] Warwick MEA, Binions R. Advances in thermochromic vanadium dioxide films. Journal of Materials Chemistry A. 2014;**2**(10):3275-3292

[37] Li Y, Ji S, Gao Y, et al. Core-shell VO_2@TiO_2 nanorods that combine thermochromic and photocatalytic properties for application as energy-saving smart coatings. Scientific Reports. 2013;**3**:1370

[38] Sun G, Cao X, Zhou H, et al. A novel multifunctional thermochromic structure with skin comfort design for smart window application. Solar Energy Materials & Solar Cells. 2017;**159**:553-559

[39] Sun G, Cao X, Li X, et al. Low-temperature deposition of VO_2 films with high crystalline degree by embedding multilayered structure. Solar Energy Materials and Solar Cells. 2017;**161**:70-76

[40] Sun G, Zhou H, Cao X, et al. Self-assembled multilayer structure and enhanced thermochromic performance of spinodally decomposed TiO_2-VO_2 thin film. ACS Applied Materials & Interfaces. 2016;**8**(11):7054-7059

[41] Li S, Li Y, Qian K, et al. Functional fiber mats with tunable diffuse reflectance composed of electrospun VO_2/PVP composite fibers. ACS Applied Materials & Interfaces. 2014;**6**(1):9-13

[42] Li Y, Ji S, Gao Y, et al. Core-regenerated vapor–solid growth of hierarchical stem-like VO_x nanocrystals on VO_2@TiO_2 core–shell nanorods: Microstructure and mechanism. Crystal Engineering and Communications. 2013;**15**(41):8330-8336

[43] Li S, Li Y, Jiang M, et al. Preparation and characterization of self-supporting thermochromic films composed of VO_2(M)@SiO_2 nanofibers. ACS Applied Materials & Interfaces. 2013;**5**(14):6453-6457

[44] Li Y, Ji S, Gao Y, et al. Modification of Mott phase transition characteristics in VO_2@TiO_2 core/shell nanostructures by misfit-strained heteroepitaxy. ACS Applied Materials & Interfaces. 2013;**5**(14):6603-6614

[45] Li R, Ji S, Li Y, et al. Synthesis and characterization of plate-like VO_2(M)@SiO_2 nanoparticles and their application to smart window. Materials Letters. 2013;**110**:241-244

[46] Chen Y, Zeng X, Zhu J, et al. High performance and enhanced durability of thermochromic films using VO_2@ZnO core-shell nanoparticles. ACS Applied Materials & Interfaces. 2017;**9**(33):27784-27791

[47] Ke Y, Wen X, Zhao D, et al. Controllable fabrication of two-dimensional patterned VO_2 nanoparticle, nanodome, and nanonet arrays with tunable temperature-dependent localized surface plasmon resonance. ACS Nano. 2017;**11**(7):7542-7551

[48] Zhu J, Huang A, Ma H, et al. Hybrid films of VO_2 nanoparticles and a nickel(ii)-based ligand exchange thermochromic system: Excellent optical performance with a temperature responsive colour change. New Journal of Chemistry. 2017;**41**(2):830-835

[49] Li Y, Jiang P, Xiang W, et al. A novel inorganic precipitation-peptization method for VO_2 sol and VO_2 nanoparticles preparation: Synthesis, characterization and mechanism. Journal of Colloid and Interface Science. 2016;**462**:42-47

[50] Wan J, Ren Q, Wu N, et al. Density functional theory study of M-doped (M = B, C, N, mg, Al) VO_2 nanoparticles for thermochromic energy-saving foils. Journal of Alloys and Compounds. 2016;**662**:621-627

[51] Li M, Wu H, Zhong L, et al. Active and dynamic infrared switching of VO_2 (M) nanoparticle film on ITO glass. Journal of Materials Chemistry C. 2016;**4**(8):1579-1583

[52] Lan S, Cheng C, Huang C, et al. Synthesis of sub-10 nm VO_2 nanoparticles films with plasma-treated glass slides by aqueous sol-gel method. Applied Surface Science. 2015;**357**:2069-2076

[53] Liu H, Wan D, Ishaq A, et al. Sputtering deposition of sandwich-structured V_2O_5/metal (V, W)/V_2O_5 multilayers for the preparation of high-performance thermally sensitive VO_2 thin films with selectivity of VO_2 (B) and VO_2 (M) polymorph. ACS Applied Materials & Interfaces. 2016;**8**(12):7884-7890

[54] Mlyuka NR, Niklasson GA, Granqvist CG. Thermochromic VO_2-based multilayer films with enhanced luminous transmittance and solar modulation. Physica Status Solidi a—Applications and Materials Science. 2009;**206**(9):2155-2160

[55] Mlyuka NR, Niklasson GA, Granqvist CG. Thermochromic multilayer films of VO_2 and TiO_2 with enhanced transmittance. Solar Energy Materials and Solar Cells. 2009;**93**(9):1685-1687

[56] Ji Y, Li S, Niklasson GA, et al. Durability of thermochromic VO_2 thin films under heating and humidity: Effect of Al oxide top coatings. Thin Solid Films. 2014;**562**:568-573

[57] Zhu J, Zhou Y, Wang B, et al. Vanadium dioxide nanoparticle-based thermochromic smart coating: High luminous transmittance, excellent solar regulation efficiency, and near room temperature phase transition. ACS Applied Materials & Interfaces. 2015;**7**(50):27796-27803

[58] Lv W, Huang D, Chen Y, et al. Synthesis and characterization of Mo-W co-doped VO_2(R) nano-powders by the microwave-assisted hydrothermal method. Ceramics International. 2014;**40**(8):12661-12668

[59] Piccirillo C, Binions R, Parkin IP. Nb-doped VO_2 thin films prepared by aero sol-assisted chemical vapour deposition. European Journal of Inorganic Chemistry. 2007;**25**:4050-4055

[60] Burkhardt W, Christmann T, Meyer BK, et al. W- and F-doped VO_2 films studied by photoelectron spectrometry. Thin Solid Films. 1999;**345**(2):229-235

[61] Li SY, Niklasson GA, Granqvist CG. Thermochromic fenestration with VO_2-based materials: Three challenges and how they can be met. Thin Solid Films. 2012;**520**(10):3823-3828

[62] Li M, Magdassi S, Gao Y et al. Hydrothermal synthesis of VO_2 polymorphs: advantages, challenges and prospects for the application of energy efficient smart windows. Small. 2017;**13**(36), 1701147:1-25

[63] Jin P, Xu G, Tazawa M, et al. Design, formation and characterization of a novel mutifunctional window with VO_2 and TiO_2 coatings. Applied Physics A: Materials Science & Processing. 2003;**77**(3-4):455-459

[64] Zhu BQ, Tao HZ, Zhao XJ. Effect of buffer layer on thermochromic performances of VO_2 films fabricated by magnetron sputtering. Infrared Physics & Technology. 2016;**75**:22-25

[65] Panagopoulou M, Gagaoudakis E, Boukos N, et al. Thermochromic performance of Mg-doped VO_2 thin films on functional substrates for glazing applications. Solar Energy Materials & Solar Cells. 2016;**157**:1004-1010

[66] Long S, Zhou H, Bao S, et al. Thermochromic multilayer films of $WO_3/VO_2/WO_3$ sandwich structure with enhanced luminous transmittance and durability. RSC Advances. 2016;**6**(108):106435-106442

[67] Sun GY, Cao X, Gao X et al. Structure and enhanced thermochromic performance of low-temperature fabricated VO_2/V_2O_3thin film. Applied Physics Letters. 2016;**109**(14), 143903:1-5

[68] Powell MJ, Quesada-Cabrera R, Taylor A, et al. Intelligent multifunctional $VO_2/SiO_2/TiO_2$ coatings for self-cleaning, energy-saving window panels. Chemistry of Materials. 2016;**28**(5):1369-1376

[69] Li D, Shan Y, Huang F, et al. Sol-gel preparation and characterization of SiO_2 coated VO_2 films with enhanced transmittance and high thermochromic performance. Applied Surface Science. 2014;**317**:160-166

[70] Lee M, Cho J. Better thermochromic glazing of windows with anti-reflection coating. Thin Solid Films. 2000;**365**(1):5-6

[71] Lee M. Thermochromic glazing of windows with better luminous solar transmittance. Solar Energy Materials and Solar Cells. 2002;**71**(4):537-540

[72] Zhang J, Wang J, Yang C, et al. Mesoporous SiO_2/VO_2 double-layer thermochromic coating with improved visible transmittance for smart window. Solar Energy Materials & Solar Cells. 2017;**162**:134-141

[73] Jin P, Xu G, Tazawa M, et al. A VO_2-based multifunctional window with highly improved luminous transmittance. Japanese Journal of Applied Physics. 2002;**41**(Part 2, No. 3A):L278-L280

[74] Xu G, Jin P, Tazawa M, et al. Optimization of antireflection coating for VO_2-based energy efficient window. Solar Energy Materials and Solar Cells. 2004;**83**(1):29-37

[75] Panagopoulou M, Gagaoudakis E, Aperathitis E, et al. The effect of buffer layer on the thermochromic properties of undoped radio frequency sputtered VO_2 thin films. Thin Solid Films. 2015;**594**:310-315

[76] Koo H, Xu L, Ko KE, et al. Effect of oxide buffer layer on the thermochromic properties of VO_2 thin films. Journal of Materials Engineering and Performance. 2013;**22**(12):3967-3973

[77] Koo H, You H, Ko KE, et al. Thermochromic properties of VO_2 thin film on SiN_x buffered glass substrate. Applied Surface Science. 2013;**277**:237-241

[78] Zhu J, Huang A, Ma H, et al. Composite film of vanadium dioxide nanoparticles and ionic liquid-nickel-chlorine complexes with excellent visible thermochromic performance. ACS Applied Materials & Interfaces. 2016;**8**(43):29742-29748

[79] Wang X, Cao Y, Yang C, et al. Vanadium dioxide film protected with an atomic-layer-deposited Al_2O_3 thin film. Journal of Vacuum Science & Technology A: Vacuum, Surfaces, and Films. 2016;**34**(1), 01A106):1-7

[80] Saitzek S, Guinneton F, Sauques L, et al. Thermochromic CeO_2-VO_2 bilayers: Role of ceria coating in optical switching properties. Optical Materials. 2007;**30**(3):407-415

[81] Saitzek S, Guirleo G, Guinneton F, et al. New thermochromic bilayers for optical or electronic switching systems. Thin Solid Films. 2004;**449**(1-2):166-172

[82] Pan GT, Yang YL, Chong SH, et al. The durability study of thermochromic vanadium dioxide films with the addition of barrier coatings. Vacuum. 2017;**145**:158-168

[83] Fahlteich J, Fahland M, Schönberger W, et al. Permeation barrier properties of thin oxide films on flexible polymer substrates. Thin Solid Films. 2009;**517**(10):3075-3080

[84] Zhan Y, Xiao X, Lu Y, et al. Enhanced thermal stability and thermochromic properties of VO_x -based thin films by room-temperature magnetron sputtering. Solar Energy Materials and Solar Cells. 2018;**174**:102-111

[85] Qian X, Wang N, Li Y, et al. Bioinspired multifunctional vanadium dioxide: Improved thermochromism and hydrophobicity. Langmuir. 2014;**30**(35):10766-10771

[86] Zhou H, Li J, Bao S, et al. Use of ZnO as antireflective, protective, antibacterial, and biocompatible multifunction nanolayer of thermochromic VO_2 nanofilm for intelligent windows. Applied Surface Science. 2016;**363**:532-542

Chapter 2

Nanopyramid Structures with Light Harvesting and Self-Cleaning Properties for Solar Cells

Amalraj Peter Amalathas and Maan M. Alkaisi

Additional information is available at the end of the chapter

http://dx.doi.org/10.5772/intechopen.75314

Abstract

In this chapter, inverted and upright nanopyramid structures with light-harvesting properties and self-cleaning hydrophobic surfaces suitable for solar cells are presented. Periodic nanopyramid structures with 400–700 nm features were fabricated using interference lithography and combined dry and wet etching processes. The inverted nanopyramids (INP) were applied at the front side of the solar cells using UV nanoimprint lithography. These structures provided effective light-trapping properties and led to oblique angle light scattering and a significant reduction in reflectance resulting in higher power conversion efficiency. The second type, the periodic upright nanopyramid (UNP) structures were applied on a glass substrate by UV nanoimprint process. The glass cover is also utilized as a protective encapsulant front layer. The use of the upright nanopyramid structured cover glass in the encapsulated solar cell has also enhanced the power conversion efficiency due to the antireflection and strong light-scattering properties compared to the bare cover glass. In addition, the upright nanopyramid structured cover glass exhibited excellent self-cleaning of dust particles by rolling down water droplets. These results suggest that the nanopyramid structures with light-harvesting and self-cleaning properties can improve the performance of different types of solar cells, including thin films and glass-based PVs.

Keywords: solar cells, light-harvesting, self-cleaning, nanopyramids, laser interference lithography, nanoimprint lithography

1. Introduction

Reducing optical losses in the solar cells has always been a key factor in enhancing the conversion efficiency. In general, efficient light management has been achieved by textured surfaces that enhance the light collection and increasing the effective optical path length of the light within the absorber layer of a solar cell [1]. Various texturing methods have been carried out such as texturing at the rear side [2] or the front side of a solar cell [3] or pre-texturing the thin film solar cell substrates [4, 5] in addition to the wide variety of light management schemes that are based on microscale structures that have been investigated to enhance the power conversion efficiency of solar cells. However, the use of nanostructures for improving the light absorption and trapping in solar cells is a more promising method compared to the traditional microsized surface texturing [6]. This is because of the lower level of induced damage and the ease of coating different surfaces and materials.

Nanostructures can be fabricated by various techniques, including electron beam lithography (EBL) [7], laser interference lithography (LIL) [8, 9], nanoimprint lithography (NIL) [10, 11], nanosphere lithography (NSL) [12] and block copolymer lithography (BCPL) [13]. Among them, the UV nanoimprint lithography (UV-NIL) is emerging as a powerful technique for fabricating nanoscale structures on large scale surfaces with simple, high-throughput, low-cost and high-resolution manufacturing capability [14]. Various nanostructures such as nanowires [15], nanorods [16], nanocones [17], nanopyramids [18], nanopillars [19] and metal nanostructures such as nanogrooves [20] and nanoparticle arrays [21] have been extensively studied. Despite their excellent light-trapping properties, texturing the active solar cell layer or introducing metal nanostructures within the cell results in poor charge carrier collection due to increased surface recombination. Fang Jiao et al. [22] demonstrated that the imprinting of moth-eye-like structures on the front side of monocrystalline Si solar cell surface enhanced the conversion efficiency by 19% compared to the planar solar cell through coupling the incident light into the absorber layer.

This chapter describes an approach of surface texturing which is different from other reported methods such as texturing the active material or using metal nanostructures. It is expected that nanopyramids coating approach might be enhanced solar cell performance without introducing additional surface recombination and excellent solar cell self-cleaning functionality.

Solar cell modules are installed in an outdoor environment for the vast majority of applications. Therefore, whatever the type of solar cell, glass is commonly incorporated as an encapsulation for preventing damage from dust, moisture and external shock [23, 24]. However, some of the incident light onto the solar cells will be lost through optical reflection due to the refractive index mismatch between the air and cover glass and through scattering or absorption by contaminants [25, 26]. In Section 2.3, it is shown that the amount of the incident light reaching the solar cell could be enhanced by incorporating antireflective and light-scattering nanostructures at the cover glass surface. Moreover, it is also demonstrated in Section 2.4 that the nanostructured cover glass has self-cleaning property and efficiently maintains the performance of solar cells in harsh environments.

The oblique light-scattering effect offered by the nanopyramids improves the light harvesting of the solar cells as a result of prolonged optical path length within the solar cells and thus, increasing the conversion efficiency [27, 28]. Several other research groups [29–31] have studied the use of cover glass that combines the antireflective and scattering effects with self-cleaning properties and examined their influence on the overall efficiency of the solar cells.

In this chapter, nanopyramid structures with light-harvesting properties and self-cleaning functionality are demonstrated on monocrystalline Si solar cells. Firstly, the fabrication process of coating monocrystalline solar cells with the periodic inverted or upright nanopyramid (UNP) structures using LIL and UV-NIL are presented. Secondly, the optical properties and surface wetting behavior of the upright nanopyramid (UNP) structured cover glass are presented. Also, the electrical performance of the solar cells with upright nanopyramid structured cover glass is examined in detail and compared to the performance of bare cover glass. Finally, the optical, electrical and wetting properties of the solar cells coated with the inverted nanopyramid (INP) structures are investigated.

2. Upright nanopyramid structured cover glass for solar cells

2.1. Fabrication of upright nanopyramid structures on a glass substrate

The UV nanoimprint lithography process is used for the replication of the upright nanopyramid (UNP) structures on glass substrates. The process flow diagram of the UV imprint is shown in **Figure 1**. First, the periodic inverted nanopyramid structures were formed on the Si master mold using laser interference lithography and subsequent pattern transfer process using reactive ion etching followed by KOH wet etching. Details of the fabrication process of the master mold are described in Ref. [9]. A UV curable resist (OrmoStamp) was spincoated onto a glass substrate and afterward the substrate was placed over the Si mold with the inverted nanopyramids inside the imprint tool. An imprint pressure of up to 4 mbar was applied to transfer the patterns with a

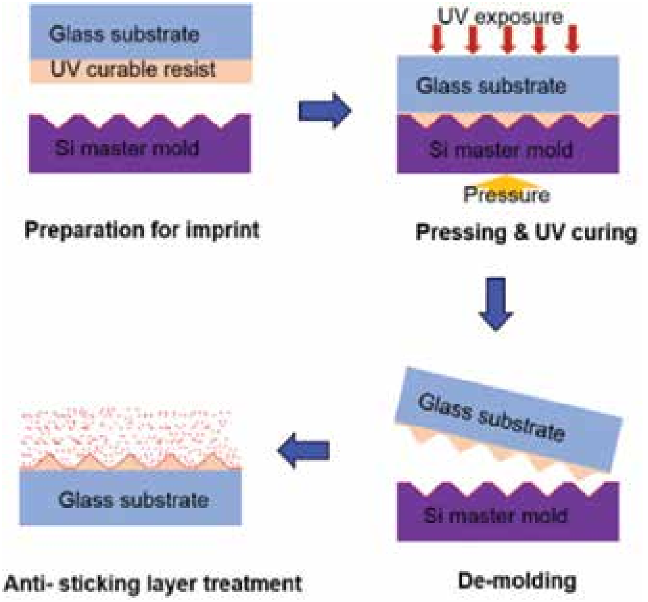

Figure 1. The schematic diagram of the overall fabrication process of upright nanopyramid structures on the glass.

UV light illumination of wavelength 365 nm. The upright nanopyramid pattern was successfully replicated from the Si mold onto the glass substrate with high fidelity. After the UV nanoimprint process, F_{13}-TCS-based SAM was coated onto the upright nanopyramid patterned glass substrate in order to increase the hydrophobicity of the surface. More details of the UV nanoimprint process parameters and the tools which were employed can be found in Ref. [32].

The surface morphologies of the inverted and upright nanopyramid structures were examined by using scanning electron microscope (SEM) (JEOL 7000F FE-SEM) and atomic force microscope (AFM, DI3000). **Figure 2(a)** and **(c)** presents the SEM images and AFM image of the Si master mold with inverted nanopyramid structures, respectively. **Figure 2(b)** and **(d)** shows the SEM images and AFM images of the upright nanopyramid structured glass replicated from the master mold, respectively. As illustrated in **Figure 2(b)**, the inverted nanopyramid patterns on the Si master mold were transferred onto the UV curable resist coated glass substrate without any distortion and deformation using UV nanoimprint lithography. This is also confirmed in the AFM image in **Figure 2(d)**. As shown in **Figure 2**, the 450 nm wide and 310 nm high UNP structures with 125 nm separation were replicated uniformly over an area of 10x10 mm after the imprint process.

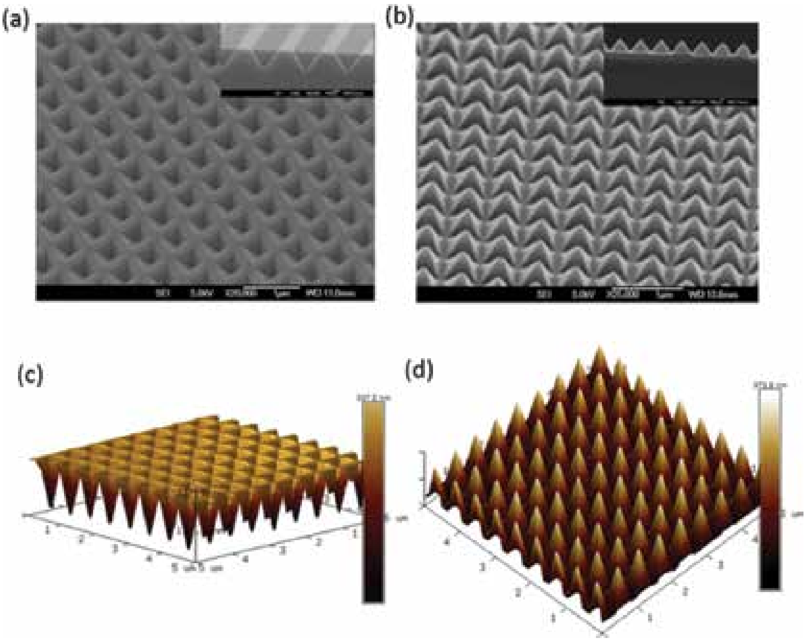

Figure 2. 30°-tilted view SEM images of (a) inverted nanopyramid Si master mold and (b) upright nanopyramid structured on the glass, and the inset images are the cross-sectional views of SEM images. Three-dimensional AFM images (c) inverted nanopyramid Si master mold and (d) upright nanopyramid structured glass.

2.2. Solar cell fabrication

Monocrystalline Si solar cells were fabricated by the process shown in **Figure 3**. A single-side-polished, Czochralski (CZ) grown, 350 μm thick, boron doped p-type silicon wafer with <100>

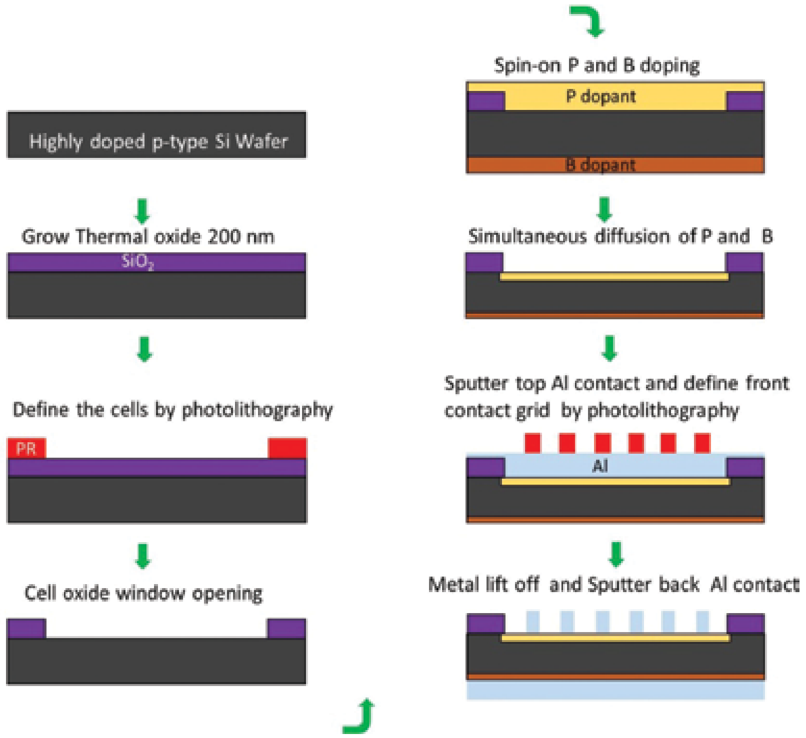

Figure 3. The schematic representation of monocrystalline Si solar cell fabrication process.

crystal orientation and resistivity of 0.5–1.0 Ωcm was used as the substrate. After piranha cleaning and 1:10 dilute HF dipping, a 200 nm thermal oxide was grown on the wafer using quartz tube furnace and dry/wet oxidation was done at 1000°C. The 10 mm × 10 mm individual cells were defined by photolithography, and buffered HF etching was performed to isolate the individual cells by opening windows in the oxide. The wafer backside was doped with boron dopant (B202 form Filmtronics) to create the back surface field effect. The emitter junction was formed by spin-on phosphorus doping processes using P509 dopant from Filmtronics. The diffusion was performed in a quartz tube furnace at 950°C for 30 min in a 20% O_2 and 80% N_2 environment. The phosphosilicate glass (PSG) on the wafer surface was removed using the diluted 10% HF solution. The 300-nm thick aluminum front and back contact were deposited by DC sputtering. In creating the top contact, top contact patterns were defined by photolithography before the metal deposition.

2.3. Optical properties and device performance

The total and diffuse transmittance of UNP patterned glass or unpatterned bare glass were measured using a UV–visible spectrophotometer at room temperature with an integrating sphere over the wavelength range of 300–1200 nm. **Figure 4(a)** illustrates the comparison between the total and diffuse transmittance of the glass substrates with and without UNP patterns, which were measured using an integrating sphere with the incoming light entered from the patterned glass substrate side. As shown in **Figure 4(a)**, the total transmittance of the

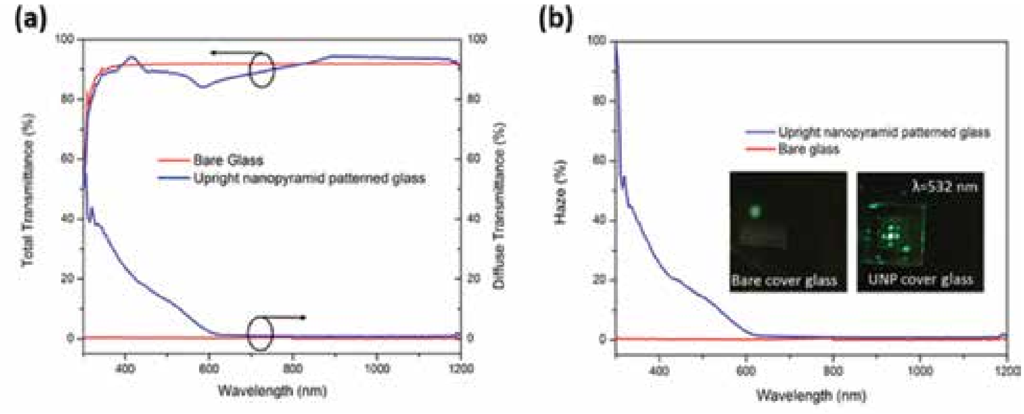

Figure 4. (a) Measured total and diffuse transmittance spectra of the bare glass and the UNP patterned glass as a function of wavelength and (b) the optical haze spectra of the bare glass and the UNP patterned glass as a function of wavelength. Photographs of diffracted light patterns of the corresponding samples obtained from the green diode laser with a wavelength of 532 nm are also displayed in the inset.

UNP patterned glass was slightly lower than that of the bare glass in the wavelength range of 450–800 nm which may be caused by the diffraction losses due to the higher order diffracted waves [33, 34]. However, the diffuse transmittance of the UNP patterned glass was increased up to 24% in the visible wavelength region due to higher orders of diffracted waves in the transmission, whereas the bare glass substrate shows almost no diffuse transmittance over a wide wavelength range as illustrated in **Figure 4(a)**.

The haze value (H), which is determined by the ratio of the diffuse transmittance (T_d) to the total transmittance (T_t), that is, $H = T_d/T_t$, indicates the light-scattering properties of the samples. When the incident light passed through the bare cover glass, the H value is close to zero as shown in **Figure 4(b)**. In contrast, the H value is significantly increased for patterned glass, especially, in the wavelength range 300–600 nm, which signifies that strong light scattering is achieved by UNP structured glass. This light-scattering behavior can also be confirmed in the insets of **Figure 4(b)**. For the bare cover glass, there is almost no light diffraction, whereas the UNP patterned glass shows high order diffraction patterns using a green diode laser at a wavelength of 532 nm. This scattering effect will result in changes in the propagation direction of light from normal to the oblique incidence in the solar cell. As a result, the optical path length of the incident light is elongated, and hence the light absorption in the active layer of the solar cell is also improved by the patterned glass. Indeed, the high haze optical property due to the light scattering effect would positively enhance the power conversion efficiency of the solar cells with the UNP patterned glass compared to the bare cover glass [35–37]. This is especially important for thin film devices.

Numerical simulations were performed using the finite-difference time-domain (FDTD) method by Lumerical solutions Inc. to illustrate how the incoming light couples with and without upright nanopyramid structure. **Figure 5** shows the FDTD simulation model layout of the UNP structured glass substrate in perspective view and XZ view. Perfectly matched layers (PML) and periodic boundary conditions were used in the perpendicular and horizontal directions.

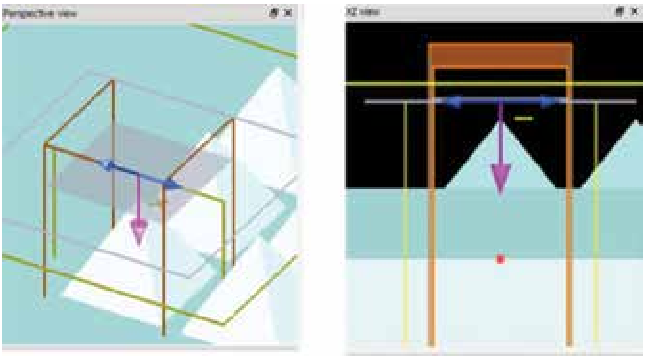

Figure 5. FDTD simulation model layout of the UNP structured glass substrate: (a) perspective view and (b) XZ view.

The cross-sectional electric field distributions at different wavelength obtained for the incident light propagating from air to the glass substrate with and without upright nanopyramid structure are depicted in **Figure 6**. As shown in **Figure 6**, upright nanopyramid structures show wide angular range light-scattering patterns, especially in the wavelength range below 600 nm and provide oblique light transmission from air and the glass while there is no scattering of light for bare cover glass. These results demonstrate that the upright nanopyramid structured

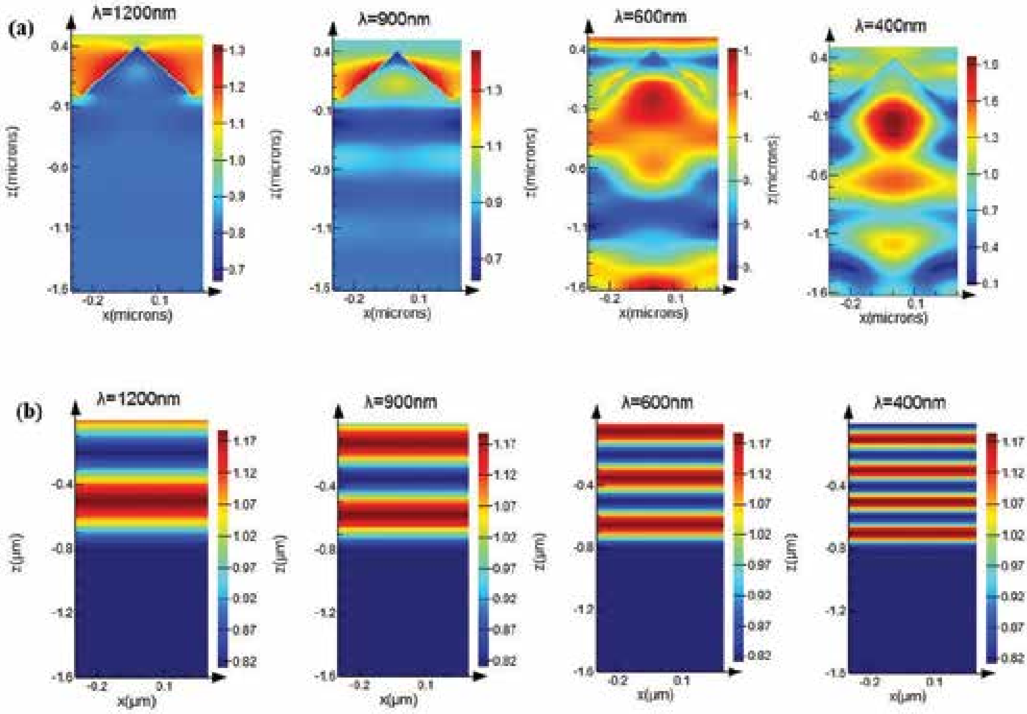

Figure 6. The cross-sectional electric field distribution profiles at different wavelength by FDTD analysis: (a) upright nanopyramid structured glass with a period of 600 nm, base of 500 nm and height of 400 nm and (b) bare flat glass.

glass enhances the diffuse transmittance of the cover glass or any substrate used for solar cells applications. Thus, these structures can lead to the power conversion efficiency enhancement of encapsulated solar cells due to the improved light harvesting in the absorption layer of the solar cells caused by the combined effects of strong light scattering and antireflection coating [37, 38].

In order to verify the effect of the periodic upright nanopyramid patterns, the patterned glass and the bare glass substrate were employed as a cover encapsulation glass on the monocrystalline Si solar cell. **Figure 7(a)** shows the current density-voltage characteristics of the encapsulated monocrystalline Si solar cell with and without UNP patterned cover glass. The monocrystalline Si solar cell performances are summarized in **Table 1**.

There was no significant change in the open circuit voltage (V_{OC}), but a significant enhancement in the short-circuit current density (J_{SC}) was observed as expected. The fill factor (FF) of monocrystalline Si solar cell was slightly enhanced from 55.23 to 59.76% with UNP patterned cover glass. Such improvement in FF could be attributed to the enhanced density of free carriers [39] induced by the increased number of photons entering the active layer of the solar cell and reducing the effective series resistance. The value of J_{SC} for the monocrystalline Si solar cell without cover glass was 34.38 $mAcm^{-2}$. This value was decreased to 31.60 $mAcm^{-2}$ with a bare cover glass. This reduction in J_{SC} indicates that the cover glass reduces the number of photons entering the active layer of the solar cell through reflection and absorption processes. However, by replacing the bare glass with UNP patterned cover glass, J_{SC} value was increased to 32.39 $mAcm^{-2}$ for encapsulated monocrystalline Si solar cell. Hence, the use of the upright nanopyramid patterned glass as a cover glass is an effective way to improve the power conversion efficiency (PCE). The encapsulated monocrystalline Si solar cell with patterned glass efficiency has increased by 10.97% compared to the encapsulated monocrystalline Si solar cell with bare cover glass. The experiment was repeated with commercially manufactured polycrystalline solar cell and similar trend was observed. This enhancement is mainly due to the strong light scattering effect via the upright nanopyramid structures.

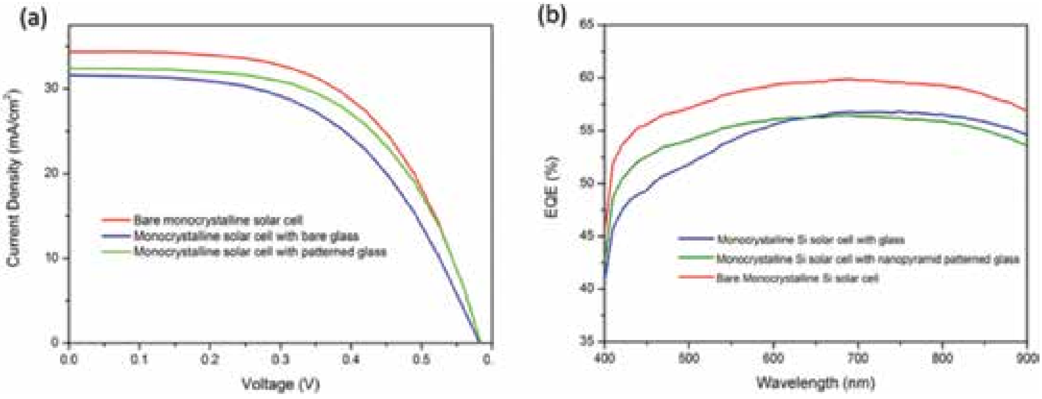

Figure 7. (a) Current density-voltage characteristics and (b) external quantum efficiency (EQE) spectra of encapsulated monocrystalline Si solar cell with and without the upright nanopyramid patterned cover glass and bare cover glass.

Monocrystalline Si solar cells	V_{OC} (V)	J_{SC} ($mAcm^{-2}$)	FF (%)	PCE (%)
Without cover glass	0.58	34.38	59.82	11.93
Bare cover glass	0.58	31.60	55.23	10.12
UNP patterned cover glass	0.58	32.39	59.76	11.23

Table 1. Device characteristics of encapsulated monocrystalline Si solar cells with and without the UNP patterned cover glass and the bare cover glass.

As shown in **Figure 7(b)**, the solar cells with upright nanopyramid patterned cover glass exhibited improved EQE values in comparison with the bare cover glass, particularly in the wavelength region of 400–600 nm. This is due to the increased photogenerated carriers generated by its higher haze properties. This result was precisely matched with the optical haze value result shown in **Figure 4**. From these results, the periodic upright nanopyramid patterned glass offers a better-graded index medium to the incident light compared to the bare glass [25]. Therefore, the patterned cover glass can reduce the Fresnel reflectance and scatter more incident light into the solar cells' emitter area and prolong the optical path length, therefore, improving the light trapping and increasing the overall conversion efficiency.

2.4. Surface wettability and self-cleaning behaviors

In real outdoor environments, the cover glass layer of the solar cell can easily be contaminated by dust particles which interfere with the incident light directed into the solar cell active layer and thus reducing the solar cells' performance. Therefore, the nanopyramids covered glass encapsulation has the advantages of acting as an antireflection layer and as self-cleaning surface and will maintain the solar cell performance under real outdoor environment condition [40, 41]. The water wetting behaviors of the samples with different morphologies were investigated. **Figure 8** shows (a) the photographs of a water droplet on (I) the bare glass, (II) UNP structured glass and (III) SAM-coated UNP structured glass and (b) sequential photographs of water droplet self-cleaning process for (I) the bare cover glass and (II) UNP structured glass.

As shown in **Figure 8(a)**, the bare glass exhibited a hydrophilic surface with a water contact angle (θ_{CA}) of ~36° while UNP patterned glass showed a hydrophobic behavior with a θ_{CA} value of ~112°. This hydrophobic behavior is associated to the enhanced surface roughness of the UNP patterned glass, which can be demonstrated by the Cassie-Baxter Equation [42]. Moreover, F_{13}-TCS-based SAM was coated onto the UNP patterned glass in order to enhance its hydrophobic surfaces. In this case, the contact angle of the SAM-coated UNP glass was increased to 132° as shown in **Figure 8(a)**. These contact angle ($\theta_{CA)}$ values are comparatively lower than those reported with superhydrophobicity (i.e., $\theta_{CA} > 150°$) in previous studies [43, 44]. However, it can be observed that the black dust particles on the surface of UNP patterned glass were cleared away by the rolling down water droplets without any remaining dust particles or water droplets at the surface, as shown in **Figure 8(b)**. In contrast, the dust particles remained on the bare glass even with rolling down water droplets. Thus, the dust particles partially remained especially at the edge of the bare glass. The conclusion is that the UNP patterned cover glass has dual functionality of light-harvesting and self-cleaning properties and would enhance the practicability of solar cells in real outdoor environments.

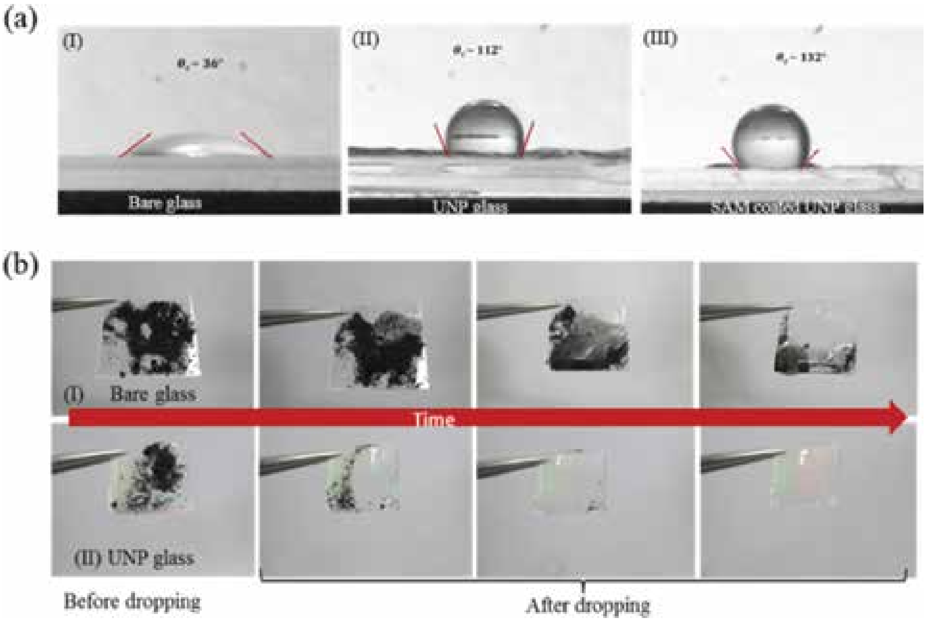

Figure 8. Photographs of (a) a water droplet on (I) bare glass, (II) UNP glass and (II) SAM-coated UNP glass and (b) sequential photographs of a self-cleaning process for (I) the bare glass and (II) UNP glass. θ_{CA} is the water contact angle.

3. Inverted nanopyramid structures

3.1. Fabrication of inverted nanopyramid structures by UV-NIL

Figure 9 illustrates the schematic diagram of overall imprint process steps for the coating of inverted nanopyramid structures on a solar cell front surface. The periodic inverted nanopyramid structures were fabricated on Si master mold by LIL and subsequent pattern transfer process using reactive ion etching followed by KOH wet etching. Details on the fabrication process of the master mold are described in Ref. [9]. The upright nanopyramid patterns were successfully replicated from the Si mold onto the glass substrate using UV nanoimprint process resulting in high fidelity as described in Section 2.1. The upright nanopyramid structured glass was used as a stamp in the second imprint process to produce the inverted nanopyramid patterns. After the UV nanoimprint process, F_{13}-TCS-based SAM was coated onto the upright nanopyramid patterned glass substrate to act as an anti-sticking layer. More details of the UV nanoimprint process parameters and the tools which were used are described in Ref. [11].

In order to determine and measure the influence of the inverted nanopyramid structure on improving the solar cell conversion efficiency, the inverted nanopyramid structures were printed onto monocrystalline Si solar cells. The monocrystalline Si solar cells were fabricated as described in Section 2.2. **Figure 10(a)** shows the top view SEM images of the periodic inverted nanopyramid Si master stamp. The upright nanopyramid replica stamp (**Figure 10(b)**)

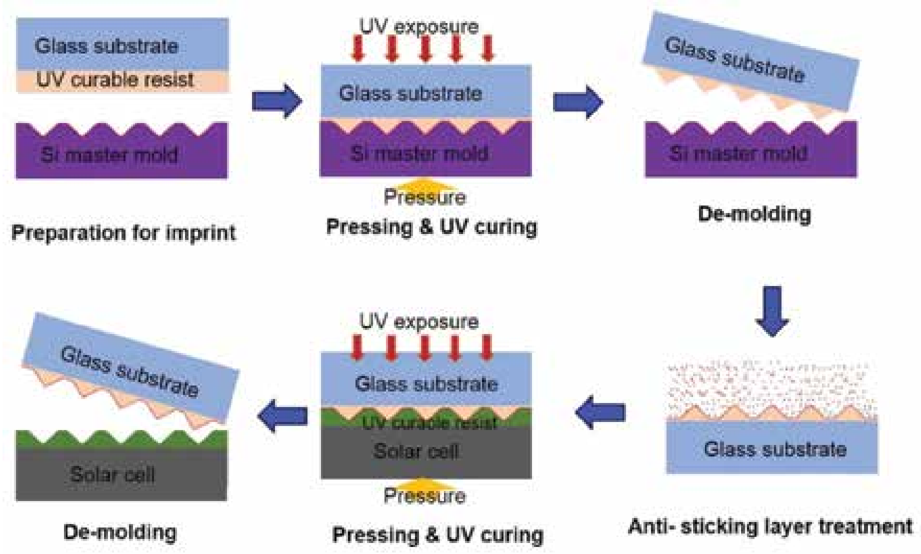

Figure 9. The schematic diagram of the overall fabrication process of inverted nanopyramid structures on the front surface of the solar cells.

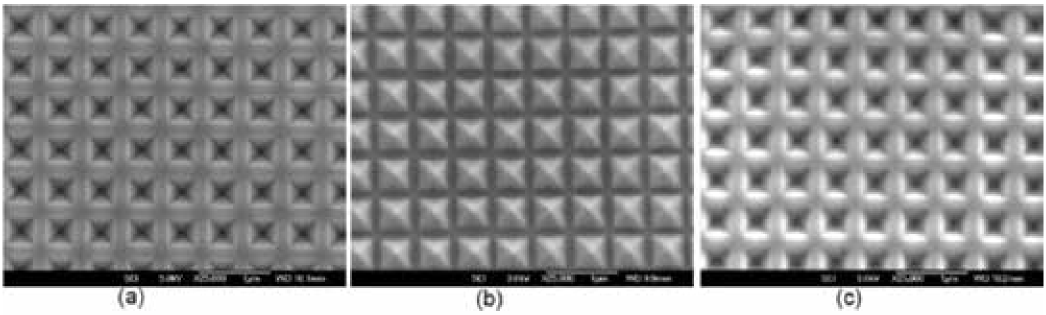

Figure 10. Top view of SEM image of: (a) the inverted nanopyramid Si master mold, (b) the upright nanopyramid replica stamp and (c) the periodic inverted nanopyramid imprinted from the upright pyramids mold on the front surface of the solar cells.

was imprinted from the master Si stamp (**Figure 10(a)**). The periodic inverted nanopyramid imprinted onto the surface of the solar cells (**Figure 10(c)**) was obtained from the upright nanopyramid replica stamp. It can be seen that the inverted nanopyramid structures were transferred to the surface of the solar cell with high fidelity.

3.2. Optical properties and device performance

Figure 11 shows the reflectance of the monocrystalline Si surface with and without the coating of inverted nanopyramid structures measured as a function of wavelength. It can be observed that the surface reflectance of the monocrystalline Si with the inverted nanopyramid layer was significantly decreased over the broad wavelength ranging from 300 nm to

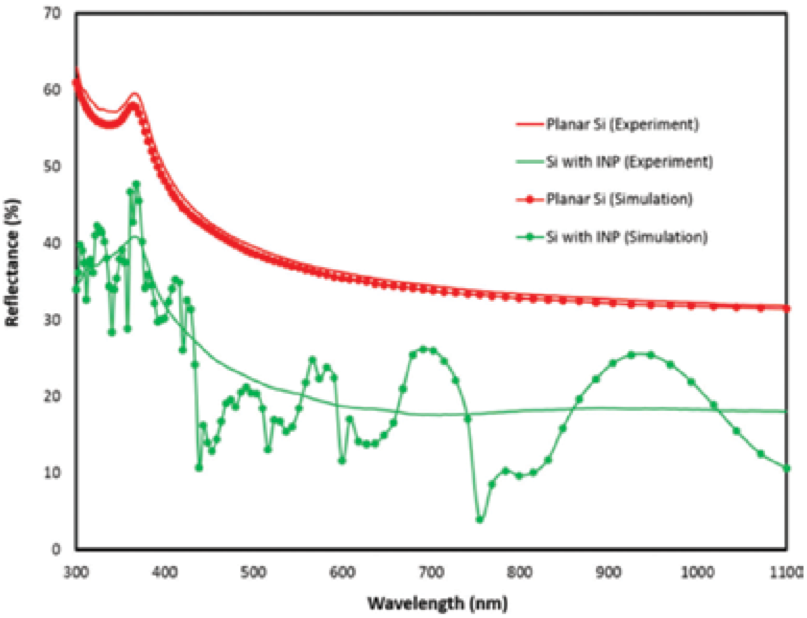

Figure 11. Experimental and FDTD-simulated optical reflectance spectra of Si surface with and without INP structure as a function of wavelength.

1200 nm due to the gradual change in the refractive index between the air and Si surfaces. This is compared with the planar solar cells with no nanopyramid pattern (red curve in **Figure 11**), which resulted in 40% reflections over the visible range.

FDTD simulations were performed with and without inverted nanopyramid structure to verify the reflection attained from the experiments, resulting in simulated reflectance spectra, as also illustrated in **Figure 11**. It is apparent that the theoretical reflection measurement for planar Si substrate is close to the experimental results. The overall trend of simulated reflectance spectra is quite consistent with that of the experiment data, with noticeable decrease of reflectance for inverted nanopyramid structures. Concurrently, the fluctuations of the reflectance can be associated with the limitation of the modeling where the OrmoStamp layer is assumed to have a uniform refractive index over the broad wavelength range under study. Moreover, the cross-sectional electric field intensity distributions at different wavelengths were simulated for incident light propagating from air to the Si substrate with and without inverted nanopyramid structure as shown in **Figure 12**.

As shown in **Figure 12**, the existence of inverted nanopyramid structure results in less intensity and weaker interference of the reflected waves. Hence, these structures are suitable antireflection coatings. In addition, it can be observed from the strong electric field distribution inside the inverted nanopyramid structure that the EM wave energy can be effectively coupled to the inverted nanopyramid structures. This is because more incident photons are coupled to the device due to the formation of a gradual refractive index gradient profile provided by the inverted nanopyramid structure.

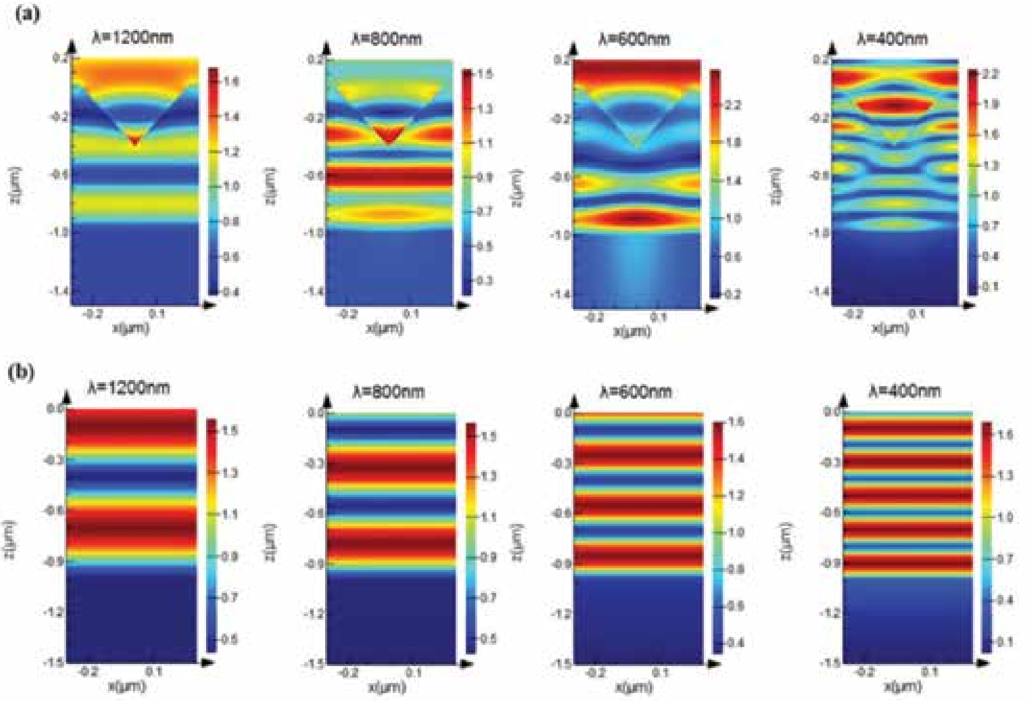

Figure 12. The cross-sectional electric field distribution profiles at different wavelengths employing FDTD analysis (a) INP coated Si with a period of 600 nm, the base size of 500 nm and depth of 400 nm and (b) planar Si subjected to same light conditions.

Figure 13(a) and **(b)** shows the J-V characteristics and EQE spectra of the monocrystalline Si solar cell with and without the inverted nanopyramid structures. The photovoltaic parameters of the monocrystalline Si solar cells with and without nanopyramid structures extracted from these J-V curves are summarized in **Table 2**.

With the use of inverted nanopyramid structures, the J-V characteristics show that there was no significant change in the open circuit voltage (V_{OC}). However, the short-circuit current density (J_{SC}) of planar monocrystalline Si solar cell increased from 29.422 to 32.793 mAcm^{-2}. This J_{SC} increment was mainly due to the reduced reflectance resulting from the inverted nanopyramid structure over a broad wavelength range as shown in **Figure 11**. As a result, the conversion efficiency of the monocrystalline Si solar cell with inverted nanopyramid was increased significantly from 8.122 to 9.075%. This efficiency is 11.73% higher than the one obtained for the planar, not patterned, monocrystalline Si solar cell. The EQE measurement is carried out under a monochromatic illumination with a tungsten-halogen lamp coupled to a monochromator. The EQE values of the tested monocrystalline Si solar cell with inverted nanopyramid layer were significantly higher over the entire wavelength range compared to the non-patterned solar cells. For instance, the EQE value increased by about 8% at wavelength of 450 nm. This higher EQE values for the solar cells with inverted nanopyramid indicate enhanced light trapping and reduced reflections due to the imprinted nanostructures on top of the solar cell surface. This result is precisely matched with the reflectance values obtained in **Figure 11**.

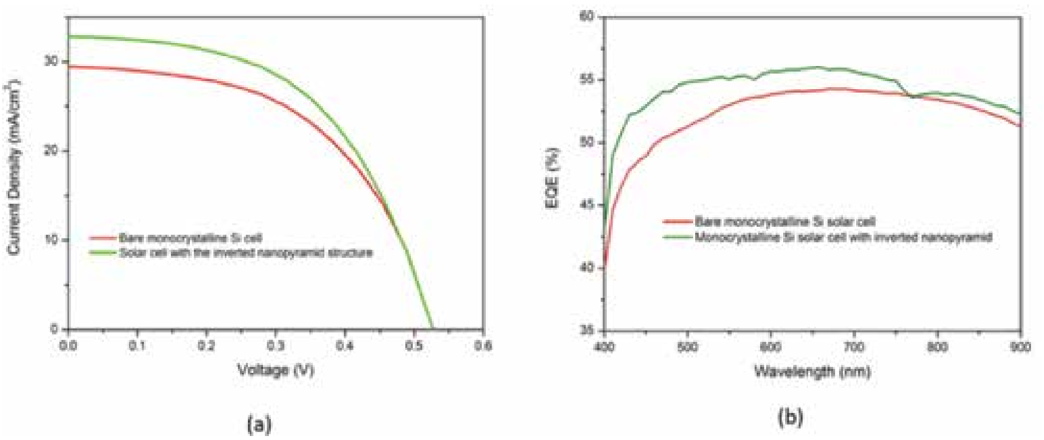

Figure 13. (a) Current density-voltage (J-V) characteristics and (b) EQE spectra of a monocrystalline Si solar cell with and without the inverted nanopyramid structures.

These results demonstrate that the periodic inverted nanopyramid structures reduced the reflections, increased the short-circuit current and improved the efficiency of the monocrystalline silicon solar cells under this study. This is due to the formation of a gradual refractive index gradient between air and the solar cell, which can reduce the Fresnel reflectance and direct more incident light inside the solar cell active layer. The combined light trapping and antireflection effect have been improved, and the optical path length has been prolonged by the inverted nanopyramid structures resulting in increasing the overall conversion efficiency of the monocrystalline Si solar cells. In addition, the nanopyramid coating can be applied after the solar cell fabrication is completed to eliminate any losses due to surface damage by the etching processes for example [45].

Monocrystalline Si solar cells	V_{OC} (V)	J_{SC} (mAcm^{-2})	FF (%)	PCE (%)
Without nanopyramid	0.525	29.442	52.55	8.122
With nanopyramid	0.58	32.793	52.71	9.075

Table 2. Device characteristics of monocrystalline Si solar cells coated with glass with and without the inverted nanopyramid structures.

3.3. Surface wettability

In outdoor environments, solar cells are exposed to the elements and can be easily contaminated by dust particles which interfere with incident light affecting the cell light absorption and thus, reducing the device performance. Therefore, self-cleaning properties at the front surface of the solar cell would maintain the cell performance when exposed to dusty environments [40, 41].

Figure 14 shows the contact angle values of water droplets measured on the planar solar cell, inverted nanopyramid patterned solar cell and SAM-coated inverted nanopyramid patterned solar cell. As shown in **Figure 14**, the contact angle of the solar cell was increased from 55 to

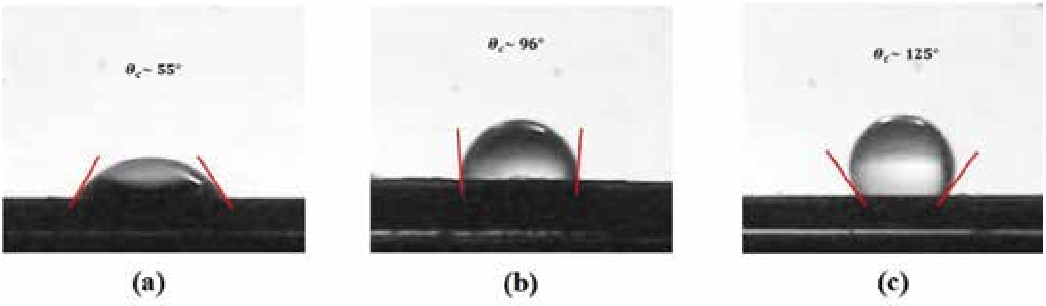

Figure 14. Photographs of a water droplet on: (a) planar solar cell, (b) patterned solar cell with nanopyramids and (c) SAM-coated patterned solar cell. θ c is the water contact angle.

96° after the formation of inverted nanopyramid structure, which exhibited a hydrophobic behavior. Moreover, the hydrophobicity was enhanced with SAM-coated inverted nanopyramid structures. In this case, the contact angle of the SAM-coated patterned solar cell was increased to 125°. As a result, solar cells with inverted nanopyramids can utilize the self-cleaning functionality induced by the high hydrophobic surface properties in addition to the utilization of their antireflection properties.

4. Conclusions

In this chapter, periodic upright and inverted nanopyramid structures were utilized as light-trapping and self-cleaning nanostructures. Low-cost, high-resolution LIL and UV-NIL technologies were used to fabricate the master mold and form these structures. The performance of the solar cells was improved in terms of overall efficiency and reduced reflections. In addition, a superhydrophobic property of the nanopyramids was explored in terms of adding a self-cleaning functionality to the front side encapsulation. The inverted nanopyramid structures were fabricated on Si substrate by LIL and subsequent pattern transfer process using reactive ion etching followed by KOH wet etching. The periodic inverted nanopyramid structures on a silicon substrate were used as a master mold for the imprint process. During the first nanoimprint process, the upright nanopyramid structures were fabricated on the glass substrate by simple, high-throughput and low-cost UV-NIL using Si master mold with inverted nanopyramid structures. The upright nanopyramid structured glass substrates were tested for protective cover glass for solar cell applications and were utilized as a mold for the second imprint process used to form the inverted pyramids.

The diffuse transmittance and haze ratio values were significantly increased for the upright nanopyramid patterned glass, especially, in the wavelength range 300–600 nm compared to the bare glass. This indicates that antireflection and strong light-scattering functions are obtained due to the upright nanopyramid graded refraction index structures. The use of upright nanopyramid structured glass as a cover glass lead to improve the power conversion efficiency of the encapsulated monocrystalline Si solar cell by about 10.97%. This is mainly due to the increased light scattering and prolongs the optical path length caused by the upright nanopyramid structures compared to the reference cells with bare glass. In addition, the fluorinated upright nanopyramid structured cover glass exhibited larger contact angle ($\theta_{CA} \sim 132°$) and excellent self-cleaning properties.

In the second nanoimprint process, the periodic inverted nanopyramid structures were fabricated on the monocrystalline solar cell front surface using a UV-NIL. The pyramid coating can be applied after cell fabrication to eliminate any losses due to surface damage by the etching processes. The inverted nanopyramid structures decreased the reflectance and increased the external quantum efficiency over a broad wavelength range. The periodic inverted nanopyramid structure has successfully reduced the Fresnel reflection and led to directing and trapping more incident light into the monocrystalline Si solar cells, thereby improving the short-circuit current density and enhancing the power conversion efficiency. The power conversion efficiency of the monocrystalline Si solar cell with inverted nanopyramid structures was improved by 11.73% compared to the planar solar cell. Moreover, the surface of the solar cells exhibited hydrophobic properties due to increased contact angle caused by the nanostructure patterns and the self-assembled monolayer coating. The enhanced hydrophobicity provided the solar cells with an added self-cleaning functionality. These results suggest that the periodic inverted nanopyramid and upright nanopyramid structures with light-harvesting and self-cleaning properties have considerable potential for various types of solar cells and optical systems in real outdoor environments.

Author details

Amalraj Peter Amalathas* and Maan M. Alkaisi

*Address all correspondence to: amalraj.peteramalathas@pg.canterbury.ac.nz

Department of Electrical and Computer Engineering, MacDiarmid Institute for Advanced Materials and Nanotechnology, University of Canterbury, Christchurch, New Zealand

References

[1] Chattopadhyay S, Huang Y, Jen Y-J, Ganguly A, Chen K, Chen L. Anti-reflecting and photonic nanostructures. Materials Science and Engineering: R: Reports. 2010;**69**:1-35. DOI: 10.1016/j.mser.2010.04.001

[2] Söderström K, Escarré J, Cubero O, Haug FJ, Perregaux S, Ballif C. UV-nano-imprint lithography technique for the replication of back reflectors for n-i-p thin film silicon solar cells. Progress in Photovoltaics: Research and Applications. 2011;**19**:202-210. DOI: 10.1002/pip.1003

[3] Wang B, Gao T, Leu PW. Broadband light absorption enhancement in ultrathin film crystalline silicon solar cells with high index of refraction nanosphere arrays. Nano Energy. 2016;**19**:471-475. DOI: 10.1016/j.nanoen.2015.10.039

[4] Hsu CM, Battaglia C, Pahud C, Ruan Z, Haug FJ, Fan S, Ballif C, Cui Y. High-efficiency amorphous silicon solar cell on a periodic nanocone back reflector. Advanced Energy Materials. 2012;**2**:628-633. DOI: 10.1002/aenm.201100514

[5] Moreno M, Daineka D, i Cabarrocas PR. Plasma texturing for silicon solar cells: From pyramids to inverted pyramids-like structures. Solar Energy Materials and Solar Cells. 2010;**94**:733-737. DOI: 10.1016/j.solmat.2009.12.015

[6] Li Y, Zhang J, Yang B. Antireflective surfaces based on biomimetic nanopillared arrays. Nano Today. 2010;**5**:117-127. DOI: 10.1016/j.nantod.2010.03.001

[7] Kanamori Y, Sasaki M, Hane K. Broadband antireflection gratings fabricated upon silicon substrates. Optics Letters. 1999;**24**:1422-1424. DOI: 10.1364/Ol.24.001422

[8] Amalathas AP, Alkaisi MM. Enhancing the performance of solar cells with inverted nanopyramid structures fabricated by UV nanoimprint lithography. In: 2016 IEEE 43rd Photovoltaic Specialists Conference (PVSC). IEEE; 2016. pp. 0346-0349. DOI: 10.1109/PVSC.2016.7749608

[9] Amalathas AP, Alkaisi MM. Periodic upright nanopyramid fabricated by ultraviolet curable nanoimprint lithography for thin film solar cells. International Journal of Nanotechnology. 2017;**14**:3-14. DOI: 10.1504/Ijnt.2017.082435

[10] Wu W, Hu M, Ou FS, Li Z, Williams RS. Cones fabricated by 3D nanoimprint lithography for highly sensitive surface enhanced Raman spectroscopy. Nanotechnology. 2010;**21**:255502. DOI: 10.1088/0957-4484/21/25/255502

[11] Amalathas AP, Alkaisi MM. Efficient light trapping nanopyramid structures for solar cells patterned using UV nanoimprint lithography. Materials Science in Semiconductor Processing. 2017;**57**:54-58. DOI: 10.1016/j.mssp.2016.09.032

[12] Hulteen JC, Van Duyne RP. Nanosphere lithography: A materials general fabrication process for periodic particle array surfaces. Journal of Vacuum Science & Technology A. 1995;**13**:1553-1558. DOI: 10.1116/1.579726

[13] Cheng JY, Ross CA, Thomas EL, Smith HI, Vancso GJ. Fabrication of nanostructures with long-range order using block copolymer lithography. Applied Physics Letters. 2002;**81**:3657-3659. DOI: 10.1063/1.1519356

[14] Guo LJ. Nanoimprint lithography: Methods and material requirements. Advanced Materials. 2007;**19**:495-513. DOI: 10.1002/adma.200600882

[15] Puglisi RA, Garozzo C, Bongiorno C, Di Franco S, Italia M, Mannino G, Scalese S, La Magna A. Molecular doping applied to Si nanowires array based solar cells. Solar Energy Materials and Solar Cells. 2015;**132**:118-122. DOI: 10.1016/j.solmat.2014.08.040

[16] Lu Y, Lal A. High-efficiency ordered silicon nano-conical-frustum array solar cells by self-powered parallel electron lithography. Nano letters. 2010;**10**:4651-4656. DOI: 10.1021/nl102867a

[17] Tsui KH, Lin Q, Chou H, Zhang Q, Fu H, Qi P, Fan Z. Low-cost, flexible, and self-cleaning 3D Nanocone anti-reflection films for high-efficiency photovoltaics. Advanced Materials. 2014;**26**:2805-2811. DOI: 10.1002/adma.201304938

[18] Sivasubramaniam S, Alkaisi MM. Inverted nanopyramid texturing for silicon solar cells using interference lithography. Microelectronic Engineering. 2014;**119**:146-150. DOI: 10.1016/j.mee.2014.04.004

[19] Lin Q, Hua B, Leung S-F, Duan X, Fan Z. Efficient light absorption with integrated nanopillar/nanowell arrays for three-dimensional thin-film photovoltaic applications. ACS Nano. 2013;**7**:2725-2732. DOI: 10.1021/nn400160n

[20] Ferry VE, Sweatlock LA, Pacifici D, Atwater HA. Plasmonic nanostructure design for efficient light coupling into solar cells. Nano Letters. 2008;**8**:4391-4397. DOI: 10.1021/nl8022548

[21] Luo L-B, Xie C, Wang X-H, Yu Y-Q, Wu C-Y, Hu H, Zhou K-Y, Zhang X-W, Jie J-S. Surface plasmon resonance enhanced highly efficient planar silicon solar cell. Nano Energy 2014;**9**:112-120. DOI: 10.1016/j.nanoen.2014.07.003

[22] Jiao F, Huang Q, Ren W, Zhou W, Qi F, Zheng Y, Xie J. Enhanced performance for solar cells with moth-eye structure fabricated by UV nanoimprint lithography. Microelectronic Engineering. 2013;**103**:126-130. DOI: 10.1016/j.mee.2012.10.012

[23] Jorgensen G, Terwilliger K, DelCueto J, Glick S, Kempe M, Pankow J, Pern F, McMahon T. Moisture transport, adhesion, and corrosion protection of PV module packaging materials. Solar Energy Materials and Solar Cells. 2006;**90**:2739-2775. DOI: 10.1016/j.solmat.2006.04.003

[24] Shin JH, Han KS, Lee H. Anti-reflection and hydrophobic characteristics of M-PDMS based moth-eye nano-patterns on protection glass of photovoltaic systems. Progress in Photovoltaics: Research and Applications. 2011;**19**:339-344. DOI: 10.1002/pip.1051

[25] Verma LK, Sakhuja M, Son J, Danner A, Yang H, Zeng H, Bhatia C. Self-cleaning and antireflective packaging glass for solar modules. Renewable Energy. 2011;**36**:2489-2493. DOI: 10.1016/j.renene.2011.02.017

[26] Son J, Kundu S, Verma LK, Sakhuja M, Danner AJ, Bhatia CS, Yang H. A practical superhydrophilic self cleaning and antireflective surface for outdoor photovoltaic applications. Solar Energy Materials and Solar Cells. 2012;**98**:46-51. DOI: 10.1016/j.solmat.2011.10.011

[27] Battaglia C, Escarré J, Söderström K, Charrière M, Despeisse M, Haug F-J, Ballif C. Nanomoulding of transparent zinc oxide electrodes for efficient light trapping in solar cells. Nature Photonics. 2011;**5**:535-538. DOI: 10.1038/Nphoton.2011.198

[28] Ferry VE, Verschuuren MA, MCv L, Schropp RE, Atwater HA, Polman A. Optimized spatial correlations for broadband light trapping nanopatterns in high efficiency ultrathin film a-Si: H solar cells. Nano letters. 2011;**11**:4239-4245. DOI: 10.1021/nl202226r

[29] Gwon HJ, Park Y, Moon CW, Nahm S, Yoon S-J, Kim SY, Jang HW. Superhydrophobic and antireflective nanograss-coated glass for high performance solar cells. Nano Research. 2014;**7**:670-678. DOI: 10.1007/s12274-014-0427-x

[30] Han K-S, Lee H, Kim D, Lee H. Fabrication of anti-reflection structure on protective layer of solar cells by hot-embossing method. Solar Energy Materials and Solar Cells. 2009;**93**:1214-1217. DOI: 10.1016/j.solmat.2009.01.002

[31] Leem JW, Yu JS. Artificial inverted compound eye structured polymer films with light-harvesting and self-cleaning functions for encapsulated III–V solar cell applications. RSC Advances. 2015;**5**:60804-60813. DOI: 10.1039/c5ra05991g

[32] Amalathas AP, Alkaisi MM. Upright nanopyramid structured cover glass with light harvesting and self-cleaning effects for solar cell applications. Journal of Physics D: Applied Physics. 2016;**49**:465601. DOI: 10.1088/0022-3727/49/46/465601

[33] Song YM, Choi HJ, Yu JS, Lee YT. Design of highly transparent glasses with broadband antireflective subwavelength structures. Optics Express. 2010;**18**:13063-13071. DOI: 10.1364/OE.18.013063

[34] Lee SH, Leem JW, Yu JS. Transmittance enhancement of sapphires with antireflective subwavelength grating patterned UV polymer surface structures by soft lithography. Optics Express. 2013;**21**:29298-29303. DOI: 10.1364/OE.21.029298

[35] Dudem B, Leem JW, Lim JH, Lee SH, Yu JS. Multifunctional polymers with biomimetic compound architectures via nanoporous AAO films for efficient solar energy harvesting in dye-sensitized solar cells. RSC Advances. 2015;**5**:90103-90110. DOI: 10.1039/c5ra16276a

[36] Janthong B, Moriya Y, Hongsingthong A, Sichanugrist P, Konagai M. Management of light-trapping effect for a-Si: H/μc-Si: H tandem solar cells using novel substrates, based on MOCVD ZnO and etched white glass. Solar Energy Materials and Solar Cells. 2013;**119**:209-213. DOI: 10.1016/j.solmat.2013.06.045

[37] Ho C-H, Lien D-H, Chang H-C, Lin C-A, Kang C-F, Hsing M-K, Lai K-Y, He J-H. Hierarchical structures consisting of SiO_2 nanorods and p-GaN microdomes for efficiently harvesting solar energy for InGaN quantum well photovoltaic cells. Nanoscale. 2012;**4**:7346-7349. DOI: 10.1039/C2NR32746E

[38] Lin C-A, Lai K-Y, Lien W-C, He J-H. An efficient broadband and omnidirectional light-harvesting scheme employing a hierarchical structure based on a ZnO nanorod/Si_3N_4-coated Si microgroove on 5-inch single crystalline Si solar cells. Nanoscale. 2012;**4**:6520-6526. DOI: 10.1039/C2NR32358C

[39] Qi B, Wang J. Fill factor in organic solar cells. Physical Chemistry Chemical Physics. 2013;**15**:8972-8982. DOI: 10.1039/c3cp51383a

[40] Lee SH, Han KS, Shin JH, Hwang SY, Lee H. Fabrication of highly transparent self-cleaning protection films for photovoltaic systems. Progress in Photovoltaics: Research and Applications. 2013;**21**:1056-1062. DOI: 10.1002/pip.2203

[41] Kim YD, Shin JH, Cho JY, Choi HJ, Lee H. Nanosized patterned protective glass exhibiting high transmittance and self-cleaning effects for photovoltaic systems. Physica Status Solidi (a). 2014;**211**:1822-1827. DOI: 10.1002/pssa.201330643

[42] Cassie A, Baxter S. Wettability of porous surfaces. Transactions of the Faraday Society. 1944;**40**:546-551. DOI: 10.1039/TF9444000546

[43] Tserepi A, Vlachopoulou M, Gogolides E. Nanotexturing of poly (dimethylsiloxane) in plasmas for creating robust super-hydrophobic surfaces. Nanotechnology. 2006;**17**:3977. DOI: 10.1088/0957-4484/17/15/062

[44] Park K-C, Choi HJ, Chang C-H, Cohen RE, McKinley GH, Barbastathis G. Nanotextured silica surfaces with robust superhydrophobicity and omnidirectional broadband super-transmissivity. ACS Nano. 2012;**6**:3789-3799. DOI: 10.1021/nn301112t

[45] Kumaravelu G, Alkaisi M, Bittar A, MacDonald D, Zhao J. Damage studies in dry etched textured silicon surfaces. Current Applied Physics. 2004;**4**:108-110. DOI: 10.1016/j.cap.2003.10.008

Chapter 3

Fabrication of ZnO Thin Film through Chemical Preparations

Ersan Y. Muslih and Badrul Munir

Additional information is available at the end of the chapter

http://dx.doi.org/10.5772/intechopen.74985

Abstract

Zinc oxide (ZnO) is a compound that has unique physical and chemical properties. It has a direct band gap at 3.4 eV (without dopant), a high bonding energy (60 meV), and a high thermal and mechanical stability at room temperature. Thus, ZnO thin film can be suitably applied in many fields, and it also has many functions such as UV light emitters, hydrophobic coating, transparent thin film in electronic devices, piezoelectric material, transducers, gas-sensing, and a transparent conductive oxide (TCO) layer in thin film solar cells. ZnO thin film could be prepared by many chemical preparations such as chemical bat deposition (CBD), chemical vapor deposition (CVD), sol–gel spin coating, doctor blade, printing deposition, and electrochemical deposition (ED). This chemical process is a low-cost, simple, and easy preparation process to be adjusted or doped by other elements.

Keywords: zinc oxide, thin film, chemical preparations, TCO, solar cells

1. Introduction

Zinc oxide (ZnO) is a II-VI semiconductor group which has a wurtzite as the most stable compound structure and has unique physical and chemical properties. In physical properties, ZnO has a high thermal stability, which starts to melt and boil at 1975°C; in optical properties, it has a high transparency and a direct band gap at 3.4 eV, which can be tuned by doping several elements such as Al, Ga, or In [1]. ZnO also has a low resistivity, which is about $1–2 \times 10^{-4}$ Ωcm [2], a high thermal stability, a high electrochemical coupling coefficient, and a high bonding energy (60 meV) [1]. Due to all these unique properties, ZnO becomes a promising material, which can be applied in many fields as a sensor, converter, catalyst, and even as an important part in solar cells. This study aims to review ZnO as a transparent conductive oxide (TCO) in solar cells.

2. Zinc oxide as thin film in solar cells

In solar cells, ZnO plays important roles in collecting the energy from sunlight in various solar cells such as silicone-based solar cell (first-generation solar cell), thin film (second-generation), organic, multijunction, dye-sensitized (third-generation), hybrid and perovskite solar cells (fourth generation). In the first to the third generation of solar cell, ZnO plays a role as transparent conductive oxide (TCO), except in organic solar cell in which ZnO acts as a junction for exciton separation [3].

Transparent conductive oxide (TCO) is very important for harvesting electricity from sunlight and can improve solar cell efficiency. This layer is used to place on top of thin film solar cells and has a high transmittance (greater than 80% in the visible spectrum area) but has a low resistivity (less than 10^{-4} Ωcm). These properties will minimize the probability of the received photon absorbed by the layers before the absorber layer or reflected back. **Table 1** shows several properties of ZnO as TCO on solar cells.

In addition, TCO should have a higher band gap than the absorber layer and the buffer layer, approximately 3.2 eV. If all of the layers are stacked together, they will make a gradation of band gap energy from low band gap energy (absorber layer) to the high energy (the top contact). This gradation can help electrons of the absorbed photons in the absorber layer to move

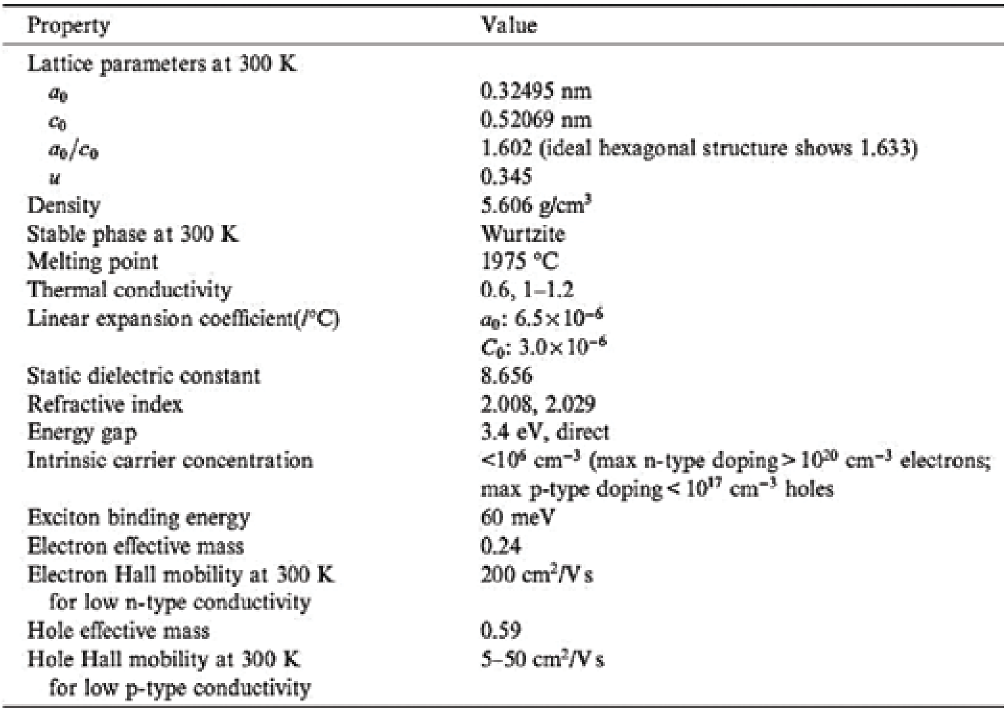

Property	Value
Lattice parameters at 300 K	
a_0	0.32495 nm
c_0	0.52069 nm
a_0/c_0	1.602 (ideal hexagonal structure shows 1.633)
u	0.345
Density	5.606 g/cm^3
Stable phase at 300 K	Wurtzite
Melting point	1975 °C
Thermal conductivity	0.6, 1–1.2
Linear expansion coefficient(/°C)	a_0: 6.5×10^{-6} C_0: 3.0×10^{-6}
Static dielectric constant	8.656
Refractive index	2.008, 2.029
Energy gap	3.4 eV, direct
Intrinsic carrier concentration	$<10^6$ cm^{-3} (max n-type doping $>10^{20}$ cm^{-3} electrons; max p-type doping $<10^{17}$ cm^{-3} holes
Exciton binding energy	60 meV
Electron effective mass	0.24
Electron Hall mobility at 300 K for low n-type conductivity	200 cm^2/V s
Hole effective mass	0.59
Hole Hall mobility at 300 K for low p-type conductivity	5–50 cm^2/V s

Table 1. Properties of ZnO [1].

past the other layers to the top layer. On the other hand, the holes move to the back-contact as a hole summation in solar cells. Since the electrons and holes move to the opposite side, this makes a difference potential on either side and produces electricity. If the band gap gradation is not sequentially arranged, it will disturb electron and hole movement. As a consequence, the electricity will not appear. **Figure 1** shows illustrations of electrons and holes, movement through several layers with different band gaps in the CIGSe ($CuInGeSe_4$) solar cell.

Besides its physical properties, ZnO is a common material as TCO for thin film solar cell because this material is non-toxic and abundant. However, ZnO still lacks in optical and electrical (opto-electrical) properties. Thus, some of elements or molecules have been successfully developed to improve its optoelectrical properties such as Al, Ga, B, In, Y, Sc, F, V, Si, Ge, Ti, Zr, Hf, In_2O_3 and SnO_2 [6]. Some of elements provide a significant change in optical and electrical properties of ZnO. **Table 2** shows some changes of ZnO optical and electrical properties as TCO after being doped by some elements.

ZnO thin film could be prepared by physical or vacuum methods such as radio frequency (RF) magnetron sputtering or direct current (DC) sputtering, pulsed laser deposition (PLD), and e-beam evaporation [12–15]. However, all of these methods need particular vacuum equipments and investment. Contrary from physical or vacuum methods, chemical methods are well known as a low-cost method because it does not require particular equipment or expensive investment. Thus, chemical process becomes a promising and low-cost process.

There are several processes for depositing ZnO by using chemical process, such as chemical bath deposition (CBD)/dip coating, chemical vapor deposition (CVD)/spray pyrolysis, sol-gel spin coating, doctor blade coating, printing deposition, and electrochemical deposition. Even though there are various deposition techniques, the steps of each technique are the same. The first step is preparing the precursor which can be in a solution, sol-gel, colloidal, or even in a dispersion precursor form. The second step is depositing using various techniques, and the last step is drying or heat treatment to remove the solvent and to develop the ZnO thin film. Common steps in the preparation of ZnO by chemical process are shown in **Figure 2**.

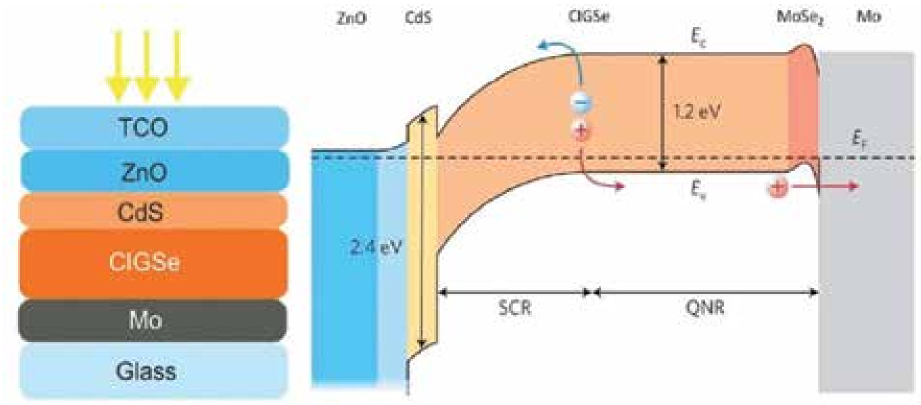

Figure 1. A schematic layer structure of a classical CIGSe solar cell [4] and a schematic band profile of a typical CIGSe solar cell under zero bias voltage condition [5].

Dopants	Optimum content in target (%)	Thickness (nm)	Resistivity (Ωcm)	Transmittance (%)	References
Al	2	500	4.5×10^{-4}	88	[7]
Ga	5	200	8.12×10^{-4}	>90	[8]
In	40	>1000	4.02×10^{-4}	>85	[9]
F	2	200	4.83×10^{-4}	>90	[10]
Si	2	~150	6.2×10^{-4}	~80	[11]

Table 2. Properties of ZnO films with different dopants.

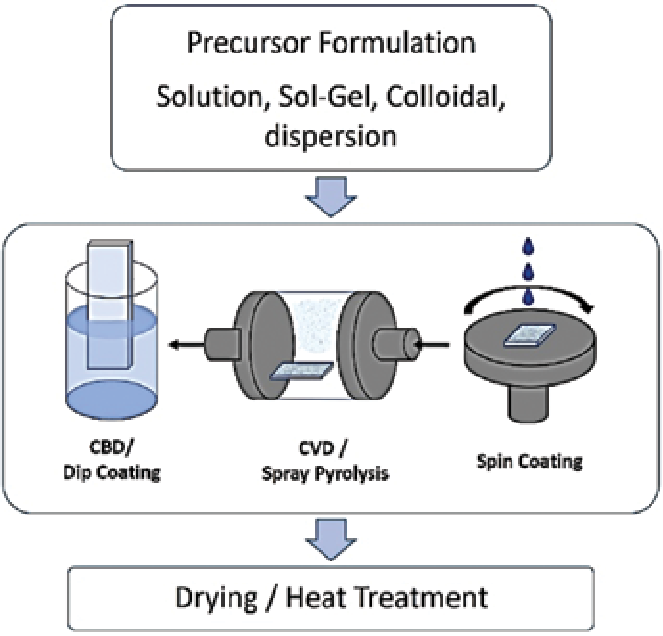

Figure 2. A common preparation step to fabricate ZnO thin film by chemical processes.

In the chemical preparation process, to adjust ZnO thin films into p or n semiconductor, it is done by adding some particular element of salt such as aluminum salt or boron salt into the precursor mixture.

Some of experiments only need a single step of heat treatment to develop the ZnO thin film, but in spin-coating method, several repetition steps of coating and heat treatment are required in order to get the desired thickness, and this repetition step is called as preheat treatment. Contrary with the spin coating, chemical vapor deposition (CVD) or spray pyrolysis method may not have specific drying or heat treatment steps because in this method, the heat treatment is done simultaneously with deposition. To adjust the thickness in CVD or spray pyrolysis, it is adjusted by the deposition time.

3. Chemical deposition methods

3.1. Chemical bath deposition/dip coating

Chemical bath deposition (CBD) or dip coating is the simplest and low-cost deposition method because this method does not need expensive and special equipment. In addition, it also has a simple deposition principle. The arrangement of equipment is shown in **Figure 3**.

At the precursor preparation, zinc oxide is prepared from zinc-salt compound such as zinc acetate dihydrate, zinc nitrate, zinc chloride, and zinc sulfate [17–21]. After these kinds of zinc salts were dissolved in the solution, zinc in the salt becomes a cation which can react with anion from basic compound, as well as form a seed of nuclei which adhere on the substrate. Besides that, zinc cation also reacts with other compounds in the precursor mixture such as surfactants which act as a binder and form zinc complex compound or in order to get desire properties of the mixture such as viscosity or homogeneity. **Table 3** shows various zinc salts and other compounds as precursor mixture.

Further, this seed of nuclei will develop as zinc-salt precipitation which adheres on the substrate, and after drying or heat treatment under various atmospheres, it becomes oxidized and forms a zinc oxide as thin film. The schematic of this preparation is shown in **Figure 4**.

This is the reaction mechanism of ZnO thin film fabrication.

$$[\mathrm{Zn}\,(\mathrm{NH_3})_4]^{2+} + \mathrm{H_2O} \rightarrow \mathrm{Zn}^{2+} + \mathrm{NH}^{4+} + \mathrm{OH}^-$$

$$\mathrm{Zn}^{2+} + \mathrm{OH}^- \rightarrow \mathrm{Zn}\,(\mathrm{OH})_2$$

$$\mathrm{Zn}\,(\mathrm{OH})_2 \rightarrow \mathrm{ZnO} + \mathrm{H_2O}$$

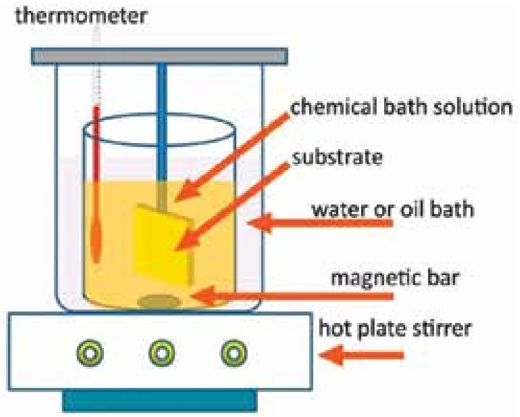

Figure 3. The arrangement of CBD equipment [16].

Zinc salt	Other additive compounds	References
$Zn(CH_3COO)_2$	2-methoxyethanol, mono-ethanolamine	[17]
$Zn(NO_3)_2$	NaOH, sodium n-dodecyl sulfate, triethanolamine	[18]
$ZnCl_2$	NH_4OH, hexadecyl(trimethyl)azanium bromide	[19]
$ZnSO_4$	NH_4OH, NH_4HCO_3	[20]

Table 3. Various zinc salts and other compounds as precursor mixture.

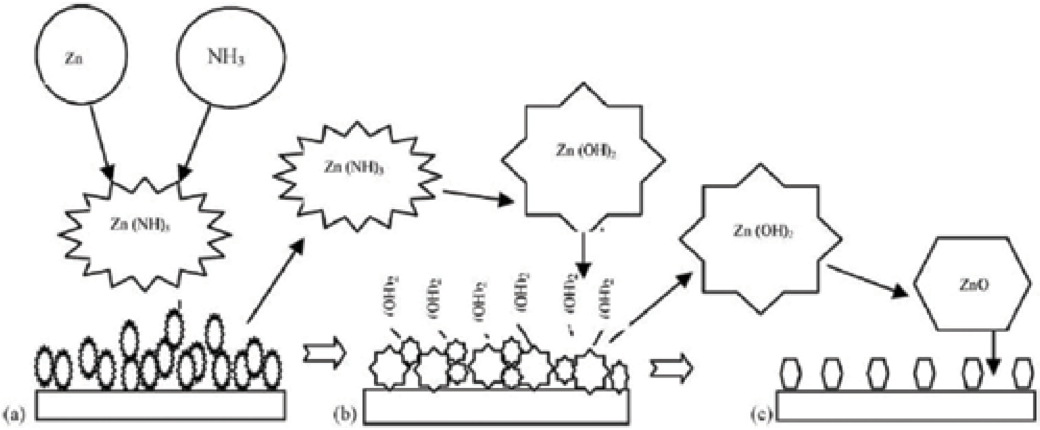

Figure 4. Mechanism of ZnO thin film growth [21].

Temperature (°C)	Duration (hour)	Atmosphere	References
100	1	Air	[23]
300	0.5	Oxygen	[24]
300–600	1	Air	[25]
400–800	1	Air	[26]

Table 4. Various annealing temperatures and atmospheres/heat treatment step.

At drying or heat treatment step, the heat treatment can be done at various temperatures and atmospheres. These various processes have the effect to the shape, morphology, optical, and electrical properties of zinc oxide thin film [22]. **Table 4** shows various annealing temperatures and atmospheres or heat treatment step.

In addition to these, the concentration of precursor of zinc salt as zinc source and other additive concentrations also give significant role to ZnO thin film [22]. The effect of zinc and surfactant concentrations can be seen in **Figure 4**. The increase of zinc and surfactant concentration shows an increase of ZnO thin film crystallinity. Besides crystallinity, the effect of the increase of the concentration also affects the reaction rate of nucleation between zinc and anion, in which it becomes faster. However, besides concentration, the reaction rate is also affected by the temperature reaction.

3.2. Chemical vapor deposition/spray pyrolysis

The preparation of chemical vapor deposition (CVD) or spray pyrolysis is similar with CBD. The zinc precursor must be solved in a solution and has to be evaporated. Evaporation of precursor can be done by several ways. First, zinc precursor must be easy to evaporate or in other words it should be a volatile precursor. Second, by using high temperature, the zinc ingot as precursor can evaporate, and the last step is by using devices such as an atomizer or an ultrasonic transducer that can atomize the precursor or make a mist of it. The arrangement of CVD equipment is shown in **Figure 5**.

In **Figure 5**, zinc precursor solution has changed into mist by ultrasonic apparatus and carried by inert gas into the heat furnace chamber with a substrate placed inside the chamber as a target to develop the ZnO thin film. The temperatures of CVD in several experiments are shown in **Table 5**.

After the precursor mist or vapor is carried and arrived at the heater chamber, some of the zinc precursor particles undergo a reaction with a molecule that contains oxygen in the chamber and forms a larger molecule. Then, this molecule is attached on to the substrate. Due to the high temperature or enough energy, this molecule decomposes into zinc that reacts with the

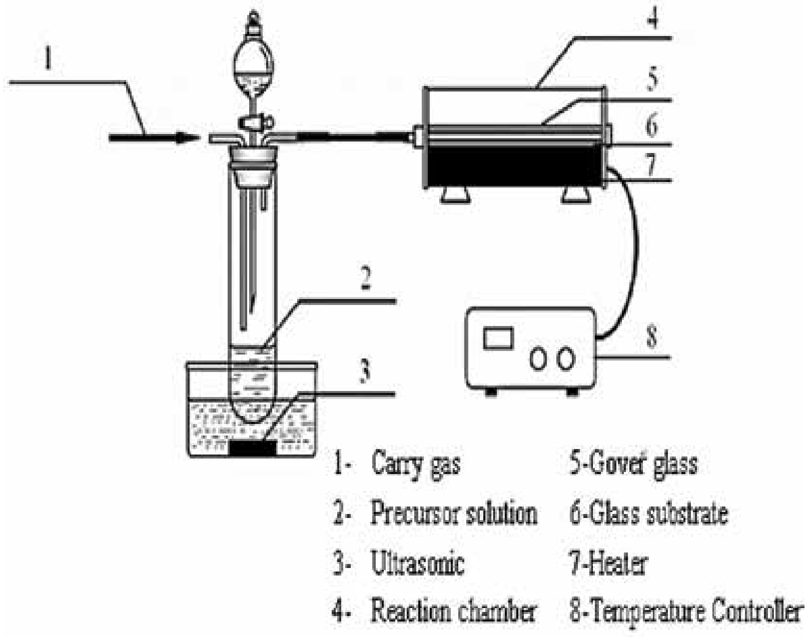

Figure 5. CVD using the ultrasonic transducer to produce a precursor mist [27].

Temperature (°C)	Zinc source	Atmosphere	References
90	Zinc acetate	O_2, N_2O, H_2O	[28]
135–235	Diethylzinc	He-Diborane 2%	[29]
120	Dimethylzinc	O_2	[30]
300–375	Zinc acetate	N_2, O_3	[31]

Table 5. Several ZnO thin film CVD condition.

oxygen and then forms a zinc oxide behind. The solvent is evaporated and leaves the chamber with the carrier gas, and at the same time, zinc oxide gets developed as zinc oxide thin film. Or the reaction mechanism could undergo another possibility, when zinc precursor is arrived at the chamber, and it will attach on the substrate and then undergo a reaction or bonding with another molecule which contains oxygen. Due to the high temperature and enough energy to decompose, the zinc precursor molecule and oxygen containing molecule react to the zinc oxide and release some decomposed solvents, which get carried out with gas, and finally the zinc oxide molecule becomes zinc oxide thin film. This schematic is shown in **Figure 6**.

3.3. Spin coating

Spin-coating method uses the energy of the substrate rotation to remove excess or unattached precursor and flatten the thin film. While the precursor drops on the substrate, it will attach on the substrate but the spread is uneven. When the substrate starts to spin, the precursor will spread along the substrate surface due to the centripetal force. A high spin velocity means a high centripetal force to remove the excess of precursor from the substrate. The amount of precursor in the substrate depends on the spin velocity and the precursor's ability to adhere or attach on the substrate, which is usually called as adhesivity or wet ability. It makes the precursor to attach strongly on the substrate. Besides that, the viscosity also has a role on it. If the precursor has a high viscosity, it will slowly move due to the centripetal force. Consequently, it takes a longer spinning time or a higher spin velocity. The schematic of the spin coater is shown in **Figure 7**.

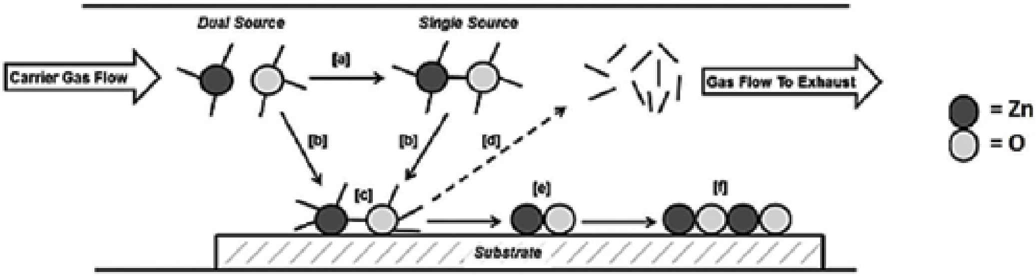

Figure 6. ZnO thin film fabrication. Mechanism with CVD [32].

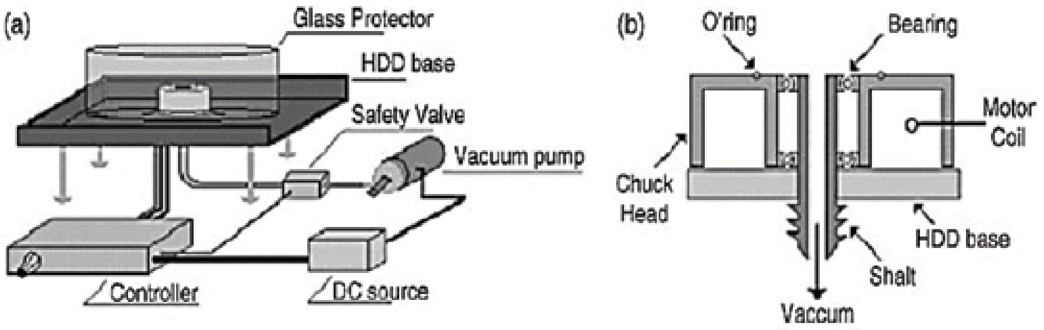

Figure 7. Schematic representation of a home-built spin coater (a) and details of the rotor (b) [33].

After the precursor is attached on the substrate, the next stage is drying stage or evaporating the solvent. One thing that should be considered is that the evaporation of the solvent is affected by the viscosity of the precursor. Thus, it is really important to find out the optimum viscosity of the precursor. A high viscosity means difficult to spread well on the substrate surface, and it means that there is a high surface tension which makes it evaporate slowly. The evaporation of the precursor's solvent is called as preheat treatment. Once the solvent evaporates, it will leave the zinc particle on the substrate and makes the layer thinner. In this method, the desired thickness cannot be achieved by a single process. It should be done in several preheat treatment stages to get the desired thickness. After the preheat treatment, the next stage is to fabricate the zinc oxide from the attached zinc on the substrate by oxidizing heating process. The schematic of alignment process on spin coating is shown in **Figure 8**.

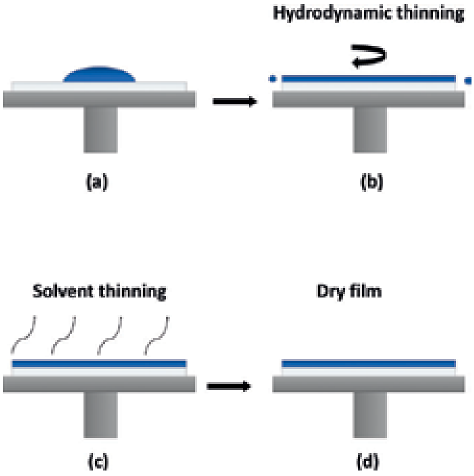

Figure 8. Schematic of the four stages of spin coating (a) Deposition, (b) Spin up, (c) Spin off, (d) Drying [34].

Precursor's form	Zinc source	Other compounds	Mixture condition	References
Sol-gel	Zinc acetate dihydrate	2-methoxyethanol, monoethanolamine	Stirring for 30 min at 60°C, aged for 72 h at room temperature	[35]
Solution	Zinc acetate dihydrate	2-methoxyethanol, monoethanolamine	Stirred at 65°C for 90 min	[36]
Solution	Zinc acetate dihydrate	Ethanol, NH_4OH	pH 10, room temperature	[37]
Solution	Zinc acetate dihydrate	Ethanol, acetylacetone	Room temperature	[38]

Table 6. Precursor conditions.

Spin condition	Preheat condition	Heat treatment condition	Atmosphere	References
2000 rpm for 30 s	200°C, 10 s	400°C for 1 h	—	[35]
3000 rpm for 30 s	260°C, 10 min	400°C for 3 h	Oxygen	[36]
700 rpm for 10 s	100°C for 10 min	500°C for 2 h	Air	[37]
2000 rpm for 10 s	Room temperature, 3 min	500°C for 2 h	Oxygen	[38]

Table 7. Heat treatment condition.

The precursor solution in spin-coating method is different from the chemical bath deposition and chemical vapor deposition. Precursor preparation in spin coating is more varied. It is not only a solution precursor but also a sol–gel or a colloidal form. Additionally, in this method, the quality on the thin film is affected not only by the concentration of zinc source and other additives but also by the rotation speed, time of spin coating, viscosity, and adhesivity of the precursor solution as mentioned earlier. **Table 6** shows several conditions of ZnO spin coating.

Besides that, another thing that brings this method unique lies on the preheat treatment step. The function of this step is to make the coated film dried and attached on the substrate. The repetition of this step is to get a desired thickness. **Table 7** shows the condition of several preheat treatments and heat treatments.

4. Conclusions

In the thin film solar cells, zinc oxide (ZnO) layer acts as a transparent conductive oxide (TCO), which is an important part of solar cells. This thin film can be fabricated by various chemical processes as alternative of vacuum process, where the production is economically cost-effective but still has the same function and properties as vacuum methods.

Author details

Ersan Y. Muslih[1]* and Badrul Munir[2]

*Address all correspondence to: ersanmuslih@gmail.com

1 Department of Mechanical Engineering, Trisakti University, Jakarta, Indonesia

2 Department of Metallurgy and Materials Engineering, University of Indonesia, Depok, Indonesia

References

[1] Pearton SJ et al. Recent progress in processing and properties of ZnO. Progress in Materials Science. 2005;**50**:293-340. DOI: 10.1016/j.pmatsci.2004.04.001

[2] Kim KH, Wibowo RA, Munir B. Properties of Al-doped ZnO thin film sputtered from powder compacted target. Materials Letters. 2006;**60**:1931-1935. DOI: 10.1016/j.matlet.2005.12.055

[3] Steiger P et al. Hydrothermally grown ZnO electrodes for improved organic photovoltaic devices. Thin Solid Films;**2017**:417-423. DOI: 10.1016/j.tsf.2017.11.021

[4] Azimi H, Yi H, Brabec CJ. Towards low-cost, environmentally friendly printed chalcopyrite and kesterite solar cells. Energy & Environmental Science. 2014;**7**:1829-1849. DOI: 10.1039/C3EE43865A

[5] Chirilă A et al. Highly efficient Cu (In, Ga) Se2 solar cells grown on flexible polymer films. Nature Materials. 2011;**10**:857-861. DOI: 10.1038/nmat3122

[6] Minami T. Transparent conducting oxide semiconductors for transparent electrodes. Semiconductor Science and Technology. 2005;**20**:35-44. DOI: 10.1088/0268-1242/20/4/004

[7] Gondoni P et al. Structural and functional properties of Al: ZnO thin films grown by pulsed laser deposition at room temperature. Thin Solid Films. 2012;**520**:4707-4711. DOI: 10.1016/j.tsf.2011.10.072

[8] Park S-M, Ikegami T, Ebihara K. Effects of substrate temperature on the properties of Ga-doped ZnO by pulsed laser deposition. Thin Solid Films. 2006;**513**:90-94. DOI: 10.1016/j.tsf.2006.01.051

[9] Socol G et al. High quality amorphous indium zinc oxide thin films synthesized by pulsed laser deposition. Thin Solid Films. 2011;**520**:1274-1277. DOI: 10.1016/j.tsf.2011.04.196

[10] Cao L et al. Highly transparent and conducting fluorine-doped ZnO thin films prepared by pulsed laser deposition. Solar Energy Materials and Solar Cells. 2011;**95**:894-898. DOI: 10.1016/j.solmat.2010.11.012

[11] Das AK, Misra P, Kukreja LM. Effect of Si doping on electrical and optical properties of ZnO thin films grown by sequential pulsed laser deposition. Journal of Physics D: Applied Physics. 2009;**42**:165405. DOI: 10.1088/0022-3727/42/16/165405

[12] Mahdhi H, Djessas K, Ben Ayadi Z. Synthesis and characteristics of ca-doped ZnO thin films by rf magnetron sputtering at low temperature. Materials Letters. 2018;**214**:10-14. DOI: 10.1016/j.matlet.2017.11.108

[13] Seawsakul K et al. Effects of sputtering power toward the Al-doped ZnO thin film prepared by pulsed DC magnetron sputtering. Materials Today: Proceedings. 2017;**4**:6466-6471. DOI: 10.1016/j.matpr.2017.06.154

[14] Look DC. Mobility vs thickness in n+-ZnO films: Effects of substrates and buffer layers. Materials Science in Semiconductor Processing. 2016;**69**:2-8. DOI: 10.1016/j.mssp.2016.11.026

[15] Shettigar N et al. Tuning the third-order nonlinear optical properties of in: ZnO thin films by 8 MeV electron beam irradiation. Journal of Physics and Chemistry of Solids. 2017;**110**:260-265. DOI: 10.1016/j.jpcs.2017.06.020

[16] Wang X, Ahmad M, Sun H. Three-dimensional ZnO hierarchical nanostructures: Solution phase synthesis and applications. Materials. 2017;**10**:1304. DOI: 10.3390/ma10111304

[17] Saleem M et al. Effect of zinc acetate concentration on the structural and optical properties of ZnO thin films deposited by sol-gel method. International Journal of Physical Sciences. 2012;**7**:2971-2979. DOI: 10.5897/IJPS12.219

[18] Li P et al. Growth of well-defined ZnO microparticles with additives from aqueous solution. Journal of Solid State Chemistry. 2005;**178**:855-860. DOI: 10.1016/j.jssc.2004.11.020

[19] Ma C-l, Sun X-d. Preparation of nanocrystalline metal oxide powders with the surfactant-mediated method. Inorganic Chemistry Communications. 2002;**5**:751-755. DOI: 10.1016/S1387-7003(02)00546-4

[20] Cao Z et al. Synthesis and UV shielding properties of zinc oxide ultrafine particles modified with silica and trimethyl siloxane. Colloids and Surfaces A: Physicochemical and Engineering Aspects. 2009;**340**:161-167. DOI: 10.1016/j.colsurfa.2009.03.024

[21] Kumar PS et al. Growth and characterization of ZnO nanostructured thin films by a two step chemical method. Applied Surface Science. 2008;**255**:2382-2387. DOI: 10.1016/j.apsusc.2008.07.136

[22] Saleem M et al. Effect of zinc acetate concentration on the structural and optical properties of ZnO thin films deposited by sol-gel method. International Journal of Physical Sciences. 2012;**7**:2971-2979. DOI: 10.5897/IJPS12.219

[23] Baviskar PK et al. Wet chemical synthesis of ZnO thin films and sensitization to light with N_3 dye for solar cell application. Journal of Physics D: Applied Physics. 2009;**42**:125108. DOI: 10.1088/0022-3727/42/12/125108

[24] Urgessa ZN et al. Patterned growth of ZnO nanorods by chemical bath deposition. Physica B: Condensed Matter. 2017. DOI: 10.1016/j.physb.2017.06.061

[25] Kumar N, Kaur R, Mehra RM. Photoluminescence studies in sol–gel derived ZnO films. Journal of Luminescence. 2007;**126**(2):784-788. DOI: 10.1016/j.jlumin.2006.11.012

[26] Wang M et al. Influence of annealing temperature on the structural and optical properties of sol–gel prepared ZnO thin films. Physica Status Solidi. 2006;**203**:2418-2425. DOI: 10.1002/pssa.200521398

[27] Liu L et al. Effects of intermittent atomization on the properties of Al-doped ZnO thin films deposited by aerosol-assisted chemical vapor deposition. Thin Solid Films. 2016; **605**:163-168. DOI: 10.1016/j.tsf.2015.09.011

[28] Kim JS et al. Characterization of high quality c axis oriented ZnO thin films grown by metal organic chemical vapor deposition using zinc acetate as source material. Thin Solid Films. 1992;**217**:133-137. DOI: 10.1016/0040-6090(92)90619-M

[29] Faÿ S et al. Rough ZnO layers by LP-CVD process and their effect in improving performances of amorphous and microcrystalline silicon solar cells. Solar Energy Materials & Solar Cells. 2006;**90**:2960-2967. DOI: 10.1016/j.solmat.2006.06.003

[30] Rowlette PC et al. Plasma-enhanced atomic layer deposition of semiconductor grade ZnO using dimethyl zinc. Chemical Vapor Deposition. 2009;**15**:15-20. DOI: 10.1002/cvde.200806725

[31] Pacio M et al. Study of (100) orientated ZnO films by APCVD system. Materials Science and Engineering B. 2010;**174**:38-41. DOI: 10.1016/j.mseb.2010.04.030

[32] Marchand P et al. Aerosol-assisted delivery of precursors for chemical vapour deposition: Expanding the scope of CVD for materials fabrication. Dalton Transactions. 2013;**42**:9406-9422. DOI: 10.1039/C3DT50607J

[33] Bianchi RF et al. Spin coater based on brushless dc motor of hard disk drivers. Progress in Organic Coating. 2006;**57**:33-36. DOI: 10.1016/j.porgcoat.2006.05.004

[34] Daniel TW. Toolan et al. Development of in situ studies of spin coated polymer films. Journal of Materials Chemistry C. 2013;**4**:603-616. DOI: 10.1039/c2tc00026a

[35] Saleem M et al. Effect of zinc acetate concentration on the structural and optical properties of ZnO thin films deposited by sol-gel method. International Journal of Physical Sciences. 2013;**7**:2971-2979. DOI: 10.5897/IJPS12.219

[36] Khan ZR et al. Influence of zinc concentration on band gap and sub-band gap absorption on ZnO nanocrystalline thin films sol-gel grown. Materials Science - Poland. 2017;**35**:246-253. DOI: 10.1515/msp-2017-0039

[37] Smirnov M, Baban C, Rusu GI. Structural and optical characteristics of spin-coated ZnO thin films. Applied Surface Science. 2010;**256**:2405-2408. DOI: 10.1016/j.apsusc.2009.10.075

[38] Muslih EY, Kim KH. Preparation of zinc oxide (ZnO) thin film as transparent conductive oxide (TCO) from zinc complex compound on thin film solar cells: A study of O_2 effect on annealing process. IOP Conference Series: Materials Science and Engineering. 2017;**214**. DOI: 10.1088/1757-899X/214/1/012001

Porous Carbon Materials as Supreme Metal-Free Counter Electrode for Dye-Sensitized Solar Cells

Mohammad Aftabuzzaman and Hwan Kyu Kim

Additional information is available at the end of the chapter

http://dx.doi.org/10.5772/intechopen.75398

Abstract

Counter electrode (CE), as one of the key components of dye-sensitized solar cells (DSSCs), plays a significant role in the overall efficiency and cost of the device. Platinum metal has long been considered one of the most efficient CEs for DSSCs, but its scarcity, high cost, and low stability in I^-/I_3^- redox couple limit its application in the large scale. In this chapter, we provide a broad overview on porous carbon materials as supreme metal-free counter electrode for DSSCs. In the first part, we concisely discuss on the importance and working principle of DSSCs and then the influence of counter electrode on the photovoltaic performance of DSSCs. Afterward, we review different synthetic methods and precursors of porous carbon materials and their efficiency in DSSCs. In the last section, we discuss in detail with example how to characterize and evaluate the device performance using porous carbon materials as counter electrode. Finally, we finish this chapter with a brief summary and outlook of porous carbon materials as counter electrodes in DSSCs.

Keywords: porous carbon, synthesis, characterization, counter electrode, dye-sensitized solar cells

1. Introduction

As the third-generation solar cells, dye-sensitized solar cell (DSSC) is one of the most promising alternatives to the silicon solar cells, due to their simple assembly procedure, good plasticity, transparency, mechanical robustness, ability to work at wider angles, and in low light and environmental friendliness [1, 2]. After a significant breakthrough in the photoelectric conversion efficiency (7.1–7.9%) of DSSCs in 1991, through introducing mesoporous film of

TiO_2 nanocrystalline to adsorb dye instead of planar semiconductor electrode by O'Regan and Grätzel research group [3], DSSCs have stimulated a great research interest over the following 25 years and attained an efficiency of ca. 14% [4, 5].

The working principle of DSSCs is not similar to conventional solar cell, but it is similar to natural photosynthesis process where light absorption and charge carrier transportation have different substances, as shown in **Figure 1**. DSSCs consist of three important components: dye-coated TiO_2 film, counter electrode (CE), and electrolyte (or redox shuttle). In the DSSCs, after photoexcitation of sensitized dye, electrons from the LUMO level of dye molecule are injected into the conduction band of semiconductor metal oxide. Then, electrons transport to the anode and flow to the counter electrode (CE) via an external circuit. Finally, mediator electrolyte through reduction and oxidation carries electrons from counter electrode to the HOMO level of dye molecules, and dye is regenerated. This cycle is repeated again and again, and the device generates electric power continuously.

In this overall process of electron transfer, counter electrode plays a significant role on the photovoltaic parameters of DSSCs. The theoretical maximum photovoltage or open-circuit voltage of the DSSCs is higher than the output voltage after loading. This voltage loss is due to the mass transfer overpotential and the kinetic overpotential or charge transfer over potential. The former is mainly attributed to the ionic conductivity of electrolytes and the transportation of mediator species from the CE to the photoanode, whereas the latter is from the electrocatalytic activity of the CE surface toward mediator [6, 7]. The catalytic activity of the CEs can be

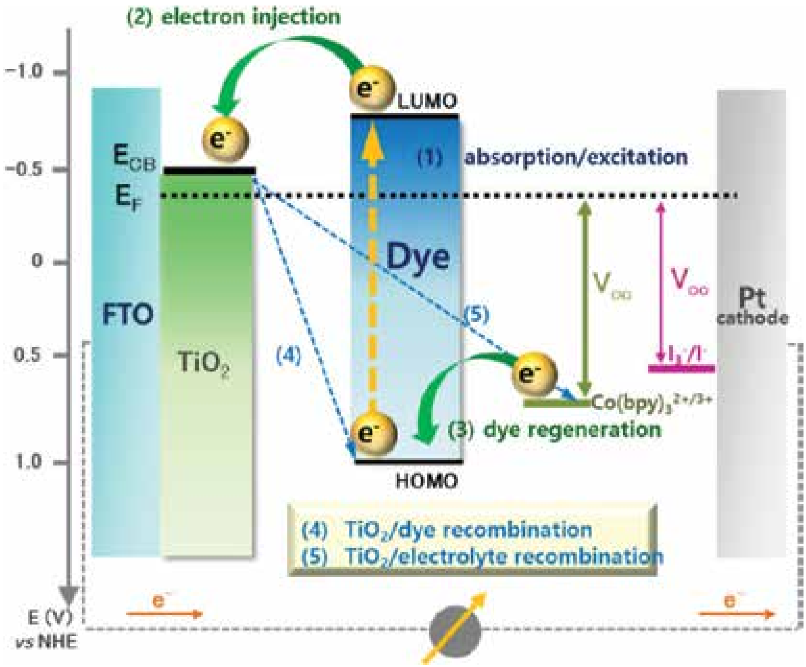

Figure 1. Schematic representation of the working principle of DSSCs.

explained in terms of current density J_o which is calculated from the charge transfer resistance (R_{ct}) by Eq. (1):

$$J_o = \frac{RT}{nFR_{ct}} \tag{1}$$

where R, T, n, and F are the gas constant, the temperature, the number of electrons transferred in the elementary electrode reaction ($n = 2$), and the Faradays constant, respectively.

The overall performance of solar cell is evaluated by the solar-to-electrical energy conversion efficiency, η, which is given by Eq. (2):

$$\eta = \frac{J_{SC}V_{OC}FF}{P_{in}} \tag{2}$$

where J_{sc} is the short-circuit current, V_{oc} is the open-circuit voltage, FF is the fill factor, and P_{in} is the incident light intensity. FF depends on the charge transfer resistance, on series resistance, as well as on the overvoltage for diffusion and electron transfer. Low charge transfer resistance, series resistance, and overvoltage for diffusion and electron transfer lead to a higher FF value, thus resulting in greater efficiency and pushing the output power of the solar cell closer toward its theoretical maximum.

As low-cost and environmentally friendly materials, porous carbon has high surface area, high catalytic activity, high stability in I^-/I_3^- redox shuttle, and better performance than the Pt CEs. The goal of this chapter is to discuss about the synthesis, characterization, and photovoltaic performance of porous carbon materials as supreme counter electrode for DSSCs.

2. Porous carbon materials as counter electrodes for DSSCs

As counter electrode (CE) is one of the most crucial components regulating the efficiency of DSSCs by catalyzing the reduction of the redox couples used as mediators to regenerate the sensitizer after electron injection, it is important to find a low-cost, high-efficiency, easy scalability, and corrosion-stable counter electrode. Platinum (Pt) has been widely employed as the standard CE in DSSCs due to its high catalytic reduction for redox shuttles, good chemical stability, and high conductivity. However, Pt is an expensive and scarce noble metal, which causes a problem for its large-scale production.

Carbon materials are one of the promising substitutes of Pt CE due to their low cost, environmentally friendly, scale availability, high surface area, high catalytic activity, high electrical conductivity, high thermal stability, good corrosion resistance toward iodine, high reactivity for triiodide reduction, etc. In 1996, Kay and Grätzel first explored graphite-carbon black mixture as CE and achieved a power conversion efficiency of 6.7% [8]. Thereafter, intensive research efforts have been focused on carbonaceous materials, such as carbon black, mesoporous carbon, graphite [9], graphene [10, 11], carbon nanotubes [12–15], and carbon nanofibers [16–18], and they have been successfully employed as counter electrodes.

Among the carbonaceous materials, porous carbon materials have captured extensive attention as CE materials for DSSCs, owing to its exceptional properties, including ultrahigh surface areas, large pore volumes, and tunable pore sizes and shapes, and also exhibit nanoscale effects in their mesopore channels and on their pore walls. High surface areas provide a large number of reaction or interaction sites for surface- or interface-related processes such as adsorption and catalysis. Moreover, mesopore channels facilitate the transport of atoms, ions, and large molecules through the bulk of the material and assist to overcome charge transfer resistance [19, 20].

2.1. Synthetic methods of porous carbon materials and photovoltaic performance in DSSCs

Porous carbon materials are mainly produced by activation [21, 22] and templating [19, 23–25] methods from different precursors, and the efficiency of porous carbon electrodes depends on synthesis methods and precursors. The synthetic process of porous carbons by activation is simple, low-cost, and environmentally friendly. Also, activated carbons (ACs) have excellent chemical and thermal stability as well as relatively good electrical conductivity. ACs are derived from different types of carbon-rich organic precursors (coffee waste, wood, pitch, coal, polymers, etc.) by carbonization in inert atmosphere with subsequent physical and/or chemical activation or plasma surface treatment. Depending on the activation process and the used carbon precursors, a variety of ACs with different physicochemical properties and well-developed specific surface area (SSA) from 500 to 3000 $m^2\ g^{-1}$ have been prepared and used as CEs for DSSCs. The high surface area of activated carbons can considerably contribute to improving the catalytic activity of the CEs in DSSCs.

Imoto et al. firstly reported that porous carbon materials prepared with an activation process were superior to a Pt-sputtered electrode as the DSSC CEs. Moreover, they observed that the photovoltaic performance was strongly influenced by the roughness factor and the apparent charge transfer resistance of DSSC CEs. Generally, the roughness factor of the carbon electrode becomes larger when a porous carbon material with larger surface area was used. Thus, the photovoltaic performance was improved with increasing the roughness factor of the carbon-based CE. Also, the apparent charge transfer resistance for redox reaction of I^-/I_3^- couple on the porous carbon CE decreased with increasing the roughness factor. Therefore, back transfer of the photoinjected electrons to the oxidized dyes and/or I_3^- ions was inhibited which in turns improved the FF value significantly. Furthermore, the V_{oc} value for the carbon counter electrode compared to the Pt counter electrode was increased by about 60 mV, maybe because of a positive shift of the formal potential for I^-/I_3^- couple [26].

Nitrogen-doped porous carbon nanorods (N-PCNRs) with high accessible surface area were prepared by Wang group through carbonization of polyaniline (PANI) nanorods and consequent chemical activation and explored as the DSSC CEs. The unique combination of the porosity with high accessible surface area, nitrogen doping, and nanorod structure endows the N-PCNR electrode with an excellent electrocatalytic activity for the I_3^- reduction, which is illuminated by electrochemical measurement. Under simulated AM 1.5 illumination (100 mW cm^{-2}), the DSSC based on N-PCNR counter electrode achieves a conversion efficiency of 7.01%, which is nearly close to that of the cell based on Pt CE (7.25%).

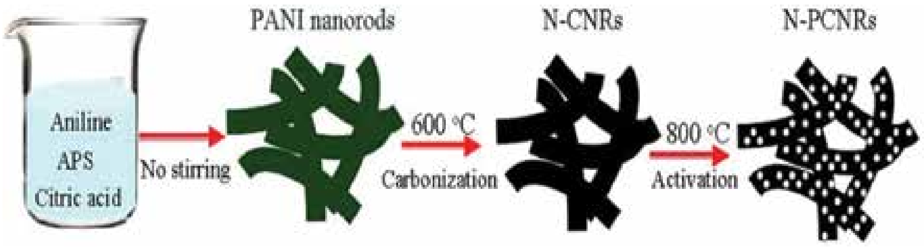

Figure 2. Preparation of nitrogen-doped porous carbon nanorods (N-PCNRs) [27] (copyright (2017) Elsevier).

In their experiment, PANI nanorods were firstly prepared by polymerization of aniline in aqueous solution using ammonium persulfate (APS) as the initiator, as shown in **Figure 2**. Ten grams of aniline and 7 g of citric acid were mixed in 500 mL of distilled water, and then 20 g of ammonium persulfate was dissolved in 150 mL of distilled water. Afterward, ammonium persulfate solution was added into the mixture solution of aniline and citric acid with vigorous stirring. The resulting solution was left standing at about 3°C for 20 h. The obtained dark green sample was filtered and washed with distilled water and then dried under vacuum at 50°C. The as-prepared PANI nanorods were pyrolyzed at 600°C under nitrogen atmosphere for 3 h to obtain nitrogen-doped carbon nanorods (N-CNRs). Finally, N-PCNRs were prepared by activating N-CNRs with KOH [27].

Recently, H. K. Kim group synthesized anchovy-derived nitrogen and sulfur Co-doped porous carbons (AnCs) by a simple carbonization and alkali activation method for DSSC CEs, as shown in **Figure 3**. Typically, a three-step strategy was used to prepare the activated carbon. Firstly, a dried anchovy powder was weighed and transferred into a quartz tubular furnace and then pre-carbonized at 300°C for 1 h under atmosphere, yielding a pre-carbonized material. An activation and carbonization process was sequentially carried out as follows: The pre-carbonized material was mixed with various mass ratios of KOH and then directly heated at an elevated temperature (700, 800, 900°C) for 2 h under inert nitrogen atmosphere. Finally,

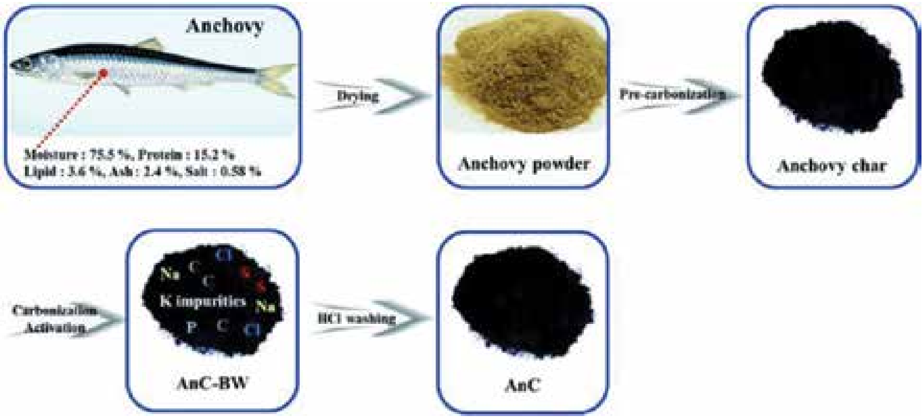

Figure 3. Approximate composition of a dried anchovy powder and schematic illustration for the preparation of anchovy-derived nitrogen and sulfur co-doped porous carbon materials [28] (copyright (2017) Royal Society of Chemistry).

the anchovy-derived activated carbon obtained was washed several times with aqueous 2 M HCl solution and deionized water in order to remove the potassium compounds and any impurities. After filtration, the samples were dried at 70°C in an electric vacuum oven.

The anchovy-derived activated carbons as a DSSC CE exhibited superior PCE of 12.72% to the Pt CE with 12.23%. It is ascribed to an improved fill factor caused by its better electrocatalytic ability [28]. To the best of our knowledge, this PCE is the highest efficiency value reported for DSSCs based on carbon nanomaterial-based CEs. **Table 1** summarizes porous carbon materials produced by activation and their precursors with photovoltaic performance.

Although activated carbon possesses high surface area, but most of the pores are micropore which may increase diffusion impedance of electrolytes into the pore of CEs especially for the bulkier redox couples like $Co(bpy)_3^{2+/3+}$. Templating method is used to synthesize mesopore and macropore carbon materials with connected channel. Depending on the template used, templating method can be classified into two classes: hard template and soft template. Typically, silica nanoparticles, zeolites, anodic aluminum oxide (AAO) films, and mesoporous silica have been used as the hard templates. The synthetic process involves the impregnation of carbon precursor into the porous structure of pre-synthesis template following the carbonization and removal of the template. On the other hand, soft templating involves the self-assembly of copolymers and their direct removal through carbonization. Various commercially available triblock copolymers PEO-PPO-PEO (PO, propylene oxide; EO, ethylene oxide), such as F127 ($EO_{106}PO_{70}EO_{106}$), P123 ($EO_{20}PO_{70}EO_{20}$), and F108 ($EO_{132}PO_{50}EO_{132}$), have been extensively used as the soft templates.

Hierarchical nanostructured carbon with a hollow macroporous core of ca. 60 nm in diameter in combination with mesoporous shell of ca. 30 nm in thickness was synthesized and explored as CE in metal-free organic dye-sensitized solar cells exhibited in **Figure 4** [33]. The superior

CE	Precursor	Dye-electrolyte	R_{ct} (Ω cm^2)	FF (%)	J_{sc} (mA cm^{-2})	PCE (%)	PCE-Pt (%)	Reference
AnCs	Anchovy	SM-315-$Co(bpy)_3^{2+/3+}$	7.56	75.9	18.78	12.72	12.23	[28]
Carbon chunks	Coffee waste	N719-I^-/I_3^-	0.46	72.6	15.09	8.32	8.07	[21]
N-PCNRs	Polyaniline	N719-I^-/I_3^-	2.2	63.0	15.85	7.01	7.25	[27]
HPC	Pine cone	N719-I^-/I_3^-		51.6	13.51	4.98	6.25	[29]
a-NCs	Resol	N719-I^-/I_3^-	7.5	55.0	17.92	6.9	7.1	[30]
Porous carbon	Commercial	N719-I^-/I_3^-	2.2	67.5	15.5	6.1	7.0	[31]
Flexible carbon	Commercial	N719-I^-/I_3^-	0.9	67.3	13.3	6.17	6.37	[32]
Bellfine AP	Commercial	N719-I^-/I_3^-		60.7	7:93	3.89	3.61	[26]

Table 1. Carbon materials produced by activation and their precursors with photovoltaic performance.

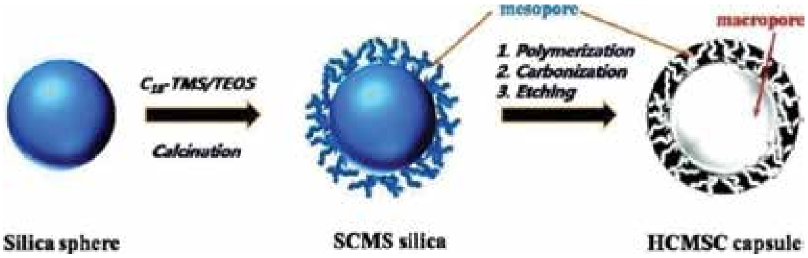

Figure 4. Typical synthetic scheme for HCMSC capsule [33] (copyright (2010) American Chemical Society).

structural characteristics, particularly, the unique hierarchical core/shell nanostructure along with 3D large interconnected interstitial volume with large specific surface area and mesoporous volume, were observed compared with other porous carbon counterparts such as activated carbons and ordered mesoporous carbon CMK-3 (fabricated by replication through nano-casting of SBA-15 silica and using phenol as the carbon source) and Pt counter electrode. This hierarchical core/shell nanostructural feature with 3D large interconnected interstitial volume facilitates mass transportation in hollow macroporous core/mesoporous shell carbon (HCMSC), which was synthesized by replicating through nano-casting of solid core/mesoporous shell silica and phenol and paraformaldehyde as precursor, and enables HCMSC to have highly boosted catalytic activity toward the reduction of I_3^- and so substantially enhanced photovoltaic performance. HCMSC as a DSSC CE displays a V_{oc} of 0.74 V, which is superior to that of the Pt CE by 20 mV. Moreover, it also exhibits a fill factor of 0.67 and an energy conversion efficiency of 7.56%, which are markedly higher than those of its carbon counterparts and comparable to that of Pt (i.e., fill factor of 0.70 and conversion efficiency of 7.79%). In addition, superb chemical stability was observed by HCMSC in the liquid electrolyte containing I^-/I_3^- redox couples, and its initial efficiency of ca. 87% was attained by the HCMSC counter electrode-based solar cell, even after 60 days of aging.

Gokhale et al. introduced a laser photochemical process to synthesize broccoli-type hierarchical morphology for use as a metal-free CE in DSSCs. The method includes pulsed excimer laser irradiation on a thin layer of liquid halo-aromatic organic solvent containing o-dichlorobenzene (DCB). The obtained coating reflects a self-assembled carbon nanoparticle and process-controlled morphology that yields a PCE of 5.1% which was comparable to the PCE of 6.2% with the conventional Pt-based counter electrode [24].

Wang et al. designed and fabricated a novel bioinspired Pt- and FTO-free integrated pure carbon counter electrode for DSSCs with orderly mesoporous carbon (OMC) as the catalytic layer and a porous carbon sheet as a conducting substrate (see in **Figure 5**). On a porous conducting substrate, a stiff, crustose lichen-like, integrated carbon-carbon architectured composite as a catalytic layer was made by a sequential process of spin coating, infiltration, and pyrolysis of polymer precursor. To fabricate the integrated pure carbon electrode, porous carbon plates (PCPs) were firstly prepared by a bulk molding-carbonization process using cheap coal powder as precursor. The permeation of electrolyte through the porous substrate has been fairly resolved by impermeable pretreatment through a repeat pitch impregnation-carbonization treatment of paraffin-protected PCPs. A phenol-formaldehyde resin solution including

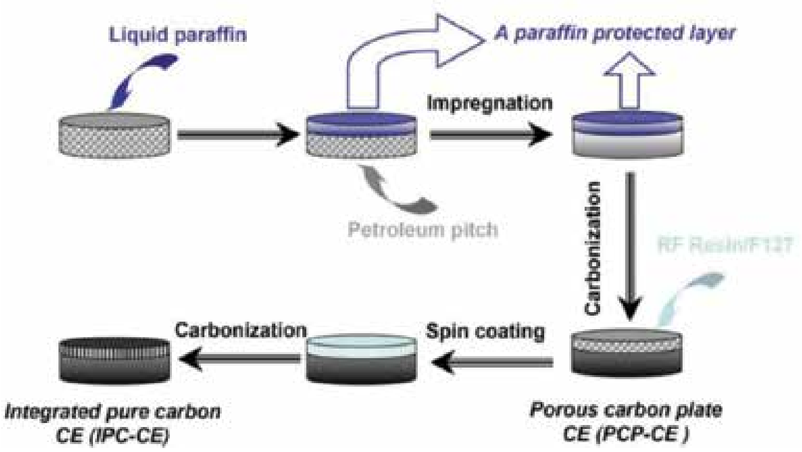

Figure 5. The fabrication procedure of the integrated pure carbon counter electrode for DSSCs [34] (copyright (2013) Royal Society of Chemistry).

Pluronic F127 ($EO_{106}PO_{70}EO_{106}$) as a template was spin coated onto the open pore side of the conductive substrate and then carbonized at 800°C under inert nitrogen atmosphere. By an evaporation-induced self-assembly (EISA) mechanism, an identical mesostructured resin film was formed. Successively, a catalytic mesoporous carbon layer that was embedded in the porous carbon plate was produced by carbonization. The architecturally integrated carbon-based CE displays very low charge transfer resistance (R_{ct}), owing to the large specific surface area of the OMC layer that is accessible to the redox couple, and low series resistance (R_s), due to the high conductivity of the carbon sheet (sheet resistance of 488 mΩ cm^{-1}). The values of R_s and R_{ct} are far lower than those of the platinized fluorine-doped tin oxide glass (Pt/FTO) electrode. DSSCs with this CE show higher PCE of 8.11% than the Pt/FTO-based devices with the PCE of 8.16% [34].

Heteroatom-doped mesoporous carbons have received a great attention because of their enhanced electrocatalytic activity resulted from heteroatoms [35, 36]. The electrocatalytic properties of these systems are typically attributed to high charge polarization arising from the difference in electronegativity between carbon and heteroatom leading to enhanced charge transfer capability and thus increased catalytic activity. Also, to enhance the ordered graphitic layer and stability, porous carbon materials are mixed with polymer, transition metal, and other nanocarbon materials like graphene and CNTs [37–41].

Wang et al. synthesized activated N-doped porous carbons (a-NCs) by pyrolysis and alkali activation of graphene-incorporated melamine formaldehyde resin (MF). To prepare a-NCs, firstly a homogeneous mixture of activated graphene (a-G) with melamine and formaldehyde was prepared and pre-carbonized in Teflon-lined autoclave at 140°C for 4 h to form graphene-incorporated MF resin. The as-prepared graphene-incorporated MF resin composite then carbonized at 800°C for 2 h in N_2 atmosphere followed by activation with KOH, yielding a-NCs. a-NCs with the moderate N-doping level, mesopore-rich porous texture, and incorporation of graphene enable the applications of a-NCs in electrode materials with high specific surface area and good conductivity for dye-sensitized solar cell (DSSCs). At the optimum activation temperature of 700°C, the obtained sample, labeled as a-NC700, possesses a satisfactory graphitization, a specific surface area of 1302 m^2 g^{-1} and an N fraction of 4.5%. A PCE of 6.9% is reached, when as-prepared a-NC700 used as a DSSC CE, which is comparable to that of the Pt CE-based DSSC (7.1%) [30].

H. K. Kim group prepared copolymer-templated nitrogen-enriched nanocarbons (CTNCs) and observed the better PCEs for both I^-/I_3^- and $Co(bpy)_3^{2+/3+}$ redox couples. CTNCs were synthesized by the pyrolysis of PAN-b-PBA copolymer as shown in **Figure 6**.

The block copolymer was pyrolyzed at 600–1000°C for 0.5 h under N_2 gas flow (150 mL min^{-1}) at a heating rate of 10°C min^{-1}, after stabilization through the cross-linking of the PAN block at 280°C for 1 h under air flow (150 mL min^{-1}) at a heating rate of 1°C min^{-1}, purged with N_2 gas for 1 h during cooling. Superior performance in catalytic activity toward the reduction of $Co(bpy)_3^{2+/3+}$ compared to the conventional Pt CE was observed. The detected remarkable activity of CTNCs is owing to their distinctive electronic properties stemming from the presence of nitrogen heteroatoms placed on the edges of nanographitic domains in combination with high specific surface area delivered by a three-dimensional, hierarchical pore structure. Overall, the application of CTNC CEs enhanced the efficiency and fill factor (FF) of JK-306 dye and $Co(bpy)_3^{2+/3+}$ redox couple-based DSSCs at one sun illumination, up to 10.32 and 73.5%, respectively, suggesting the substantial potential of these materials as an striking substitute to expensive Pt-based CEs [42].

Hasin group prepared Co or Ni species incorporated N-doped mesoporous carbon (Co-N-MC or Ni-N-MC) with high specific surface area and observed brilliant electrocatalytic activity toward the electrochemical reaction of I^-/I_3^- redox couple in DSSC systems as compared with N-doped mesoporous carbon (N-MC) displayed in **Figure 7**.

Co-N-MC and Ni-N-MC were synthesized on the basis of replication through nano-casting of SBA-15 mesoporous silica. The polymerization of aniline was conducted in the pore of SBA-15 mesoporous silica functionalized with alkyldiamine group. Cobalt(II) or nickel(II) ion was doped in the polyaniline (PANI) within the pores of SBA-15 followed by pyrolyzing in

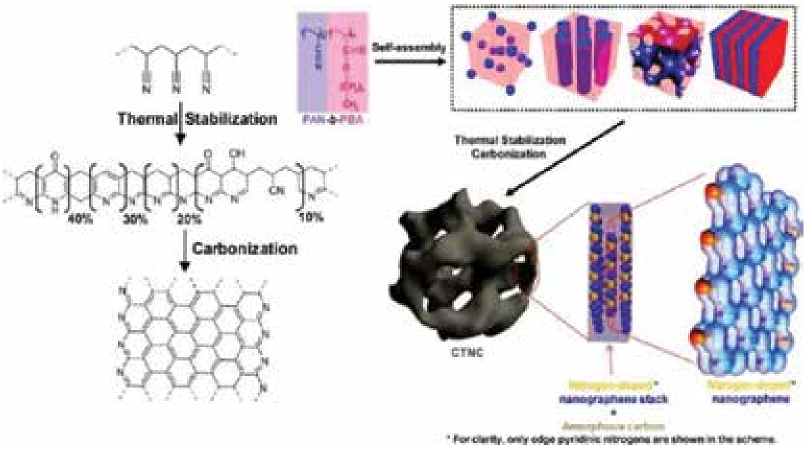

Figure 6. Schematic representation of preparation of CTNC [42] (copyright (2015) Royal Society of Chemistry).

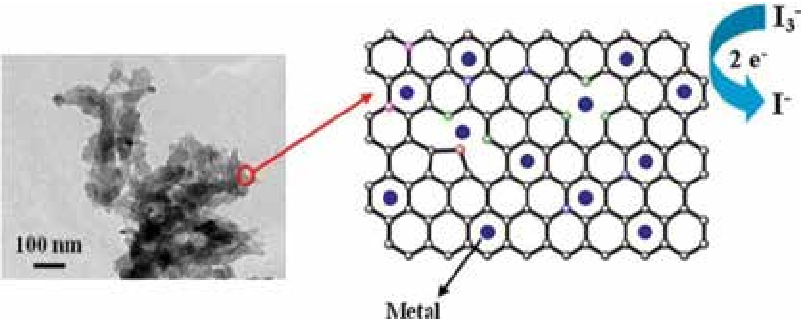

Figure 7. Immobilized Co or Ni on N-doped mesoporous carbons [43] (copyright (2017) Elsevier).

quartz tube. The considerable photoelectric conversion efficiency of Co-N-MC- and Ni-N-MC-based DSSCs is ascribed to the good electrical conductivity in their frameworks and the dominating contents of pyridinic and quaternary N species over pyrrolic N in their structural configuration. Furthermore, significantly lower charge transfer resistance (R_{ct}) associated with metal doping of the Co-N-MC and Ni-N- MC and excellent structural surface properties can also be responsible to enhance the photovoltaic performance. The fill factor (FF) and power conversion efficiency (η) of DSSC utilizing Ni-N-MC counter electrode (FF = 0.70 and η = 8.42%) were higher compared to the DSSC using platinized counter electrode (FF = 0.66 and η = 8.22%). Additionally, Ni-N-MC counter electrode exhibited good electrochemical stability after experiencing ten CV cycles. Moreover, compared to platinized electrode in catalyzing the T_2/T^- organic redox system, all N-MC, Co-N-MC, and Ni-N-MC show better performance. The integration of electrocatalytic Co or Ni species and N-doped mesoporous carbon matrix is an alternative approach for counter electrode electrocatalyst to diminish the cost of DSSCs [43]. Precursors and photovoltaic performance of porous carbon materials synthesized by soft- and hard-templating methods are summaries in **Tables 2** and **3**, respectively.

2.2. Morphological and structural characterization of porous carbon materials

The morphology of porous carbon materials is usually characterized by using scanning electron microscopy (SEM) or field emission scanning electron microscopy (FE-SEM) and transmission electron microscopy (TEM). **Figure** 8(**a**)–(**c**) shows the FE-SEM images for the surface morphology and microstructures of honeycomb-like activated porous carbons (HPCs) [29]. As shown in **Figure** 8(**a**), the micro-sized particles of the as-prepared sample revealed a honeycomb-like morphology containing a huge number of minute holes over its entire frameworks. Magnified view of FE-SEM image of the sample confirmed the interconnected macroporous structures with sizes of ~100–600 nm (in **Figure** 8(**b**)). Moreover, a close inspection reveals that the pore and surface wall of HPC sample comprised of many mesopores and micropores as shown in **Figure** 8(**c**). In addition, the TEM image in **Figure** 8(**d**) also confirmed the honeycomb-like morphology with the porous property.

X-ray diffraction (XRD) and Raman spectroscopy are used to ascertain the extent of crystallinity in the structure of porous carbon samples. Porous carbon materials display diffraction peaks at about 24 and 44°, which are the equivalent of hexagonal graphitic 002 (2θ = 24°) and

CE	Precursor	Dye-electrolyte	R_{ct} (Ω cm^2)	FF (%)	J_{sc} (mA cm^{-2})	PCE (%)	PCE-Pt (%)	Reference
CTNC	PBA-b-PAN	JK-306-Co(bpy)$_3^{2+/3+}$	0.31	73.5	14.57	10.32	9.80	[42]
		JK-306-I$^-$/I$_3^-$		72.9	14.58	7.88		
HPCs	Resol	N719-I$^-$/I$_3^-$	4.68	65.0	14.97	7.22	7.25	[25]
MC	Resol	N719-I$^-$/I$_3^-$	17.2	61.0	14.32	6.06	6.29	[19]
OMC	Coal powder	N719-I$^-$/I$_3^-$	6.99	73.0	14.26	8.11	8.16	[34]
Broccoli-carbon	O-dichlorobenzene	N719-I$^-$/I$_3^-$		46.1	13.86	5.1	6.2	[24]
HPC	Resol	N719-I$^-$/I$_3^-$	0.3	67.0	15.44	6.48	6.45	[44]
OMC	Resol	Thiocyanate-I$^-$/I$_3^-$	6.5	68.0	14.13	7.69	8.25	[45]
MC	Resol	N3-I$^-$/I$_3^-$	0.7	65.0	15.5	6.18	6.26	[46]

Table 2. Porous carbon material synthesis by soft template and their precursors with photovoltaic performance.

101 (2θ = 44°) crystal planes as shown in **Figure 9**(**a**) [50]. To identify the degree of graphitization, Raman spectra are used as follows: Two peaks at 1340 and 1590 cm^{-1} that is assigned to the D band and G band are observed as shown in **Figure 9**(**b**).

The breathing mode vibration of A$_{1g}$, associated with the disordered carbon or defective graphitic carbon appeared at around 1353 cm^{-1} corresponding to the D band. Another peak related to the G band appeared at around 1590 cm^{-1}, which specifies the in-plane stretching vibration mode of E$_{2g}$ in sp^2 sp^{2}C–C bond vibrations, as in graphitic phase [51].

CE	Precursor	Dye-electrolyte	R_{ct} (Ω cm^2)	FF (%)	J_{sc} (mA cm^{-2})	PCE (%)	PCE-Pt (%)	Reference
Carbon framework	Quinoline	N719-I$^-$/I$_3^-$	0.14	69.0	16.54	8.75	7.55	[36]
S-PC	Pitch	N719-I$^-$/I$_3^-$	3.99	67.0	14.98	6.97	7.28	[47]
NMC	Resol	N719-I$^-$/I$_3^-$		60.0	15.46	7.02	7.26	[35]
MSU-F–C	Resol	N719-I$^-$/I$_3^-$	8.75	70.0	14.95	8.18	8.85	[48]
HCMSC	Resol	N719-I$^-$/I$_3^-$	0.5	67.0	16.86	7.56	7.79	[49]
Fe-MCF-C	Divinylbenzene	N719-I$^-$/I$_3^-$		69.0	14.70	7.89		[23]

Table 3. Porous carbon material synthesis by hard template and their precursors with photovoltaic performance.

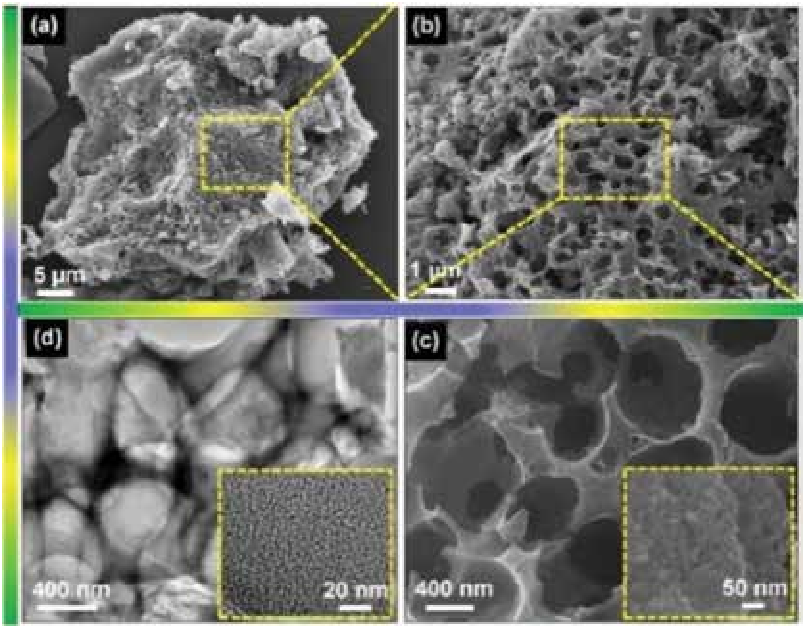

Figure 8. (a–c) FE-SEM images and (d) TEM images of the carbonized HPC sample under inert gas atmosphere [29] (copyright (2017) Elsevier).

Additionally, X-ray photoelectron spectroscopy (XPS) analysis gives the information about the presence of surface functional groups in the porous carbon. In **Figure 9**(**c**), the high-resolution XPS spectrum of C1s in the binding energy range between 280 and 288 eV revealed several carbon-based functional groups, which are assigned to the C–OH, C–C/C–H, C–O, and C=O bonds, respectively. Meanwhile, as shown in **Figure 9**(**d**), the deconvoluted XPS spectra of the O 1 s exhibited the three distinct peaks at the binding energies of 526–538 eV, which are attributed to the C–OH, C=O groups and chemisorbed water molecules, respectively [29].

The surface area and pore volume of porous carbon materials are measured through the experiments of adsorption-desorption isotherms, as shown inset in **Figures 9**(**a**) and **10**(**b**). Porous carbon materials typically exhibit III/IV isotherms with pronounced hysteresis loops, indicating the larger surface area.

The specific surface area is calculated from the Brunauer-Emmett-Teller (BET) equation, and the pore size distribution is derived from the desorption branches of the isotherms using the Barrett-Joyner-Halenda (BJH) method (**Figure 10**(**b**)) [52].

2.3. Electrochemical characterization of porous carbon material-based counter electrodes

The catalytic properties of counter electrodes in DSSCs are usually characterized by electrochemical impedance spectroscopy (EIS) [53, 54]. EIS measurements are performed in a symmetric thin-layer cell (called dummy cell) comprising two identical electrodes and same electrolyte used in the full DSSCs. The Nyquist plots for porous carbon CE consist of three

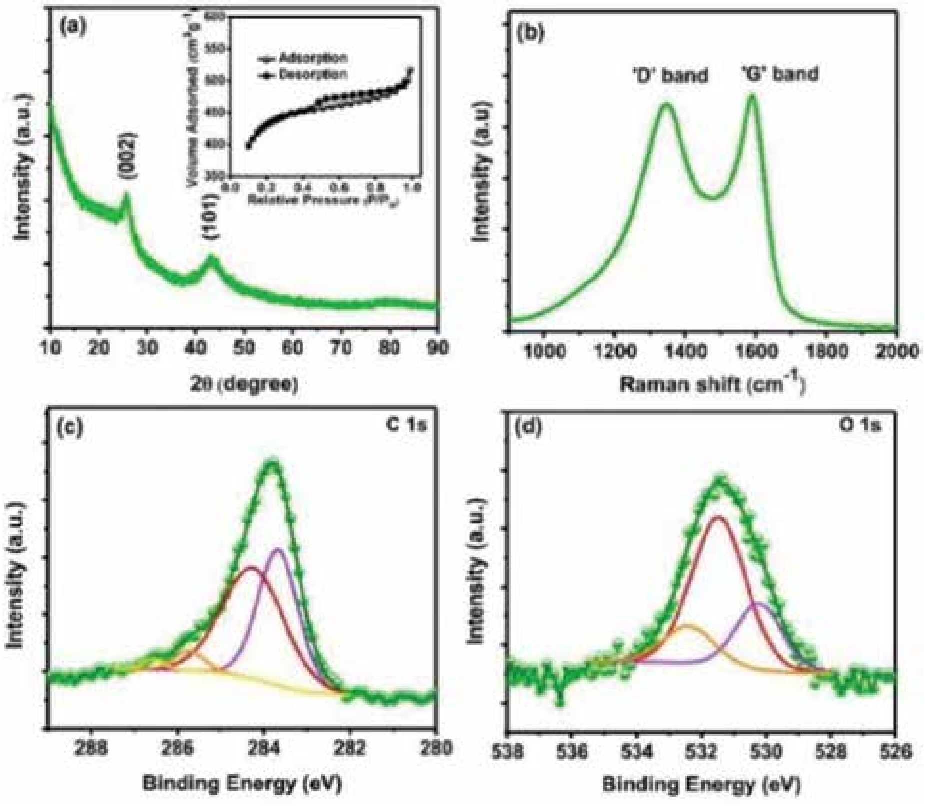

Figure 9. (a) XRD pattern, (b) Raman spectrum, and (c-d) XPS spectra of the HPC sample. The inset of (a) shows the nitrogen adsorption–desorption isotherm of the HPC sample [29] (copyright (2017) Elsevier).

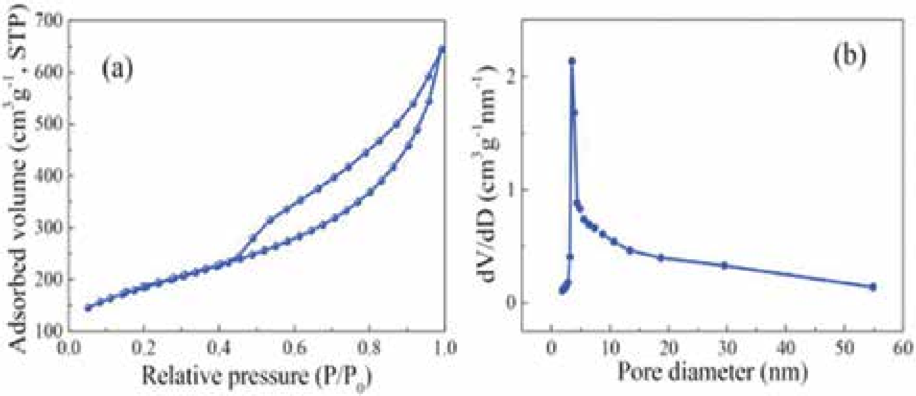

Figure 10. Nitrogen adsorption-desorption isotherms (a) and BJH pore-sized distributions (b) of the S-PC [47] (copyright (2015) Elsevier).

semicircles, which are assigned in the order of increasing frequency to the Nernst diffusion impedance in the bulk electrolyte (< 10 Hz), the charge transfer processes at the electrode/electrolyte interface (2500–25 Hz), and the Nernst diffusion impedance in the pores of electrode materials (100–2.5 KHz) in **Figure 11**(**a**).

The equivalent circuit elements for fitting the EIS data, which is well known as a Randles-type equivalent circuit, comprise of the ohmic serial resistance (R_s), the resistance-capacitance (RC) network consisting of the charge transfer resistance (R_{ct}) and the corresponding capacitance (C) at the electrode/electrolyte interface, and the Nernst diffusion impedance in the bulk electrolyte (N_{bulk}) between electrodes and the pores of electrode materials (N_{pore}) as shown in **Figure 11**(**b**) [55]. The impedance spectrum of the Pt/electrolyte interface diverges to some extent from the behavior of a RC network with an ideal capacitance owing to the roughness of the TCO substrate surface. This effect can be defined by a term called as "constant phase element (CPE)." The impedance Z_{CPE} of a CPE is given by Eq. (3) [53, 56]:

$$Z_{CPE} = B\,(i\omega)^{-\beta} \tag{3}$$

where ω is the angular frequency, B is the CPE parameter, and β is the CPE exponent ($0 \le \beta \le 1$, for ideal capacitance $\beta = 1$).

The parameter N_{pore} can be omitted for Pt CE where the catalytic reaction occurs on virtually nonporous surface (the equivalent circuit for the symmetric cell comprising of Pt CEs is shown in the inset of **Figure 11**(**a**)). As a result, the Nyquist plot for Pt electrode exhibits two semicircles, allocating in the order of decreasing frequency to the charge transfer process at Pt electrode/electrolyte interface and Nernst diffusion of redox couple in electrolyte. From the

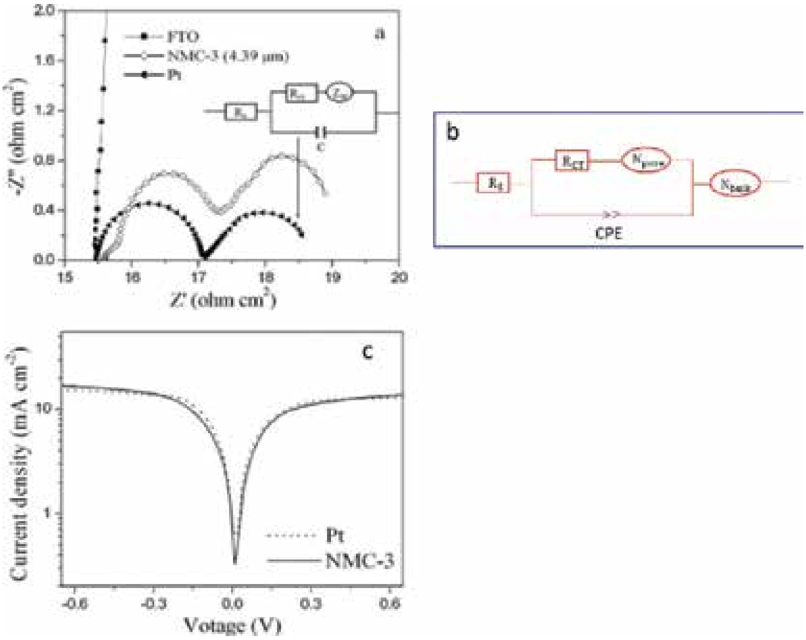

Figure 11. (a) Nyquist plots of the symmetric cells consisting of FTO glass, NMC-3, and Pt electrodes, respectively, equivalent circuit element for Pt CE in the inset. (b) Equivalent circuit element for NMC-3 porous carbon. (c) Tafel polarization curves of the symmetric cells fabricated with two identical Pt and NMC-3 electrodes [35] (copyright (2013) Elsevier).

diameter of the high-frequency semicircle, R_{ct} value of the Pt CE can be estimated directly. The charge transfer resistance, R_{ct}, of the porous carbon CEs depends on the thickness of electrodes. The data listed in **Table 4** show that the R_{ct} of NMC-3 electrode decreases with increasing thickness of NMC-3 layer. R_{ct} value of NMC-3 electrode decreases by 10.36 Ω cm^2 (from 11.81 to 1.45 Ω cm^2), once the thickness of NMC-3 layer increases by 3.44 m (from 0.95 to 4.39 m). This result is mainly owing to the increase in active surface area of NMC-3 film with the thicker NMC-3 layer.

Nevertheless, R_{ct} value barely changes with additional increase of the thickness of NMC-3 layer. The optimum thickness of NMC-3 layer is 4.39 m, which is considerably lower than that of the commonly studied carbon nanoparticle CE in DSSCs. Also, R_s value does not change significantly with the thickness of NMC-3 layer. This is due to the preparation of NMC-3 electrodes on the same FTO substrate, and also the R_s value is controlled mainly by the electrical properties of the FTO substrate. Capacitance, C, increases systematically with the thickness of NMC-3 layer as expected due to an increase in active surface area.

Lower R_{ct} denotes more efficient reduction of redox couples at the CE-electrolyte interface, which in turn reduces charge recombination process and increases the dye-regeneration process at the dye-coated TiO_2/electrolyte interface. Electrochemically active surface areas (EASAs) were estimated from the results of chronoamperometric (CA) measurements according to the Randles-Sevcik equation to expose the question of whether the lower R_{ct} originates from an intrinsically higher catalytic activity or the high surface area of porous carbon [42]. It was found that the intrinsically higher catalytic activity of porous carbon electrodes was mainly responsible for lower charge transfer at the interface.

Tafel polarization measurements are carried out in a symmetric cell similar to the one used in EIS experiment. Usually, the Tafel curve comprises of three distinguishable zones, the polarization zone at low potential (voltage range of −120 to 120 mV), the Tafel zone at middle potential (with a sharp decrease), and the diffusion zone at high potential (horizontal part). The exchange current density (J_o), which is directly associated to the electrocatalytic ability of an electrode, can be calculated by extrapolating the intercept of the anodic and cathodic branches of the corresponding curves in the Tafel zone. **Figure 11(c)** displays the Tafel polar-

Thickness of NMC layer (μm)	**R_s (Ω)**	**R_{ct} (Ω cm^2)**	**C (μF cm^{-2})**
0.95	15.41	11.81	15.8
1.68	15.44	7.75	26.9
3.16	15.45	4.09	34.6
4.39	15.52	1.45	42.6
6.53	15.57	1.5	49.7

Table 4. Electrochemical impedance parameters for NMC-3 electrode with various thicknesses of carbon layer (35) (copyright (2013) Elsevier).

ization curves of the NMC-3 and electrodepositing Pt electrodes. The cathodic and anodic branches of the Tafel curves show a steep slope for NMC-3 and Pt electrodes, indicating a high J_o on the surface of NMC-3 and Pt electrodes. This implies that NMC-3 can have an electrocatalytic ability as effective as Pt electrode toward the I^-/I_3^- redox reaction. Furthermore, the limiting diffusion current density of the NMC-3 and Pt electrodes is observed to be of the same magnitude. This result describes that the bimodal mesopore structure can deliver an advantageous network for the diffusion of the electrolyte.

Furthermore, cyclic voltammetry of dummy cell is used to verify the electrocatalytic activity of porous carbon. The peak-to-peak separation (E_{pp}) and the peak current are two important parameters for comparing catalytic activities of both CEs. A smaller E_{pp} and larger peak currents indicate higher catalytic performance. **Figure 12(a)–(b)** shows the comparison of the CV curves of CTNC-800 and Pt electrodes in the $Co(bpy)_3^{2+/3+}$ system acquired at different scan rates (25–200 mV s^{-1}).

EIS is also used to check the stability of porous carbon CEs. **Figure 13(a)** and (**b**) shows the electrochemical stability of the dummy cells with CTNC-800 and Pt CEs under cumulative potential cycling with $Co(bpy)_3^{2+/3+}$ in acetonitrile. After 100 cycles, although only a very modest increase of R_{ct} values was observed from 0.35 to 0.45 Ω cm^2 for CTNC-800 CEs, but for Pt CEs, the R_{ct} values increased from 3.10 to 11.26 Ω cm^2 by nearly 400%. The sluggish decline of R_{ct} for CTNC-800 compared to Pt clearly implies the higher stability of CTNC-800 in the acetonitrile $Co(bpy)_3^{2+/3+}$ electrolyte as shown in **Figure 13(c)**. Superior electrochemical stability of

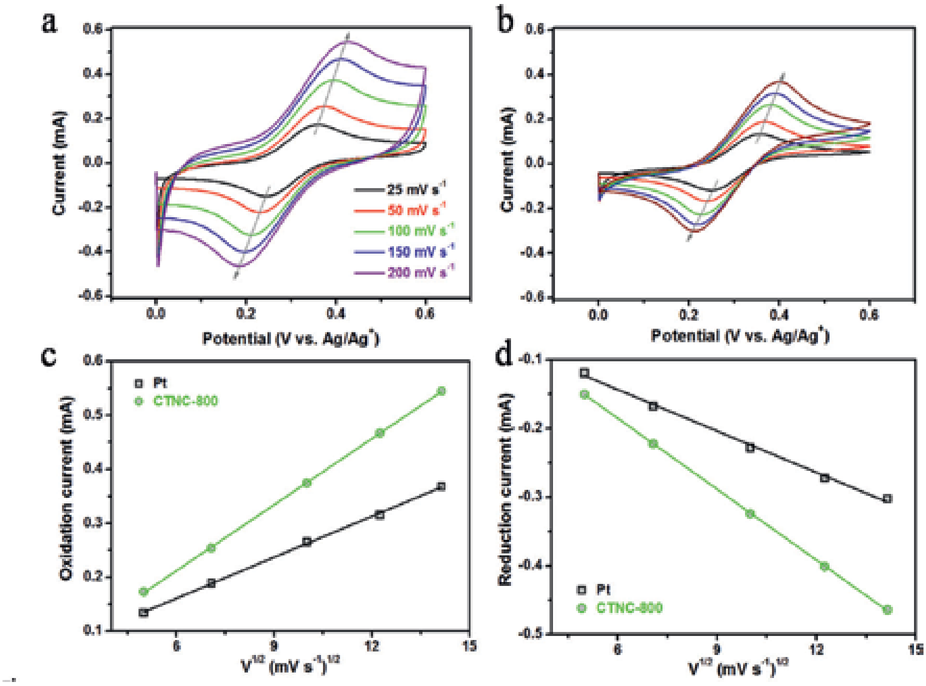

Figure 12. Cyclic voltammograms using CTNC-800 (a) and Pt (b) cathodes in with various scanning rates. The oxidation (c) and reduction (d) peak currents with respect to the square root of scanning rate [42]. Copyright (2015) Royal Society of Chemistry.

CTNC-800 was also confirmed by the EIS measurements of dummy cells after aging the two electrodes at room temperature and open circuit in **Figure 13(d)**. The EIS curve of the CTNC-800 electrode over the period of 14 days was nearly unchanged, while the EIS curves for Pt showed evidence of a progressive increase of the resistance upon aging.

The greater slopes of the linear dependence of the reduction and oxidation currents against the square root of potential and higher peak current of CTNC-800 electrodes at all scan rate confirm the better catalytic activity of CTNC-800 toward the reduction of $Co(bpy)_3^{2+/3+}$ than the Pt CE.

2.4. Photovoltaic performance evaluation of DSSCs with porous carbon CEs

To evaluate the photovoltaic performance of DSSCs employing porous carbon CEs, generally a prescribed amount of carbon materials is grounded in a mortar with 0.1 ml tetrabutyl titanate and 8 ml n-butanol to obtain the carbon paste. Then, the electrode is prepared by coating carbon paste on FTO glass using doctor-blade method and heated at a certain temperature for 30 min. On the other hand, photoanode is prepared by depositing TiO_2 film with the thickness of 10 μm on FTO glass substrate by doctor-blade method and then sintered at a certain tem-

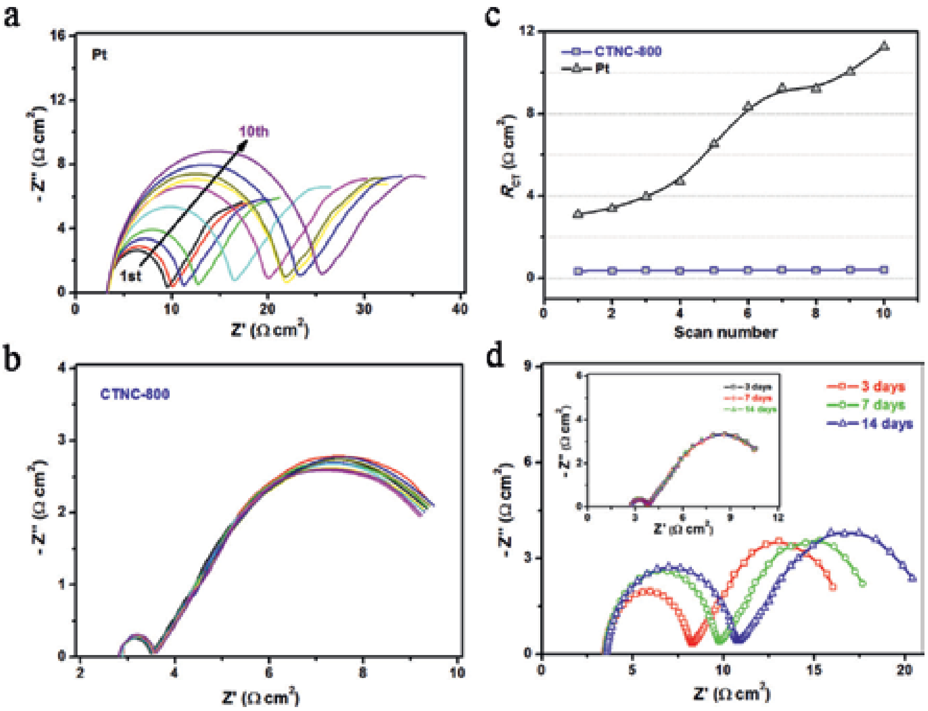

Figure 13. Electrochemical stability under potential-cycling on dummy cells with Pt (a), CTNC-800 (b) in acetonitrile solution of . The sequence of measurements was as follows: 10 × CV scans (from 0V → 1V → 1V → 0V → 1 V, scan rate 50) followed by 30 s relaxation at 0 V followed by an EIS measurement at 0 V from Hz to0.1 Hz. This sequence of electrochemical stability testing was repeated 10 times. (c) changes in the Pt and CTNC-800 according to the potential cycling. (d) Nyquist plots of symmetrical dummy cells consisting of Pt and CTNC-800 (inset) collected after 3 days (black), 7 days (red) and 14 days (green) of aging at room temperate and open circuit [42]. Copyright (2015) Royal Society of Chemistry.

perature for 30 min. After that, the sintered TiO_2 electrodes are immersed into a solution containing dye in ethanol for a long time at room temperature to adsorb dye on TiO_2 photoanode.

A DSSC device is fabricated by clamping a dye-sensitized TiO_2 photoanode, a drop of electrolyte, and a counter electrode. For I^-/I_3^- redox shuttle, a mixture of 0.5 M 1-methyl-3-propylimidazolium iodide, 0.3 MLiI, 0.06 M I_2, and 0.4 M 4-tert-butylpyridine in 3-methoxypropionitrile is used as the electrolyte of DSSCs [35]. Finally, the photovoltaic performance of DSSC device is evaluated under AM 1.5 solar simulator illumination at 100 mW cm^{-2}.

Figure 14 compares the photocurrent density-voltage (J-V) curves of the DSSCs with NMC-3, Pt, and FTO glass counter electrodes. The photovoltaic parameters of the DSSCs, including short-circuit current density (J_{sc}),), open-circuit voltage (V_{oc}), fill factor (FF), and power conversion efficiency (η), are summarized in **Table 5**. The DSSC with FTO glass as counter electrode exhibits a V_{oc} of 0.49 V, a J_{sc} of 4.13 mA cm^{-2}, and a FF of 0.10, leading to a poor power conversion efficiency of 0.20%. When NMC-3 porous carbon material is employed as the counter electrode in DSSC, the DSSC attains a V_{oc} of 0.71 V, J_{sc} of 15.46 mA cm^{-2}, FF of 0.64, and η of 7.02%. This power conversion efficiency is considerably comparable to 7.26% of the DSSC with Pt counter electrode. The outstanding photovoltaic performances of the DSSCs with NMC-3 counter electrode mostly originate from the vivid electrocatalytic performance of NMC-3 electrode associated with the nitrogen doping, bimodal mesopore structure, and large surface area.

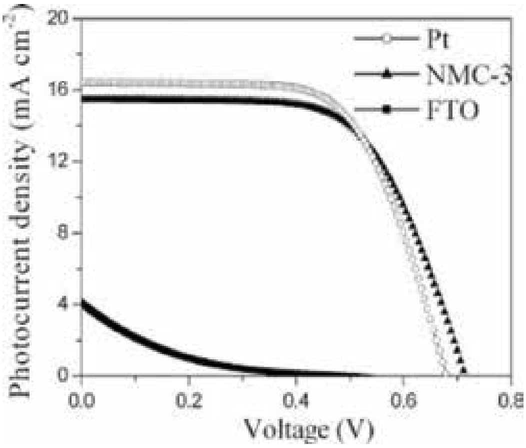

Figure 14. Photocurrent density-voltage curves of DSSCs with Pt, NMC-3, and FTO glass counter electrodes [35] (copyright (2013) Elsevier).

Counter electrode	V_{oc} (V)	J_{sc} (mA cm^{-2})	FF	η (%)
Pt	0.68	16.43	0.65	7.26
NMC-3	0.71	15.46	0.64	7.02
FTO	0.49	4.13	0.10	0.20

Table 5. Photovoltaic parameters of the DSSCs using Pt, NMC-3, and FTO glass counter electrode [35] (copyright (2013) Elsevier).

3. Conclusions and outlook

Dye-sensitized solar cells (DSSCs) have aroused intense interest and been regarded as one of the most prospective solar cells, due to low-cost, flexibility, simple device fabrication, and high conversion efficiency under weak light, in comparison to the conventional photovoltaic devices. Very recently, G2E in Swiss and G24i in the UK including Korean and Japan companies have demonstrated commercial and prototyped components based on DSSC technology with liquid electrolytes. However, the unit costs, long-term device stability, and power conversion efficiency must be further improved for real-life applications. For this purpose, considerable efforts have been devoted to the search for low-cost Pt-free catalysts that exhibit high electrochemical activity and fast electron transfer kinetics, while a platinum (Pt) metal is still known as the highly efficient and extensively used counter electrode (CE) in DSSCs; however, it has more or less problems that make it improper for the real-life application in DSSCs, such as its high manufacturing cost owing to its natural scarcity and insufficient long-term instability to the I^-/I_3^- redox couple in DSSCs. As a result, significant efforts have been devoted to finding possible alternatives to Pt, including carbon blacks, carbon nanotubes, functionalized graphene, and heteroatom-doped graphene nanoplatelets as efficient metal-free electrocatalysts. An ideal counter electrode in DSSCs must possess the following properties: high electrocatalytic ability and high conductivity, optimum thickness, high surface area and porous nature, low charge transfer resistance, high electrochemical and mechanical stability, energy level that matches the potential of the redox couple electrolyte, high reflectivity, and good adhesivity with TCO. High electrocatalytic ability and low charge transfer resistance of CEs increase FF and J_{sc} and subsequently PCE of the DSSC. In this chapter, porous carbon materials have been considered as one of the promising candidates for the alternative to PT CE, since they have high surface area and porous nature, chemical corrosion resistance, electrochemical and mechanical stability, low cost, and simple preparation methods compared to Pt counter electrodes. Especially, heteroatom-doped porous carbon materials, such as CTNCs and AnCs, exhibited better electrocatalytic ability, lower charge transfer resistance, and higher PCE than the Pt CEs in $Co(bpy)_3^{2+/3+}$-based electrolyte which make them promising candidates as metal-free CE for DSSCs and open a new research area for porous carbon CEs in $Co(bpy)_3^{2+/3+}$-based DSSCs. However, they are not sufficiently active in iodide electrolytes, which are more common and desirable electrolytes. In the future, better electrocatalytic ability and electrochemical stability of carbon-based materials toward both redox couples of iodide and cobalt electrolytes still need to be significantly improved for the practical application of DSSCs.

Acknowledgements

This work was supported by the National Research Foundation of Korea (NRF) grant funded by the Korean government (MSIT) through the Mid-career Researcher Program (2017R1A2A1A17069374), the Functional Districts of the Science Belt Support Program (2017K000494), and the Korea Research Institute of Chemical Technology (KRICT & Project No. KK1702-A00).

Author details

Mohammad Aftabuzzaman and Hwan Kyu Kim*

*Address all correspondence to: hkk777@korea.ac.kr

Global GET-Future Lab and KU-KRICT CRC, Department of Advanced Materials Chemistry, Korea University, Sejong, Korea

References

[1] Zhang Q, Park K, Xi J, Myers D, Cao G. Recent progress in dye-sensitized solar cells using nanocrystallite aggregates. Advanced Energy Materials. [Internet]. 2011 Nov 1 [cited 2017 Oct 6];**1**(6):988-1001. Available from: http://doi.wiley.com/10.1002/aenm.201100352

[2] Hagfeldt A, Boschloo G, Sun L, Kloo L, Pettersson H. Dye-sensitized solar cells [Internet]. Chemical Reviews. 2010 Nov 10 [cited 2017 Oct 8];**110**(11):6595-6663. Available from: http://pubs.acs.org/doi/abs/10.1021/cr900356p

[3] O'Regan B, Grätzel M. A low-cost, high-efficiency solar cell based on dye-sensitized colloidal TiO2 films. Nature [Internet]. 1991 Oct 24 [cited 2017 Oct 6];**353**(6346):737-740. Available from: http://www.nature.com/doifinder/10.1038/353737a0

[4] Eom YK, Kang SH, Choi IT, Yoo Y, Kim J, Kim HK. Significant light absorption enhancement by a single heterocyclic unit change in the π-bridge moiety from thieno[3,2-b]benzothiophene to thieno[3,2-b]indole for high performance dye-sensitized and tandem solar cells. Journal of Materials Chemistry A [Internet]. 2017;**5**(5):2297-2308. Available from: http://xlink.rsc.org/?DOI=C6TA09836C

[5] Kakiage K, Aoyama Y, Yano T, Oya K, Fujisawa J, Hanaya M. Highly-efficient dye-sensitized solar cells with collaborative sensitization by silyl-anchor and carboxy-anchor dyes. Chemical Communication [Internet]. 2015;**51**(88):15894-15897. Available from: http://xlink.rsc.org/?DOI=C5CC06759F

[6] Li K, Yu Z, Luo Y, Li D, Meng Q. Recent progress of counter electrodes in nanocrystalline dye-sensitized solar cells. Journal of Materials Science & Technology [Internet]. 2007;**23**(5):577. Available from: http://d.wanfangdata.com.cn/periodical_clkxjsxb-e200705001.aspx

[7] Papageorgiou N. Counter-electrode function in nanocrystalline photoelectrochemical cell configurations. Coordination Chemistry Reviews [Internet]. 2004 [cited 2017 Nov 1];**248**:1421-1446. Available from: https://ac.els-cdn.com/S0010854504000645/1-s2.0-S0010854504000645-main.pdf?_tid=8ab64572-becd-11e7-8ea1-00000aacb35f&acdnat=1509517748_8164d715bb1caf309a882f60b5800677

[8] Grätzel M, Kay A. Low cost photovoltaic modules based on dye sensitized nanocrystalline titanium dioxide and carbon powder. Sol Energy Mater Sol Cells [Internet]. 1996;**44**(1):99-117. Available from: http://linkinghub.elsevier.com/retrieve/pii/0927024896000633

[9] Wei YS, Jin QQ, Ren TZ. Expanded graphite/pencil-lead as counter electrode for dye-sensitized solar cells. Solid State Electron [Internet]. 2011;**63**(1):76-82. Available from: http://dx.doi.org/10.1016/j.sse.2011.05.019

[10] Kavan L, Yum JH, Grätzel M. Graphene nanoplatelets outperforming platinum as the electrocatalyst in co-bipyridine-mediated dye-sensitized solar cells. Nano Letters. 2011; **11**(12):5501-5506

[11] Kavan L, Yum JH, Nazeeruddin MK, Grätzel M. Graphene nanoplatelet cathode for Co(III)/(II) mediated dye-sensitized solar cells. ACS Nano. 2011;**5**(11):9171-9178

[12] Imbrogno A, Pandiyan R, Barberio M, Macario A, Bonanno A, El khakani MA. Pulsed-laser-ablation based nanodecoration of multi-wall-carbon nanotubes by Co-Ni nanoparticles for dye-sensitized solar cell counter electrode applications. Materials for Renewable and Sustainable Energy [Internet]. 2017;**6**(2):11. Available from: http://link.springer.com/10.1007/s40243-017-0095-3

[13] Siuzdak K, Klein M, Sawczak M, Wróblewski G, Słoma M, Jakubowska M, et al. Spray-deposited carbon-nanotube counter-electrodes for dye-sensitized solar cells. Physica Status Solidi (A) Applications and Materials. 2016;**213**(5):1157-1164

[14] Sedghi A, Nourmohammadi Miankushki H. Effect of Multi Walled carbon nanotubes as counter electrode on dye sensitized solar cells. International Journal of Electrochemical Science [Internet]. 2014;**9**:2029-2037. Available from: www.electrochemsci.org

[15] De Volder, Michael FL. Tawfick SH, Ray HB, A. John H. Carbon nanotubes: Present and future commercial applications. Science (80-). 2013;**339**(6119):535-539

[16] Yousef A, Brooks RM, El-Newehy MH, Al-Deyab SS, Kim HY. Electrospun Co-TiC nanoparticles embedded on carbon nanofibers: Active and chemically stable counter electrode for methanol fuel cells and dye-sensitized solar cells. International Journal of Hydrogen Energy [Internet]. 2017;**42**(15):10407-10415. Available from: http://dx.doi.org/10.1016/j.ijhydene.2017.01.171

[17] Guo H, Zhu Y, Li W, Zheng H, Wu K, Ding K, et al. Synthesis of highly effective Pt/carbon fiber composite counter electrode catalyst for dye-sensitized solar cells. Electrochim Acta [Internet]. 2015;**176**:997-1000. Available from: http://dx.doi.org/10.1016/j.electacta.2015.07.103

[18] Wang G, Kuang S, Zhang W. Helical carbon nanofiber as a low-cost counter electrode for dye-sensitized solar cells. Materials Letters [Internet]. 2016;**174**:14-6. Available from: http://dx.doi.org/10.1016/j.matlet.2016.03.076

[19] Chen M, Shao L-L, Qian X, Liu L, Ren T-Z, Yuan Z-Y. Mesoporous carbon counter electrode materials for dye-sensitized solar cells: The effect of structural mesopore ordering. Chemical Engineering Journal [Internet]. 2014;**256**:23-31. Available from: http://linkinghub.elsevier.com/retrieve/pii/S1385894714008523

[20] Jiang QW, Li GR, Wang F, Gao XP. Highly ordered mesoporous carbon arrays from natural wood materials as counter electrode for dye-sensitized solar cells. Electrochemistry Communications [Internet]. 2010;**12**(7):924-927. Available from: http://dx.doi.org/10.1016/j.elecom.2010.04.022

[21] Chung DY, Son YJ, Yoo JM, Kang JS, Ahn CY, Park S, et al. Coffee waste-derived hierarchical porous carbon as a highly active and durable electrocatalyst for electrochemical energy applications. ACS Applied Materials & Interfaces. 2017;**9**(47):41303-41313

[22] Zhao B, Huang H, Jiang P, Zhao H, Huang X, Shen P, et al. Flexible counter electrodes based on mesoporous carbon aerogel for high-performance dye-sensitized solar cells. Journal of Physical Chemistry C. 2011;**115**(45):22615-22621

[23] Ramasamy E, Lee J. Ferrocene-derivatized ordered mesoporous carbon as high performance counter electrodes for dye-sensitized solar cells. Carbon N Y [Internet]. 2010;**48**(13):3715-3720. Available from: http://dx.doi.org/10.1016/j.carbon.2010.06.033

[24] Gokhale R, Agarkar S, Debgupta J, Shinde D, Lefez B, Banerjee A, et al. Laser synthesized super-hydrophobic conducting carbon with broccoli-type morphology as a counter-electrode for dye sensitized solar cells. Nanoscale [Internet]. 2012;**4**(21):6730. Available from: http://xlink.rsc.org/?DOI=c2nr32082g

[25] Shao LL, Chen M, Yuan ZY. Hierarchical porous carbons as a metal-free electrocatalyst of triiodide reduction for dye-sensitized solar cells. Journal of Power Sources [Internet]. 2014;**272**:1091-1099. Available from: http://dx.doi.org/10.1016/j.jpowsour.2014.09.028

[26] Imoto K, Takahashi K, Yamaguchi T, Komura T, Nakamura JI, Murata K. High-performance carbon counter electrode for dye-sensitized solar cells. Solar Energy Materials & Solar Cells. 2003;**79**(4):459-469

[27] Wang G, Yan C, Hou S, Zhang W. Low-cost counter electrodes based on nitrogen-doped porous carbon nanorods for dye-sensitized solar cells. Materials Science in Semiconductor Processing [Internet]. 2017;**63**(November 2016):190-195. Available from: http://dx.doi.org/10.1016/j.mssp.2017.02.018

[28] Kim CK, Choi IT, Kang SH, Kim HK. Anchovy-derived nitrogen and sulfur co-doped porous carbon materials for high-performance supercapacitors and dye-sensitized solar cells. RSC Advances [Internet]. 2017;**7**(57):35565-35574. Available from: http://dx.doi.org/10.1039/C7RA06102A%0Ahttp://xlink.rsc.org/?DOI=C7RA06102A

[29] Nagaraju G, Lim JH, Cha SM, Yu JS. Three-dimensional activated porous carbon with meso/macropore structures derived from fallen pine cone flowers: A low-cost counter electrode material in dye-sensitized solar cells. Journal of Alloys and Compounds [Internet]. 2017;**693**:1297-1304. Available from: http://dx.doi.org/10.1016/j.jallcom.2016.10.015

[30] Wang L, Gao Z, Chang J, Liu X, Wu D, Xu F, et al. Nitrogen-doped porous carbons as electrode materials for high-performance supercapacitor and dye-sensitized solar cell. ACS Applied Materials & Interfaces. 2015;**7**(36):20234-20244

[31] Li K, Luo Y, Yu Z, Deng M, Li D, Meng Q. Low temperature fabrication of efficient porous carbon counter electrode for dye-sensitized solar cells. Electrochemistry Communications [Internet]. 2009;**11**(7):1346-1349. Available from: http://dx.doi.org/10.1016/j.elecom.2009.04.025

[32] Chen J, Li K, Luo Y, Guo X, Li D, Deng M, et al. A flexible carbon counter electrode for dye-sensitized solar cells. Carbon N Y [Internet]. 2009;**47**(11):2704-2708. Available from: http://dx.doi.org/10.1016/j.carbon.2009.05.028

[33] Fang B, Fan SQ, Kim JH, Kim MS, Kim M, Chaudhari NK, et al. Incorporating hierarchical nanostructured carbon counter electrode into metal-free organic dye-sensitized solar cell. Langmuir. 2010;**26**(13):11238-11243

[34] Wang C, Meng F, Wu M, Lin X, Wang T, Qiu J, et al. A low-cost bio-inspired integrated carbon counter electrode for high conversion efficiency dye-sensitized solar cells. Physical Chemistry Chemical Physics [Internet]. 2013;**15**(34):14182. Available from: http://xlink.rsc.org/?DOI=c3cp52525b

[35] Wang G, Kuang S, Wang D, Zhuo S. Nitrogen-doped mesoporous carbon as low-cost counter electrode for high-efficiency dye-sensitized solar cells. Electrochim Acta [Internet]. 2013;**113**:346-353. Available from: http://dx.doi.org/10.1016/j.electacta.2013.09.107

[36] Xiao N, Song J, Wang Y, Liu C, Zhou Y, Liu Z, et al. Nitrogen-doped porous carbon with well-balanced charge conduction and electrocatalytic activity for dye-sensitized solar cells. Carbon N Y. 2018;**128**:201-204

[37] Li L, Sui H, Zhang W, Li X, Yang K, Hagfeldt A, et al. Mesoporous carbon-imbedded W $_2$ C composites as flexible counter electrodes for dye-sensitized solar cells. Journal of Materials Chemistry C [Internet]. 2016;**4**:6778-6783. Available from: http://xlink.rsc.org/?DOI=C6TC01601D

[38] Selamat MH, Ahmad AH. Application of dye-sensitized solar cell (Dssc) from polyurethane (Pu)/diol-nai electrolyte with activated carbon (Ac) composite electrode. 2016;**10**(2):2-4

[39] Shao L-L, Chen M, Ren T-Z, Yuan Z-Y. Ordered mesoporous carbon/graphene nanosheets composites as counter electrodes in dye-sensitized solar cells. Journal of Power Sources [Internet]. 2015;**274**:791-798. Available from: http://linkinghub.elsevier.com/retrieve/pii/S0378775314017169

[40] Chen M, Shao L-L, Qian X, Ren T-Z, Yuan Z-Y. Direct synthesis of cobalt nanoparticle-imbedded mesoporous carbons for high-performance dye-sensitized solar cell counter electrodes. Journal of Materials Chemistry C [Internet]. 2014;**2**(48):10312-10321. Available from: http://xlink.rsc.org/?DOI=C4TC02270J

[41] Park S-H, Jung H-R, Kim B-K, Lee W-J. MWCNT/mesoporous carbon nanofibers composites prepared by electrospinning and silica template as counter electrodes for dye-sensitized solar cells. Journal of Photochemistry and Photobiology A: Chemistry [Internet]. 2012;**246**:45-49. Available from: http://linkinghub.elsevier.com/retrieve/pii/S101060301200384X

[42] Ju MJ, Choi IT, Zhong M, Lim K, Ko J, Mohin J, et al. Copolymer-templated nitrogen-enriched nanocarbons as a low charge-transfer resistance and highly stable alternative to platinum cathodes in dye-sensitized solar cells. Journal of Materials Chemistry A [Internet]. 2015;**3**(8):4413-4419. Available from: http://xlink.rsc.org/?DOI=C4TA07012G

[43] Hasin P, Amornkitbamrung V, Chanlek N. Economical nanocomposites of cobalt or nickel species and polyaniline-derived N-doped mesoporous carbons for dye-sensitized

solar cells as counter electrodes. Journal of Catalysis [Internet]. 2017;**351**:19-32. Available from: http://dx.doi.org/10.1016/j.jcat.2017.03.021

[44] Wang G, Huang C, Xing W, Zhuo S. Micro-meso hierarchical porous carbon as low-cost counter electrode for dye-sensitized solar cells. Electrochimica Acta [Internet]. 2011;**56**(16):5459-5463. Available from: http://dx.doi.org/10.1016/j.electacta.2011.03.024

[45] Ramasamy E, Chun J, Lee J. Soft-template synthesized ordered mesoporous carbon counter electrodes for dye-sensitized solar cells. Carbon N Y [Internet]. 2010;**48**(15):4563-4565. Available from: http://dx.doi.org/10.1016/j.carbon.2010.07.030

[46] Wang G, Xing W, Zhuo S. Application of mesoporous carbon to counter electrode for dye-sensitized solar cells. Journal of Power Sources. 2009;**194**(1):568-573

[47] Yang W, Ma X, Xu X, Li Y, Raj SI, Ning G, et al. Sulfur-doped porous carbon as metal-free counter electrode for high-efficiency dye-sensitized solar cells. Journal of Power Sources [Internet]. 2015;**282**:228-234. Available from: http://dx.doi.org/10.1016/j.jpowsour.2015.02.060

[48] Ramasamy E, Lee J. Large-pore sized mesoporous carbon electrocatalyst for efficient dye-sensitized solar cells. Chemical Communications [Internet]. 2010;**46**(12):2136. Available from: http://xlink.rsc.org/?DOI=b920916f

[49] Fan SQ, Fang B, Kim JH, Jeong B, Kim C, Yu JS, et al. Ordered multimodal porous carbon as highly efficient counter electrodes in dye-sensitized and quantum-dot solar cells. Langmuir. 2010;**26**(16):13644-13649

[50] Wickramaratne NP, Perera VS, Park BW, Gao M, McGimpsey GW, Huang SD, et al. Graphitic mesoporous carbons with embedded prussian blue-derived iron oxide nanoparticles synthesized by soft templating and low-temperature graphitization. Chemistry of Materials. 2013;**25**(14):2803-2811

[51] Sadezky A, Muckenhuber H, Grothe H, Niessner R, Pöschl U. Raman microspectroscopy of soot and related carbonaceous materials: Spectral analysis and structural information. Carbon N Y. 2005;**43**(8):1731-1742

[52] Cheng Q, Ji L, Wu K, Zhang W. Morphology-dependent electrochemical enhancements of porous carbon as sensitive determination platform for ascorbic acid, dopamine and uric acid. Scientific Reports [Internet]. 2016;**6**(January):1-8. Available from: http://dx.doi.org/10.1038/srep22309

[53] Hauch A, Georg A. Diffusion in the electrolyte and charge-transfer reaction at the platinum electrode in dye-sensitized solar cells. Electrochimica Acta. 2001;**46**(22):3457-3466

[54] Papageorgiou N. An iodine/triiodide reduction electrocatalyst for aqueous and organic media. Journal of the Electrochemical Society [Internet]. 1997;**144**(3):876. Available from: http://jes.ecsdl.org/cgi/doi/10.1149/1.1837502

[55] Roy-Mayhew JD, Bozym DJ, Punckt C, Aksay IA. Functionalized graphene as a catalytic solar cells. ACS Nano. 2010;**4**(10):6203-6211

[56] Cördoba-Torres P, Mesquita TJ, Nogueira RP. Relationship between the origin of constant-phase element behavior in electrochemical impedance spectroscopy and electrode surface structure. Journal of Physical Chemistry C. 2015;**119**(8):4136-4147

New Organic Polymers for Solar Cells

Renat B. Salikhov, Yuliya N. Biglova and
Akhat G. Mustafin

Additional information is available at the end of the chapter

http://dx.doi.org/10.5772/intechopen.74164

Abstract

From the moment of conductive polyacetylene discovery, semiconducting polymers and other organic thin films and multilayers are important for a wide range of applications, including electronics, photovoltaics and sensors. The main idea of this chapter is the synthesis of new conjugated donor and acceptor polymers and development of organic solar cells on their basis. As donor polymers were used modified polyanilines (PANIs) and its dopants, as acceptor compounds - the fullerene C_{60} derivatives. Experimental prototypes of organic solar cells were obtained on the basis of binary donor-acceptor layers and bulk heterojunctions, consisting of novel polyaniline derivatives and fullerene-contained polymers. The current-voltage characteristics of solar cells were measured and the values of such parameters, such as open-circuit voltage, short-circuit current, fill factor and power conversion efficiency, were calculated. Comparison of parameters of the various types of organic solar cells was held.

Keywords: organic solar cell, polyaniline, fullerene-containing monomer and polymer, power conversion efficiency

1. Introduction

Organic materials with semiconductor properties have recently become the object of intensive research aimed at developing various elements of organic electronics: field-effect transistors, light-emitting diodes, memory cells, solar cells and sensors. After the opening of conductive polyacetylene [1], conjugated polymers are considered as a replacement for inorganic semiconductors. In the field of the development of organic solar cells (OSCs), real progress has been possible since the mid-1990s after the synthesis of conductive conjugated polymers of the latest generation used for the production of modern light-emitting diodes and field-effect transistors.

Such polymers have excellent mechanical properties, the ability to process, a variety of forms and derivatives. They have a high absorption coefficient in the optical range, which allows their use in the form of ultra-thin films (about 100 nm thickness). The advantages mentioned above, as well as the possibility of depositing films from solutions at normal pressure onto flexible substrates of a large area, make it possible to manufacture an OSC using such relatively cheap methods as inkjet printing and stamping technique [2]. Despite these positive factors for the use of polymers, commercialization of the OSC is hampered both by relatively low-power conversion efficiency (PCE) of ~6–7% and by the need for protective encapsulation from environmental influences.

Almost all known types of organic photovoltaic cells can be divided into two main groups. The first group consists of batteries with a binary structure in which the photoactive components of the donor and acceptor types are deposited in separate layers. The second group includes batteries with a bulk heterojunction, in which there is only one photoactive layer, which is a mixture of a donor and an acceptor. In polymer solar cells, the active layers of the device must be located between two layers of conducting electrodes, one of which is transparent to incident light. Typically, for this purpose, a compound comprising indium tin oxide (ITO) coatings (a mixture of indium and tin oxides) applied to a glass or a flexible polymer substrate is used. In addition, the ITO layer is coated with a film of a conductive polymer used to transport holes—poly(3,4-ethylenedioxythiophene): poly(styrene sulfonate) (PEDOT: PSS). This film also serves to smoothen the surface of the ITO and prevent shunts from surface irregularities and to improve the efficiency of hole collection because of better matching of energy levels between the electrode yield and the highest occupied molecular orbital (HOMO) level of the donor polymer level. On the opposite side of the active layer, a metal electrode with a low work function is applied. In general, this is an aluminum electrode, which can be further modified by applying a thin layer (~1 nm) of LiF under it, which increases the efficiency of solar cells [3]. Lighting of such an element by sunlight is carried out from the side of a transparent glass or polymer substrate. Radiation is absorbed in the working polymer or composite layer, and electron-hole pairs (excitons) are generated, which then decay into electrons and holes collected on opposite electrodes. These processes are usually represented using energy diagrams (**Figure 1**).

The photovoltaic effect underlying the operation of the OSC consists of the generation of current carrier-electron and holes-in semiconductor materials when they are irradiated with light. The nature of the relatively low-efficient polymer OSCs in comparison with their inorganic analogs lies in the different mechanisms of photogeneration of free-charge carriers in such structures. When the inorganic semiconductors are illuminated by photons with an energy greater than the band gap, that is, the energy difference between the valence band and the conduction band, free charge carriers (electrons and holes) are generated, which are then separated by the pn junction of the solar cell.

In organic semiconductors, as a result of the absorption of photons, electrons from higher occupied molecular orbitals are excited to lower free molecular orbitals. An important difference

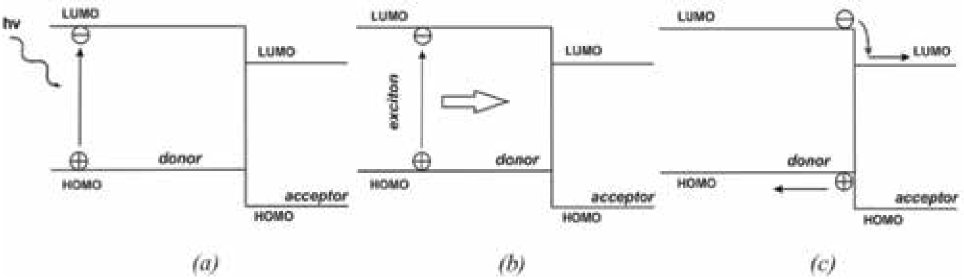

Figure 1. Energy diagrams of polymer binary system: (a) photon absorption, (b) exciton generation and (c) charge separation processes.

in the mechanisms of photogeneration in inorganic and organic materials is the fact that in free inorganic solar cells, free charge carriers are formed in the bulk of the material, whereas in OSC, as a result of their relatively low dielectric permittivity, such materials are bound by Coulomb interaction electron–hole pairs—excitons. To separate excitons and obtain free charges, an additional dissociation energy of excitons (binding energy) is required, which for different organic semiconductors is 0.2–1.0 eV. Generation of charges due to dissociation of excitons can be realized at the boundary of two organic semiconductors (donor and acceptor), that is, on a heterojunction.

By shifting the energy levels between the corresponding orbitals, organic materials can work as donors or electron acceptors. At the donor-acceptor interface, the process of charge transfer occurs, which leads to the appearance of holes in a material with a low ionization potential (donor) and electrons in a material with a high electron affinity (acceptor). These carriers are still connected by the Coulomb interaction but can be separated by an internal electric field (or built-in potential) of the solar cells, which is created in connection with the difference in the work function of the two different electrodes in the sandwich configuration of organic heterojunctions. Holes move through the donor material to the electrode with a high work function and electrons through the acceptor layer to the electrode with a low work function. The characteristic distance traveled by the exciton during its lifetime, that is, the diffusion length l_D, in organic semiconductors, is limited by a distance of about 10 nm due to their short lifetime and low mobility [4]. Obviously, only photons near the heterojunction plane, absorbed by the characteristic length l_D, contribute to the photocurrent. Only excitons that appear at distances comparable to l_D can effectively move toward the interface, thereby ensuring the generation of charge carriers. In practice, in the OSC with a binary structure, only a small part, about 0.01 absorbed photons, can contribute to the photocurrent.

A flat binary heterostructure consisting of two organic materials with shifted energy levels for the realization of the process of dissociation of an exciton into free charges was first demonstrated by Tang in 1986 [5]. It was shown that a photovoltaic effect occurs in a two-layer donor-acceptor system: metal phthalocyanine/perylene compound with a rather high efficiency. The coefficient of converting the energy of light into electrical energy was about 1%. An increase in light conversion efficiency of up to 2.5% was achieved in solar cells based on fullerene C_{60} as an acceptor material in combination with Cu or Zn phthalocyanines.

An important step in improving the efficiency of the OSC was the transition to a bulk heterojunction, which is realized by mixing donor and acceptor materials. The principle of operation of an OSC based on a bulk heterojunction is determined by the fundamental property of polymer materials, which consists of the striving for phase separation at the nanometer level. In the OSC of this type, the donor-acceptor interface, which penetrates the entire volume of the material, ensures the dissociation of excitons, as well as the transport of electrons and holes to the electrodes.

For the first time, solar batteries based on volumetric heterojunction obtained from solutions were reported in 1995. Since then, the number of publications in this field has started to grow exponentially, and the PCE has increased from 1 to 5% [6–10].

In the early years, poly [2-methoxy, 5-(20-ethyl-hexyloxy)-*p*-phenylene vinylene) (MEH-PPV)/C_{60} composites were later replaced by a better processed combination of poly [2-methoxy-5-(30,70-dimethyloctyloxy)-1,4-phenylene vinylene] (MDMO-PPV)/[6,6]-phenyl-$C_{61/71}$-butyric acid methyl ester ([60]PCBM or [70]PCBM). Because of the rather large band gap and low mobility of PPV-type polymers, the efficiency at best remained at 3%, and the general interest in this class of materials disappeared [11].

Recently, research efforts have focused on poly (alkyl-thiophenes) and in particular on poly (3-hexyl-thiophene) (P3HT). In 2002, the first encouraging results for P3HT: [60]PCBM solar cells at a 1: 3 weight ratio were published. At this time, the short-circuit current density was the largest ever observed in an organic solar cell (8.7 mA/cm^2) [12].

A mixture of P3HT: [60]PCBM was and remains dominant in studies of organic solar cells. Consider the material P3HT, which absorbs photons with a wavelength of less than 675 nm (energy of the band gap $Eg \approx 1.85$ eV). Assuming that in the P3HT: [60]PCBM mixture the polymer determines the optical gap of the composite, it is possible to calculate both the density of the absorbed photons and the absorbed power density. A typical spectrum of light incident on the Earth's surface is given by the standard AM1.5G. This standard defines parameters such as an integrated power density of 1000 W/m^2 (100 mW/cm^2), and an integrated photon flux of 4.31×10^{21} 1/s × m, distributed over a wide range of wavelengths (280—4000 nm) required for the characteristics of solar cells. The P3HT layer: [60]PCBM can absorb, at best, 27% of the available photons and 44.3% of the available power. Despite this, the real efficiency value for an organic solar cell based on P3HT: [60]PCBM does not exseed 5% [13].

To further increase the efficiency of solar cells, it is necessary to develop donor polymers that absorb light in an even longer wavelength region than P3HT, that is, the absorption boundary should lie at wavelengths greater than 700 nm. Such polymers should have a band gap (the difference in the energies of the lowest unoccupied molecular orbital [LUMO] and HOMO) of less than 2 eV.

The number of known donor polymers providing acceptable light conversion efficiency in photovoltaic cells is still small. In addition to the synthesis of new polymers, work is also under way to obtain new fullerene compounds for the purpose of using them instead of the [60]PCBM in photovoltaic cells.

In this regard, the aim of our chapter was the development of new acceptor components based on modified fullerene C_{60} and donors, based on soluble derivatives of polyaniline for use in organic solar cells.

2. Fullerene-containing polymers for organic solar cells

The inclusion of fullerene molecules into polymer chains as photo- and electroactive moieties (the subject of intense and competitive research in recent years) should lead to creating new materials with unique structural, electrochemical and photophysical properties. In recent years, many works that extensively use the metathesis strategy to obtain materials for photovoltaic cells have been published [14]. For example, the synthesis of vinyl-type polynorbornenes whose structure contains fragments of [60]PCBM, a conventional electron with drawing component of the active layer in organic photovoltaic cells, was proposed by Eo et al. [15]. Photovoltaic cells where the fullerene-containing copolymer acted as the n-type semiconductor in the active layer were developed based on these polymers. Also of interest are several works [16, 17] in which fullerene-containing monomers (FCMs) were subjected

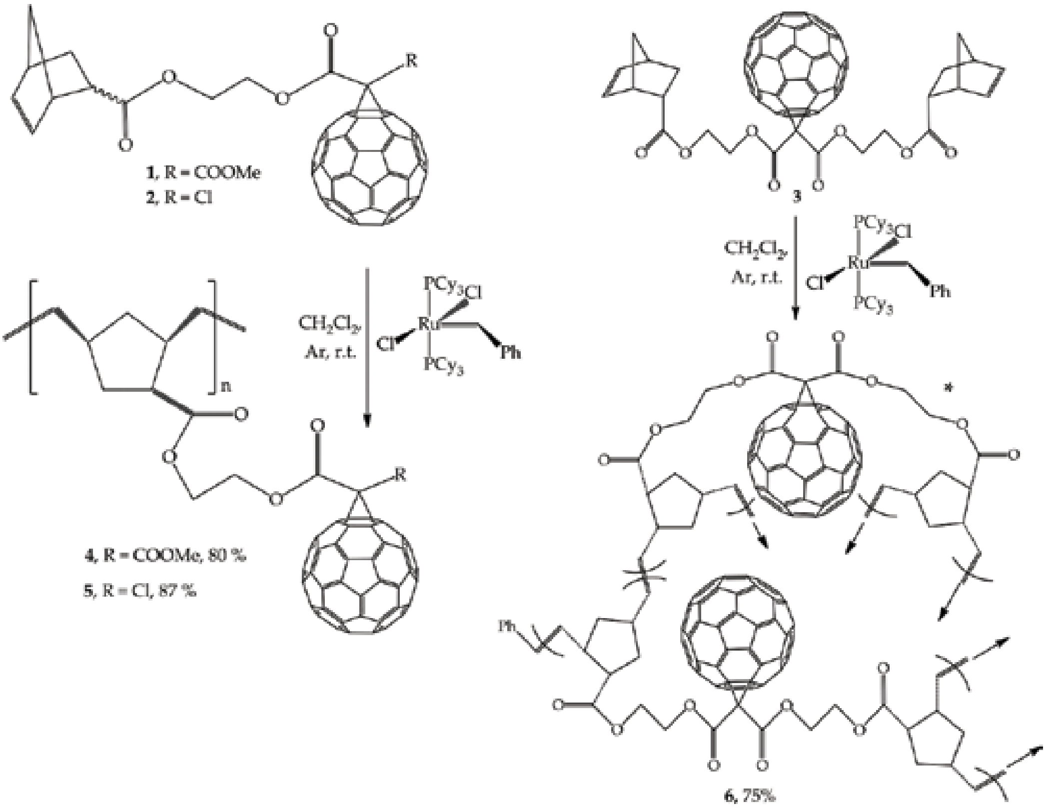

Figure 2. Ring-opening metathesis polymerization of fullerene-containing norbornene monomers.

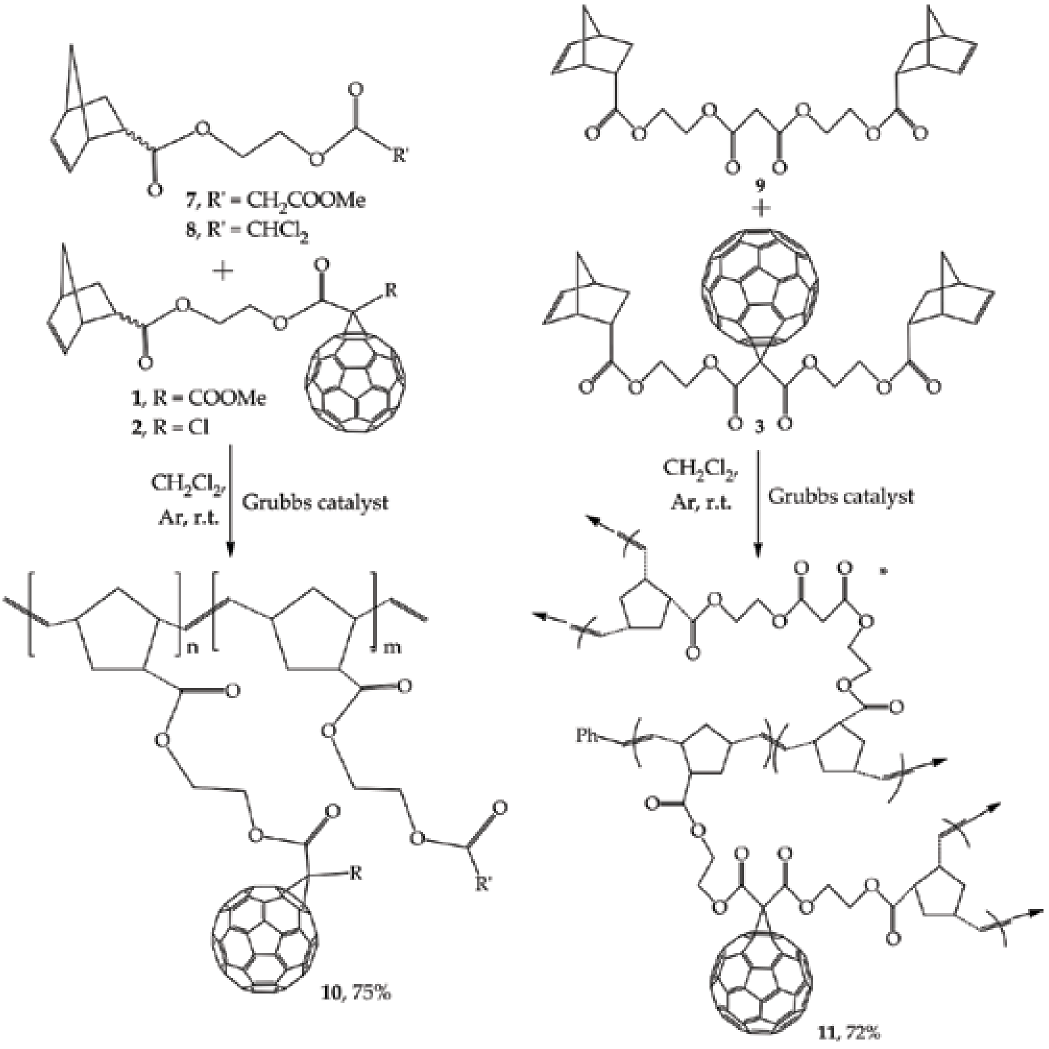

Figure 3. Ring-opening metathesis copolymerization of fullerene-containing norbornene monomers with related fullerene-free compounds.

to metathesis polymerization using a Grubbs catalyst and the products were tested in solar cells. This part of our work was devoted to synthesize new fullerene-containing polymers and copolymers from norbornene-type monomers in the presence of the first-generation Grubbs catalyst $[(PCy_3)_2Cl_2RuCHPh]$.

Investigated in the work the fullerene-containing norbornene monomers include (**Figure 2**): {(1-methoxycarbonyl)-1-[(2-bicyclo[2.2.1]hept-5-en-2-yl)ethoxycarbonyl]-1,2-methano}-1, 2-dihydro-C_{60}-fullerene (endo:exo = 6:1) **1** [18], {(1-chloro-1-[(2-bicyclo[2.2.1]hept-5-en-2-yl) ethoxycarbonyl]-1,2-methano}-1,2-dihydro-C_{60}-fullerene (endo) **2** [18] and bis[2-{[(2S*)-bicyclo[2.2.1]hept-5-en-2-yl]etoxycarbonyl}-1,2-dihydro-C_{60}-fullerene **3** [19].

The ring-opening metathesis polymerization of monomers **1–3** was carried out in the presence of the first-generation Grubbs catalyst at room temperature in CH_2Cl_2 in an argon atmosphere. In both cases, the consumption of the starting norbornenes **1–3** (TLC monitoring) and the precipitation of the polymers were observed for the first 3 h (**Figure 2**).

Synthesized homopolymers **4–6** were found to be insoluble in common organic solvents ($CHCl_3$, C_6H_6, PhMe, C_5H_4F and EtOAc), and to swell only partially in dimethyl sulfoxide, therefore, it seemed impossible to characterize their structures by spectral methods and to estimate their molecular weights.

Note that the results obtained do not contradict the other data available in this field. Some works showed that the incorporation of C_{60} fullerene into the polymer, in many cases, significantly deteriorates its solubility, which is due to the formation of intermolecular bonds involving polynorbornene fragments and C_{60} fullerene, as well as due to the restricted solubility of fullerene itself [14].

One of the possible ways to prepare soluble fullerene-containing polymers is involvement of fullerene monomers into copolymerization with highly soluble comonomers. This process is accompanied by the "effect of dilution" of rigid C_{60}-containing units due to the decrease in the concentration of fullerene molecules in the polymer chain, which has a favorable effect on the solubility of the final polymer. To reproduce this effect, norbornenes **1**, **2** and **3** were copolymerized with related fullerene-free compounds 2-[(bicyclo[2.2.1]hept-5-en-2-yl-carbonyl)oxy]ethylmethyl malonate (exo:endo = 6:1) **7** [18, 20], 2-[(2,2-dichloroacetyl)-oxy]ethyl bicyclo[2.2.1]hept5-ene-2-carboxylate (exo:endo = 6:1) **8** [18, 20] and bis[2-{[(2S*)-bicyclo[2.2.1]hept-5-en-2-yl carbonyl]oxy}ethyl)malonate **9** [19], respectively (**Figure 3**).

In all cases, the metathesis polymerization resulted in the formation of copolymers **10, 11** ($CHCl_3$, dimethylsulfoxide) soluble in some organic solvents with good degrees of conversion.

3. Soluble functionalized polyanilines

The development of a new generation of sensor devices is associated primarily with two conductive high-molecular compounds, namely, PANI and polypyrrole, which have been used in highly selective devices for the diagnosis of mixtures of gases and liquids, the so-called "electronic noses" and "electronic tongues" [21]. Biomedical studies of PANI are extremely promising. It has been shown that PANI can be used as a biocompatible electrode: electrical signals supplied to an in-vivo deposited polymer layer encourage the acceleration of tissue regeneration [22]. There is a wide range of already available and potentially possible applications of PANI. Nevertheless, the practical use of this material is limited by a number of serious problems. The first problem is related to the synthesis of PANI with reproducible properties. Samples of the polymer can contain a wide variety of aniline oxidation products with electrical conductivities that differ dozens of times. These products also differ in their spectral and magnetic characteristics and can have a fundamentally different morphology. Such an uncertainty leads to ambiguous results and requires a thorough investigation of the oxidative polymerization of aniline.

The second problem is related to the creation of materials for practical applications. A significant disadvantage of PANI is that it does not melt and is practically insoluble in conventional organic solvents. Therefore, PANI belongs to the category of non-recyclable materials. Furthermore, this polymer is a powder that has no adhesion to other materials.

Concerning this, it is obvious that the synthesis is a key process in the preparation of not only PANI but also PANI-based composites. Despite the apparent simplicity, the oxidative polymerization of aniline is a complex multistage reaction. The conventional procedure for chemical synthesis of PANI includes the oxidative polymerization of the monomer in an aqueous solution of an inorganic acid [23]. These conditions provide the formation of an unmeltable powder that is insoluble in the majority of available organic solvents. In order to eliminate the above disadvantages, PANI can be modified in different ways. An alternative version of the optimization of the performance characteristics of the polymer is the functionalization of the initial monomer rather than of the target product. In particular, the introduction of *o*-toluidine and *o*-anisidine (instead of aniline) into the polymerization process leads to the precipitation of high-molecular compounds soluble in organic solvents. Further, the homopolymer based on *o*-toluidine can be used in the design of electrochromic and photovoltaic devices. There are examples where the electrochemical polymerization of *o*-toluidine was performed with different solutions of acids used as electrolytes. In particular, Borole et al. [24] used sulfuric acid, *n*-toluenesulfonic acid, sulfamic acid and sulfosalicylic acid. A comparative analysis of the synthesized substances demonstrated that the maximum electrical conductivity was exhibited by a polymer soluble in the majority of conventional solvents, which was isolated with the participation of sulfonic acids. In a number of works, the method was proposed for the synthesis of high-molecular compounds with high electrical conductivity and good solubility by varying the ratio of comonomers (electrochemical polymerization). This made it possible to synthesize copolymers based on *o*-anisidine and *o*-toluidine [25]. It was noted that the most stable films are formed from a copolymer in which the content of pyrrole is more than 50% with respect to *o*-toluidine.

We carried out research identifying the most effective representatives and expanding the range of electrically conductive high-molecular compounds, primarily using functionalized aniline and researching the electrophysical and physicochemical properties of the target products.

Taking into account that the electrical conductivity of a high-molecular compound increases with the elongation of the conjugation chain, we turned to the development of the polymerization process of the functionalized derivative of aniline, rather than the aniline itself, and to the investigation of the physical and physicochemical properties of the obtained products.

The monomer used for the oxidative polymerization was the previously synthesized 2-(1-methyl-2-buten-1-yl)aniline **12** [26] with an alkenyl substituent that occupies the *o*-position of the aromatic ring and increases the conjugation chain. The diversity of the molecular structure, morphology and properties of the oxidation products of aniline is associated with the presence of the main reagents, namely, the monomer and the growing chain in unprotonated and protonated forms, as well as with the existence of two mechanisms of oxidation: the chain reaction of electrophilic substitution and the recombination of cation-radical centers. The contribution from the two reactions depends on the protonation state of the reagents and, consequently, on the pH of the reaction medium.

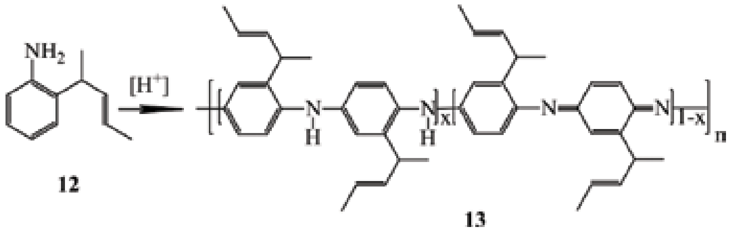

Figure 4. Homopolymerization of 2-(1-methyl-2-buten-1-yl)aniline **12.**

The homopolymerization of **12** was carried out by means of its oxidation, which resulted in the formation of a dark-green precipitate of polymer **13** in aqueous solutions of acids. The most frequently used oxidizing agent was ammonium persulfate. It is believed that the use of ammonium persulfate leads to the formation of a high molecular weight polymer with a high electrical conductivity.

The oxidation of aniline was performed in an acidic medium with hydrochloric acid at the pH = 0–2 according to the scheme shown in (**Figure 4**). Aniline-derivative copolymers **14–16** were synthesized in different molar ratios of *o*-toluidine and **12** (1:3. 1:1. 3:1, respectively) according to procedures similar to those used for the synthesis of homopolymer **13**. The yield of the copolymer was ~80%.

4. Charge transport in thin polymer films

Electronic conductivity of organic molecular compounds differs from that of metal and inorganic semiconductors such as silicon and germanium. The well-known band theory of crystal lattice is a good base to understand the conduction mechanism of crystalline molecular solids and conjugated and unconjugated polymers. At the same time, the applicability of the ideal elongated chain model to materials with a complicated morphology is naturally limited. Even within the frames of the idealized model, the inorganic conductors and semiconductors differ considerably from polymers. Besides, in polymers, the screening of interactions between charge carriers is less; electron–electron and electron–hole interactions play an important role causing considerable localization of electron states as compared with inorganic materials [27]. Absence of macroscopic ordering means inadequacy of band conduction model to describe electron conductivity of bulk polymer materials, though it can be used to a limited extent when studying the conduction process.

In amorphous layers of thin organic films the terms "conduction band" and "valence band" are usually replaced by the terms of the LUMO and the HOMO, respectively. The states' density is mainly described quite satisfactorily by Gaussian distribution of localized molecular orbitals of individual molecules [28].

Depending on the size of barrier on the interface of electrode with polymer film, electric current flowing through the sample can be of injection type, that is, limited by space charge. In this case, one of the electrodes should be an ohmic one, that is, it should provide more charge carriers in time unit than the sample is able to transport, not breaking Poisson's law. Otherwise, charge carrier transport across the interface will be limited by the barrier. The tunneling model of Fowler-Nordheim (FN) and Richardson-Schottky's (RSch) thermionic emission model are usually used to study injection in polymers in a rather strong electric field [29–31].

A thermal electron emission from hot metal is called thermionic emission. Electronic emission from metal contact into vacuum or dielectric conduction band by their thermal transportation through the potential barrier in electric field is called Schottky emission. Taking into account image forces in parabolic approximation, it is possible to get the Richardson-Schottky equation for current density [32]:

$$J = A \cdot T^2 exp\left[\frac{-e(\varphi_B - eF/4\pi\varepsilon\,\varepsilon_0)}{kT}\right], \tag{1}$$

where J is a current density, A is the Richardson constant, e is an electron charge, ϕ_B is a barrier height, F is a field density, ε is a dielectric permeability of a sample, ε_0 is the electric constant, k is the Boltzmann constant and T is temperature. An important assumption in RSch model is that electron can be taken out from the metal once it gets enough heat energy to cross the potential barrier which is formed by a superimposition of the external field and images forces.

According to the quantum theory, electron wave function within dielectric area located between two electrodes is different from zero. Wave function exponentially decreases with a distance into the barrier. If the barrier is very narrow, the probability to pass through the barrier for an electron has a finite value depending on the height and form of the potential barrier. Tunneling (auto-emission) can be observed in the case of a wide barrier if its effective thickness decreases under the influence of a strong electric field.

In the FN model image forces are disregarded and the tunneling of electrons from metal through a triangle barrier to free states of conduction area is considered. When the field intensity increases, the height and width of the potential barrier decreases to such an extent that a new physical effect appears and prevails: quantum mechanic tunneling of electron across the potential barrier. Current caused by the tunnel emission facilitated by a field is described by Fowler-Nordheim equation. In this case the current density can be described by the expression [33]:

$$J(F) = B\,F^2 exp\left(-\frac{4\sqrt{2\,m_{eff}(e\,\varphi_B)^3}}{3\hbar eF}\right) \tag{2}$$

which is independent of temperature. Here, m_{eff} is the effective mass of a charge carrier in polymer and $\hbar$ is Planck's constant.

In spite of disadvantages of both FN and RSch concepts, they have been applied successfully to describe injections of a charge carrier in organic light-emitting diodes. For example, the FN model was applied to give reasonable values for the barrier height and to take into account independence of the temperature characteristic $J(F)$ in strong fields [34]. Thermionic emission prevails at the high temperatures and relatively low electric fields. Current caused by tunnel emission takes place at low temperatures and high values of electric fields.

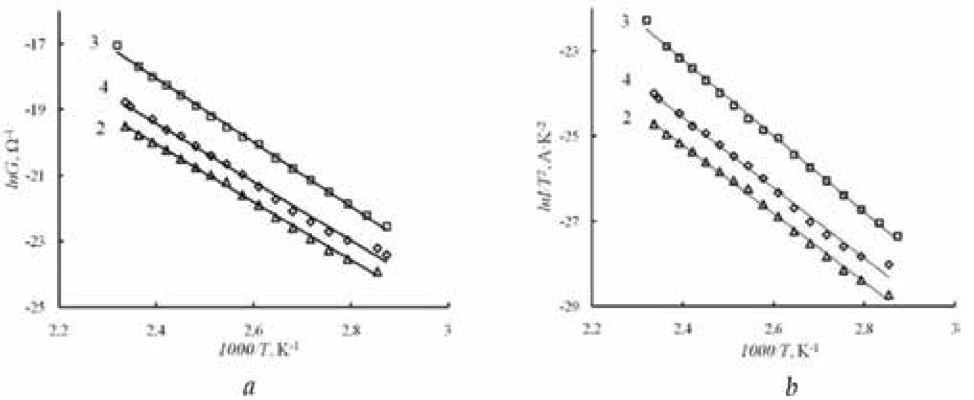

Figure 5. Dependences of (a) the electrical conductance and (b) I/T^2 on the inverse temperature for films of copolymers (o-toluidine with 2-(1-methyl-2-buten-1-yl)aniline) in different molar ratios: (2) 1:3, (3) 1:1, and (4) 3:1.

In Biglova et al.'s works [35], the temperature dependences of the electrical conductance were measured for films of different polyaniline forms. The measurements were carried out for soluble forms of the modified polyaniline homopolymer, that is, **12**, and its copolymers with o-toluidine in different molar ratios. The temperature measurements of the electrical conductance *G* of the polymer films in the range from 300 to 450 K demonstrated that the dependence of *G* on the temperature *T* has an exponential character:

$$G = G_0 \exp\left(-\frac{\Delta E}{2kT}\right). \tag{3}$$

In the *lnG – 1000/T* coordinates, the experimental points, within the limits of error, fall on a straight line (**Figure 5**). The quantity *ΔE* (**Table 1**) can be interpreted as the interval between HOMO and LUMO (an analog of the band gap) in semiconductor polymer films.

From the data presented in **Table 1**, it follows that the band gap varies from sample to sample and lies in the energy range from 1.39 to 1.66 eV. The dependence of the band gap on the molar ratio of the copolymers used for the preparation of thin films is an extremely important characteristic for their practical application in various electronic devices. The polymer compounds studied in this chapter can be used for the subsequent development of electronic devices similar to those based on inorganic $Ga_{1-x}Al_xAs$ heterostructures.

In order to understand how charge transfer occurs through the metal-polymer interface, we measured the temperature dependences of the current I flowing through the film structure. In the *lnI/T^2–1000/T* coordinates, the graphical dependences, within the error of measurement, are well approximated by straight lines (**Figure 5**) in accordance with Eq. (1). The current density is defined as $J = I/S$, where *S* is the cross-sectional area of the film, which remains unchanged during the measurement. Therefore, the graphical dependences can be constructed using the values of the current flowing through the sample, rather than the values of current density. According to Eq. (1), the slopes of the straight-line sections are proportional to the Schottky barrier height φ_B. The results of the calculations are presented in **Table 1**.

№	E_{ox}^{1}, V	E_{red}^{1}, V	E_{HOMO}, eV*	E_{LUMO}, eV**	E_g, eV		φ_{B}, eV
					CVA	**EP**	
13	0.54	−1.07	−5.31	−3.73	1.61	1.55	0.71
14	0.49	−1.11	−5.29	−3.69	1.60	1.52	0.69
15	0.44	−1.13	−5.24	−3.67	1.57	1.68	0.77
16	0.29	−1.25	−5.09	−3.55	1.54	1.53	0.70

*$E_{HOMO} = -(E_{ox}^{1} + 4.8)$ (eV)

**$E_{LUMO} = -(E_{red}^{1} + 4.8)$ (eV)

CVA—cyclic voltammetry; EP—electrophysical measurements.

Table 1. Electrochemical characteristics of the synthesized polyaniline derivatives.

The analysis of the dependences obtained in this study allows the assumption that the main mechanism of charge carrier transfer through the interface between the metal substrate and the polymer film is the Schottky thermionic emission, which determines carrier transport in the temperature range from 300 to 450 K. This confirms the conclusion that the transfer of charge carriers through the metal-polymer interface occurs as a result of the above-barrier transport. In this case, the barrier height is determined by the difference between the work function of the metal and the electron affinity of the polymer. For example, the calculation according to the results of the electrophysical measurements for film samples of copolymers **15** gives the barrier height of 0.77 eV (**Table 1**). Taking into account that the work function of aluminum is 4.26 eV and the electron affinity of the polymer lies in the range from 3.5 to 3.6 eV, we obtain the barrier height ranging from 0.76 to 0.66 eV, that is, we have the value comparable to that calculated within the framework of the Schottky model. Since the field addition in Eq. (1) does not exceed 0.1 eV, it is ignored. Thus, the above calculations are further evidence in favor of the model of above-barrier transport at the metal-polymer interface.

The obtained values of HOMO and LUMO indicate that the polyanilines studied in our work can be used for the development of new organic solar cells [36, 37]. The short-circuit current of the photo-converter is closely related to the difference in the energy between the HOMO of the PANI (donor) and the LUMO of the acceptor. The most appropriate acceptor can be represented by a methanofullerene [38]. This difference also determines the open-circuit voltage. Moreover, the band gap of the donor determines the minimum energy or the maximum wavelength of the absorbed photons. For the effective absorption in the visible part of the solar spectrum, the band gap should be in the range from 1.4 to 1.5 eV.

Thus, the poly-2-(1-methyl-2-buten-1-yl)aniline/methanofullerene heterojunction, which is composed of newly synthesized compounds, is optimal for manufacturing a laboratory sample of a solar energy photoconverter.

5. Organic solar cells based on thin polymer films

The technique of formation of thin films of polyanilines and fullerene-containing polymers by vacuum deposition from a Knudsen effusion cell was used [36]. The length of the cylindrical

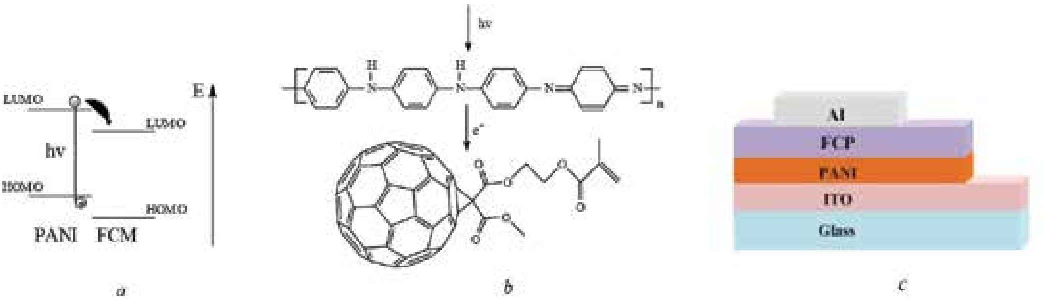

Figure 6. (a) An energy level diagram of the PANI/FCM system; (b) process of photon absorption and charge separation in this structure; (c) multilayer film structure of OSC.

cell was 25 mm, the internal diameter was 4 mm and the working temperature varied within the range 500–650 K. Thermal heating of fullerene-containing monomers (FCMs) during deposition led to their polymerization. Some thin films were formed by the spin coating technique from a solution of fullerene-containing monomers. All the obtained films were uniform in thickness, and their conductivity was about 0.1–1.0 mS/cm.

To increase the conductivity of polyaniline layers, the temperature conditions of deposition from the Knudsen cell were selected. The temperature range of 500–550 K proved to be the most optimal. In addition, protonation of the freshly prepared films in vapors of hydrochloric acid solution was carried out. For PANI films a conductivity value of 1.0 mS/cm was achieved as a result.

The surface condition and thickness of the deposited films were monitored on the basis of analysis of AFM images obtained by a NanoScan 3D. The thickness of photoactive layers varied and took on values within the range 100–200 nm. It should be noted that a too large thickness of the films leads to exciton recombination and reduces the efficiency of charge separation. On the contrary, the incident photon absorption and quantity of formed excitons decrease in overly thin films.

The organic solar cell test samples based on the donor-acceptor polymer systems described earlier were formed on a glass substrate with conductive and transparent ITO layers. Resistance of ITO layers was about of 10 Ω/□. For experimental structures of the OSC in this research the following organic substances were used: PANI, conventional fullerene and a novel synthesized monomer—monosubstituted methanofullerene derivative [38] (**Figure 6a** and **b**). The aluminum films fabricated by thermo-diffusion deposition in vacuum were applied as the upper electrode. **Figure 6c** presents the structure of the OSC in which thin films of PANI and fullerene-containing polymers were used as photoactive layers.

The current–voltage characteristics (CV characteristics) of all the prepared OSC samples were measured and the numerical values of such parameters such as open-circuit voltage, short-circuit current, filling factor and PCE were calculated on their basis. Measuring the CV characteristics of a photovoltaic cell is usually done by exposing it to steady-state illumination and a known temperature. The sun or a sunlight simulator can act as a light source. Estimations of the coefficient of efficiency were based on standard sun intensity $P_0 = 1000$ W/m^2 (AM 1.5 G conditions).

The values of these parameters for the various OSC experimental structures studied in this work appeared to be $J_{sc} = 0.6–1.8$ mA/cm^2 (short-circuit current), $V_{oc} = 0.6–0.8$ V (open-circuit voltage) and FF = 0.6–0.8 (filling factor). The highest values of PCE for the investigated organic solar cells were about 2%. These values were obtained for the structures based on methanofullerene derivatives.

Thus, it was demonstrated that a combination of PANI with fullerene-containing polymers is very important for formation of OSC on the basis of binary donor-acceptor systems. The solar cells investigated here differ from earlier ones [39] that they can be fabricated on the flexible substrates.

6. Polymerizable methanofullerene as a buffer layer material for organic solar cells

In recent years, new combinations of semiconductor materials based on fullerene derivatives (n-type materials) and electron-conjugated polymers (p-type materials) are being actively developed all over the world. It is believed that the high efficiency of conversion of light in organic solar cells can be achieved only by using charge-selective buffer layers [40]. Usual materials for producing such layers are PEDOT: PSS and a number of inorganic oxides. Since PEDOT: PSS exhibits acidic properties, its use adversely affects the duration of the operation of solar cells. At the same time, the metal oxides in high oxidation states (MoO_3, V_2O_5 and WO_3) show oxidizing properties on the materials of the photoactive layer facilitating their breakage. The problem is observed even with relatively unreactive titanium dioxide TiO_2 [41].

The greatest prospects in terms of practical implementation have inverted configuration organic solar cells that do not contain high active metals and have significantly increased operational stability. However, the creation of these devices requires development of selective electron-transport buffer layers (ETL) based on semiconductor materials of n-type. We have fabricated inverted solar cells which ITO cathode, fullerene-containing buffer layer or ETL, photoactive layer, hole-transporting layer MoO_3 and Ag anode (**Figure 7**).

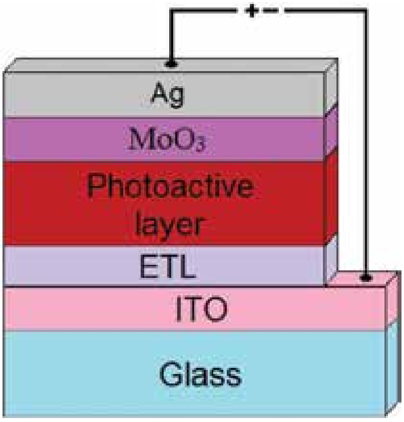

Figure 7. Schematic architecture of an inverted organic solar cell.

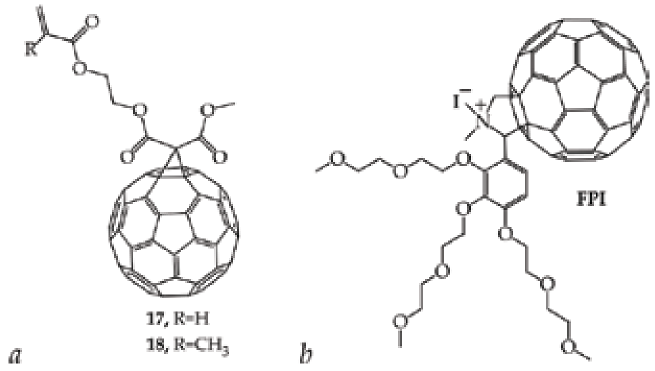

Figure 8. The molecular structures of the materials used to form ETL buffer layer of the devices.

The photoactive layer of organic solar cells was created on the basis of the traditional composites: the acceptor component [60]PCBM or [70]PCBM and conjugated polymer P3HT or poly[[9-(1-octylnonyl)-9H-carbazole-2,7-diyl]-2,5-thiophenediyl-2,1,3-benzothiadiazole-4,7-diyl-2,5-thiophenediyl] (PCDTBT).

In our study we propose usage of earlier synthesized {(1-methoxycarbonyl)-1-[2-(acryloyloxy) ethyloxycarbonyl]-1,2-methane}-1,2-dihydro-C_{60}-fullerene **17** [42] and {(1-methoxycarbonyl)-1-[2-(methacryloyloxy)ethyloxycarbonyl]-1,2-methane}-1,2-dihydro-C_{60}-fullerene **18** [38], containing in their structure unsaturated acrylate and methacrylate fragments (**Figure 8a**), taking into account that buffer layer must comply with the number of requirements. First, the forming method of its film must be straightforward and reasonably technological. Covering the ITO surface with methanofullerene solution in chlorobenzene, as it turned out, was a pretty simple buffer layer-forming approach, which did not request such processes as vacuum thermal evaporation and high-temperature annealing. Second, the formed film should be resistant to the effect of other solvents. Therefore, after laying one on the ITO surface we have had before us challenge of FCM insolubilization. For that reason solid-state radical polymerization has been conducted, which resulted in the creation of fullerene-containing polyacrylates and polymethacrylates.

At the first stage, the influence of the temperature of the heating of the buffer layer on the efficiency of light conversion in solar batteries was studied on the example of photoactive materials [60]PCBM and P3HT [43].

The current-voltage characteristics of organic solar cells (**Figure 9**) were measured under standard conditions using simulated solar light of AM 1.5 spectrum and intensity of 100 mW/cm^2 (calibrated Si diode used as reference) and a general-purpose source meter Keithley 400. The resulting parameters of the solar cells are given in **Table 2**.

The obtained data clearly demonstrate the positive effect on the characteristics of solar cell buffer layers produced by polymerization of fullerene derivatives **17** and **18**. Particularly exciting were high open-circuit voltages of 637–652 mV achieved by using polymerized **18** as a buffer layer. We would like to emphasize that such high voltages are very rare for the P3HT-[60]PCBM solar cells.

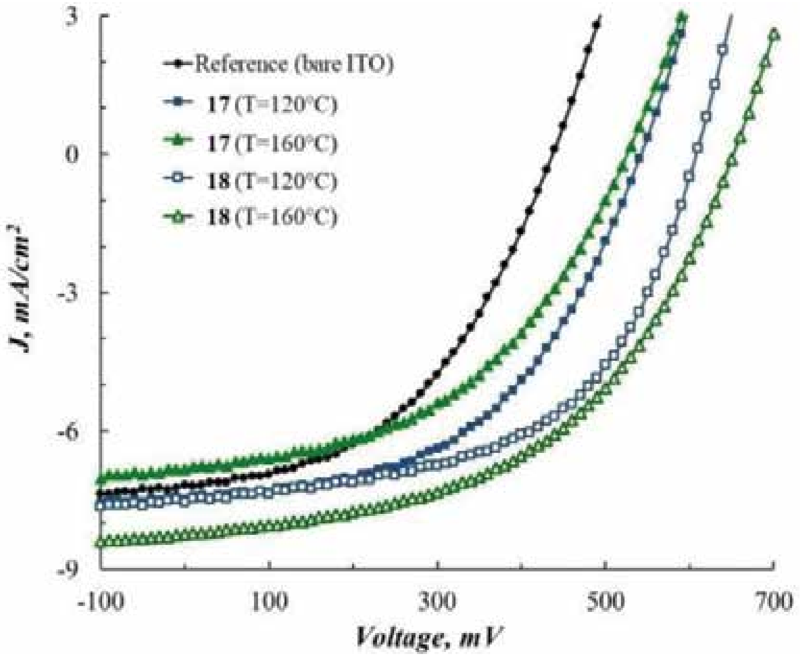

Figure 9. Selected CV characteristics of the inverted P3HT/[60]PCBM solar cells prepared on bare ITO (reference) and using buffer layers formed from polymerized **17** or **18.**

Buffer layer	$T_{(polymerization)}$, °C*	V_{oc}, mV	J_{sc}, mA/cm²	FF, %	PCE, %
—	—	437	7.2	46	1.5
17	120	542	7.5	50	2.0
	160	526	6.8	47	1.7
18	120	608	7.5	55	2.5
	160	652	8.2	50	2.7
	200	528	7.8	38	1.6

*annealing temperature of the buffer layer material **17** and **18** is provided.

Table 2. Parameters of the best inverted solar cells fabricated on bare ITO and using buffer layers formed from polymerized **17** and **18**.

At the second stage, we studied the impact of buffer layers on PCE and their forming methods on the substrate surface on the example of photoactive materials [70]PCBM and PCDTBT [44].

In recent years, a composite of PCDTBT: [70]PCBM was frequently used as an active layer in the standard organic solar cells OSC. This is based on the fact that the absorbance of [70] PCBM is much stronger than that of [60]PCBM and this property is very important for photovoltaic materials.

Four types of devices have been fabricated: without buffer layer (reference device) and with concentration of **17** in buffer layer 0.625, 1.25 and 2.5 mg/ml. Their current–voltage characteristic is given in **Table 3**.

Concentration 1, mg/ml	V_{oc}, mV	J_{sc}, mA/cm^2	FF, %	PCE, %
—	446	8.7	36	1.4
0.625	618	11.1	39	2.7
1.250	587	9.1	39	2.1
2.500	620	8.6	36	1.8

Table 3. Current-voltage characteristics of inverted solar cells using different concentrations of **17**.

Table 3 shows that PCEs of the devices with ETL are higher than PCE of the reference device. The data in **Table 3** also marks a strong increase in open-circuit voltage at the implementation of 17, which is also noticeable, while other characteristics differ. The most probable explanation is that an n-type semiconductor facilitates photoelectric work function increase, and in turn Voc depends on the work function. A low FF highlights the need to conduct an additional optimization for active-layer forming to improve photovoltaic cell morphology, since FF depends on photoactive film morphology. Authors reported that FF can achieve 60–70% for the PCDTBT:[70]PCBM system. With this value of FF, our devices could achieve PCE of 4.5–4.8%. Thus highest performance has been demonstrated by the device with minimal concentration of 1. It is obvious that more optimal PCEs are arranged in the low-value areas of concentration. Properly, the less the concentration of the compound, the less the thickness of the formed layer. Presumably, further studies on increasing solar cells' efficiency will be held using small thickness of the buffer layer

At the third stage, we investigated the effect of the concentration of the buffer layer on the efficiency of light conversion in solar batteries as the example of photoactive materials [60]PCBM and P3HT or PCDTBT [45]. For this we propose ETL in inverted organic solar cells using a polymerizable mixture of acrylate derivative of [60]fullerene **17** and pyrrolidinofullerene

Photoactive materials	Concentration of 17 in the precursor solution, mg/mL*	V_{oc}, mV	J_{sc}, mA/cm^2	FF, %	PCE, %
P3HT/[60]PCBM	—	409	6.9	46	1.3
	1.25	582	7.4	42	1.8
	2.50	591	6.5	43	1.7
	5.00	486	7.0	43	1.5
PCDTBT/[60]PCBM	—	585	6.6	42	1.6
	0.625	618	11.1	39	2.7
	1.25	677	8.3	54	3.0
	2.50	707	9.1	46	2.9
	5.00	712	7.5	41	2.2

*note that concentration of FPI in the precursor solutions was always 25 mol % with respect to the amount of **17.**

Table 4. Parameters of inverted P3HT/[60]PCBM and PCDTBT/[60]PCBM organic solar cells comprising **17** + FPI buffer layers as a function of **17** concentration in the precursor solution.

(FPI) (synthesized according to a published procedure [46]) (**Figure 8b**). The main parameters of the solar cells are given in **Table 4**.

The obtained results suggest that the electron-selective buffer layers based on the blends of the fullerene derivatives FPI and polymerizable **17** can be successfully used for fabricating inverted organic solar cells. The power conversion efficiencies for the inverted devices presented in this chapter were only 25–30% lower than the parameters of the standard-configuration organic solar cells. However, the latter contains reactive metal (calcium in our case) cathode that induces inherent instability leading to the rapid deterioration of the device parameters even under an inert atmosphere. Inverted devices showed lower open-circuit voltages (approximately by 100 mV) and fill factors as compared to the standard ones. Apparently, the electron work function of the fullerene-based buffer layer material is too high with respect to the conduction band (LUMO level) position of the n-type component of the photoactive layer ([60]PCBM).

Therefore, a Schottky-type barrier might be formed at the interface between the photoactive and the buffer layers. This might be a plausible reason for the observed reduction of the open-circuit voltages and fill factors of the inverted devices. To solve this problem, further research is needed with the aim to design some novel fullerene-based buffer-layer materials with lower-electron work functions.

7. Conclusion

In sum, the work carried out showed the advisability of application of new organic materials for solar cell development. A combination of PANI with fullerene-containing polymer was used for formation of OSC on the basis of binary donor-acceptor systems. The poly-2-(1-methyl-2-buten-1-yl)aniline/methanofullerene bulk heterojunction, which is composed of newly synthesized compounds, is optimal for the manufacturing of solar cells.

The potential use of polymerizable acrylate and methacrylate fullerene derivatives to form a buffer electron-selective charge-transport layer in inverted-configuration solar cells was demonstrated. Achieved light conversion efficiency indicates prospects of further development in this research. Optimization of technological conditions of the thin films fabrication and correct selection of the organic materials composition will provide higher values of OSC efficiency.

Author details

Renat B. Salikhov*, Yuliya N. Biglova and Akhat G. Mustafin

*Address all correspondence to: salikhovrb@ya.ru

Bashkir State University, Ufa, Russia

References

[1] Chiang CK, Fincher CR, Park YW Jr, Heeger AJ, Shirakawa H, Louis EJ, Gau SC, MacDiarmid AG. Electrical conductivity in doped polyacetylene. Physical Review Letters. 1977;**39**:1098-1101. DOI: 1010.1103/PhysRevLett.39.1098

[2] Shaheen SE, Ginley DS, Jabbour GE. Organic-based photovoltaics: Toward low-cost power generation. MRS Bulletin. 2005;**30**:10-19. https://www.calpoly.edu/~rechols/Phys422/MRS2005Intro.pdf

[3] Markov DE, Hummelen JC, Blom PWM, Sieval AB. Dynamics of exciton diffusion in poly(p-phenylene vinylene) fullerene heterostructures. Physical Review B. 2005;**72**:045216. DOI: doi.org/10.1103/PhysRevB.72.045216

[4] Dennler G, Lungenschmied C, Neugebauer H, Sariciftci NS, Labouret A. Flexible, conjugated polymer-fullerene-based bulk-heterojunction solar cells: Basics, encapsulation, and integration. Journal of Materials Research. 2005;**20**:3224-3233. DOI: Doi.org/10.1557/jmr.2005.0399

[5] Scharber MC, Muhlbacher D, Koppe M, Denk P, Waldauf C, Heeger AJ, Brabec CJ. Design rules for donors in bulk-heterojunction solar cells – Towards 10% energy-conversion efficiency. Advanced Materials. 2006;**18**:789-794. DOI: 10.1002/adma.200501717

[6] Kim JY, Kim SH, Lee HH, Lee K, Ma W, Gong X, Heeger AJ. New architecture for high-efficiency polymer photovoltaic cells using solution-based titanium oxide as an optical spacer. Advanced Materials. 2006;**18**:572-576. DOI: 10.1002/adma.200501825

[7] Peet J, Kim JY, Coates NE, Ma WL, Moses D, Heeger AJ, Bazan GC. Efficiency enhancement in low-bandgap polymer solar cells by processing with alkane dithiols. Nature Materials. 2007;**6**:497-500. DOI: 10.1038/nmat1928

[8] Kim JY, Lee K, Coates NE, Moses D, Nguyen TQ, Dante M, Heeger AJ. Efficient tandem polymer solar cells fabricated by all-solution processing. Science. 2007;**317**:222-225. DOI: 10.1126/science.1141711

[9] Gaudiana R, Brabec CJ. Organic materials: Fantastic plastic. Nature Photonics. 2008;**2**:287-289. DOI: 10.1038/nphoton.2008.69

[10] Green MA, Emery K, Hishikawa Y, Warta W. Solar cell efficiency tables. Progress in Photovoltaics: Research and Applications. 2008;**16**:61-67. DOI: 10.1002/pip.842

[11] Brabec CJ, Shaheen SE, Winder C, Sariciftci NS, Denk P. Effect of LiF/metal electrodes on the performance of plastic solar cells. Applied Physics Letters. 2002;**80**:1288. DOI: https://doi.org/10.1063/1.1446988

[12] Schilinsky P, Waldauf C, Brabec CJ. Recombination and loss analysis in polythiophene based bulk heterojunction photodetectors. Applied Physics Letters. 2002;**81**:3885. DOI: https://doi.org/10.1063/1.1521244

[13] Dennler G, Scharber MC, Brabec CJ. Polymer-fullerene bulk-heterojunction solar cells. Advanced Materials. 2009;**21**:1323-1338. DOI: 10.1002/adma.200801283

[14] Eo M, Han D, Park M, Hong M, Do Y, Yoo S, Lee M. Polynorbornenes with pendant PCBM as an acceptor for OPVs: Ring-opening metathesis versus vinyl-addition polymerization. European Polymer Journal. 2014;**5**:37-44. DOI: 10.1016/j.eurpolymj.2013.11.018

[15] Eo M, Lee S, Park M, Lee M, Yoo S, Do Y. Vinyl-type polynorbornenes with pendant PCBM: A novel acceptor for organic solar cells. Macromolecular Rapid Communications. 2012;**33**:1119-1125. DOI: 10.1002/marc.201200023

[16] Mehrotra S, Nigam A, Malhotra R. Effect of [60] fullerene on the radical polymerization of alkenes. Chemical Communications. 1997;**0**:463-464. DOI: 10.1039/A605555I. http://pubs.rsc.org/en/content/articlelanding/1997/cc/a605555i#!divAbstract

[17] Nayak P, Alva S, Yang K, Dhal P, Kumar J, Tripathy S. Comments on the analysis of copolymers of C_{60} with vinyl monomers obtained by free radical polymerization. Macromolecules. 1997;**30**:7351-7354. DOI: 10.1021/ma970318k

[18] Miftakhov M, Mikheev V, Torosyan S, Biglova Y, Gimalova F, Menshov V, Mustafin A. Fullerene containing norbornenes: Synthesis and ring-opening metathesis polymerization. Tetrahedron. 2014;**70**:8040-8046. DOI: 10.1016/j.tet.2014.08.039

[19] Biglova Y, Mikheev V, Torosyan S, Biglova R, Miftakhov M. Synthesis and ring-opening metathesis polymerization of fullerene-containing α, ω-bis-norbornenes. Mendeleev Communications. 2015;**25**:202-203. DOI: 10.1016/j.mencom.2015.05.014

[20] Biglova Y, Mustafin A, Torosyan S, Biglova R, Miftakhov M. Ring-opening metathesis polymerization (ROMP) of fullerene-containing monomers in the presence of a first-generation Grubbs catalyst. Kinetics and Catalysis. 2017;**58**:111-121. DOI: 10.1134/S0023158417020021

[21] Kondratiev V, Pogulaichenko N, Tolstopjatova E, Malev V. Hydrogen peroxide electroreduction on composite PEDOT films with included gold nanoparticles. Journal of Solid State Electrochem. 2011;**15**:2383-2393. DOI: 10.1007/s10008-011-1494-5

[22] Otero T, Martinez J, Arias-Pardilla J. Biomimetic electrochemistry from conducting polymers. A review: Artificial muscles, smart membranes, smart drug delivery and computer/neuron interfaces. Electrochimica Acta. 2012;**84**:112-128. DOI: 10.1016/j.electacta.2012.03.097

[23] Tarver J, Yoo J, Dennes T, Schwartz J, Loo Y. Polymer acid doped polyaniline is electrochemically stable beyond pH 9. Chemistry of Materials. 2009;**21**:280-286. DOI: 10.1021/cm802314h

[24] Borole D, Kapadi U, Mahulikar P, Hundiwale D. Electrochemical behaviour of polyaniline, poly (o-toluidine) and their copolymer in organic sulphonic acids. Materials Letters. 2004;**58**:3816-3822. DOI: 10.1016/j.matlet.2004.07.035

[25] Borole D, Kapadi U, Mahulikar P, Hundiwale D. Electrochemical synthesis and characterization of conducting copolymer: Poly (o-aniline-co-o-toluidine). Materials Letters. 2006;**60**:2447-2452. DOI: 10.1016/j.matlet.2006.01.014

[26] Abdrakhmanov I, Mustafin A, Sharafutdinov V. Claisen Rearrangement in Aromatic Amines. Gilem; 2014. p. 168. DOI: 10.1002/chin.198913176

[27] Hadziioannou G, Hutten PF. Semiconducting Polymers. Chemistry, Physics and Engineering. Wiley-VCH Verlag GmbH; 2000. p. 613. DOI: 10.1002/3527602186.fmatter

[28] Schmechel R, Seggern H. Electronic traps in organic transport layers. Physica Status Solidi. 2004;**201**:1215-1235. DOI: 10.1002/pssa.200404343

[29] Gadiev RM, Lachinov AN, Salikhov RB, Rakhmeev RG, Kornilov VM, Yusupov AR. The conducting polymer/polymer interface. Applied Physics Letters. 2011:98-173305. DOI: https://doi.org/10.1063/1.3584135

[30] Salikhov RB, Bunakov AA, Lachinov AN. Charge transfer in thin polymer films of polyarylenephthalides. Physics of the Solid State. 2007;**49**:185-188. https://link.springer.com/article/10.1134/S1063783407010295

[31] Salikhov RB, Rakhmeev RG, Lachinov AN. Transport layer at the boundary of two polymer films. Technical Physics Letters. 2008;**34**:495-497. https://link.springer.com / article/10.1134/S1063785008060138

[32] Sze SM. Physics of Semiconductor Devices. 2nd ed. New York: J.Wiley; 2002. 564 p

[33] Fowler RH, Nordheim L. Electron emission in intense electric fields. Proceedings of the Royal Society of London A. 1928;**119**:173-181. DOI: 10.1098/rspa.1928.0091

[34] Parker ID. Carrier tunneling and device characteristics in polymer light-emitting diodes. Journal of Applied Physics. 1994;**75**:1656. DOI: 10.1063/1.356350

[35] Biglova YN, Salikhov RB, Abdrakhmanov IB, Salikhov TR, Safargalin IN, Mustafin AG. Preparation and investigation of soluble functionalized polyanilines. Physics of the Solid State. 2017;**59**:1253-1259. DOI: 10.1134/S106378341706004X

[36] Salikhov RB, Biglova YN, Yumaguzin YM, Salikhov TR, Miftakhov MS, Mustafin AG. Solar-energy photoconverters based on thin films of organic materials. Technical Physics Letters. 2013;**39**:854-857. https://link.springer.com/article/10.1134/S1063785013100106

[37] Salikhov RB, Biglova YN, Salikhov TR, Yumaguzin YM. New polymers for organic solar cells. Journal of Nanoelectronics and Optoelectronics. 2015;**9**:792-794. https://doi.org/10.1166/jno.2014.1679

[38] Torosyan S, Biglova Y, Mikheev V, Khalitova Z, Gimalova F, Miftakhov M. Synthesis of fullerene-containing methacrylates. Mendeleev Communications. 2012;**22**:199-200. DOI: 10.1016/j.mencom.2012.06.009

[39] Wang W, Schiff EA. Polyaniline on crystalline silicon heterojunction solar cells. Applied Physics Letters. 2007;**91**:133504. DOI: 10.1063/1.2789785

[40] Yang P, Chen S, Liu Y, Xiao Z, Ding L. A pyridine-functionalized pyrazolinofullerene used as a buffer layer in polymer solar cells. Physical Chemistry Chemical Physics. 2013;**15**:17076-17078. DOI: 10.1039/C3CP53426J

[41] Kim D, Jeong M, Seo H, Kim Y. Oxidation behavior of P3HT layers on bare and TiO_2-covered ZnO ripple structures evaluated by photoelectron spectroscopy. Physical Chemistry Chemical Physics. 2015;**17**:599-604. DOI: 10.1039/C4CP03665D

[42] Torosyan S, Biglova Y, Mikheev V, Gimalova F, Mustafin A, Miftakhov M. New monomers for fullerene-containing polymers. Russian Journal of Organic Chemistry. 2014;**50**:179-182. DOI: 10.1134/s1070428014020067

[43] Biglova Y, Susarova D, Akbulatov A, Mustafin A, Troshin P, Miftakhov M. Acrylate and methacrylate derivatives of fullerenes as electron-selective buffer layer materials for inverted organic solar cells. Mendeleev Communications. 2015;**25**:348-349. DOI: 10.1016/j.mencom.2015.09.010

[44] Biglova Y, Akbylatov A, Torosyan S, Susarova D, Mustafin A, Miftakhov M. New methanofullerene as a buffer layer in organic solar cells. Physica B: Condensed Matter. 2015;**458**:114-116. DOI: 10.1016/j.physb.2014.11.025

[45] Biglova Y, Susarova D, Akbulatov A, Mumyatov A, Troshin P. Polymerizable methanofullerene bearing pendant acrylic group as a buffer layer material for inverted organic solar cells. Mendeleev Communications. 2015;**25**:473-475. DOI: 10.1016/j.mencom.2015.11.026

[46] Li C, Chueh C, Yip H, O'Malley K, Chen W, Jen A. Effective interfacial layer to enhance efficiency of polymer solar cells via solution-processed fullerene-surfactants. Journal of Materials Chemistry. 2012;**22**:8574-8578. DOI: 10.1039/c2jm30755c

Section 2

New Concepts in Solar Energy Materials

A BIM-Based Study on the Sunlight Simulation in Order to Calculate Solar Energy for Sustainable Buildings with Solar Panels

Zhao Xu and Jingfeng Yuan

Additional information is available at the end of the chapter

http://dx.doi.org/10.5772/intechopen.74161

Abstract

With the construction industry moving rapidly toward building information modeling (BIM), pursuit of sustainability in buildings will require the use of renewable energy analysis tools in the early stages of building design, as well as establishment of BIM-compliant practices. Planning for sunlight is essential to obtain sustainable benefits from the sun in and around buildings, which process requires understanding and making allowances in building attributes that affect how sunlight can be used. This chapter presents a model for simulation of sunlight's effect on building design under BIM technology while calculating the potential energy capacity of roof- and façade-mounted photovoltaic solar panels. For this purpose, it is suggested in the study to use statistical construction data as well as 3D digital models obtained from BIM software (Revit and THSWARE) to measure the useful sunlight duration and derivable energy of representative sample of buildings. By measuring the solar energy absorbed by the building facades, the electricity converted from solar energy and collateral savings can be calculated. Taking the cost of solar panels and feasibility of the project into consideration, this study shows using solar panels of a certain quality contributes greatly to social, economic, and environmental benefits.

Keywords: BIM, sunlight, solar energy, solar panels, sustainable design

1. Introduction

As many nations face pressure from shrinking energy resources, awareness and concerns about sustainable building design are growing. As a result, green building that applies sustainable design is holistic concept increasing significance in the construction sector. Policies that advocate energy conservation for green buildings have been promoted, wherein the building energy efficiency upgrade program for reducing power consumption in buildings is one of the crucial contents outlined in the policy. Green building's three main pillars are environmental, economic, and social in aspect. Considered a paramount method to maintain quality of life, designed to replace use of environmentally harmful products, we could say that sustainable design is an important process involving science and arts from all fields [1]. In China, estimates indicate that more than 80% of annual new buildings and over 95% of existing buildings have high-energy consumption designs [2]. Low energy-efficiency buildings account for 98% of more than 4 × 1010 m^2 of urban buildings in China [3]. As well, the advent of "green legislation" together with increased green building construction is forcing architects, planners, and builders to consider the environmental impact of buildings they design and construct [4]. Aside from the moderate amount of sunlight required for the health and comfort of occupants, solar radiation is particularly useful as an energy resource [5]. Apart from this, sunlight provides light more efficiently than electric light sources, while producing less heat for the same amount of light. With the development of sustainable design, researchers are attaching much more importance to energy savings related to sun exposure on buildings, an important component of sustainable development. One of the performance analyses done by architects is to predict how buildings are performing in terms of their luminous environment as a result of daylighting [6]. If energy savings from harvesting sunshine on buildings are considered in the building design stage, an optimal energy design can be selected.

Demand for solar power has expanded in recent years for domestic and industrial needs. Solar power is produced by collecting sunlight and converting it into electricity, which is normally done by use of large, flat solar panels composed of many individual solar cells. Solar arrays are most often located remotely, although urban sitting is becoming more popular as well. As the cost of solar energy falls, more and more buildings are being outfitted with photovoltaic systems and some even generate more electricity than they use, which structures are called "energy positive," an impressive feat. In some areas, solar-enabled buildings actually turn a profit from surplus energy, which is sold to local utility companies and fed it onto the grid. In practice, photovoltaic materials (like solar panels) are normally used to replace conventional building materials in parts of the building envelope such as roofs, skylights, and facades. As a principle or ancillary source of electrical power, solar panels are increasingly incorporated into the construction of new buildings, although existing buildings may be retrofitted with similar technology.

However, current analysis of solar energy extraction in comparison with the complexity of sunlight models needed for energy calculations clearly reflects the limited use of building information modeling, as well as the lack of effective visualization techniques. Sunlight analysis is performed by hand calculations or by computer simulation tools. In the process of hand calculation, the preparation of initial data can be a very lengthy and laborious, consisting as it does mostly of manual or semimanual translation from architectural model data to simulation data, which often results in numerous coding errors [7]. To solve the problem, graphic user interfaces have been created in simulation tools for defining model geometry. In addition, 3D digital technology, such as building information modeling (BIM), has been applied to sunlight simulation. BIM integrates all kinds of relevant information from construction projects, while related software enables energy consumption to be predicted and adjusted during the design stage, thus providing great convenience for sustainable design.

The objective of this research is to simulate sunlight's effect on building design using BIM technology and to calculate the potential energy capacity of surface-mounted photovoltaic solar panels. To measure the useful sunlight duration of a representative sample of buildings, statistical construction data were applied, as well as 3D digital models obtained from BIM software (Revit and THSWARE). Among the factors considered were building type, orientation, roof and surfaces, location, shading, and climatic information. Subsequently, the solar energy potential of a structure can be estimated by calculating the effective sunshine duration on surfaces available for solar panel installation, from which the economic benefit of surface-mounted solar panels can be evaluated. Furthermore, the cost of solar panels is considered here in determination of cost-benefit value and increased sustainability of solar panel installation on the sample building.

2. Background

2.1. BIM and sustainable design

With the importance of BIM becoming increasingly appreciated, BIM and sustainable design strategies in the building industry have drawn more and more attention. A number of published papers on BIM-related sustainable design have focused mostly on energy usage analysis alone [8]. Wang and Xuan [9] suggest a BIM-based parametric design method to establish the BKE (Bio-inspired Kinetic Envelop) system combined with utilization of solar radiation to make buildings acclimate to temperature swings, thus minimizing the energy needs. Wong and Fan [8] find two most significant benefits of BIM for sustainable building design: integrated project delivery (IPD) and design optimization. Hardin [10] established three main areas of sustainable design with a direct relationship to BIM, which are "material selection and use," "site selection and management," and "systems analysis." In addition, Azhar and Brown [11] investigate the development of a conceptual framework to illustrate the use of BIM for sustainability analyses throughout the project life-cycle.

In previous study on the integration BIM and building performance, it has been indicated that BIM can aid in the sunlight analysis [12]. BIM technologies offer new insights into the dynamic relationship and specificities of sunlight conditions and the individual building's use and properties, helping us identify the balancing points of solar gains and daylight conditions resulting from urban geometry [13]. Welle et al. [14] designed an automated product model decomposition and re-composition methodology for BIM-centric climate-based daylighting simulation called the BIM-Centric Daylight Profiler for Simulation (BDP4SIM). Joo et al. [15] developed a tool capable of analyzing various design schemes during the early stages of design by building a reasonable BIM data system for sustainability analysis and using the architectural BIM model to carry out sunshine and energy analysis in a Web environment. Generally, two main methods are used for sunlight analysis in building design. One method is the graphing method, which includes normal shadow-graph, pole shadow-graph, instantaneous shadow-graph, and hours shadow overlay. The other method is the modeling test, which performs analysis based on a scale-model of buildings and a sundial. Though the sun spacing coefficient table was widely used in China during the late 1990s, table's usefulness is restricted by some limitations that require compliance during early building layout design, where the sun spacing factor is applied in parallel with layer settings for the building. Shadow graphs created for software applications offer a new detailed representation of shadow constraints. Overall, the solar analysis model using BIM has advantage of being importable to related software, generating shadow animations for target periods and simulation results that can be saved on BIM database for property management and quality control.

2.2. Solar energy and buildings

Solar energy is the portion of the sun's energy available at the earth's surface for useful applications, such as exciting electrons in a photovoltaic cell and indoor illumination. Solar energy system is currently the most widely installed renewable energy system in the building sector in an effort to reduce the energy consumption of buildings [16]. Developing the calculation model for solar energy in buildings is helpful to describe the mathematical relations between the solar energy and building attributes such as orientation, location, height, area, etc. An important aspect in calculating solar energy is the accuracy of the developed model, which is evaluated using initial data input [17]. The large volume of residential building construction in recent years and the deficit of conventional energy sources justify any initiatives conducive to the construction of self-sustainable residential buildings that are capable of producing their own energy for illumination, HVAC, electrical appliances, etc. [18].

The design of alternative energy devices is a predictable way to develop a wide range of new technologies for a more sustainable future. To achieve energy sustainability, the installation of building-integrated solar panels is a viable option. Solar panels are a type of semiconductor device that converts the energy from sunlight into electric energy. Solar panels do not use chemical reactions to produce electric power, and they have no moving parts. Rooftop and vertical surfaces on buildings are convenient installation position to supply solar energy to meet growing energy demands. Depending on material, solar panels can be classified into different kinds: silicon solar cell, compound solar cells, polymer solar cell, nanocrystal solar cell, organic solar cell, and plastic solar cell. Many of factors play part in determining the practicality of a given solar installation and the selection of solar panels. One major factor is the available sunlight. Considering the sun is what combines with the photovoltaic panels to produce the energy, an area rich in sunlight is highly desirable [19]. Glasnovic and Margeta [19] performed an analysis of photovoltaic pumps versus diesel pumps and concluded that photovoltaic pumps were more efficient than diesel pump. Photovoltaic solar cells are thin silicon disks that convert sunlight into electricity. These disks act as energy sources for a wide variety of uses, such as rooftop panels on buildings. The past decade has seen a remarkable evolution in mainstream silicon solar cell technology, documented by greatly increased production volumes and greatly reduced costs.

By using solar panels, electricity costs from outside sources are negated by the electricity produced by the building's surface installations. Additionally, emissions that are the environmental cost of burning coal to produce electricity are significantly reduced. Although solar energy is renewable, more efficient than fossil fuel and environmentally friendly, it is costly. According to Borenstein [20], the high cost of power from solar panels has been a major deterrent to the technology's market penetration, while the current direct cost of photovoltaic solar panels is widely acknowledged to be much greater than fossil fuel generation or many other renewable energy sources. The initial cost of the solar panels may be expensive, but it is the only cost plus their installation provides potential complete relief from electric utility costs. Maintenance can be perceived as an added cost, but in reality, all the panels need is dusting and/or washing. Therefore, the cost analysis of solar panels is an important factor to be considered when making decisions about solar systems in building design.

3. Methodology

3.1. Analysis method

The importance of developing an integrated approach for potential solar energy analysis of buildings using BIM technology has been established above. Integration of quantitative results for energy consumption by building objects and 3D visualization of spatial modeling requires a well-managed framework that combines sunlight simulation and the calculation of solar energy. Such a framework should be designed to transmit data in the basic steps used for developing an effective building sunshine model. Our research aims to estimate the solar energy consumption and cost analysis of photovoltaic solar energy systems that could be installed on the rooftops and vertical walls of buildings with the use of BIM for building performance simulation and sunlight analysis. In order to estimate total harvestable solar energy and to analyze cost of photovoltaic systems, the following four-level research framework was executed (see **Figure 1**):

Level 0: CAD drawing. The building object selected in this study was described according to construction drawings made on AutoCAD Architecture. Original 2D image information is provided in regard to points, lines, surfaces, text, etc.

Level 1: 3D modeling. In the course of preparing 3D building models, the virtual data are exported from the CAD system to a suitable CAD exchange format (e.g., DWG), then processed to re-build the plan in a 3D environment with the aid of BIM software system (e.g., Revit). The BIM 3D model is used to generate traditional building abstractions: plans, sections, details, and elevations. 3D models produced using BIM also possess interactive viewing properties.

Level 2: Sunlight simulation. Building environment analysis (like energy analysis and sun-hour analysis) is normally carried out as part of BIM based design. In this step, the representative rooftop and surface area of the sample building are selected. Sunlight simulation is made by input of the Industrial Foundation Classes (IFC) model into the sunlight analysis program, followed by additional related analysis on occlusion relationship, sunshine duration sheet, isohel map, shadow outlines, etc.

Level 3: Solar energy analysis. The main objective of Level 3 is to assess the geometric characteristics under sunlight models in solar energy analysis. This step obtains dimensions of the useful rooftop and vertical surfaces, where photovoltaic solar panels could be installed, from which the solar energy generation potential and the energy costs are calculated for the sample building.

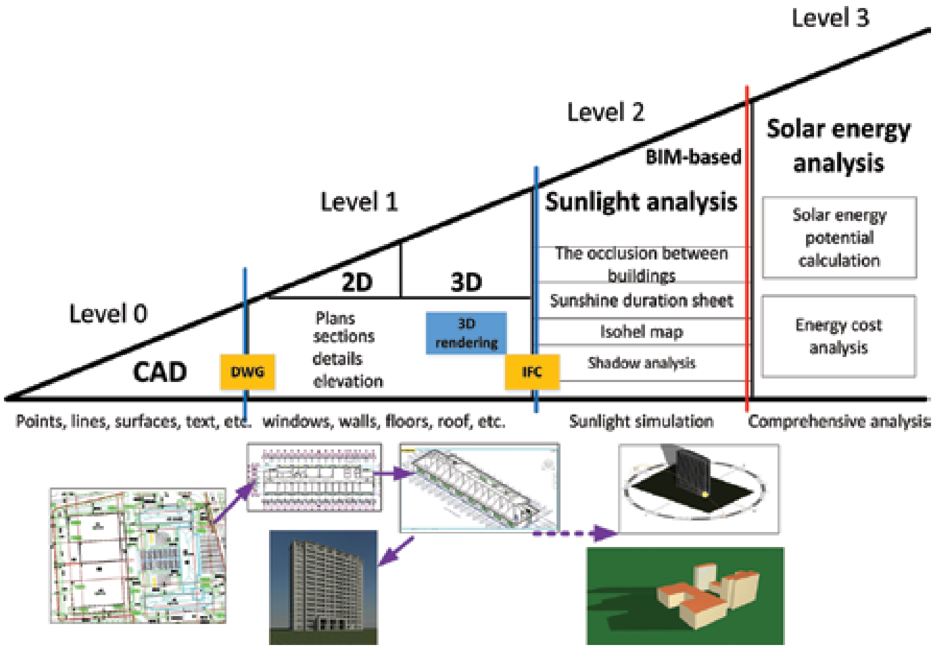

Figure 1. Overview of four-level research framework for solar energy analysis.

3.2. Simulation models and settings

The study case in this paper refers to the Civil Building located on the Jiulonghu Campus of Southeast University in Nanjing, China. The Civil Building is designed to be a 16-storey, technology-rich learning environment, hosting over 1000 classroom seats in-state-of-the-laboratory classrooms, with conference rooms and professors' offices. The building will be home to undergraduate and graduate students in Department of Civil Engineering and all staffs in that department. Surrounded by the newly-built Traffic Building, Laboratory Building (Building B) and Lecture Hall (Building A3), the sample building is sheltered from the sun in this sunlight simulation and analysis. The sample building's structure information is listed in **Table 1**.

In order to achieve the objective stated above, a schema converter is proposed in this paper to facilitate the information exchange between BIM tools and sunlight modeling tools. In this

Name	Status	Height (M)	Floor areas (M2)	Orientations	Use
Civil Building	Proposed	61.89	16559.05	South by east4°	Teaching
Building A3	Built	18.44	3747.08	South by east4°	Lecture and conference
Traffic Building	Built	54.67	20419.2	South by east 4°	Academic
Building B	Built	25.6	13210.18	South by east 4°	Teaching

Table 1. Information of civil building, traffic building, building A3 and B.

study, the technology for systematic sustainable design modeling that enabled sunlight simulation and analysis is driven by a Revit platform, which is able to design all of the required processes and components from a 2D building digital drawing to a 3D model. This platform uses an attribute driven modeling engine to simulate overall building design and create the network of building element relationships (inferred by the software and/or set by the user). The relationship network is the basis by which to achieve information exchange and to later generate sunlight analysis results.

3.3. Building modeling process

In this study, Autodesk Revit is applied to simulate the sample building in 3D with 2D drafting elements and export building data from the model database, as a BIM solution to plan and track various stages in the building's lifecycle from the concept to construction for architectural, structural and MEP design. The modeling process refers to generation of completed 3D models and related building information database. In general, the modeling process begins by analyzing initial data in 2D CAD environment followed by creation of Revit-parametric families, and then establishment of the Revit 3D model based on which the IFC file is transformed and exported.

3.3.1. Initial data analysis

Initial data acquisition is a process of selecting, extracting, and transforming information from the source systems. In BIM modeling, initial data are normally prepared using AutoCAD drawing, which stores layers, floors, rooms, and footprints of the buildings in 2D environment on dwg and dxf formats. The boundaries of building elements need to be determined carefully in the AutoCAD process. The optimized AutoCAD drawing will be imported into Revit in terms of creating a geometric model.

3.3.2. Revit model establishment

A key understanding is that both standard and custom-building elements can be added in Revit model by using a predefined family that is composed of elements with common parameters, allowing users to make design changes easily and to manage projects more efficiently.

Family classification and building component attribute setting are key phrases of the modeling stage. In Revit, basic building components/elements like walls, windows, doors, and so on are created using the responding category including families and family types. The building component or model element which is defined in terms of family contains a broad array of information in addition to dimensional aspects. At this stage, the initial parameters are set to define family attributes. The initial settings will affect the project environment and include types for levels, grids, drawing sheets, and viewports. The project model can be established using the generic families in Revit. After identifying the position of the building components inserted on an axis, the defined family types can be load one by one from top down, and the attributes of the model elements can be modified separately.

3.3.3. IFC transformation

Using the Revit model requires transformed of data into the IFC format for compatibility with THSWARE software, based on which sunlight would be simulated in this study. The IFC file format is designed to provide interoperability between different BIM-related software applications. Enabling importing and exporting of building objects and their properties, the IFC format covers core project information such as building elements, geometric and material properties of building products, etc. The major computer-aided design (CAD) systems, such as THSWARE, can transfer imported IFC data directly to the database elements, using a parsing subsystem described by Revit families of building elements.

3.4. Sunlight simulation settings

The Ministry of Construction for China has published a series of national codes, such as Code of Urban Residential Areas Planning and Design (GB 50180-93), Standard for Daylighting Design of Buildings (GB/T 50033-2001), Residential Building Code (GB 50368-2005), and others. With these codes, the Ministry of Construction for China has clearly prescribed requirements for the standard of available sunlight for buildings design and placement. On the basis of Code for Planning and Design on Urban Residential Areas (GB 50180-93) (2002), there is a code for sunlight standard in clause 5.0.2.1. Therefore, the sunlight simulation and analysis in this study conform to clause 5.0.2.1: The sunlight standard of buildings should accord with the regulations in **Table 2** and conform to the prescribed regulations listed below under particular conditions:

1. The sunlight on the Winter Solstice day in residential buildings for elderly people should be no less than 2 h;
2. Increasing of facilities outside the original design should not lower the original sunlight standard of adjacent residence;
3. In terms of reconstruction of old dwellings, the sunlight standard of new residential buildings could be reduced conditionally but should not be reduced to less than 1 h on the Great Cold day (Jan 20/21).

Architectural climate zone	**I, II, III, VII Climate zone**		**IV Climate zone**		**V, VI Climate zone**
	Large city	**Medium/small city**	**Large city**	**Medium/small city**	
Day for sunlight standard	Great Cold day Either 20 or 21 January depending on the year			Winter Solstice day Either 21 or 22 December depending on the year	
Sunlight hour (h)	≥2	≥3		≥1	
Effective sunlight hour	8 am~4 pm			9 am~3 pm	

Table 2. Sunlight standard of civil building.

A city with a population of one-half million people can be defined as a metropolis. Reaching that population standard, together with high level of economy, politics and culture, Nanjing qualifies as a metropolis that belongs to climatic region III, and its sunlight standard is therefore no less than 2 h of sunshine on the Great Cold day. The sunlight standard in Nanjing Technical Codes of Sunlight Analysis Management for High-Rise Building (Nanjing codes for sunlight in buildings) is adopted in this study, of which the Clause 4 (sunlight analysis object) is used for the planning of high-rise buildings.

The Civil Building with 16 stories is a high-rise building, whose planned design and blueprints are considered to conform to the prescribed regulations. Here, the sunlight simulation and analysis standard is defined in Clause 6 (technical parameter) of Nanjing Technical Codes of Sunlight Analysis Management for High-Rise Building. The start and ending times for sunlight analysis are 8 a.m. and 4 p.m. on Great Cold day, 9 a.m. and 3 p.m. on Winter Solstice day, while the calculating point is 32.04 north latitude (Nanjing), the sampling distance is 1.0 m, the time interval is 10 minutes, and the sill height is 0.9 m. The finalized start and ending time of the sunlight simulation are 8 a.m. and 4 p.m. on the Great Cold day, while standard for access to sunlight should be no less than 2 h on that day.

3.5. Sunlight simulation

The Sunlight-analysis function module of THSWARE which has an AutoCAD-oriented user interface focus on parameter setting and shelter influences. Before sunlight analysis begins, the THSWARE model is required to set some parameters including sunshine duration, window exposure, sunshine standards, simulation accuracy, etc.

3.5.1. Occlusion between buildings

For analysis of a building’s window-accessible sunlight, a precondition is to identify occlusion by neighboring structures that prevents penetration of light into living space. In **Table 3**, building occlusion relationships focus on occasions when objects block sunlight (in **Figure 2**). By overlaying the sun occlusion path of a particular sample building, the area of sun blockage could be determined by projecting lines out from this point to each surrounding object. Since the shading diagram will be constructed with all buildings, the result is always a hard-edged shading block with the observation window shaded or not.

3.5.2. Sunshine duration sheet

The sunshine duration sheet on THSWARE is designed to measure the length of time which the sun shines through a given window.

Occluded building	Occlusion building
Civil building	A3, B, Traffic building

Table 3. Occlusion between buildings.

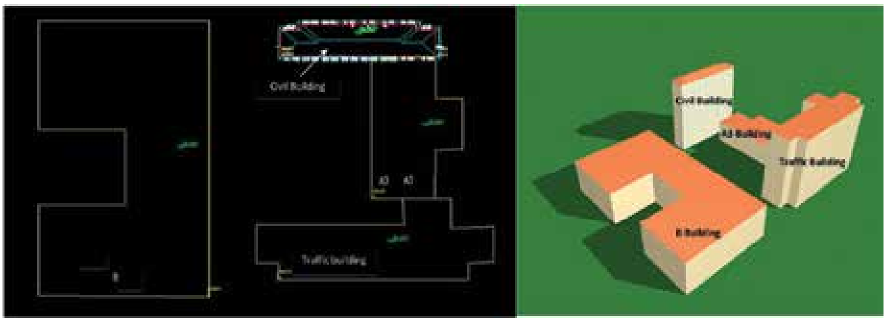

Figure 2. The occlusion between sample buildings.

Table 4 shows the simulation results of sunshine duration on the first floor of the Civil Building 8:00 AM–4:00 PM on Great Cold day, which is the last solar term in 24 solar terms and comes around January 20th or 21st each year. According to Code for Planning and Design on Urban Residential Areas (GB 50180-93) and Nanjing Technical Codes of Sunlight Analysis Management for High-rise Building, sunshine duration on Great Cold day cannot be less than 2 h. In **Table 4**, a red figure represents a window exposed to sunshine less than 2 h sunshine a day, while blue represents a window with 2 h sunshine on that day.

Analysis results are configured in the BIM model by marking the windows' positions as in **Figure 3**, where the blue line on the south face of the Civil Building represents the boundary of windows receiving less than 2 h of sunshine on Great Cold day. The serial number of the windows are 1/33-1/34, 2/36-2/38, 3/36-3/38 (windows no. 33-34 on the first floor, windows no.36-38 on the second floor, and windows no.36-38 on the third floor). On the North face of the Civil Building, the red line identifies windows areas, where the sunshine duration is zero on Great Cold day. The serial number of the windows are 1/4-1/13, 1/36-1/41 (windows no. 4–13 and No. 36–41 on the first floor).

3.5.3. *Isohel map*

An isohel is a line on a solar map which connects points that receive equal amounts of sunshine. In this study, two types of isohel map were produced to measure sunshine intensity: an isohel map for building elevation and an isohel map for the building plan.

3.5.4. *Isohel map of building elevation*

In this step, isohel maps were produced from average values of light intensity at measuring points for the area between the isohels on the building elevation including all four cardinal points, as shown in **Figures** 4 and **5**, wherein a, b represents the serial number of window located in ath floor is b.

Figure 4 shows the isohel map for the 6th–9th windows on the 10th–12th floor of the South elevation of the Civil Building. The white figures calculated in the isohel map indicate areas that will receive approximately 8 h of sunshine on Great Cold day.

Floor	Window position	Window height (m)	Sunshine duration	
			Time	Effective time duration (hour)
1st	1	0.50	12:01–14:15	02:14
	2	0.50	08:55–08:59 09:51–14:19	04:32
	3	0.50	09:55–14:23	04:28
	4–13	0.50	0	00:00
	14	0.50	09:57–14:29	04:32
	15	0.50	09:11–09:15 09:59–14:35	04:40
	16	0.50	09:19–09:21 10:05–14:41	04:38
	17	0.50	10:07–14:45	04:38
	18	0.50	10:11–14:49	04:38
	19	0.50	10:13–14:53	04:40
	20	0.50	10:15–14:59	04:44
	21	0.50	10:15–15:01	04:46
	22	0.50	10:15–15:05	04:50
	23	0.50	10:23–15:09	04:46
	24	0.50	10:39–15:13	04:34
	25	0.50	10:53–15:15	04:22
	26	0.50	11:07–15:19	04:12
	27	0.50	11:15–15:21	04:06
	28	0.50	11:35–15:25	03:50
	29	0.50	11:51–15:27	03:36
	30	0.50	12:21–15:29	03:08
	31	0.50	12:45–15:31	02:46
	32	0.50	13:35–15:35	02:00
	33	0.50	14:13–15:35	01:22
	34	0.50	15:07–15:41	00:34
	35	0.50	08:00–12:01	04:01
	36–41	0.00–0.50	0	00:00

Table 4. Sunshine duration sheet of first floor.

Figure 5 shows the isohel map for 18th windows in 16th floor on east elevation of Civil Building. The blue figures calculated on the isohel map indicate areas that will receive more than 4 h of sunshine on Great Cold day, while green figures indicate areas receiving more

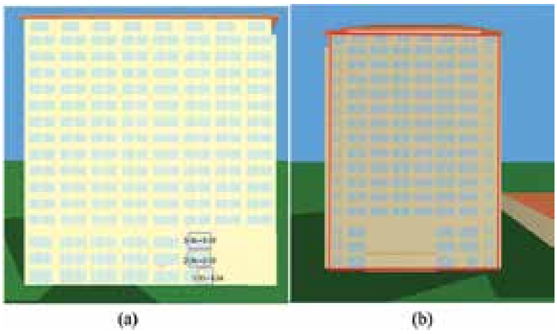

Figure 3. The windows which do not reach the sunshine requirement. (a) South face, (b) North face.

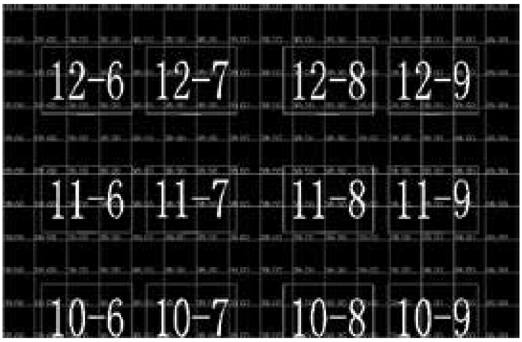

Figure 4. Isohel map for windows in 10th–12th floor on south elevation of civil building.

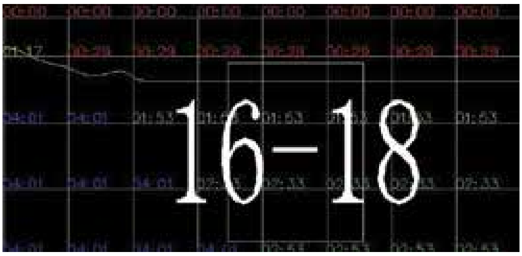

Figure 5. Isohel map for the 18th window on 16th floor of the East elevation of the building.

than 2 h of sunshine and yellow figures indicate areas with more than 1 h of sunshine. Note that the area of red figures that receives less than 1 h of sunshine is mainly the result of shadowing by the building roof.

3.5.5. Isohel map of building plane

The isohel maps of building planes, which is similar to the map of building elevation, apply plane partition according to sunshine duration. The isohel lines shown in building plane mode indicate clearly those areas receiving equal amounts of sunshine.

Figure 6 above shows division on the basis of sunshine duration of a given building plane. The image shows analysis of sunshine duration on the first floor, in which dark blue represents areas receiving sunshine for more than 4 h, light blue represents more than 3 h of light, green represents more than 2 h, yellow represents more than 1 hour, and red represents less than 1 h of light. Results indicate very little sunshine on the North plane, and the windows no. 33-34 have a sunshine duration of zero, due to occlusion by the Traffic Building (Building T) from the south, which is in accordance with the analysis above.

3.5.6. Area analysis

Area analysis (in **Figure 7**) yields sunshine duration values for different areas within the same plane of a building. Theoretically, analysis of isohel lines is in accordance with area analysis, which facilitates cross-confirmation. The object of sunlight analysis in the image above is the first floor, from which the obtained data represent the length of time that area receives sunshine. The results accord with actual conditions, where N represents sunshine duration greater than or equal to N, but less than N + 0.5 and N+ represents sunshine duration greater than or equal to N + 0.5 but less than N + 1.

3.5.7. Shadow outline and shadow range of building

1. Occlusion of and by the Civil Building

Figure 8 clearly shows the shadow size at 11:00 of each building in this study. Three windows of the South side on floors 1-3 of the Civil Building are shaded by the Traffic Building (Building T), falling it far from the insolation standards on Great Cold day of 2 h.

2. Shadow range of the Civil Building

Figure 9 shows shadow range of Civil Building and its continuous shadow envelope on the ground on Great Cold day.

3.5.8. Screenshot of sunshine simulation

This research section examines sunshine of the Civil Building 8:00–16:00 h (in **Figure 10**). The shadow area is relatively large around 8:00, while most windows on the North side can

Figure 6. Isohel map of building plane.

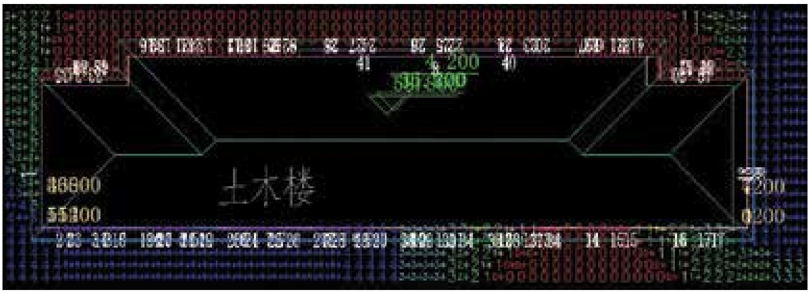

Figure 7. Area analysis map.

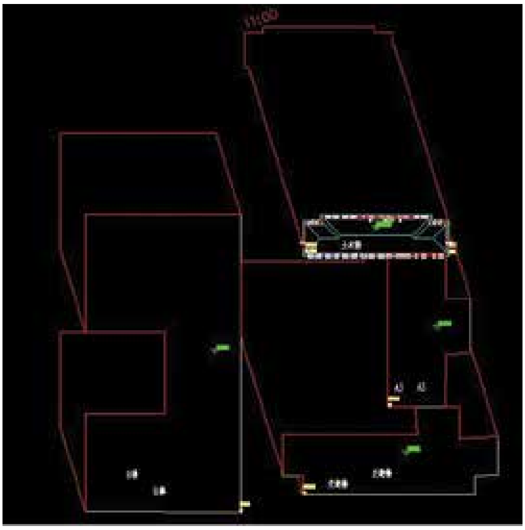

Figure 8. Shadow outline of civil building.

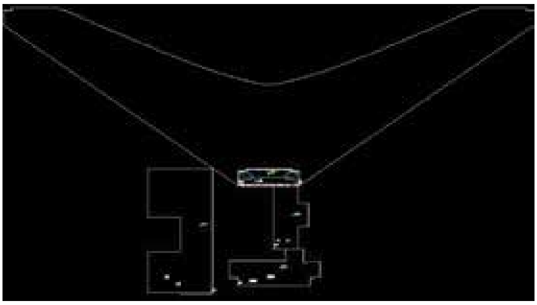

Figure 9. Shadow range of civil building.

receive sunshine. The shadow area at 12:00 is much less than any other time of the day, which means that windows receiving sunshine increase and sunshine duration is much longer. 16:00 is the latest time point used for analyzing sunshine duration on the Civil Building on Great

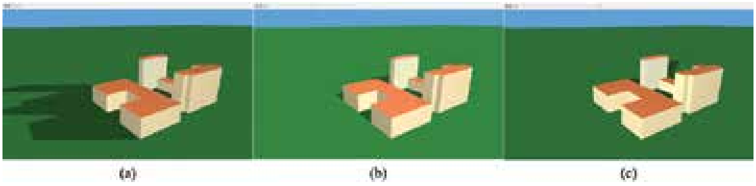

Figure 10. Sunshine simulation at (a) 8:00 A.M., (b) 12:00 P.M., and (c) 16:00 P.M.

Cold day, and the shadow is accordingly stretches. According to the three images above, no windows on the nightside can receive sunshine at any time of the day, which is in accordance with the sunshine analysis of windows as shown above.

4. Results and discussion

4.1. The assumption of energy calculation

In this study, the analyzed building is treated as one system, where the amount of solar energy gained by any facade of building is the main research target. Related data used to calculate solar energy are generated in the sunlight simulation by BIM modeling, which shows the sunshine duration on facades of a selected building. For solar energy calculation in this study, it is assumed that Civil Building meets the following conditions:

1. Solar panels can be installed on the rooftop and vertical walls with a sunshine duration more than 5 h.
2. In order to satisfy required cost savings, the solar panels will not be installed on the north-facing vertical wall of the building because of its insufficient sunshine all year around.
3. Every solar panel is made up of the same material, and the absorbed sunlight can be converted into electricity to attain efficiency in stable networks.
4. The energy cost analysis mainly considers the cost of solar panels.
5. The analysis period for energy cost is classified into Vernal Equinox, Summer Solstice, Autumn Equinox, and Winter Solstice. The duration time is assumed to be the average of each solar term.
6. According to the weather statistics over the last 3 years, the average number of sunny days each year accounted for 55%.
7. The duration of the sunshine period on the facade of the building is considered to be the average length of the period as estimated by sunlight simulation on THESWARE.
8. The rate paid for electricity is 0.88 RMB per kilowatt-hour.

The assumptions mentioned above are made in order to facilitate investigation easy and to make the comparison more realistic. In this study, direct solar radiation was calculated, ground reflected, and diffused radiations are neglected under the assumption that they will be equal for all shapes. Additionally, effects of the other factors, like shading and type of building material, are assumed to be equal for all situations. These assumptions do not change the main results of this study.

4.2. Energy consumption calculation and cost analysis

In this study, each surface of the building was first analyzed separately, and then all systems were discussed. Surfaces of the building were encoded by using abbreviations ("South," "East/West"), as seen in **Table 5**. Instant and hourly solar energy from the surface of a building depend upon some parameters, like the time of day, day of year, effective area of the wall, sunshine duration, etc. According to the BIM model of the Civil Building described above, the total area and effective area of walls on each floor can be summarized in **Table 5**. Note that the north-facing surface is not taken into consideration because its sunshine duration is less than 5 h. As well, the sunshine duration of different surfaces in each solar term is shown in **Table 6**, where the surfaces labeled in italics are the vertical walls with a sunshine duration of less than 5 hours.

In this part of the study, sunshine striking a given surface between sunrise and sunset is of concern. First, the total amount of annual solar energy striking surface for more than 5 h was

Floor	Surface	Total area (m^2)	Windows area (m^2)	Effective area (m^2)
Roof		867.8	0	867.8
1	South	255.78	89.64	166.14
	East/west	66.78	6.3	60.48
2	South	219.24	77.76	141.48
	East/west	57.24	5.67	51.57
3	South	219.24	67.2	152.04
	East/west	57.24	4.2	53.04
4-5	South	219.24	89.6	129.64
	East/west	57.24	5.67	51.57
6-10	South	219.24	89.6	129.64
	East/west	57.24	5.67	51.57
11-14	South	219.24	89.6	129.64
	East/west	57.24	5.67	51.57
15	South	219.24	89.6	129.64
	East/west	57.24	5.67	51.57
16	South	216	64	152
	East/west	56.16	5.67	50.49

Table 5. The area of the wall.

Floor	Surface	The spring equinox	The summer solstice	The autumnal equinox	The winter solstice	Effective sunshine duration in a year (h)
Roof		12	14	12	10	2376
1	South	5.4	4.8	5.4	3	920.7
	East	6	7	6	4.5	1163.25
	West	*3.3*	*4.5*	*3.3*	*2.4*	
2	South	6	4.8	6	4	594
	East	6	7	6	5	1188
	West	3.6	4.5	3.6	2.6	
3	South	7	4.7	7	4.5	1148.4
	East	6	5	6	5	1188
	West	*4*	*3*	*4*	*3*	
4-5	South	8.6	6.5	8.6	6.5	1470.15
	East	6	7	6	5	1188
	West	*4.75*	*6*	*4.75*	*3.5*	
6-10	South	12	6	12	10	1980
	East	6	7	6	5	1188
	West	6	7	6	4.8	1178.1
11-14	South	12	4	12	10	1881
	East	6	7	6	5	1188
	West	6	7	6	5	1188
15	South	12	1.5	12	10	1757.25
	East	6	6.5	6	5	1163.25
	West	6	6.5	6	5	1163.25
16	South	6.8	0.5	6.8	9	1143.45
	East	*3.4*	*3.6*	*3.4*	*3.5*	
	West	*4.3*	*4.5*	*4.3*	*4*	

Table 6. Sunshine duration of different surfaces (unit: h).

calculated for each solar term over a whole year, which calculation was performed for every surface of the building. The related and required parameters for cost calculation were then assigned. According to the sustainable design plan of the Civil Building, polycrystalline silicon solar panel at 240 W and 18% conversion efficiency (1.65 m long, 0.991 m wide, and 0.04 m light) are suitable components for a larger photovoltaic energy generation and supply system. The installed photovoltaic system will receive 3 RMB per watt capacity in construction subsidies, thus each solar panel 240 W will yield 720 RMB in subsidy.

The total number of solar panels n that can be installed on the surface is given in Eq. (1), where Ai is the combined effective area of the facade and rooftop of the Civil Building, while S is the cross-sectional area of the solar panel.

$$n_i = \left[\frac{A_i}{S}\right] \tag{1}$$

The total electrical energy Q generated by solar panels installed on the Civil Building can be calculated by Eq. (2), where η is the conversion efficiency of the solar panel, w is the power output of solar panels, and Ti is the effective sunshine duration per year of each surface.

$$Q = \eta\sum_{i=1}^{42} n_i w T_i = \eta\sum_{i=1}^{42}\left[\frac{A_i}{S}\right] w T_i \tag{2}$$

The amount of the electricity converted by solar panels can be calculated in Eq. (3).

$$Q = 18\% \times 240 \times 3600 \times \sum n_i T_i = 651860789.2\text{kJ} \tag{3}$$

As is shown in Eq. (3), the solar panels yield more than 60 billion joules of savings in electricity, which shows that the solar panels installed on "Civil Building" reduce traditional energy consumption and in turn contribute to the overall energy efficiency. To assess economic benefit of solar panels, the payback period for solar panel cost can be calculated using Eq. (4).

$$C = \sum_{i}^{42}\left[\frac{A_i}{S}\right] \times p = 2544 \times 720 = 1831680RMB \tag{4}$$

In this case, p is the price of each solar panel and C is the operating cost of solar panels. Considering an average electricity price 0.88 RMB per kilowatt-hour in Nanjing, the daily saving on electricity rates P and the recovery period T can be calculated as follows.

$$P = 0.88 \times (651860789.2/3600) = 159343.7485RMB$$

$$T = C/P = 1831680/159343.7485 = 11.5\,years$$

Through the cost analysis, after year 11, the investment status solar panels become positive, which means that after 11.5 years, the solar panel system will operate as a positive cash flow source. Based on the 30-year estimated lifespan of the solar panels, there will be more years benefitting from the solar panel installation than years paying for it. After fully analyzing all the results, the investment is definitely cost-beneficial.

5. Conclusions

The switch to alternative energy sources of electricity is increasing, especially solar energy. The installation of solar panels is advertised throughout the world including China by use of information technologies. Based on the application of building energy modeling and sunlight simulation by BIM technology, and taking advantage of information modeling with 3D visualizations, the sunshine duration and energy consumption of buildings can be calculated with a fair level of accuracy. As a widely used tool in construction sector, BIM has great prospects. With a three-dimensional digital technology, the concept of BIM integrates various kinds of relevant information from construction projects, aiding in complex building performance analyses to ensure an optimized sustainable building design. As well, related software enables energy consumption to be predicted and adjusted during the design stage, thus providing great convenience for sustainable design.

This case study presents both method and technology for integration of building energy simulation and cost calculation with building information modeling (BIM). The early feasibility study stage included sunlight simulation using Revit and THS-WARE, after which the solar energy production was investigated based on the application of solar panels. Initial sunlight analysis and energy use calculations by BIM software were generated based on a number of building specifications and environmental data. According to analysis of solar energy as absorbed by facades, the expense saved by electricity generated from the solar energy can be calculated. Taking the cost of solar panels and project feasibility into consideration, the study shows that application of the studied solar panels contributes greatly to social, economic, and environmental benefits. The energy-saving proposal is feasible in this case and realizes the sustainable design.

Though application of building information modeling (BIM) technology assists effective decisions-making as related to sustainable building design in the early stages, BIM is still developing and limited by software compatibility. If the following aspects can be improved while applying sunshine simulation to real projects through BIM, the long-term benefits of a sustainable design will be realized. (1) Strengthen software analysis area. In order to provide a more comprehensive analysis, apart from the analysis of sunlight condition of the building, indoor lighting, ventilation, and air conditioning should be taken into consideration. (2) The result of calculation on solar energy converted to electricity has effect on the development of solar panels. Optimizing the utilization of solar panels contributes to energy saving. (3) A new plug-in is needed to combine solar energy analysis with sunshine simulation, which can solve related practical problem more efficiently.

Acknowledgements

The authors' special thanks go to the National Science Council of P. R. C. for financially supporting this research (NSFC-71302138), and fund by the National Key Research and Development Program of China (2016YFC0702001-06).

Author details

Zhao Xu and Jingfeng Yuan

Address all correspondence to: bernardos@163.com

Department of Civil Engineering, Southeast University, Nanjing, China

References

[1] Sarinda J, Praweenya S, Poonarat P. Systems thinking for sustainable design: A conceptual framework of constructivist web-based learning environment management using inquiry learning process. Creative Education. 2012;**3**:35-38. DOI: 10.4236/ce.2012.38B008

[2] Cheng S. The research of green building design and application based on bim technology [Thesis]. Hunan China: Hunan University; 2013

[3] Wang RX. Green building of low power consumption. Journal of Tianjin University (Social Science). 2010;**12**(2):144-148. http://kns.cnki.net/kns/detail/detail.aspx?FileName=TDXS201002011&DbName

[4] Schlueter A, Thesseling F. Building information model based energy/exergy performance assessment in early design stages. Automation in Construction. 2009;**18**(2):153-163. DOI: 10.1016/j.autcon.2008.07.003

[5] Wu PL, Li YQ, Wen XL. Extended application of GIS for temporal simulation of sunlight on buildings in 3D environment. In: International Conference on Environmental Science and Information Application Technology Advances in Biomedical Engineering. Bali, Indonesia; 2012

[6] Kota S, Haberl JS, Clayton MJ, et al. Building Information Modeling (BIM)-based daylighting simulation and analysis. Energy and Buildings. 2014;**81**(April):391-403. DOI: 10.1016/j.enbuild.2014.06.043

[7] Bazjanac V. IFC BIM-based methodology for semi-automated building energy performance simulation. In: CIB-W78 25th International Conference on Information Technology in Construction, Santiago, Chile. July 15-17; 2008

[8] Wong KD, Fan Q. Building Information Modeling (BIM) for sustainable building design. Facilities. 2013;**3**:138-157. DOI: https://doi.org/10.1108/02632771311299412

[9] Wang JL, Xuan XD. BIM-based parametric design for integrating Bio-inspired kinetic envelopes into sustainable buildings. In: International Academic Conference of Science and Technology of Building Environment. Nanjing, Jiangsu; 2010-05-07

[10] Hardin B, McCool D. BIM and Construction Management. New York, USA: Wiley Publishing; 2009

[11] Azhar S, Brown J. BIM for sustainability analyses. International Journal of Construction Education and Research. 2009;**5**(4):276-292. DOI: 10.1080/15578770903355657

[12] Kriegel E, Nies B. Green BIM. Indianapolis, USA: Wiley Publishing; 2008

[13] Strømann-Andersen J, Sattrup PA. The urban canyon and building energy use: Urban density versus daylight and passive solar gains. Energy and Buildings. 2011;**43**(8):2011-2020. DOI: 10.1016/j.enbuild.2011.04.007

[14] Welle B, Rogers Z, Fischer M. BIM-Centric Daylight Profiler for Simulation (BDP4SIM): A methodology for automated product model decomposition and recomposition for

climate-based daylighting simulation. Building and Environment. 2012;**58**:114-134. DOI: 10.1016/j.buildenv.2012.06.021

[15] Joo JS, Kim MS, YH Song, Lim DH, Lee KI, Kim HW. Development of web based sun hours and energy analysis system using IFC. In: Asim 2012 IBPSA Asia Conference. Shanghai. China. November 25-27; 2012. http://www.ibpsa.org/proceedings/asim2012/0021.pdf

[16] Tsalikis G, Martinopoulos G. Solar energy systems potential for nearly net zero energy residential buildings. Solar Energy. 2015;**115**:743-756. DOI: 10.1016/j.solener.2015.03.037

[17] Khatib T, Mohamed A, Sopian K. A review of solar energy modeling techniques. Renewable & Sustainable Energy Reviews. 2012;**16**(5):2864-2869. DOI: 10.1016/j.rser.2012.01.064

[18] Ordóñez J, Jadraque E, Alegre J, et al. Analysis of the photovoltaic solar energy capacity of residential rooftops in Andalusia (Spain). Renewable & Sustainable Energy Reviews. 2010;**14**(7):2122-2130. DOI: 10.1016/j.rser.2010.01.001

[19] Glasnovic Z, Margeta J. Maximum area that can be economically irrigated by solar photovoltaic pumping system. Journal of Irrigation and Drainage Engineering. 2009;**135**(1):44-49. DOI: 10.1061/(ASCE)0733-9437(2009)135:1(44)

[20] Borenstein S. The Market Value and Cost of Solar Photovoltaic Electricity Production. Center for the Study of Energy Markets. University of California Energy Institute; 2008. http://escholarship.org/uc/item/3ws6r3j4.pdf

Chapter 7

Some Essential Issues and Outlook for Industrialization of Cu-III-VI_2 Thin-Film Solar Cells

Yijian Liu, Huey-Liang Hwang, Ying Wang,
Jun Zhang and Lexi Shao

Additional information is available at the end of the chapter

http://dx.doi.org/10.5772/intechopen.77023

Abstract

The concept and method of in-line sputtering and selenization become the industrial standard for Cu-III-VI_2 solar cell fabrication, but it is a difficult work to control and predict the electrical and optical performances, which are closely related to the chemical composition of the film. This chapter addresses the material design, device design, and process design using chemical compositions relating parameters. Compositional variation leads to change in the poisson equation, current equation and continuity equation governing the device design. To make the device design much realistic and meaningful, we have to build a model that relates the opto-electrical performance to the chemical composition of the film. The material and device structural parameters are input into the process simulation to give a complete process control parameters and method. We calculated neutral defect concentrations of non-stoichiometric $CuMSe_2$ (M-In, Ga) under the specific atomic chemical potential conditions. The electrical and optical performance has also been investigated for the development of full function analytical solar cell simulator. Module instability and their origins are listed. After that progress of CZTS (Cu_2ZnS_4) is briefed on the future work of CIGS ($CuInGaSe_2$). The future prospects regarding the development of CIGS thin-film solar cells (TFSCs) have also been discussed.

Keywords: Cu-III-VI_2, non-stoichiometric, material process and device design, module stability, progress of CZTS

1. Introduction

During past few decades the PV market has grown at a remarkable rate especially focused on the thin-film solar cells (TFSCs) and it is on their way to becoming a major source of electricity production around the world. Although the research and development of CIGS are still in crucial phase due to low production yields, non-reproducibility, and non-uniformity over large area confronted during the industrialization and commercialization. Governing such issues, we published our first research paper in the year 2003 on "Steps toward industrialization of Cu-III-VI_2 thin film solar cells: A novel in-line concept" [1]. After that, the concept of in-line sputtering and selenization become international standard globally. From that time, dozens of CIGS manufacturing units established worldwide but rare claim successful in production due to difficulty in controlling the local chemical composition distribution of the film. Moreover, the production efficiency of large-area photovoltaic (PV) cells and panels varies in the wide range from 6 to 13%. During the decades of fast development of Cu-III-VI_2 thin film solar cells, much more research and industrial method were proposed. In this chapter, we will depict the principles and development of some essential issues for industrialization of Cu-III-VI_2 thin film solar cells.

In the year 2003, we published another research "Preliminary steps toward industrialization of Cu-III-VI_2 thin film solar cells: development of an intelligent design tool for non-stoichiometric photovoltaic materials" [1] pointing on the problem encountered during the commercialization. Over the years, many experimental and theoretical research works published in many journals focused on various subjects of problems and its solutions for CIGS TFSCs [2–9].

In 2013, we published one more research article "Steps toward removing some obstacles of industrialization of CIGS solar cells" [10]. This article pointing to the new concept of metal organic sputtering was used to tune and tailor the film compositions based on the programme material and device design. What shown in **Figure 1** is the method of our intelligence material and device design, describing the detailed calculation of the neutral defect concentrations of non-stoichiometric $CuInSe_2$, $CuGaSe_2$, and ZnO in specific atomic chemical potential conditions ($\mu x = 0$, X = Cu, In/Ga, Zn).

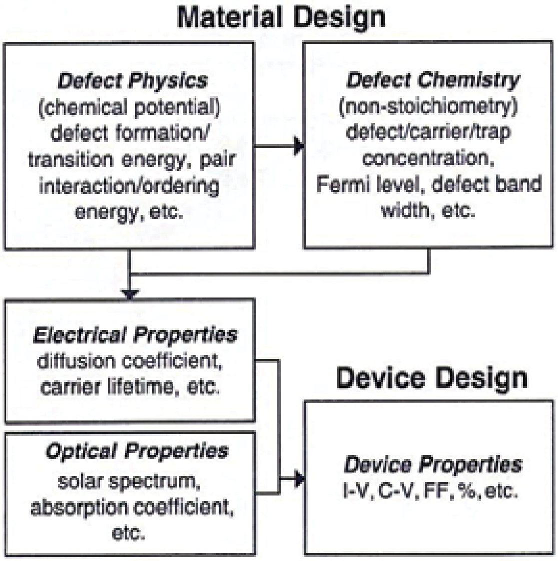

Figure 1. The scheme of our materials design and device design in which the electrical and device properties are optimized, and related to the process parameters such as, chemical potential and non-stoichiometry.

These main and key schemes of the intelligence design are the calculations of device and process design. The carrier concentration and the electrical properties of these materials with variable atomic constitutions are further calculated, which demonstrate the main functions of the CAD tool used [1, 10–13].

The present communication we have summed up the material design, device design, and process design to get deep knowledge on the chemical composition variation for obtaining the complete process control parameters. These designing tools will moderately help to overcome all the obstacles encountered during the industrialization of CIGS thin film solar cells. The future aspects of industrialization of CIGS thin film solar cells are also discussed.

2. Introduction on intelligence material design

2.1. Experimental data

We all know that Cu-III-VI$_2$ typically have a wide phase stability range, which extends a few atomic percents of the chemical composition of the thin-film, contract to III-V, and II-VI compounds. Shown in **Figure 2** is the chemical composition for a near-stoichiometric CuInSe$_2$. The variations in the CuInSe$_2$ film was detected using a transmission electron microscope (TEM) equipped with a field emission gun [10]. A similar result had also been reported for CIGS thin-film [11].

2.2. Theoretical data

In 2003, we published an example of the design tool for the non-stoichiometric compound using the concept of minimization of total free energy [1, 12, 13], which includes the configurational entropy, that defined as;

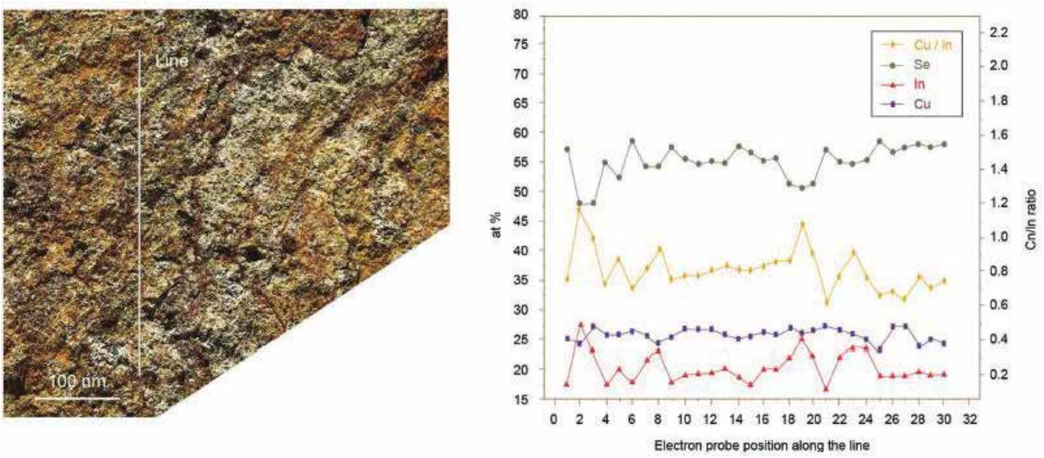

Figure 2. Chemical composition of a near-stoichiometric CuInSe$_2$ film measured consecutively by using an electron beam with a 3 nm probe size along a line marked on a TEM micrograph (left) and the plotted data (right) (corresponding to the data in **Table 1**).

	Cu(at%)	In(at%)	Se(at%)	Cu/In
Maximum	28.2	28.1	57.1	1.18
Minimum	17.2	22.6	47.9	0.62
Average	20.9	25.9	53.3	0.81
Standard deviation	2.73	1.37	2.80	0.12

Table 1. Chemical composition of a near-stoichiometric $CuInSe_2$ films.

$$G(T,\text{Crystal size}) = \Sigma n_i E_{fi} - TS_{config}, S_{config} = Kln\frac{N_{total}!}{\pi_j N_j!} \tag{1}$$

where n_i is the number of the ith defect, E_{fi} is the formation energy, S_{config} is the configurational entropy, T is the temperature, K is the Boltzmann constant, N is the total number of lattice sites, and Ni is the total number of defect sites of the i_{th} defect. We find the possible results for the co-existence of donors and acceptors in $CuMSe_2$ (M = In, Ga), which includes either the new defects produced through interaction or donor-acceptor pair/cluster formation.

Table 2 shows the defect formation energies and the defect transition levels. We also find the possible phases of $CuMSe_2$ resulted due to the compensated donor-acceptor pairs in different Cu concentration, for example, $Cu_1M_3Se_5$ phase is observed by 80% $Cu_1M_5Se_8$ and 20% $CuMSe_2$.

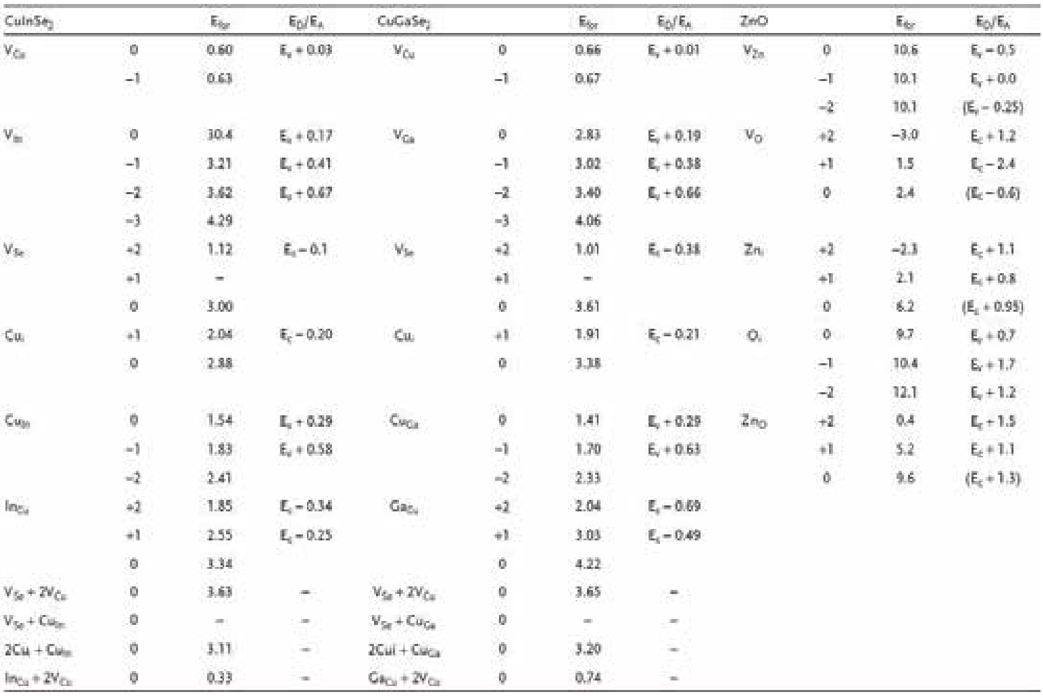

$CuInSe_2$		E_{for}	E_D/E_A	$CuGaSe_2$		E_{for}	E_D/E_A	ZnO		E_{for}	E_D/E_A
V_{Cu}	0	0.60	$E_v + 0.03$	V_{Cu}	0	0.66	$E_v + 0.01$	V_{Zn}	0	10.6	$E_v - 0.5$
	−1	0.63			−1	0.67			−1	10.1	$E_v + 0.0$
									−2	10.1	$(E_v - 0.25)$
V_{In}	0	30.4	$E_v + 0.17$	V_{Ga}	0	2.83	$E_v + 0.19$	V_O	+2	−3.0	$E_c + 1.2$
	−1	3.21	$E_v + 0.41$		−1	3.02	$E_v + 0.38$		+1	1.5	$E_c - 2.4$
	−2	3.62	$E_v + 0.67$		−2	3.40	$E_v + 0.66$		0	2.4	$(E_c - 0.6)$
	−3	4.29			−3	4.06					
V_{Se}	+2	1.12	$E_c - 0.1$	V_{Se}	+2	1.01	$E_c - 0.38$	Zn_i	+2	−2.3	$E_c + 1.1$
	+1	–			+1	–			+1	2.1	$E_c + 0.8$
	0	3.00			0	3.61			0	6.2	$(E_c + 0.95)$
Cu_i	+1	2.04	$E_c - 0.20$	Cu_i	+1	1.91	$E_c - 0.21$	O_i	0	9.7	$E_v + 0.7$
	0	2.88			0	3.38			−1	10.4	$E_v + 1.7$
									−2	12.1	$E_v + 1.2$
Cu_{In}	0	1.54	$E_v + 0.29$	Cu_{Ga}	0	1.41	$E_v + 0.29$	Zn_O	+2	0.4	$E_c + 1.5$
	−1	1.83	$E_v + 0.58$		−1	1.70	$E_v + 0.63$		+1	5.2	$E_c + 1.1$
	−2	2.41			−2	2.33			0	9.6	$(E_c + 1.3)$
In_{Cu}	+2	1.85	$E_c - 0.34$	Ga_{Cu}	+2	2.04	$E_c - 0.69$				
	+1	2.55	$E_c - 0.25$		+1	3.03	$E_c - 0.49$				
	0	3.34			0	4.22					
$V_{Se} + 2V_{Cu}$	0	3.63	–	$V_{Se} + 2V_{Cu}$	0	3.65	–				
$V_{Se} + Cu_{In}$	0	–	–	$V_{Se} + Cu_{Ga}$	0	–	–				
$2Cu_i + Cu_{In}$	0	3.11	–	$2Cui + Cu_{Ga}$	0	3.20	–				
$In_{Cu} + 2V_{Cu}$	0	0.33	–	$Ga_{Cu} + 2V_{Cu}$	0	0.74	–				

Table 2. The defect formation energies and defect transition levels used in our calculations [14].

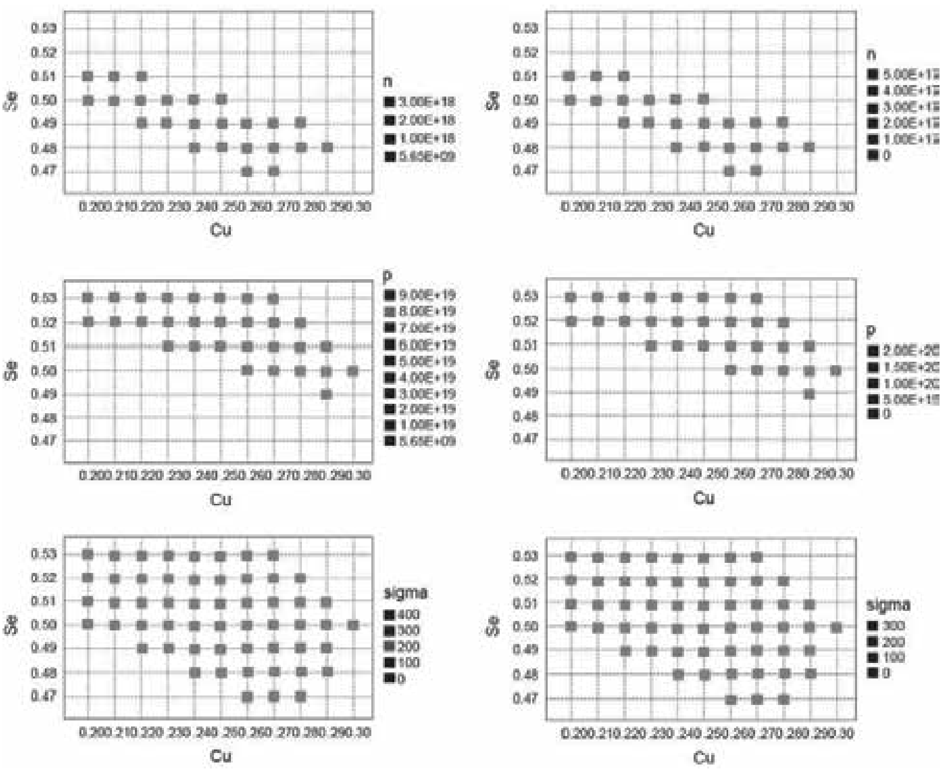

Figure 3. The calculated carrier concentration and electrical conductivity of CuInSe$_2$ (left) and CuGaSe$_2$ (right) at 300 K.

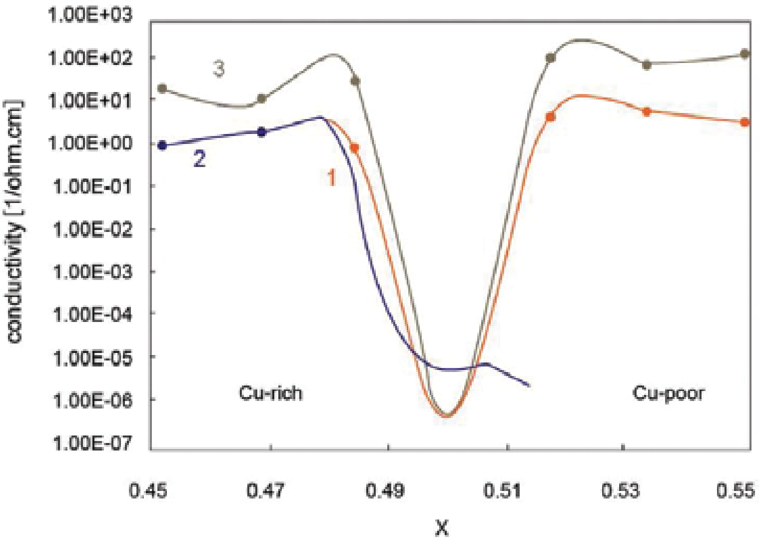

Figure 4. The measured conductivity of the CuInSe$_2$ thin-film along the Cu$_2$Se-In$_2$Se$_3$on-tie line with composition (Cu$_2$Se) 1−x(In$_2$Se$_3$)x(line 1) and the calculated range (between line 2 and 3) near the Cu$_2$Se-In$_2$Se$_3$ tie line at 300 K.

To solve the charge neutrality equation, we require several parameters, such as the carrier concentrations, Femi level at a certain temperature and ionized/neutral defect concentrations. In **Figure 3**, the calculated carrier concentration and electrical conductivity of $CuInSe_2$ and $CuGaSe_2$ at 300 K are shown. Note that in **Figure 4**, the conductivity will increase first and then decrease down to the film composition from stoichiometry to Cu-poor, after that the conductivity is even lower than that of the stoichiometry.

3. Brief on the device design

The simulator SCADS 3.2 [15] has been widely accepted for numerical analysis of CIGS solar cell devices. In 2014, the 19% efficiency of the solar cell was simulated by Naoki Ashida et al. [16]. In this report, the 2 μm thick CIGS absorber layer was divided into two regions, such as low defect density region (front side) and high defect density region (back side).

We also developed an alternate full function (indoor, outdoor, and I-V, C-V) analytic solar cell simulator, in which the following (time-independent) device equations are considered.

a. The continuity equation

$$\mathrm{O} = -\frac{1}{\mathrm{q}}\frac{\mathrm{d}}{\mathrm{dx}}\tau_p + G_p - R_p, R_p = \frac{\Delta p}{\tau_h}, \Delta p = p_n - p_{no} \tag{2}$$

$$\mathrm{O} = -\frac{1}{\mathrm{q}}\frac{\mathrm{d}}{\mathrm{dx}}\tau_n + G_n - R_n, R_n = \frac{\Delta n}{\tau_e}, \Delta n = n_p - n_{po} \tag{3}$$

b. Transport equations

$$\tau_p = \mathrm{pq}\mu_p\,\mathrm{E} - \mathrm{q}D_p\frac{\mathrm{dp}}{\mathrm{dx}} \tag{4}$$

$$\tau_n = \mathrm{nq}\mu_n\,\mathrm{E} + \mathrm{q}D_n\frac{\mathrm{dn}}{\mathrm{dx}} \tag{5}$$

We have considered all the boundary conditions (n-QNR/SCR interface, front contact, p-QNR/SCR interface, and back contact), in which QNR stands for the quasi-neutral region and SCR stands for space charge region for a typical n-CdS/p-CIGS device structure. In results of our simulation, we show that the higher efficiency cells are distributed along the line from Cu:Se = 0.3:0.5 to the stoichiometric point and the line from Cu:Se = 0.21:0.52 to the stoichiometric point. What is shown in **Figure 5** is the comparison of the computed efficiencies with the national renewable energy laboratory (NREL) experimental data, where the device structures of these cells are $ZnO/CdS/CuInSe_2$. As to the higher efficiency cells, the atomic compositions are especially concentrated near Cu:Se = 0.22:0.51 or along the line from Cu:Se = 0.22:0.51 to the stoichiometric point.

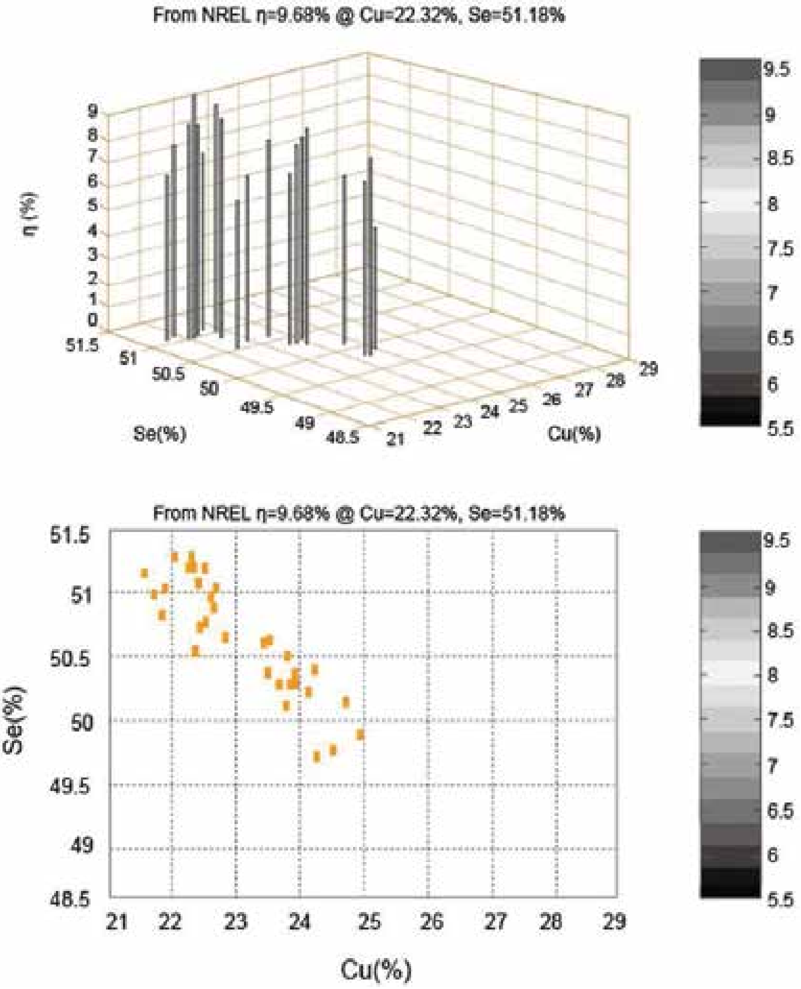

Figure 5. The comparison of the computed efficiencies as compared with NREL's database of ZnO/CdS/CuInSe$_2$ solar cells: (upper) 3D view, (lower) 2D view.

In the last decades, many studies on interface and surface compositional profile have been dealt with the advanced characterizations for the high-efficiency CIGS solar cells. A few examples are:

1. Conduction band profiles are changed by the three stage selenization [17].
2. Ordered defect compounds (ODC: CuInSe$_2$, CuIn$_3$Se$_5$, CuIn$_5$Se$_8$, etc.) resulted from CuInSe$_2$/CIGS solar cell studies, in which the X-ray photoelectron Spectroscopy (XPS) investigations depicted the depletion of Cu near the surface, and the theory as well experiments predicted ordered defect compound structured [18].
3. Shown in **Figure 6**, defect pairs (2V$_{cu}$ and In$_{cu}$) stabilizes the CuInSe$_2$ surface and band alignment gives hole barrier at the interface via the investigations by low energy electron

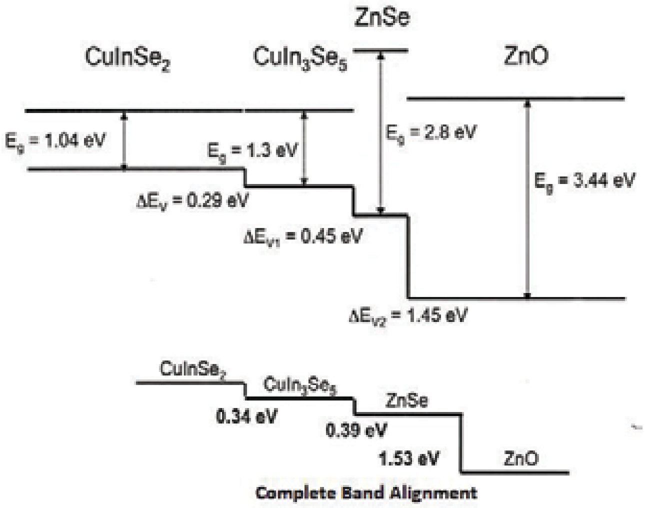

Figure 6. The complete band alignment includes the copper depletion at the interface.

diffraction (LEED), angular resolved ultraviolet photoelectron spectroscopy (ARUPS) and auger electron spectroscopy (AES) [14].

4. Secondary ion mass spectrometry (SIMS) depth profile of Cu, In, Ga, Se, Cd, and Na revealed the CdS/CIGS/ZnO diffusion phenomena as shown in **Figure 7** [19].

   Sample **Figure 7(a)** and **(b)** were obtained from the different origins, note that the difference in the Ga profile in the SIMS depth profiles are due to the different processes.

5. Defect in grains and grain boundaries [20].

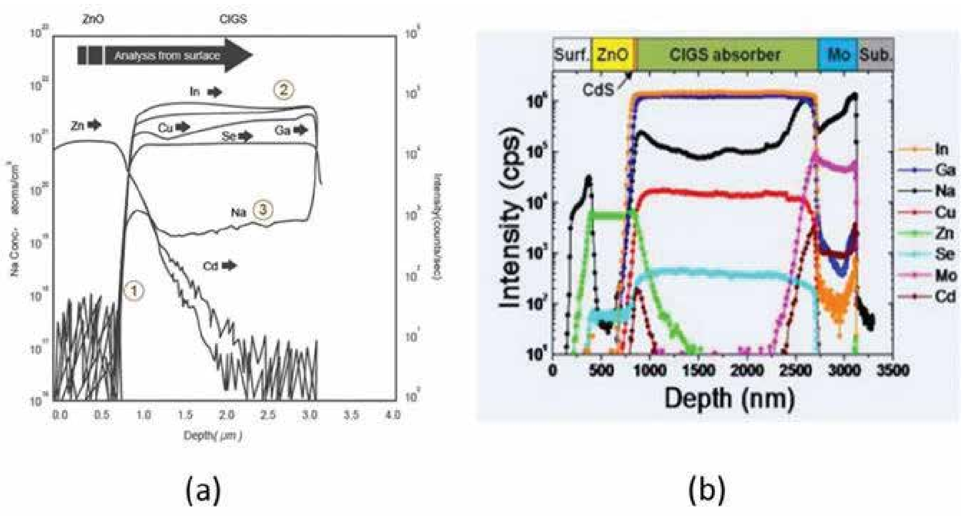

Figure 7. SIMS depth profile of Cu, In, Ga, Se, Cd, and Na. (1) CdS/CIGS and ZnO diffusion. (2) Cu, In, Ga, and Se depth profile. (3) Quantitative analysis of Na in CIGS.

The properties of the interfaces in semiconductor devices are critically dependent on the detailed atomic structure of the contact plane. Therefore, the model of the junction in chalcopyrite thin-films was simulated by the well-defined interface to classify the influence of grain boundaries, lateral inhomogeneity and chemical variations in compositions and their distributions across and aside from the contact planes. By X-ray photoelectron spectroscopy (XPS), ultra-violet photoelectron spectroscopy (UPS), Low energy electron diffraction (LEED), scanning tunneling microscopy (STM), and X-ray photoemission electron microscope (XPEEM), we can be obtain all these information using the modern analytic tools such as in-situ band alignment, band broadening, and chemical reacted interfaces. After that by experiments and incorporated with our material analysis we could determine their crystalline structure with high resolution for better accuracy and reproducibility obtained in the device design for the future industrial applications.

4. Brief on the process design

In sections above, the opto-electrical properties of the polycrystalline semiconductors are affected by structure and composition greatly.

In this section, the way of the poly-structure generation is better described through careful observation of the transfer procedures during the manufacturing process, which would be beneficial to know the deposited atoms final positions and the microstructures of the materials. The composition and the structures could be tuned based on controlling and modifying the process by adjusting the process parameters in order to obtain the desired opto-electrical properties.

We describe the better understanding of the way to generate poly-structure through careful observation of the particle transfer procedures during the manufacturing processes after knowing the final positions of the deposited atoms and the materials microstructures. On controlling and modifying the process, the composition as well structure can be tuned directly by varying the process parameters to acquire the desired opto-electrical properties.

The metallic grain structures are described by the original Thornton's zone model [21] according to the sputtering gas pressure and the substrate temperature. Since the high deposition rate, the magnetron sputtering process is most preferred for the industrial application. Also, the energy-dependent sputter yield is noted. Ellmer illustrates the inter-relationships between the process parameters (like substrate temperature and deposition rate) and the structural/optoelectrical properties in a new model [22]. However, the pressure (particles momentum) effect is not considered in this model.

4.1. Berg's model

The Berg's model is particularly utilized in the ZnO reactive sputtering. Basically, the surface coverage on the deposited film is just the composition of the film, but the composition is not easy to control since the system is unstable, where it requires the plasma diagnose sensor for feedback control. About the basic idea of the Berg's model [23, 24], the changes of the number of absorbed oxygen atoms per unit area Nx at the surfaces of the target is:

$$\frac{\mathrm{d}N_T}{\mathrm{dt}} = 2\alpha_t(1-\theta_1) - \mathrm{J/e}S_N\theta_1 \tag{6}$$

At the substrate:

$$\frac{\mathrm{d}N_S}{\mathrm{dt}} = 2\alpha_C\mathrm{F}(1-\theta_2) + \frac{J}{e}S_N\theta_1\frac{A_t}{A_C}(1-\theta_2) - \frac{J}{e}S_M(1-\theta_1)\frac{A_t}{A_C}\theta_2 \tag{7}$$

where αx is the sticking coefficients, Sx is sputtering yields, and θX is the coverage. What shown in **Figure 8** is the basic idea of Berg's model and in **Figure 9** is an example of the simulation result of the ZnO reactive sputtering system (θ_2 always <1). We also use the Berg's model to predict the composition of the compound thin-film. After that, we can also predict whether the operating point is stable. Therefore, we can investigate the time-dependent behavior of the reactive sputtering (**Figure 10**).

4.2. CISe RTP-the IEC's model

$$\mathrm{Cu_xIn_y + H_2Se\ (or\ Se)}. \tag{8}$$

After we finish the $CuInSe_2$ defect concentration calculations, we can apply the result to the model, which was developed by IEC [26] to predict the processing time under a certain process temperature.

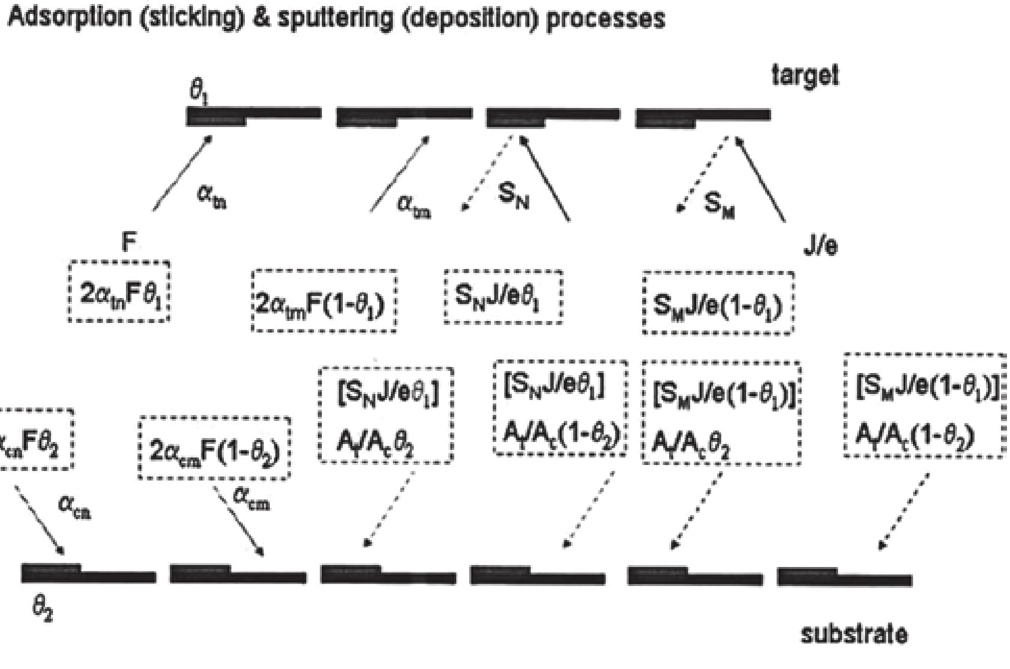

Figure 8. The basic idea of the Berg's model.

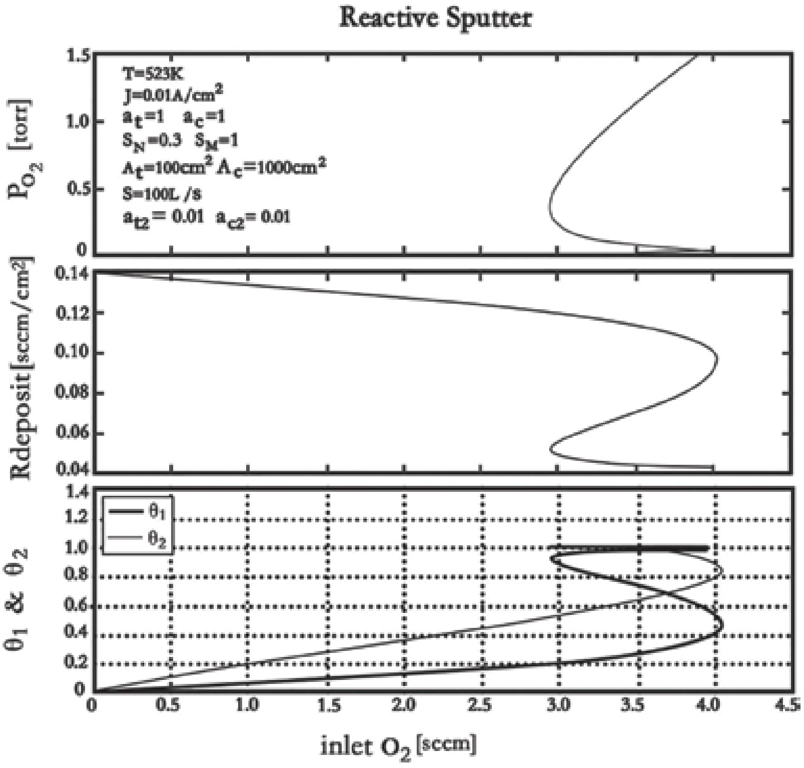

Figure 9. A simulation result of the ZnO reactive sputtering system [25].

For Cu In.

$$2In + Se \rightarrow In_2Se \; k_2 \tag{9}$$

$$In_2Se + Se \rightarrow 2InSe \; k_3 \tag{10}$$

$$2CuIn + 2Se \rightarrow Cu_2Se + In_2Se \; k_a \tag{11}$$

$$2InSe + Cu_2Se + Se \rightarrow 2CuInSe_2 \; k_7 \tag{12}$$

where $K_i = K_{io}\exp^{\left(-\frac{E_{ai}}{RT}\right)}$ and V=$\sum n_i$xN_{Avo} x$V_{unitcell}$, $n_{unitcell}$, is the film volume taken as a time-independent constant.

$n_i = [i]xV$ are the mole numbers, $n_{unitcell}$ is the number of pairs of the atoms in the unit cells. **Figure 10** shows an example of the Se or H_2Se RTP of Cu:In:Se = 0.24:0.25:0.51 CuxIny films at 450°C, μCu = 0, μIn = 0; the mole ratio of the constitute atoms (in the film) as functions of the processing time. (Film volume = (2.5 cm) 2 × 2 μm). In our non-stoichiometric case, the initial mole concentrations of Cu and in taken from our calculated data. Then, these were input to the CuxIny and in mole concentrations in order to solve the ordinary differential equation system.

Regarding building the non-stoichiometric structures, we build the XRD spectrum. The supercell values have been used to calculate the XRD spectrum of non-stoichiometric CuInSe$_2$

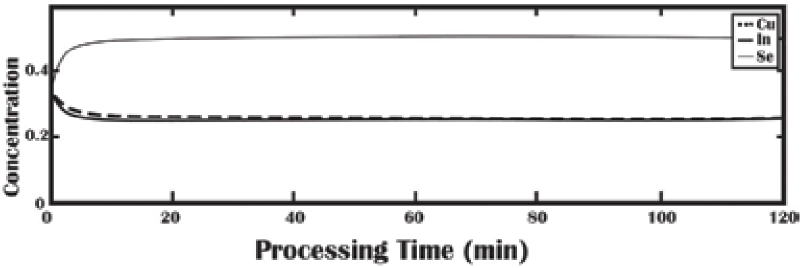

Figure 10. The Se or H_2Se RTP of Cu:In:Se = 0.24:0.25:0.51 CuxIny films at 450°C, μCu = 0, μIn = 0; the mole ratio of the constitute atoms (in the film) as functions of the processing time (120 min). (Film volume = (2.5 cm) 2 × 2 μm).

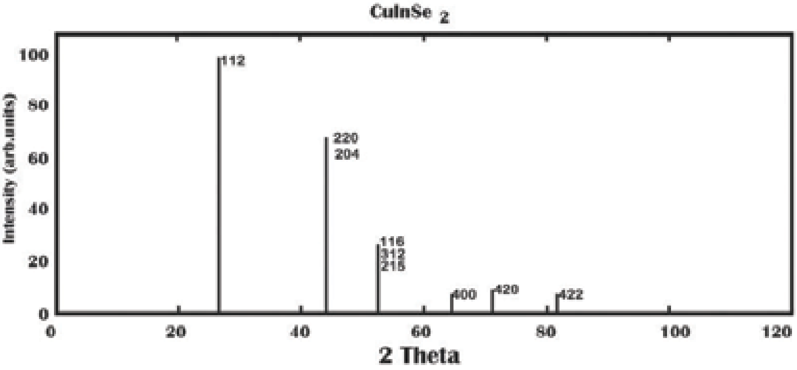

Figure 11. Simulated XRD spectra of non-stoichiometric CuInSe2; Cu:In:Se2 = 0.21:0.26:0.53.

and $CuGaSe_2$. In our work, the method described by Attia et al. [27] has been incorporated and only modify the structural factor by summing over all the atoms in the supercell. The defect site in each defect cells has been chosen randomly. We observed the presence of extra small peaks in the XRD spectrum, as shown in **Figure 11** [14].

Anomalous neutron diffraction scattering of synchrotron X-ray radiations gives more accurate data of composition distributions [28]. However, in-situ XRD is the most convenient tool for monitoring the deviations from the stoichiometric compositions. An incapability gap is indicated by the substantial increase in full width at half maximum (FWHM), in which the lattice constants depends on Ga/III and follow the Vegrad's law [29–31]. For industrial use for future process monitoring and control, more work should be done to make it more feasible to be used.

5. Some means to improve film composition control

When CIGS or other thin-films were fabricated, there will be chemical fluctuation-induced nano-domains. We developed a novel metal-organic sputtering (MO-sputtering) technique in our work, in which metal organic compound such as trimethygallium (TMGa) as the reactant was used during the reactive sputtering procedure. In **Figure 12**, the Ga/(Ga + In) ratio changes

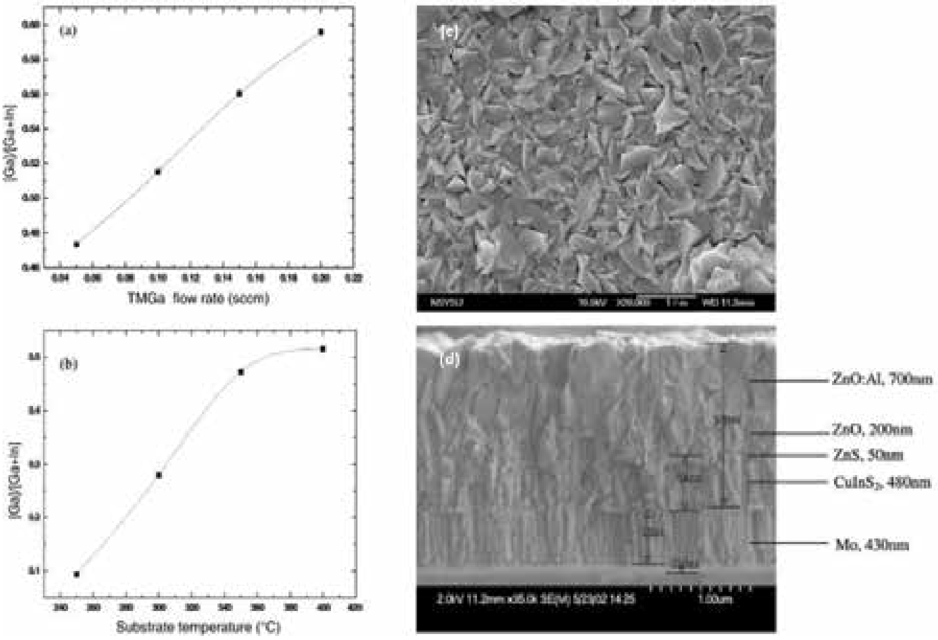

Figure 12. Preliminary result on the metal organic sputtering of CIGS PV. (a) Ga content as a function of TMGa flow rate, (b) the content of Ga as a function of substrate temperature, (c) plain view SEM image of the deposited CIGS film, and (d) cross-section.

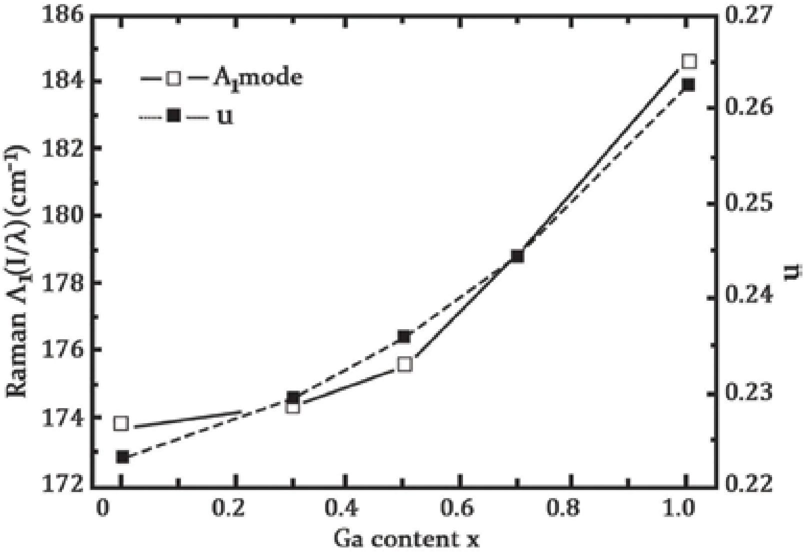

Figure 13. Room temperature Raman shift in CuIn$_1$–xGaxSe$_2$ thin-films of thickness 600 nm deposited on a glass substrate with a change in Ga content, the Raman peak shifted from 173.8 to 184.6 cm^{-1} in A1 mode and u is Se shift parameter. Reproduced with permission.

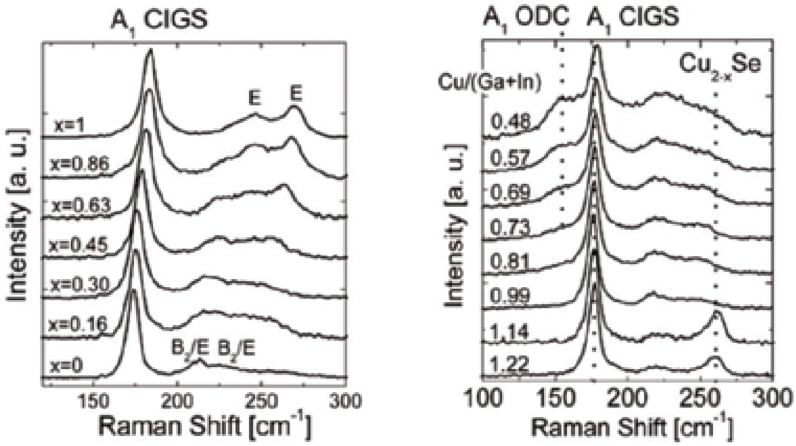

Figure 14. Micro-Raman spectroscopy results on the composition of thin-films.

as a function of TMGa flow rate and substrate temperature [1]. And the linear relationship of Ga/(Ga + In) with the TMGa flow rate to adjust the deposited film composition is particularly interesting. I could conclude from in **Figure 12** that the Raman shift as a function of the film composition change of Cu/(Ga + In) from the micro-Raman spectroscopy. It is clear that the micro-Raman shift is sensitive to the composition change of the CIGS thin-films. If we combine the use of Mo-Sputtering for the film growth and its feedback monitoring with the Raman shift, a means to better control the stoichiometry of thin-film might be provided during the manufacturing steps (**Figures 13** and **14**).

6. The stability of CIGS on an industrial scales

Degradation of modules at the moment, the highest conversion efficiency η of CIGS was 22.3% (Solar Frontier 2015) [32–38]. The three main parameters determining the cost competitiveness of electricity from PV panel is shown in **Figure 15**. The degradation rate per year is obtained by:

$$\text{Degradation}\ (\%) = \left(\frac{\eta_{\text{initial}} - \eta_{\text{final}}}{\eta_{\text{initial}} \times \text{Time}}\right) \times 100\%. \tag{13}$$

The time is given in year. **Table 3** shows the recently tested modules vary from very stable (No degradation after 7 years) to vulnerable to outdoor exposure.

Degradation depends on many parameters such as module production technologies, module type, production year, the orientation of the panel, climate, and installation location, as well as installation parameters like system voltage.

Generally, the investigation of degradation process in CIGS solar cells and modules is the complex and definite identification of failure mechanisms can be complicated.

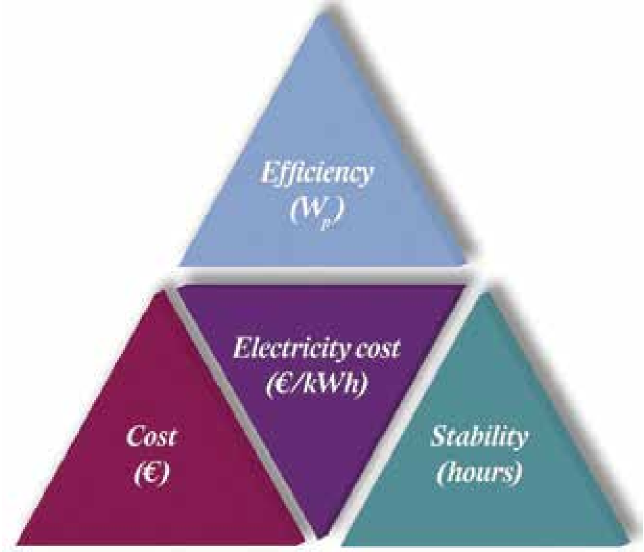

Figure 15. The three main parameters determining the cost competiveness of electricity from PV panels.

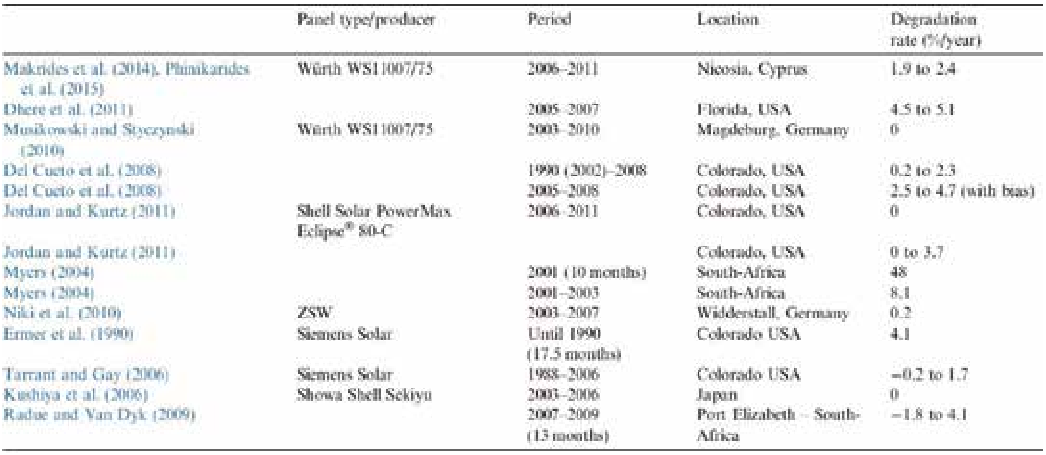

	Panel type/producer	Period	Location	Degradation rate (%/year)
Makrides et al. (2014), Phinikarides et al. (2015)	Würth WS11007/75	2006–2011	Nicosia, Cyprus	1.9 to 2.4
Dhere et al. (2011)		2005–2007	Florida, USA	4.5 to 5.1
Musikowski and Styczynski (2010)	Würth WS11007/75	2003–2010	Magdeburg, Germany	0
Del Cueto et al. (2008)		1990 (2002)–2008	Colorado, USA	0.2 to 2.3
Del Cueto et al. (2008)		2005–2008	Colorado, USA	2.5 to 4.7 (with bias)
Jordan and Kurtz (2011)	Shell Solar PowerMax Eclipse® 80-C	2006–2011	Colorado, USA	0
Jordan and Kurtz (2011)			Colorado, USA	0 to 3.7
Myers (2004)		2001 (10 months)	South-Africa	48
Myers (2004)		2001–2003	South-Africa	8.1
Niki et al. (2010)	ZSW	2003–2007	Widderstall, Germany	0.2
Ermer et al. (1990)	Siemens Solar	Until 1990 (17.5 months)	Colorado USA	4.1
Tarrant and Gay (2006)	Siemens Solar	1988–2006	Colorado USA	−0.2 to 1.7
Kushiya et al. (2006)	Showa Shell Sekiyu	2003–2006	Japan	0
Radue and Van Dyk (2009)		2007–2009 (13 months)	Port Elizabeth – South-Africa	−1.8 to 4.1

Table 3. Literature overview of degradation rates (%/year) of CIGS modules obtained from field tests at different locations.

Table 4 shows an overview of failure modules loading to CIGS module degradation and global categorization, when they are specific to CIGS or also observed for other thin-film modules. It was concluded that CIGS solar cells and modules are very sensitive to humidity. Furthermore, sensitivity to, for example, temperature (shocks), electrical bias, and illumination has been found, but the impacts of these loads are not necessarily detrimental.

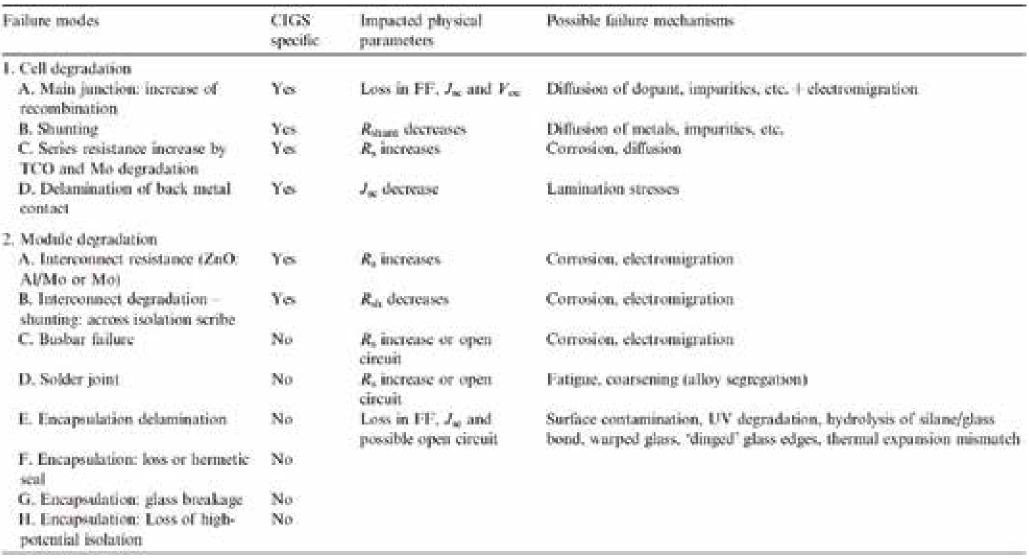

Failure modes	CIGS specific	Impacted physical parameters	Possible failure mechanisms
1. Cell degradation			
A. Main junction: increase of recombination	Yes	Loss in FF, J_{sc} and V_{oc}	Diffusion of dopant, impurities, etc. + electromigration
B. Shunting	Yes	R_{shunt} decreases	Diffusion of metals, impurities, etc.
C. Series resistance increase by TCO and Mo degradation	Yes	R_s increases	Corrosion, diffusion
D. Delamination of back metal contact	Yes	J_{sc} decrease	Lamination stresses
2. Module degradation			
A. Interconnect resistance (ZnO: Al/Mo or Mo)	Yes	R_s increases	Corrosion, electromigration
B. Interconnect degradation – shunting: across isolation scribe	Yes	R_{sh} decreases	Corrosion, electromigration
C. Busbar failure	No	R_s increase or open circuit	Corrosion, electromigration
D. Solder joint	No	R_s increase or open circuit	Fatigue, coarsening (alloy segregation)
E. Encapsulation delamination	No	Loss in FF, J_{sc} and possible open circuit	Surface contamination, UV degradation, hydrolysis of silane/glass bond, warped glass, 'dinged' glass edges, thermal expansion mismatch
F. Encapsulation: loss or hermetic seal	No		
G. Encapsulation: glass breakage	No		
H. Encapsulation: Loss of high-potential isolation	No		

Table 4. Summary of failure as observed for CIGS.

7. Progress in thin-film solar cells (TFSCs) based on Cu_2ZnSnS_4 (CZTS)

CZTS is a material, which has been found in nature. **Figure 16** shows the content and the world trading price of the elements used in light absorbers CdTe, Cu_2ZnSnS_4, and $CuInSe_2$ for thin film solar cells [25, 39–49]. It shares similar structure which the chalcopyrite materials CuInS expect that half of the in is replaced with Zn and Sn. Crystallographically speaking, CZTS has two principal structures known as stannite-type and keasterit-type. The two structures are similar expect the different arrangement of Cu and Zn atoms. However, CZTS materials usually appear in keasterit phase because it is more stable.

Thermal dynamically compared to the stannite-type. The evolution of the power conversion efficiency of CZTS based solar cells is summarized in **Figure 17**.

The recorded power conversion efficiency of CZTSSe solar cells (12.6% reported in 2013) remains significantly than that of CIGSe (22.6%).

In order to improve the efficiency of CZTS based TFSCs, a deep research of CZTS based TFSCs and the fundamental properties of CZTS, particularly the nature of defects as well as their influence on the performance of CZTS materials is crucial. CZTS TFSCs, which have produced good efficiency normally, show Cu-poor/Zn-rich in composition. Therefore, secondly, phase should exist in the light absorber. It is necessary to identify those second phases and their defects in order to optimize the fabrication process to make CZTS thin-films with desired properties.

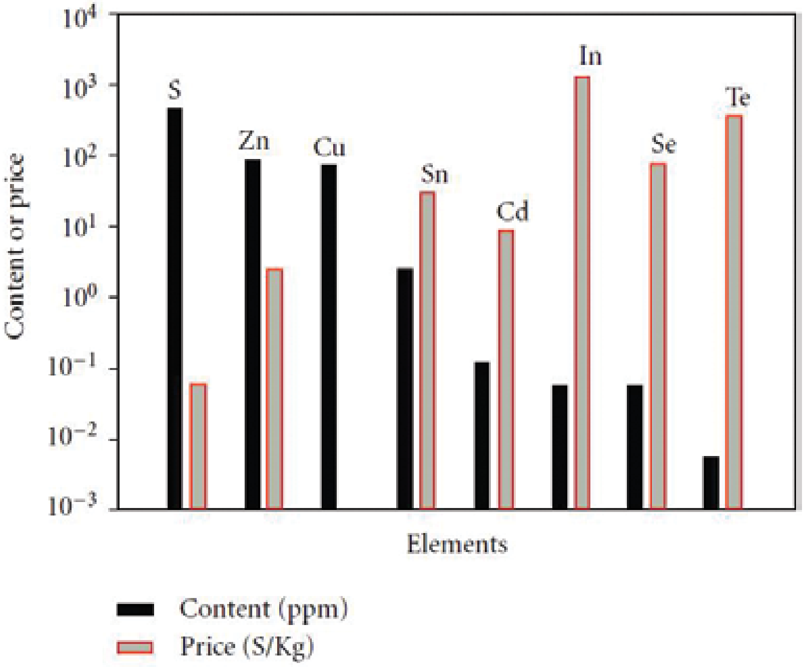

Figure 16. Content and the world trading price of the elements used in light absorbers CdTe, Cu_2ZnSnS_4, and $CuInSe_2$ for thin film solar cells.

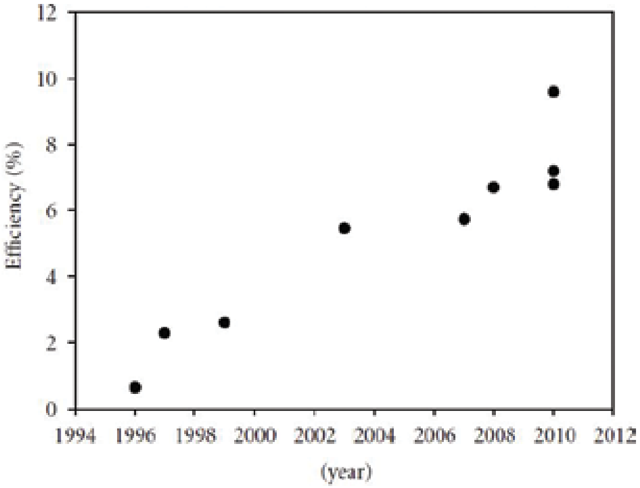

Figure 17. Evolution of the conversion efficiency of thin film solar cells using CZTS as light absorber layer.

8. Future aspects

Moreover, research institute NREL, USA and Fraunhofer ISE, Germany periodically publish the status reports on different stages of CIGS developments [49–52]. These reports greatly promote technology developments and industrialization of thin-film CIGS produces. Although, many challenges still lie ahead including optimization and control on the CIGS absorber film stoichiometry, interface, and film uniformity over large areas for the power module fabrication.

At presents, of monocrystalline and multicrystalline Si PV production, are dominant in the PV market, but the importance of TFSC will steadily rise in the coming decade. After that, in recent years the CIGS already win its own counterparts such as CdTe and a-Si (**Figure 18**) [53].

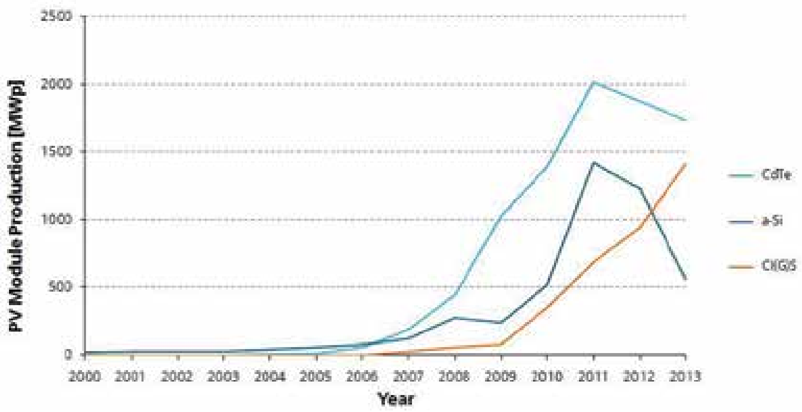

Figure 18. Thin-film technologies worldwide annual PV module production inMWp.

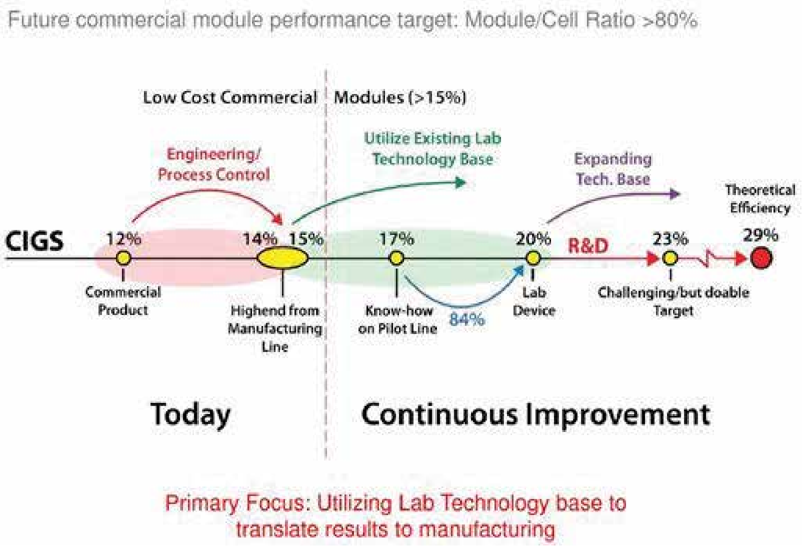

Figure 19. Closing the gap between laboratory cells and modules.

From the early report from NREL [54], it is greatly needed to develop continuous technologies to close the gap between laboratory cells and modules. And this is the purpose to develop science and technology to indicate the possibility to realize optimization and precise control of non-stoichiometric Cu-III-VI_2 compound in the future manufacturing (**Figure 19**).

9. Conclusions

In this chapter, we introduced the material designs on chemical compositions and compared some of the most important academic solar cell simulators. However, these simulators cannot load many files one by one and inevitably one analytic simulator favored especially for the non-stoichiometric PV materials, based on defect concentration of the CIGS alloy. This is the first phase to develop the comprehensive intelligent design (materials/devices/process). For industrial applications, much more refined detail work must be undertaken to further fulfill the need of PV cells for non-stoichiometric materials in a large area. For improving the process flow and performance of CIGS photovoltaic a fundamental improvement on the manufacturing technology and use of the concept of intelligent design are necessary. As CIGS PV technology matures to production on an industrial scale, the long-term stability becomes more important, which affects the cost the competitiveness of PV electricity and both the degradation rate of CIGS modules from a field test and their failure modes are listed. Moreover, the progress of thin film solar cells based on CZTS (Cu_2ZnSnS_4) is briefed, which shows future direction of material development of CIGS.

Acknowledgements

We gratefully acknowledge the financial support from ministry of science and technology of ROC.

Author details

Yijian Liu[1,2], Huey-Liang Hwang[1,2], Ying Wang[2]*, Jun Zhang[3] and Lexi Shao[3]

*Address all correspondence to: yingwang@sjtu.edu.cn

1 National Tsing Hua University, Hsinchu, Taiwan ROC

2 Shanghai Jiao Tong University, Shanghai, China

3 Lingnan Normal University, Zhanjiang, China

References

[1] Chang HH, Ueng HY, Hwang HL. Preliminary steps toward industrialization of Cu-III-VI_2 thin-film solar cells: development of an intelligent design tool for non-stoichiometric PV materials. Journal of Physics & Chemistry of Solids. 2003;**64**(9):2047-2053

[2] Jackson P, Hariskos D, Lotter E, et al. New world record efficiency for Cu(In,Ga)Se_2 thin-film solar cells beyond 20%. Progress in Photovoltaics Research & Applications. 2011; **19**(7):894-897

[3] Candelise C, Speirs JF, Gross RJK. Materials availability for thin film (TF) PV technologies development: A real concern? Renewable & Sustainable Energy Reviews. 2011;**15**(9):4972-4981

[4] Dhere NG. Scale-up issues of CIGS thin film PV modules. Solar Energy Materials & Solar Cells. 2011;**95**(1):277-280

[5] Panthani MG, Akhavan V, Goodfellow B. Synthesis of $CuInS_2$, $CuInSe_2$, and $Cu(In_xGa_{1-x})Se_2$ (CIGS) Nanocrystal "Inks" for printable photovoltaics. Journal of the American Chemical Society. 2008;**130**(49):16770

[6] Guo Q, Ford GM, Yang WC, et al. Fabrication of 7.2% efficient CZTSSe solar cells using CZTS nanocrystals. Journal of the American Chemical Society. 2010;**132**(49):17384-17386

[7] Todorov TK, Gunawan O, Gokmen T, et al. Solution-processed Cu(In,Ga)$(S,Se)_2$, absorber yielding a 15.2% efficient solar cell. Progress in Photovoltaics Research & Applications. 2013;**21**(1):82-87

[8] Chung CH, Song TB, Bob B, et al. Silver nanowire composite window layers for fully solution-deposited thin-film photovoltaic devices. Advanced Materials. 2012;**24**(40):5499-5504

[9] Akhavan VA, Goodfellow BW, Panthani MG, et al. Colloidal CIGS and CZTS nanocrystals: A precursor route to printed photovoltaics. Journal of Solid State Chemistry. 2012;**189**(24):2-12

[10] Hwang HL, Tseng BH, Jagadhamma LA, et al. Steps towards removing some obstacles of industrialization of CIGS solar cells. Physica Status Solidi. 2013;**10**(7–8):1046-1049

[11] Yan Y, Noufi R, Jones KM, et al. Chemical fluctuation-induced nanodomains in cu(in,Ga)Se_2 films[J]. Applied Physics Letters. 2005;**87**(12):225

[12] Chang HH, Ueng HY, Hwang HL. Preliminary steps toward industrialization of Cu-III-VI_2 thin-film solar cells: Development of an intelligent design tool for non-stoichiometric photovoltaic materials. Journal of Physics & Chemistry of Solids. 2003;**64**(9):2047-2053

[13] Chang HH, Ueng HY, Zhong TX. New perspectives of defect physics and defect chemistry for copper ternary chalcopyrite semiconductors. Japanese Journal of Applied Physics. 2000;**39**(S1):399

[14] Wei SH, Zunger A. Calculated natural band offsets of all II–VI and III–V semiconductors: Chemical trends and the role of cation d orbitals. Applied Physics Letters. 1998;**72**(16):2011-2013

[15] Burgelman M, Nollet P, Degrave S. Modelling polycrystalline semiconductor solar cells. Thin Solid Films. 2000;**361**(99):527-532

[16] Ashida N, Murata M, Hironiwa D, et al. Numerical analysis of Cu(In,Ga)Se_2 solar cells with high defect density layer at back side of absorber. Physica Status Solidi. 2015;**12**(6):638-642

[17] Wada T, Maeda T. Characteristics of chemical bonds in $CuInSe_2$, and its thin film fabrication processes used to fabricate solar cells (<Special Issue> Crystals Science and Technology of Solar Cells Materials -Concentrated on Crystal Growth-). 2009;**36**(4):282-289

[18] Zhang SB, Wei SH, Zunger A, et al. Defect physics of the $CuInSe_2$, chalcopyrite semiconductor. Physical Review B, Condensed Matter. 1998;**57**(16):9642-9656

[19] Yamada T. Lecture Notes on SIMS Data Presented at 19th International Conference on Ternary and Multinary Compounds; Niigata; September 2014

[20] Pettenkofer C. Energy Converting Interfaces Studied by Synchrotron Radiation. Berlin: Helmholtz-Zentrum. (pettenkofer@helmholtz-berlin.de)

[21] Thornton JA. The microstructure of sputter-deposited coatings molecular dynamics modeling of microstructure and stresses in sputter-deposited thin films. Journal of Vacuum Science & Technology. 1986;**A4**:3059

[22] Ellmer K. Magnetron sputtering of transparent conductive zinc oxide: relation between the sputtering parameters and the electronic properties. Journal of Physics D: Applied Physics. 2000;**33**(4):R17-R32(16)

[23] Berg S, Blom H, Larsson T, et al. Modeling of reactive sputtering of compound materials. Journal of Vacuum Science & Technology A Vacuum Surfaces & Films. 2015;**5**(2):202-207

[24] Berg S, Nyberg T, Blom H-O, Nender C. In: Glocker DA, Shah SI, editors. Handbook of Thin Film Process Technology. Bristol, UK: IOP Publishing; 1995

[25] Ito K, Nakazawa T. Electrical and optical properties of stannite-type quaternary semiconductor thin films. Japanese Journal of Applied Physics. 1988;**27**(11):2094-2097

[26] Orbey N, Norsworthy G, Birkmire RW, et al. Reaction analysis of the formation of $CuInSe_2$, films in a physical vapor deposition reactor. Progress in Photovoltaics Research & Applications. 1998;**6**(2):79-86

[27] Attia AA, Lachab M, Harsono S, et al. Crystal structure and composition of polycrystalline $CuInSe_2$[J]. Renewable Energy. 1995;**6**(5-6):559-565

[28] Schorr S. The crystal structure of kesterite type compounds: A neutron and X-ray diffraction study. Solar Energy Materials & Solar Cells. 2011;**95**(6):1482-1488

[29] Stephan C, Schorr S, Tovar M, et al. Comprehensive insights into point defect and defect cluster formation in $CuInSe_2$. Applied Physics Letters. 2011;**98**(9):668

[30] Schnohr CS, Kämmer H, Stephan C, et al. Atomic-scale structure and band-gap bowing in $Cu(In,Ga)Se_2$. Physical Review B. 2012;**103**(8):894-R1713

[31] Schorr S, Gurieva G. ICTMC-19; Niigata, Abstract Thu-I-2A; 2014

[32] Theelen M, Foster C, Barreau N, Steijvers H, Vroon Z, Zeman M. Influence of atmospheric species water, oxygen, nitrogen and carbon dioxide on the degradation of CIGS solar cells. Solar Energy Materials & Solar Cells. 2015;**141**:49-56

[33] Theelen M, Harel S, Verschuren M, et al. Influence of Mo/MoSe$_2$, microstructure on the damp heat stability of the Cu(In,Ga)Se$_2$, back contact molybdenum[J]. Thin Solid Films. 2016;**612**:381-392

[34] Thompson C, Hegedus S, Carcia P, Scott McLean R. The effects of device geometry and TCO/buffer layers on damp heat accelerated lifetime testing of Cu(In,Ga)Se$_2$ solar cells. IEEE Journal of Photovoltaics. 2013;**3**(1):494-499

[35] Walter T, Herberholz R, Muller C, Schock H. Determination of defect distributions from admittance measurements and application to CIGS-based heterojunctions. Journal of Applied Physics. 1996;**80**(8):4411-4420

[36] Wennerberg J, Kessler J, Stolt L. Design of grided Cu(In,Ga)Se2 thin-film PV modules. Solar Energy Materials & Solar Cells. 2001;**67**:59-65

[37] Wennerberg J. Design and stability of Cu(In, Ga)Se2-based solar cell modules. Acta Universitatis Upsaliensis. Comprehensive Summaries of Uppsala Dissertations from the Faculty of Science and Technology. Uppsala. 2002;**683**:91

[38] Wennerberg J, Kessler J, Stolt L. Cu(In,Ga)Se$_2$-based thin-film photovoltaic modules optimized for long-term performance. Solar Energy Materials & Solar Cells. 2003;**75**:47-55

[39] Olekseyuk ID, Dudchak IV, Piskach LV. Phase equilibria in the Cu$_2$S-ZnS-SnS$_2$ system. Journal of Alloys and Compounds. 2004;**368**:135-143

[40] Friedlmeier TM, Wieser N, Walter T, Dittrich H, Schock HW. Heterojuncitons based on Cu2ZnSnS4 and Cu2ZnSnSe4 thin films. In: Proceedings of the 14th European Conference of Photovoltaic Science and Engineering and Exhibition; Bedford; 1997. p. 1242

[41] Katagiri H, Saitoh K, Washio T, et al. Development of thin film solar cell based on Cu$_2$ZnSnS$_4$, thin films. Solar Energy Materials & Solar Cells. 2001;**65**(1):141-148

[42] Jafarov MA. Cu$_2$ZnSnS$_4$ thin film solar cells. Thin Solid Films. 2005;**480–481**(3):426-432

[43] Katagiri H, Jimbo K, Maw WS, et al. Development of CZTS-based thin film solar cells. Thin Solid Films. 2009;**517**(7):2455-2460

[44] Seol JS, Lee SY, Lee JC. Electrical and optical properties of Cu$_2$ZnSnS$_4$ thin films prepared by rf magnetron sputtering process. Solar Energy Materials & Solar Cells. 2003;**75**(1):155-162

[45] Liu F, Zhang K, Lai Y, et al. Growth and characterization of Cu$_2$ZnSnS$_4$ thin films by DC reactive magnetron sputtering for photovoltaic applications. Combustion & Flame. 2010; **13**(11):161-170

[46] Friedlmeier TM, Dittrich H, Schock HW. Growth and characterization of Cu$_2$ZnSnS$_4$ and Cu$_2$ZnSnSe$_4$ thin films for photovoltaic applications. Ternary and Multinary Compounds. 1998;**152**:345-348

[47] Kamoun N, Bouzouita H, Rezig B. Fabrication and characterization of Cu$_2$ZnSnS$_4$ thin films deposited by spray pyrolysis technique. Thin Solid Films. 2007;**515**:5949-5952

[48] Chen SY, Yang JH, Gong XG, Walsh A, Wei SH. Intrinsic point defects and complexes in the quaternary kesterite semiconductor Cu_2ZnSnS_4. Physical Review B. 2010;**81**:24

[49] Hamri EE, Meddah M, Boulkadat L, Elfanaoui A, Bouabid K, Nya M, Portier X, Ihlal A. Studies of non-vacuum processing of Cu-Chalcogenide thin films. Journal of Nanoscience and Nanotechnology. 2012;**12**(8):6800-6803

[50] Delahay AE, Bruns J, Rupper A, Akhtor M, Chen L, Kiss ZJ. Thin Film CIGS Photovoltaic Technology. Annual Technical Report Phase II 16 April 1999-15 April 2000

[51] Noufi R. High Efficiency CdTe and CIGS Thin Film Solar Cells! Highlights of the Technologies Challenges, presented at the 2006 IEEE 4th World Conference on Photovoltaic Energy Conversion (WCPEC-4); May 7-12, 2006; Waikyloa

[52] Ullal HS. Polycrystalline Thin-Film Solar Cell Technologies, presented at the 18th International Photovoltaic Science and Engineering Conference and Exhibition; January 19-23; Kolkata; 2009

[53] Fraunhoffer Institute for Solar Energy Systems ISE Photovoltaic Report. Freiburg 24 October 2014

[54] Noufi R. CIGS PV Technology: Challenges, Opportunities and Potential, NCPV, NREL, US; February, 2013

Plasmonic Resonances and Their Application to Thin-Film Solar Cell

Nilesh Kumar Pathak, Pandian Senthil Kumar and
Rampal Sharma

Additional information is available at the end of the chapter

http://dx.doi.org/10.5772/intechopen.75015

Abstract

This chapter furnishes the plasmonic properties of metal nanostructure and its application to thin-film solar cell. Plasmonics is an emerging branch of nanooptics where light metal interaction in subwavelength domain is studied. Metal supports surface plasmon resonance that has tunable signature, which depends on the morphology as well as surrounding media. These plasmonic resonances can be tuned in a broader range of solar spectra by changing several parameters such as size, shape and medium. Moreover, metals show scattering properties that could be utilized to enhance optical path length of photon inside the thin film of solar device. The chapter mainly focusses on the study of plasmonic resonance of smaller- and larger-sized metal nanoparticle using semi-analytical as well as numerical approach. For the estimation of optical properties like extinction spectrum and field profile of larger-sized nanoparticle, finite-difference time-domain (FDTD) method is used. The field distribution in both silver and gold nanoparticle cases has been plotted in 'on' resonance condition, which has a broader range of applications.

Keywords: plasmonics, metal nanoparticle, surface plasmon resonance, extinction cross section, thin film

1. Introduction

Plasmonics is an emerging branch wherein the interaction of electromagnetic waves to the conduction electron of metal nanoparticles is studied. Plasmonic properties of metal nanoparticles have generated a great interest among the material researchers in the recent years and have attracted them to understand the physics behind it for applying the same in various fields. The optical properties of metal nanoparticles are highly dependent on its morphology and the surrounding medium [1–4]. These optical properties include scattering, absorption and extinction cross section which are obtained by solving the Maxwell's equation after the interaction of light with the nanogeometries. The optical cross sections are generally greater than the geometrical cross section. When the light interacts with the metals, two fundamental excitations are observed. These excitations are either propagating known as surface plasmon polaritons (SPP) or non-propagating known as surface plasmon resonance (SPR). These fundamental excitations have a wide range of applications. The candidates used as plasmonic elements are metals and few semiconductors, and they have their own optical features in different regimes of electromagnetic spectrum. These metals exhibit surface plasmon resonance (SPR) properties on interaction with the incident field. The SPR depends on several parameters such as size and shape of metal and choice of the surrounding media. The influence of surrounding media on the SPR peak positions has a great interest in material research society. One can tune these SPR peak positions by choosing different surrounding media. The tunable behaviors of SPR with size shape and surrounding environments would cover a wide range of applications such as biosensor, Raman spectroscopic, waveguide and thin-film photovoltaic device [5–7].

The occurrence of the SPR resonances is due to the interaction of incident light frequency and its match with the frequency of collective oscillation of electrons inside the metal. Under such matching condition, a giant electric field is observed near the metal nanosurface, which could be used for various applications. The physics of SPR could be utilized in different fields of science and technology wherein the light metal interaction is taken into account. It could be utilized in biosensor field, thin-film plasmonic photovoltaic devices, surface-enhanced Raman scattering field and communication field also [6, 7].

The work furnishes the plasmonic properties isolated in metal nanosphere and its interaction to the silica environment. This work explores the optical properties of isolated spherical-shaped medium and small-sized metal nanoparticle. The analysis of small-sized nanoparticle has been done using dipolar model, but the restriction with this model is that it can be applied for larger-sized nanoparticle. Therefore, we have to use numerical technique in full-wave analysis that needs to be taken into account. The purpose of selecting the silica environment is due to its frequent use in the photovoltaic devices. Silica is used as a spacer layer in thin-film device fabrication, and it is also used as a core or coating material whose thickness plays an important role to tune the plasmonic resonance. Therefore, the aim of this work is to present systematic review of medium- and small-sized metal nanoparticle under the influence of silica environment.

2. Optical properties of metal nanoparticles

The optical properties of metal nanosphere embedded in semiconductor environment have been discussed under the quasi-static approximation, where we have assumed that the size of metal nanosphere is much smaller than the wavelength of incident light. In this approximation, we have taken metal nanosphere which is embedded in a semiconductor medium having constant electric field. The Laplace equation $\nabla^2\Phi = 0$ with appropriate boundary condition was solved for finding out the potential, electric field, scattering and absorption and extinction cross section [8]. The schematics of modeled structure is shown in **Figure 1**, wherein the incident field interacts with the nanosphere of radius a and dielectric $\varepsilon(\omega)$ constant embedded in surrounding environment having dielectric constant ε_m.

The potential inside and outside the sphere that are obtained after solving the Laplace equation under appropriate boundary conditions are expressed as

$$\Phi_{in} = -\frac{3\,\varepsilon_m}{\varepsilon + 2\,\varepsilon_m} E_0\, r\cos\theta \text{ and} \tag{1}$$

$$\Phi_{out} = -E_o\, r\cos\theta + \frac{r\cos\theta}{r^3} a^3 E_0\left(\frac{\varepsilon - \varepsilon_m}{\varepsilon + 2\,\varepsilon_m}\right) \tag{2}$$

After solving the potential profile, one can easily obtain the electric field expression as

$$E = -\nabla\Phi \tag{3}$$

The polarization of metal sphere under the influence of constant electric field is expressed as

$$P = 4\,\pi\varepsilon_o\,\varepsilon_m a^3 E_0\left(\frac{\varepsilon - \varepsilon_m}{\varepsilon + 2\,\varepsilon_m}\right) \tag{4}$$

and polarizability of nanosphere is

$$\alpha = 4\pi a^3\left(\frac{\varepsilon - \varepsilon_m}{\varepsilon + 2\,\varepsilon_m}\right) \tag{5}$$

where $\varepsilon, \varepsilon_m$ are the dielectric constant of sphere and medium, a is the radius of sphere and α, is the dipolar polarizability.

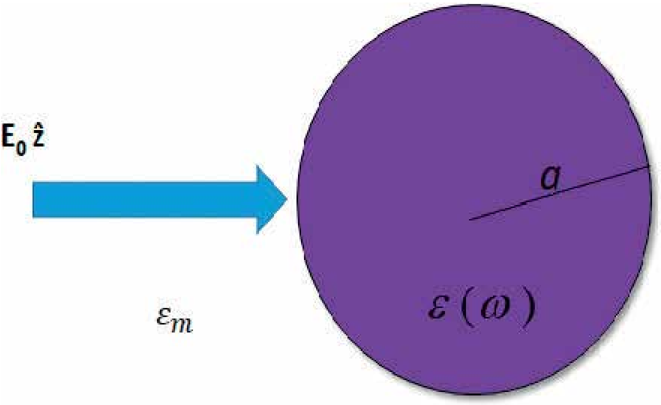

Figure 1. Optical properties of metal nanosphere placed in a uniform static electric field E_0.

The optical properties are expressed in terms of optical cross sections such as scattering and absorption, and it can be calculated by deriving the Poynting vector from the reference [8]:

$$\langle C_{scat} \rangle = \frac{k^4}{6\pi} |\alpha|^2 = \frac{8\pi}{3} k^4 a^6 \left| \frac{\varepsilon - \varepsilon_m}{\varepsilon + 2\varepsilon_m} \right|^2 \tag{6}$$

$$\langle C_{abs} \rangle = k \operatorname{Im}\{\alpha\} = 4\pi k a^3 \operatorname{Im}\left[\frac{\varepsilon - \varepsilon_m}{\varepsilon + 2\varepsilon_m} \right] \tag{7}$$

The sum of these two cross sections will give rise to the extinction cross section:

$$C_{ext} = C_{scat} + C_{abs} \tag{8}$$

If the cross sections are normalized by their geometrical cross section, then it is called by a new name known as Q-extinction. For spherical geometry, geometrical cross section is πa^2; therefore, Q-extinction for sphere is

$$Q_{extn} = \frac{C_{ext}}{\pi a^2} \tag{9}$$

There are several parameters involved in the study of optical signature of plasmonic geometry. Out of these parameters, optical constant of metal is one of most important parameters. Therefore, we have given a special attention to the same. This optical constant has a dual character: one at the bulk level and the other at the nanolevel. The nanolevel character comes via the size of the geometry, which has been derived from Drude-Lorentz model, which can be expressed as [8, 9]

$$\begin{aligned} \varepsilon(\omega) &= \varepsilon_{bulk}(\omega) + \frac{\omega_p^2}{\omega^2 + j\gamma_{bulk}\omega} - \frac{\omega_p^2}{\omega^2 - j\gamma\omega} \\ \gamma &= \gamma_{bulk} + A\frac{v_f}{a} \end{aligned} \tag{10}$$

where ω_p is the bulk plasmon frequency, ω is the frequency of incident light photon and $\tau_{bulk} = 1/\gamma_{bulk}$ is the damping constant of bulk silver metal. Where γ is the effective relaxation time, $v_f = 1.39 \times 10^6$ m/s is the Fermi velocity of electron in silver, A is geometrical parameter and its value lies between 2 to 1 (in our case we have chosen A = 1) [10] and a is the radius nanoparticle. Using the optical constant of metal at the nanolevel, extinction spectrum is studied.

3. Extinction cross section of silver and gold nanosphere: semi-analytical approach

The optical property of silver and gold nanosphere has been discussed in terms of extinction efficiency which is the ratio of extinction cross section to geometrical cross section. Wavelength-dependent extinction efficiency of silver and gold nanosphere for three different radii ranging from 5 to 7 nm has been plotted as shown in **Figure 2**. It can be observed from the spectrum that the choice of two different metals would cover two different parts of electromagnetic spectrum. For silver, SPR resonance was observed at wavelength 410 nm, while for gold, it was around 560 nm. The magnitude of extinction is a function of nanosphere radii, while its SPR peak positions are almost independent of the chosen radii. The nanoplasmonic coupling to the silica (N = 1.54) has been studied in terms of extinction efficiency and SPR resonances. The two different metals exhibit their SPR resonances in two different regimes of solar spectrum due to different optical constant and Frohlich conditions.

The simulated extinction spectra as shown in the above figures of silver and gold nanosphere clearly give the idea of extinction magnitude and SPR wavelength which can be used to compute the electric field distribution near the surface of metal nanosphere. **Figure 3**a shows the electric field profile of silver nanosphere embedded in silica environment at SPR wavelength 410 nm. The legend in the figure shows the normalized field (E/E_0) magnitude in y-z plane. The computation of electric field has been done by using COMSOL Multiphysics software with triangular fine grid. The red region shows the high-intensity zone which can be utilized for various applications [11–15].

Further, we have also done the analysis to visualize the electric field distribution of gold nanosphere of radius 50 nm embedded in silica medium as shown in **Figure 3**b. The near field has been computed at SPR wavelength 560 nm. From the field distribution, it was observed that the magnitude of field is different for silver and gold due to different SPR wavelengths. These different magnitudes of fields can be used to increase the electron hole or exciton generation rate inside the thin film of solar device.

The above semi-analytical model has certain restrictions that it is valid only for the smaller-sized metal nanoparticle. Therefore, for the analysis of optical properties of larger-sized metal nanoparticle, we required some numerical approach like discrete dipole approximation (DDA), finite-difference time-domain (FDTD), finite element method (FEM) and surface integral equation (SIE). In this chapter, we have used the FDTD technique to simulate the optical properties

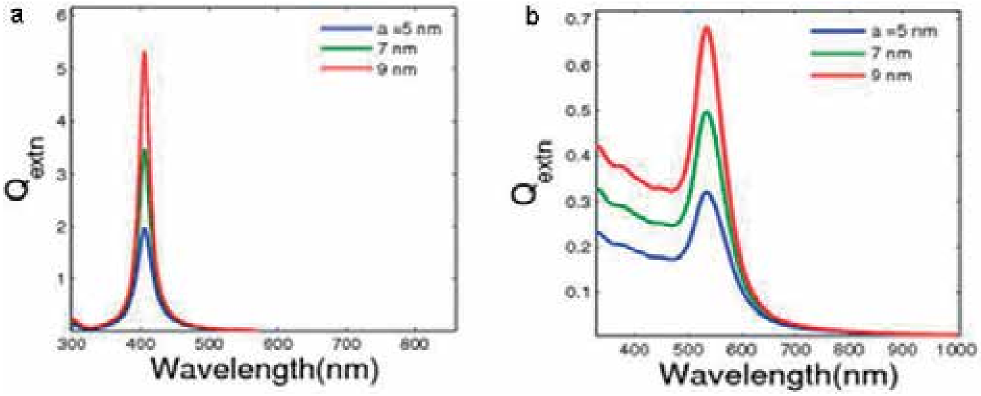

Figure 2. Wavelength-dependent extinction spectra of (a) silver and (b) gold metal nanosphere embedded in medium having refractive index N = 1.54.

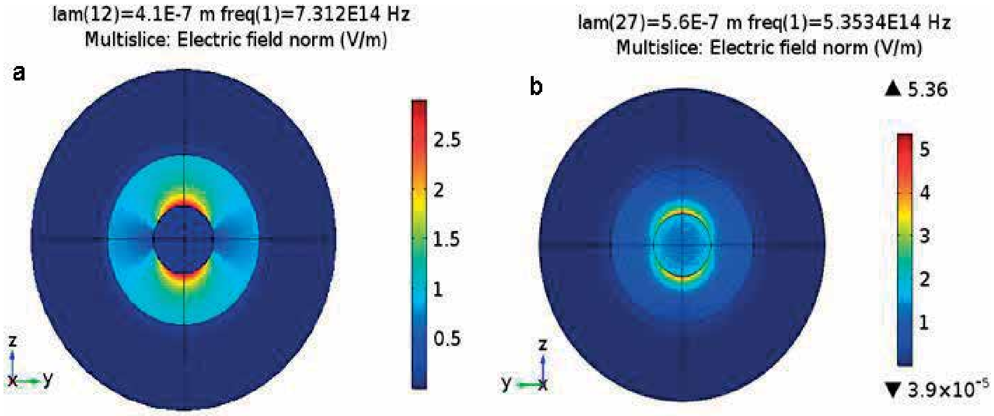

Figure 3. Electric field distribution of (a) silver and (b) gold nanosphere of radius 7 nm surrounded by silica matrix having N = 1.54.

of spherical-shaped metal nanoparticle [16]. We have used the Lumerical-based finite-difference time-domain technique to study the optical properties of noble metals. The metals are silver and gold whose optical constants are taken from the literature [8, 9]. These metals are surrounded by silica environment having constant dielectric constant. The objective of the work is to analyze the distribution of electric field near the metal surface in a resonance condition.

4. Scattering cross section of noble metal nanosphere: FDTD technique

We have plotted the scattering cross section of silver nanosphere of radius 50 nm surrounded by silica matrix as shown in **Figure 4**. In the previous study, we have chosen the smaller-sized nanoparticle whose optical properties have been studied in quasi-static domain. In quasi-static domain, we have chosen the static behavior of charge instead of oscillating behavior because the particle size is much smaller than the wavelength of light. When the particle size is smaller than the wavelength of light, in such a case, the particle feels the oscillating field because the electric field is no more static throughout the particle volume. Therefore, we have used the FDTD technique to study the plasmonic signature of larger-sized silver metal nanosphere. This shows the surface plasmon resonance at wavelength 564 nm, as shown in **Figure 4**a. We have also plotted the near-field distribution of 50 nm silver nanosphere at its SPR wavelength as shown in **Figure 4**b. The computed electric field gives the normalized field intensity magnitude 70 unit.

Further, we have also studied the optical properties of larger-sized gold nanoparticle embedded in silica matrix as shown in **Figure 5**. The scattering cross section of 50 nm gold nanosphere has been plotted using FDTD technique. Here, we have solved Maxwell's equation to obtain the cross-sectional profile, which has the dimension of area. The scattering is the reradiation of electromagnetic field which is absorbed by the surrounding media. The higher the scattering from the nanoparticle, the higher the photon absorption into the active medium. For 50 nm gold nanosphere, SPR wavelength was observed at 625 nm (**Figure 5**a), and we believe that

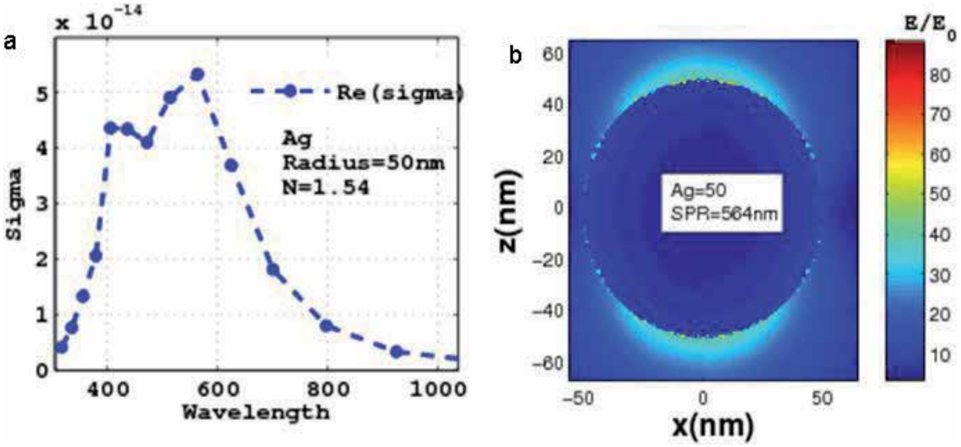

Figure 4. (a) Wavelength-dependent extinction spectra and (b) electric field distribution silver metal nanoparticle of radius 50 nm embedded in silica matrix.

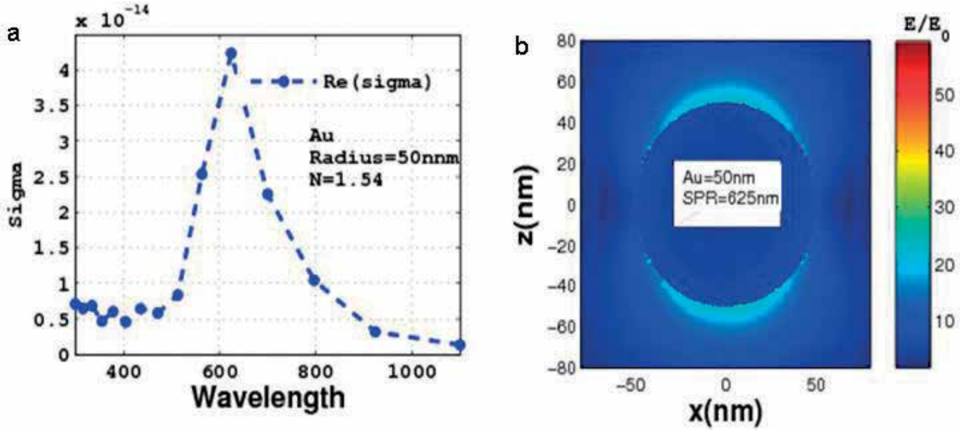

Figure 5. (a) Wavelength-dependent extinction spectra. (b) Electric field distribution of gold metal nanoparticle of radius 50 nm embedded in silica matrix.

under the SPR, maximum sun light can be harvested to produce electricity. The electric field distribution near the metal surface has also been done at SPR wavelength 625 nm as shown in **Figure 5**b. The magnitude of normalized field is indicated in scale bar. In nutshell, optical properties of two different types of metal such as silver and gold are studied in silica environment.

5. Conclusions

Here, we have analyzed the optical properties of noble metal nanoparticle in different regime electromagnetic spectra. The special emphasis has been given on the semi-analytical as well as numerical model. Two different types of numerical techniques such as FDTD and COMSOL Multiphysics are used to study the plasmonic resonances which cover a broader range of applications. The computed electric field magnitude at SPR wavelengths corresponding to smaller- and larger-sized metal nanoparticle would clearly suggest experimentalist to fabricate various sizes of nanoparticle whose SPRs are preknown.

Acknowledgements

This work is financially supported by the Science and Engineering Research Board (SERB) with File No. PDF/2016/000161, Government of India. The author acknowledges Dr. Neelam Upadhyay, scientist, Dairy Technology Division, ICAR-National Dairy Research Institute, Karnal-132001 (Haryana), for her devoting time in the preparation of this manuscript.

Conflict of interest

The authors do not have any conflict of interest.

Author details

Nilesh Kumar Pathak[1,2*], Pandian Senthil Kumar[1] and Rampal Sharma[2]

*Address all correspondence to: nileshpiitd@gmail.com

1 Department of Physics and Astrophysics, University of Delhi, Delhi, India

2 Plasma and Plasmonic Simulation Laboratory, Centre for Energy Studies, Indian Institute of Technology, Delhi, India

References

[1] Catchpole KR, Polman A. Plasmonic solar cell. Optics Express. 2008;**6**:21793-21800. DOI: 10.1364/OE.16.021793

[2] Pathak NK, Ji A, Sharma RP. Tunable properties of surface plasmon resonances: The influence of core-shell thickness and dielectric environment. Plasmonics. 2014;**9**:651-657. DOI: 10.1007/s11468-014-9677-4

[3] Maier SA. Plasmonics: Fundamentals and Applications. Berlin: Springer; 2007. DOI: 10.1007/0-387-37825-1

[4] Ji A, Sharma R, Pathak H, Pathak NK, Sharma RP. Numerical simulation of plasmonic light trapping in thin-film Si solar cells: Surface coverage effect. Journal of Physics D: Applied Physics. 2015;**48**:275101-275107. DOI: 10.1088/0022-3727/48/27/275101

[5] Bellido EP, Zhang Y, Manjavacas A, Nordlander P, Botton GA. Plasmonic coupling of multipolar edge modes and the formation of gap modes. ACS Photonics. 2017;**4**:1558-1565. DOI: 10.1021/acsphotonics.7b00348

[6] Pathak NK, Alok Ji A, Sharma RP. Study of efficiency enhancement in layered geometry of excitonic-plasmonic solar cell. Applied Physics A: Materials Science & Processing. 2014;**115**:1445-1450. DOI: 10.1007/s00339-013-8061-0

[7] Pandey GK, Pathak NK, Uma R, Sharma RP. Electromagnetic study of surface enhanced Raman scattering of plasmonic biomolecule: An interaction between nanodimer and single biomolecule. Solid State Communications. 2017;**255**:47-53. DOI: 10.1016/j.ssc.2017.03.010

[8] Bohren CF. Huffman DR. Absorption and Scattering of Light by Small Particles. A Wiley-Interscience Publication. 1983. DOI: 10.1002/9783527618156

[9] Palik ED. Handbook of Optical Constants of Solids. Orlando: Academic; 1985

[10] Kreibig U, Vollmer M. Optical Properties of Metal Clusters. Berlin: Springer; 1995. DOI: 10.1007/978-3-662-09109-8

[11] Pathak NK, Sharma RP. Study of broadband tunable properties of surface plasmon resonances of noble metal nanoparticles using Mie scattering theory: Plasmonic perovskite interaction. Plasmonics. 2016;**11**:713-719. DOI: 10.1007/s11468-015-0097-x

[12] Wustholz KL, Brosseau CL, Casadio F, Van Duyne RP. Surface-enhanced Raman spectroscopy of dyes: From single molecules to the artists' canvas. Physical Chemistry Chemical Physics. 2009;**11**:7350. DOI: 10.1039/b904733f

[13] Arora S, Singh V, Arora M, Tandon RP. An anomalous behavior in degraded bulk heterojunction organic solar cells. Physica Scripta. 2011;**84**:065803. DOI: 10.1088/0031-8949/84/06/065803

[14] Pandey GK, Pathak NK, Ji A, Pathak H, Sharma RP. Study of surface enhanced Raman scattering of single molecule adsorbed on the surface of metal Nanogeometries: Electrostatic approach. Plasmonics. 2016;**11**:1343-1349. DOI: 10.1007/s11468-016-0181-x

[15] Noguez C. Surface Plasmons on metal nanoparticles: The influence of shape and physical environment. Journal of Physical Chemistry C. 2007;**111**:3806-3819. DOI: 10.1021/jp066539m

[16] Zhang Y, Zhen YR, Neumann O, Day JK, Nordlander P, Halas NJ. Coherent anti-stokes Raman scattering with single-molecule sensitivity using a plasmonic Fano resonance. Nature Communications. 2014;**5**:4424. DOI: 10.1038/ncomms5424

Hybrid Silicon Nanowires for Solar Cell Applications

Adel Najar and Amine El Moutaouakil

Additional information is available at the end of the chapter

http://dx.doi.org/10.5772/intechopen.74282

Abstract

The global human population has been growing by around 1.1% per year; such growth rate will lead the humanity to cross the 10 billion-people threshold by the end of the first half of this century. Such increase is already putting a huge strain on the nonrenewable sources of energy like fossil fuel, which will run out and come to an end in few decades. Due to these social and economic trends, renewable sources of energy, such as solar cells, have attracted a huge interest as the ultimate alternative to solve humanity's problems. Among several emerging materials, porous silicon nanowires (PSiNWs) become an active research subject nowadays in photovoltaic application mainly due to its good light trapping effect. The etched nanowires obtained by using metal-assisted chemical etching method (MACE) can reach a low reflection in the visible range. Recently, hybrid silicon nanowires/organic solar cells have been studied for low-cost Si photovoltaic devices because the Schottky junction between the Si and organic material can be formed by solution processes at low temperature. In this chapter, we will present the synthesis of SiNWs and the last progress on the fabrication of hybrid solar cells using various organic semiconductors.

Keywords: silicon, nanowires, chemical etching, optical properties, solar cells

1. Introduction

Nanoscale silicon has been intensively investigated and explored for its applications in microelectronics, photonics, and biomedical sensors [1–3]. Specific efforts have been concentrated in the development of new silicon nanostructures, including quantum dots, nanowires, or porous silicon (PS). Porous silicon has attracted much attention, especially in enhancing photoemission. Much research efforts have been invested to realize an optical device with porous silicon [4–9], but the inefficiency [10] and instability [11] of optical characteristic in PS still remain. In addition, silicon nanowires (SiNWs) are also ideal candidate for the study of physics of low

IntechOpen

dimensional systems. It has potential impact in realizing nanoscale interconnects and functional device elements in future nanoscale electronic and optoelectronic devices [12, 13]. The field of SiNWs synthesis represents an exciting and rapidly expanding research area. Considerable efforts have been devoted to the development of versatile and controllable methods for the synthesis of SiNW. These methods can be broadly classified as: (i) bottom-up and (ii) top-down approaches. The bottom-up approach involves the construction of desirable nanostructures from the basic components, i.e., from the atomic level to the nano- or microscale wires.

This method is useful for the fabrication of low-dimensional heterostructure-based devices in large quantities [14–18]. Using bottom-up, SiNWs were first obtained by vapor-liquid-solid (VLS) method [19], followed by an etching step to create nanowires. The VLS method has been implemented in a variety of techniques, such as pulsed laser deposition (PLD) [20, 21], gas-phase molecular beam epitaxy (GS-MBE) [22], chemical vapor deposition (CVD) [23, 24], laser ablation [25, 26], and oxide-assisted growth techniques [27].

Top-down approach seeks to fabricate SiNWs from high-quality single crystal silicon wafer or thin film. Silicon nanowires have also been realized using lithographically defined patterns, or spin-coating of nanospheres as etched mask [28] followed by etching of the nanowires using plasma processing technique. Metal-assisted chemical etching method (MACE) is a simple, cost-effective, and powerful semiconductor etching technique that can produce high aspect ratio semiconductor nanostructures. By combining with metal patterning lithography or nonlithographic patterning methods, accurate control of the nanowire orientation (vertical vs. slanted), size (nano vs. microscale), shape, architecture, density, length, and doping characteristics can be achieved readily at wafer scale.

The fabrication of silicon nanowires using the metal-assisted electroless etching method has also been adopted [29–33]. The silver (Ag) ions in an ionic solution of hydrofluoric acid (HF) and hydrogen peroxide (H_2O_2) have been used to prepare the arrays of SiNWs from single crystal wafers [34, 35] The effects of various process parameters such as the etchant concentration of H_2O_2, etching time, and postetch treatment on the morphology, and optical properties of the SiNWs have also been investigated [36]. The fabrication of nanowires using this method does not require complex sample preparation steps. Furthermore, this technique is effective, having high throughput and low cost. In this chapter, we will present the synthesis of PSiNWs and the last progress of hybrid solar cells based on these nanostructures.

2. Fabrication of porous silicon nanowires (PSiNWs)

Najar et al. detailed the fabrication of PSiNWs using Ag-assisted electroless etching method from an n-type Si wafer (100) with a resistivity of 0.01–0.02 ohm cm [33]. The Si wafers were cleaned using acetone followed by ethanol for 5 min in an ultrasonic bath. Next, the wafers were immersed in a piranha solution H_2SO_4/H_2O_2(3:1) for 20 min to remove the organic deposits from the surface. The cleaned wafers were transferred into $HF/AgNO_3$ solution with a concentration of 4.8/0.005 M for Ag-deposition, followed by rinsing with de-ionized water. Then, the treated Si samples were etched in the HF/H_2O_2 solution for 45 min. Finally, samples were rinsed again for 10 min with HNO_3 solution to dissolve the excessive Ag nanoparticles (Ag NPs), leaving behind traces of Ag for catalyzing the etching reaction. Four samples were etched using HF concentration of 1.8, 2.8, 4.8, and 5.8 M, respectively, with a fixed H_2O_2 concentration of 0.5 M.

2.1. PSiNWs: Physical properties

Najar et al. studied the etching morphology of the synthesis of PSiNWs [32]. **Figure 1(a)** shows the scanning electron microcopy image of the vertically oriented PSiNWs having an average length of 13 μm after 75 min of wet etching. The nanowires distribute uniformly on the sample. **Figure 1(b)** shows the top view with tips of NWs congregates together, and the diameter of the congregated bundles is of several micrometers. These congregated bundles are uniformly distributed on the entire samples and confirmed from the cross-section images. The transmission electron microscopic (TEM) image of an individual nanowire is shown in **Figure 1(c)**, which shows that the nanowire has a diameter of ~150 nm.

A typical 2D bright-field TEM image used for volume reconstruction of the sample is presented in **Figure 2(a)–(c)**. The three successive longitudinal slices obtained from the reconstructed volume revealed a distribution of irregular size/shape vacuum spaces and silicon frame, constituting the PSiNWs.

A typical 3D-tomography observation was conducted using a TEM, and 3D reconstructions were achieved using a simultaneous iterative reconstruction algorithm of consecutive 2D slices in **Figure 2(d)** [32]. The pore sizes present a distribution from 10 to 50 nm, with an estimated measurement error of 10%, and these pores go inside the nanowire showing similar structure to porous silicon. An average distance between two neighboring pores of lower than 5 nm has been observed. These mesoporous structures are expected to show strong quantum confinement effects.

It is noted that mesopores are mostly found near the top of the nanowires with an average pore size between 10 and 40 nm. AgNPs were detected at the bottom section of the nanowires by

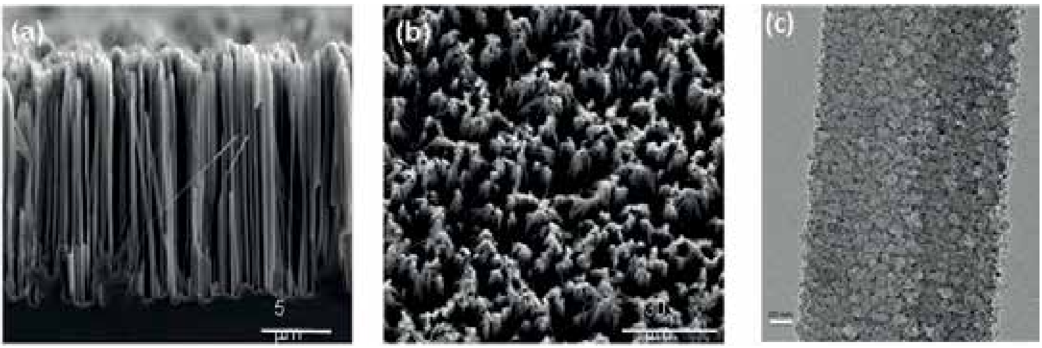

Figure 1. (a) Cross-sectional images of SEM micrograph of PSiNWs etched for 75 min, (b) top view micrograph of PSiNWs, (c) TEM image of individual nanowire, and inset of the FFT image [32].

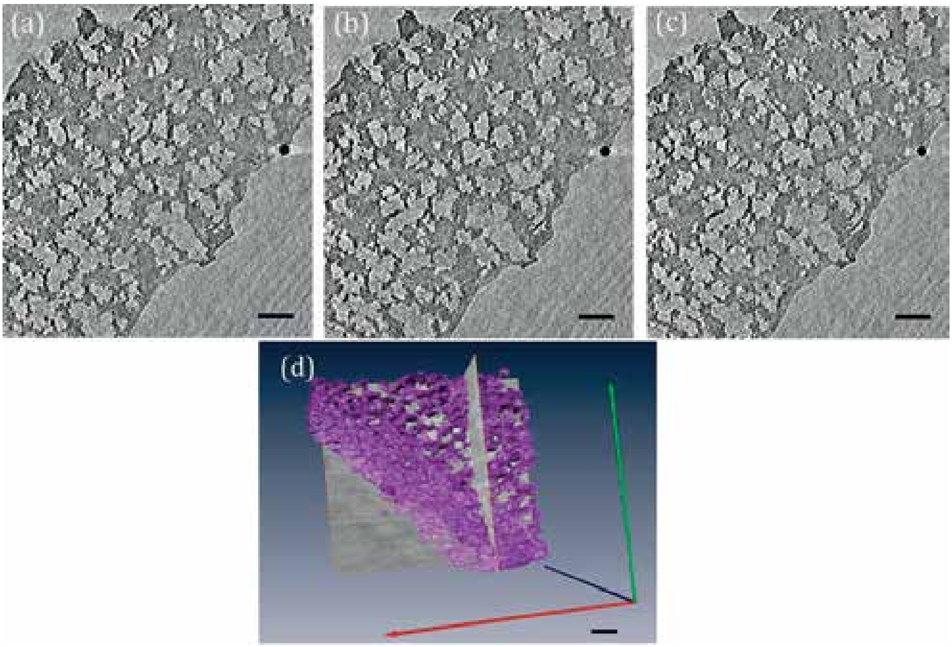

Figure 2. Panels (a), (b), and (c) represent three longitudinal slices extracted from the volume reconstruction of the PSiNW nanostructures revealing an area of highly porous medium. The bare scale is 50 nm. (d) 3D tomography TEM image of nanowires [32].

EDS analysis in STEM mode. Based on the SEM and TEM analyses, the following qualitative model for the formation of PSiNWs is proposed. In HF/H_2O_2 solution, part of the Ag is oxidized into Ag^+ by H_2O_2 [37]. The Ag^+ catalyzes the dissolution of Si through the formation of SiF_6^{2-}.

It is apparent that the transport of Ag^+ is isotropic while the AgNPs merely drop downward. Hence, the AgNPs facilitated the nanowire formation through vertical chemical etching, while the isotropic diffusion of Ag^+ promoted lateral chemical etching and pore formation as illustrated in **Figure 3(a-i** and **a-ii)** [33].

The Ag^+ may be chemically reduced by the n-type silicon nanowires [38] forming Ag particle that redeposited onto the sidewalls forming new Ag nucleation sites, and therefore the new localized lateral etching pathway. Furthermore, the nucleation of the AgNPs on the side walls would also reduce the Ag^+ concentration locally and accelerates the Ag^+ diffusion in the lateral direction. The laterally diffused Ag^+ will continue to catalyze the chemical etching of the sidewalls of Si. Since the upper Si nanowires are exposed longer to the solutions, larger Si volume dissolves at the top (and creating more mesopores) than the bottom of the nanowires (**Figure 3(b-i** and **b-ii)** and **(c-i** and **c-ii)**), being consistent with the TEM image as shown in **Figure 2(a)**. Furthermore, increasing the HF concentration accelerates the process described in our qualitative model, with the $Ag \rightarrow Ag^+ + e^-$ reversible reaction that continues to penetrate the nanowires laterally to catalyze the HF/H_2O_2 chemical reaction forming mesopores. Eventually, the mesopores merged leading to a reduction in length and pore density, with the formation of conical PSiNWs as illustrated in **Figure 3(d-i** and **d-ii)**.

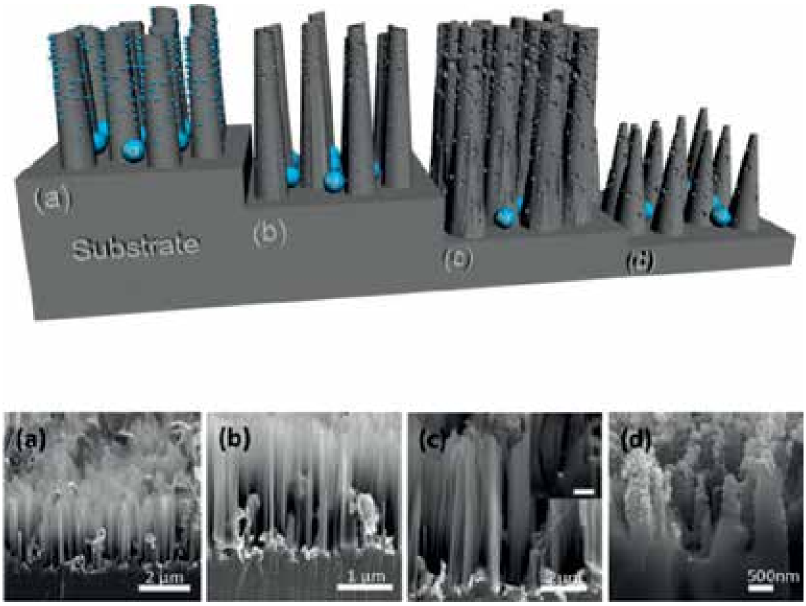

Figure 3. (a-i)–(d-i) The schematic illustration of the proposed qualitative etching model for the formation of PSiNWs using Ag-assisted HF/H_2O_2 electroless etching technique. (a-ii)–(d-ii) The corresponding SEM micrographs, prepared using various HF concentrations [33].

In this way, the higher H_2O_2 concentration increases the amount of out-diffused Ag^+, and the increase of doping concentration increases the amount of weak defective points in the silicon lattice; both are important factors for the initiation of additional etching pathways in addition to the vertical etch, which explains the observation of the increased porosity with increasing H_2O_2 concentration during the etching of highly doped n-Si wafers.

The heavy doping silicon wafer-induced porosification can be understood by a thermodynamic model that describes charge transport across the silicon-electrolyte interface driven by potential energy (**Figure 4(a)**). To et al. present a model to explain the etching mechanism [39]. In **Figure 4(a)**, the electron transports from Si to Ag^+ ions, which is composed of the processes I-IV at the Si/electrolyte interface. Electrons at E_F of Si wafers migrate to the interface by overcoming a potential energy barrier $\Delta\Phi$, consisting of the excitation barrier (E_{CB}-E_F, the process I) and the band edge bending in space charge layer (SCL) ($E_{CB'S}$-E_{CB}, the process II). Owing to the mismatch of $E_{CB,S}$ with E_{Ag+}, electrons are apt to relaxing to surface states (E_{SS}) aligned with E_{Ag+} (the process III) followed by the resonant migration to E_{Ag+} (the process IV). The increase in the doping level not only up shifts E_F toward E_{CB} to reduce $\Delta\Phi$, but also makes the SCL thinner to promote electron tunneling through the SCL (**Figure 4(b)**), to facilitate the process I and II. Hence, a large amount of Ag^+ ions nucleate on the surface and [Ag^+] (i.e., concentration of Ag^+ ions) is significantly reduced in the electrolyte. Low [Ag^+] can support only a portion of Ag nuclei to grow and scratch the bulk Si. The rest of the nongrown Ag nuclei will undergo a random scratching in a short period of time to porosify SiNWs and the bulky wafer (**Figure 4(c)**). Since the scratching of growing Ag NPs is limited by the diffusion of Ag^+ ions with low [Ag^+], the random porosification tends to be faster than the NP scratching. Consequently, the

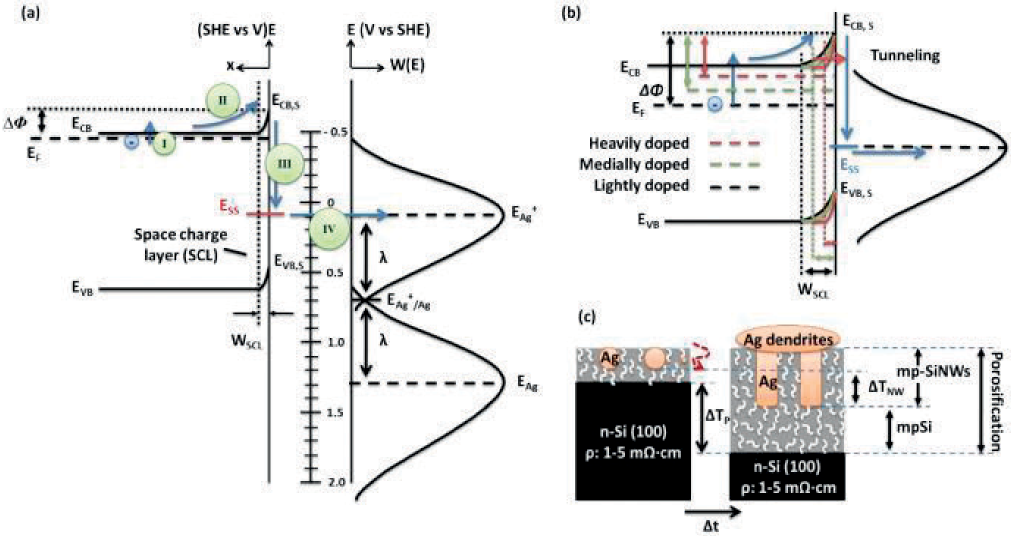

Figure 4. (a) Quasi-quantitative energy diagram at the silicon-electrolyte interface, at the beginning of one-MACE of n++ type Si(100). The energy is referred to standard hydrogen electrode (SHE) potential. Heavily doped n-Si has Fermi energy (E_F), valence, and conduction band in the bulk (E_{VB} and E_{CB}) and at the interface ($E_{VB,S}$ and $E_{CB,S}$), and space charge layer (SCL) with a width W_{SCL}. $\Delta\Phi$ is an energy barrier between E_F and $E_{CB,S}$. $E_{Ag+/Ag}$, E_{Ag+}, and E_{Ag} represent the potential energy of the redox pair, Ag^+ and Ag in the electrolyte, respectively. λ is the reorientation energy. The light blue sphere represents an electron at E_F, and the I-IV processes denote a subsequent series of electron migration from the bulk to interface. (b) Energy diagram with variation of doping levels in n-Si(100). (c) Schematic of the one-MACE evolution. For clarity, only one nongrown Ag nucleus scratching the wafer in the mpSi is shown, marked by a red dashed line. Within a period of time Δt, the evolution of the porosification and mesoporous SiNWs are denoted by ΔT_P and ΔT_{NW}, respectively [39].

electrochemical porosification tends to generate a hybrid structure composed of an array of mpSiNWson mpSi (**Figure 4 (a)–(d)**). On the contrary, the light and media doping increases ΔΦ to prevent Ag^+ ions from severely consuming. High [Ag^+] substantially supports most Ag NPs grow and scratch the wafer to create SiNWs, and effectively suppresses the porosification. This model can also account for the creation of mesoporous SiNWs via one-MACE of p++ type Si.

2.2. HF concentrations vs. morphology of PSiNWs

The modification of HF or H_2O_2 concentrations affects the morphology of PSiNWs. In the presence of Ag catalyst, an increase in HF or H_2O_2 concentration in electroless etching method is analogous to an increase in the current density in electrochemical-based methods [40, 41]. In both cases, increasing the H_2O_2 or HF concentration increases the oxidation rate and dissolution rate, respectively, resulting in nanostructures with varying optical properties. In **Figure 5(a)–(h)**, Najar et al. shows the cross-sectional SEM micrographs and TEM images acquired from the NW samples grown with HF concentrations of 1.8, 2.8, 4.8, and 5.8 M in a fixed H_2O_2 concentration of 0.5 M [33].

The variation of NWs length and NWs diameter with increasing HF concentrations was measured and analyzed using SEM and TEM, and the results are tabulated in **Table 1**. The NWs length shows significant changes, while the NWs diameter varies from 80 to 210 nm for samples indicating the dominant effect of vertical etching enhanced by Ag catalyst with preferential etching along the low atomic density plane in [001]. An increase in aspect ratio from about 9 to 12 and 27 has been calculated for NWs samples etched with 1.8, 2.8, and 4.8 M HF concentration

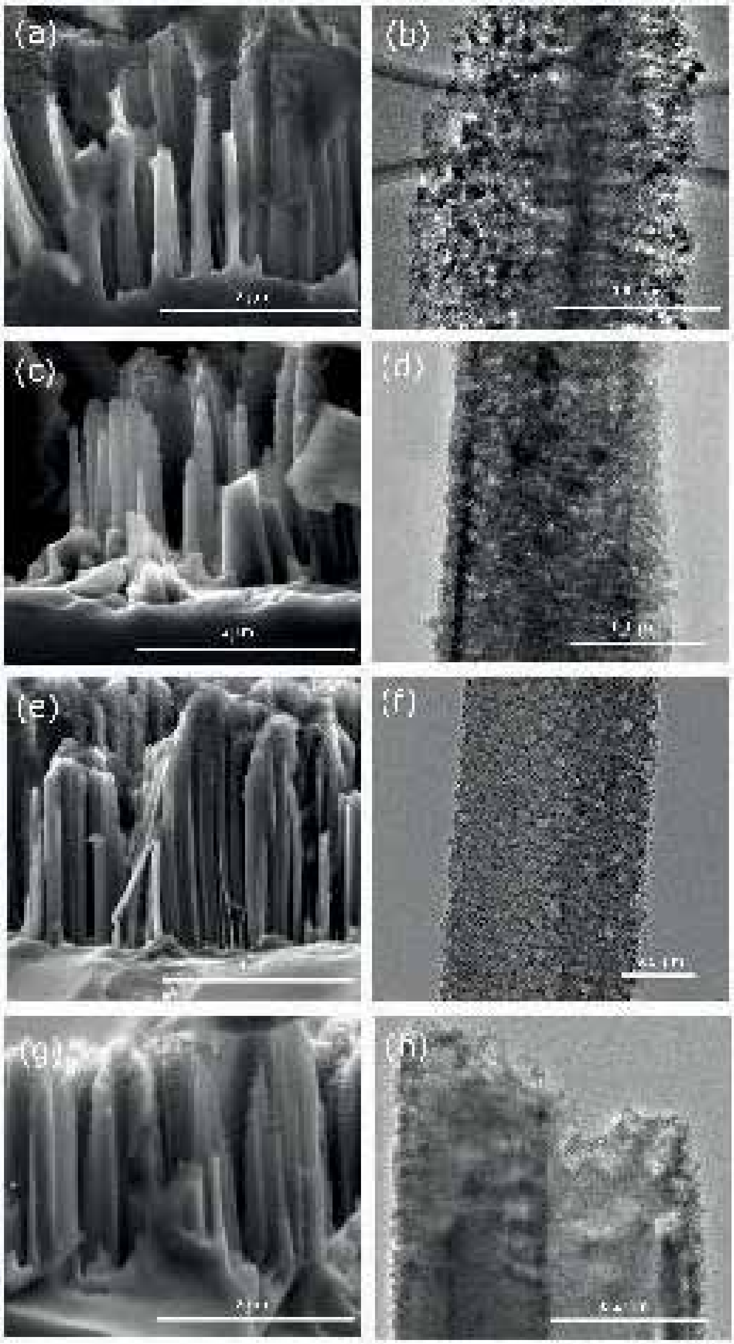

Figure 5. (a)–(h) SEM and TEM micrographs of PSiNWs fabricated with increasing HF concentration from 1.8, 2.8, 4.8, up to 5.8 M [33].

PSiNWs physical parameters	HF concentration			
	1.8 M	2.8 M	4.8 M	5.8 M
NWs length (μm)	1.3–1.8	2–2.2	4.8–5.3	1.6–1.8
NWs diameter (nm)	160–210	100–180	80–200	150–200
Aspect ratio (longest length/largest diameter)	~9	~12	~27	~9

Table 1. Effect of HF concentration on PSiNWs length, NWs diameter, and aspect ratio analyzed from SEM micrographs [33].

(**Figure 5(a)**, **(c)**, and **(e)**). However, the aspect ratio reduces to about 9 for NWs etched with (**Figure 5(g)**) signifying a change in etching mechanism with faster lateral chemical etch.

2.3. Effect of HF concentration on PL

It is known that the mesoporous silicon nanostructure gives rise to strong visible emission [42]. Optical properties of the PSiNWs samples have been investigated using PL spectroscopy. **Figure 6(a)** shows the PL spectra of the samples etched with HF concentrations of 1.8, 2.8, 4.8, and 5.8 M with a constant H_2O_2 concentration of 0.5 M. It is observed that the asymmetric PL spectra have two dominant peaks around 700 and 760 nm. The sample etched with 4.8 M HF concentration has an additional hump at 670 nm. The highest PL peak at 760 nm is related to the emission from Si–O bond [42, 43].

In our case, we observe in **Figure 6(a)** that the increase in integrated intensities of the broadband PL emissions correlates well with the increase in pore densities for samples etched using 1.8–4.8 M HF concentrations. With an HF concentration of 5.8 M, a reduction in PL integrated intensity is again consistent with a reduction in the pore density of PSiNWs.

After HNO_3 and HF treatments for 5 min to remove the oxide, all samples show similar PL peak wavelength at 800 nm (**Figure 6(c)**). However, samples without HF treatment show a significant blueshift with PL wavelength peak at 700 nm (**Figure 6(a)**). This blueshift and increase of PL intensity have been attributed to the presence of defect states in Si-Ox.

This has been correlated with the redshift of PL spectrum that suggests the interfacial between Si and surface oxide, as well as the quantum confinement effect, and plays a critical role in the light emission process (i.e., the presence of nanocrystallites with size <5 nm that has been confirmed by HRTEM).

Several mechanisms have been proposed to explain the origin of strong PL emission for the indirect bandgap silicon material. These include (i) the quantum confinement effects of free excitons within the Si-nanocrystallites and (ii) SiOx/Si interface defects and/or defect states in the surface oxide, related to Si-O bond [42, 44, 45]. Comparing the PL spectra before and after the HF treatment, we believe that existence of oxide plays a significant role in changing the emission property of the nanowires.

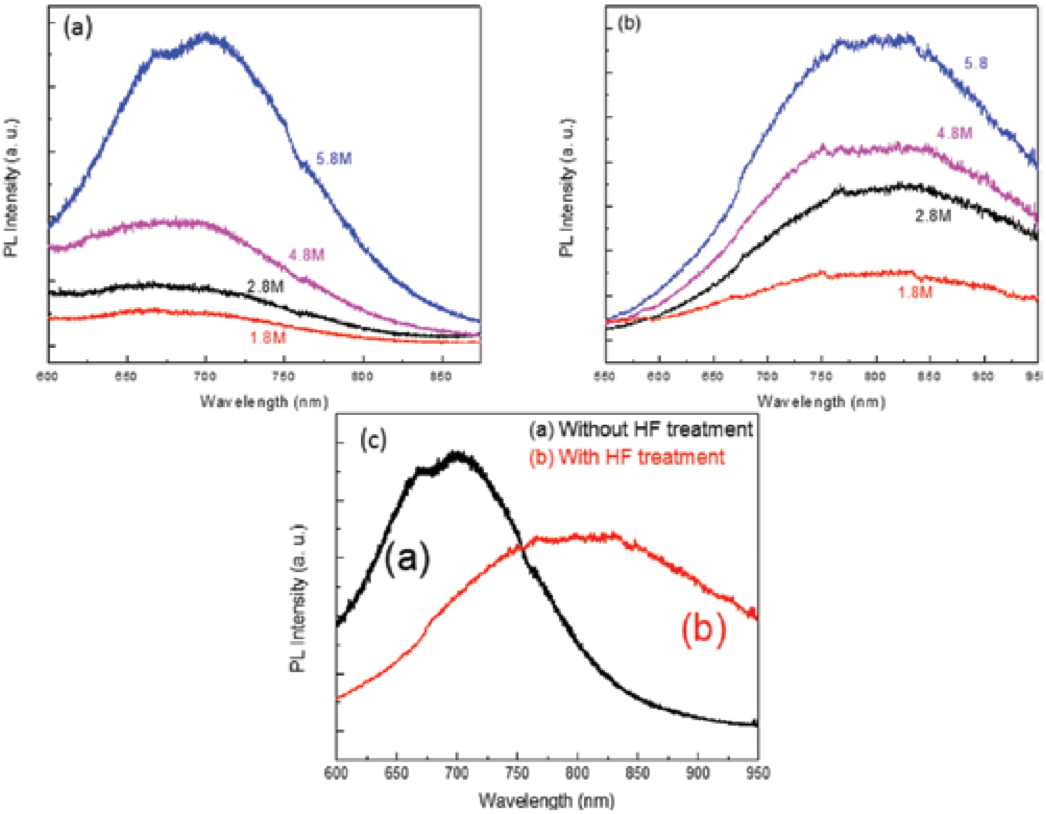

Figure 6. PL spectra of PSiNWs as a function of HF concentration etched for 45 min (a): 1.8, 2.8, 4.8, and 5.8 M, (b) after HNO_3 treatment followed by HF (5%), and (c) with and without HF treatment [33].

The quantum confinement effect dictates that the characteristic size of the Si-nanocrystallites should be less than the Bohr radius of the free exciton of bulk Si, which is around 5 nm [46]. From the TEM analysis, Si-nanocrystallites of <5 nm has been observed (**Figure 7(a)**). The inset of **Figure 7(a)** shows the calculated fast-Fourier transform (FFT) of PSiNWs prepared using 4.8 M HF concentration. The FFT revealed the spatial frequencies corresponding to {111}, {220}, and {311} d-spacing of Si crystal structure. The presence of these d-spacing implies that the PSiNW was oriented along the <110> direction. This was expected as the (001) Si wafer was used to fabricate the NWs, and etching was vertical with respect to the substrate surface. Also, the energy-filtered TEM analysis of the top region of the PSiNW, as shown in **Figure 7(b)**, confirms the existence of Si nanocrystallites and silica amorphous structures, indicating the possible strong PL emission from the highly quantum-confined Si nanocrytallite structures. This prediction correlates positively with our previous discussion on the effect of pore density on PL enhancement. The above argument further confirms our observation that samples etched with HF concentration of 5.8 M (i.e., with low pore and Si-nanocrystallites densities) results in a decrease in PL intensity. The evolution of PL peak intensity with HF concentration is hence consistent with the physical changes in the PSiNWs developed in our etching model.

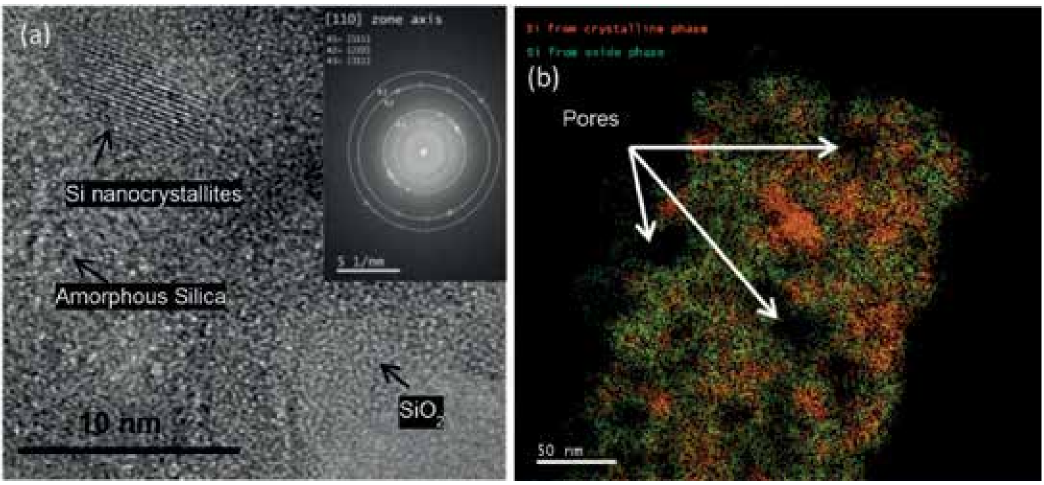

Figure 7. (a) HRTEM and (b) EFTEM analyses of the top section of a PSiNW etched using 4.8 M concentration of HF [33].

However, SiO_2 alone should not give rise to the PL emission; rather, defect states would contribute to PL emission. Indeed, Najar et al. observed Si^{1+} (Si_2O) and Si^{3+} (Si_2O_3) using X-ray hotoelectron spectroscopy (XPS) signatures, which may originate from dangling bonds and volumetric stress that distorted the PSiNWs forming localized defect states.

Therefore, the emissions from surface/defect states in oxide may contribute to the red PL emission, in agreement with the results obtained in [47], in addition to the contribution from quantum confinement effect.

3. Organic-inorganic hybrid nanowire solar cells

As a platform for cost-effective crystalline Si (c-Si) solar cells, an organic-inorganic hybrid structure has been proposed to replace the conventional p–n junction. The hybrid structure is composed of a transparent conducting polymer and c-Si [48, 49]. A Schottky junction at the conducting polymer/c-Si interface can easily be created using a simple spin coating process at room temperature, while a conventional Si p–n junction is formed via a high-temperature doping process [50]. In order to enhance the light-trapping efficiency, Si nanostructures such as nanopyramids [49] and nanowires [51] have been applied, leading to an increase in the short-circuit current density (J_{SC}).

Han-Dom Um et al. demonstrate an embedded metal electrode for highly efficient organic-inorganic hybrid nanowire solar cells as shown in **Figure 8** [52]. The electrode proposed here is an effective alternative to the conventional bus and finger electrode, which leads to a localized short circuit at a direct Si/metal contact and has a poor collection efficiency due to a nonoptimized electrode design. In this design, an Ag/SiO_2 electrode is embedded into a Si substrate while being positioned between Si nanowire arrays underneath poly(3,4-ethylenedi oxythiophene):poly(styrenesulfonate) (PEDOT:PSS), facilitating suppressed recombination at

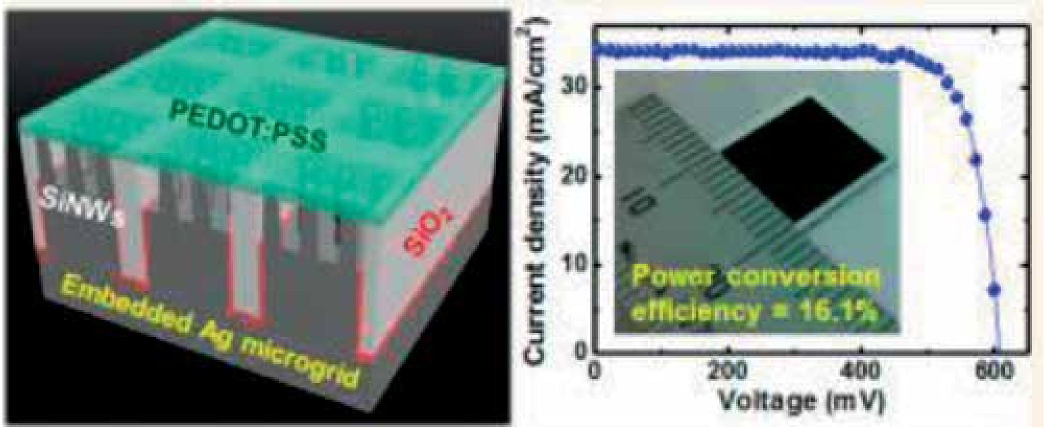

Figure 8. Embedded metal electrode for highly efficient organic-inorganic hybrid nanowire solar cells, and I-V characteristic of the solar cell [52].

the Si/Ag interface and notable improvements in the fabrication reproducibility. With an optimized microgrid electrode, the 1-cm^2 hybrid solar cells exhibit a power conversion efficiency of up to 16.1% with an open-circuit voltage of 607 mV and a short-circuit current density of 34.0 mA/cm^2. This power conversion efficiency is more than twice as high as that of solar cells using a conventional electrode. The microgrid electrode significantly minimizes the optical and electrical losses. This reproducibly yields a superior quantum efficiency of 99% at the main solar spectrum wavelength of 600 nm. In particular, the solar cells exhibit a significant increase in the fill factor of 78.3% compared to that of a conventional electrode (61.4%), this is because of the drastic reduction in the metal/contact resistance of the 1 μm-thick Ag electrode. Hence, the use of this embedded microgrid electrode in the construction of an ideal carrier collection path presents an opportunity in the development of highly efficient organic-inorganic hybrid solar cells.

Liu et al. fabricated a hybrid silicon nanowire/polymer heterojunction solar cell combined with a polypyrrole-based supercapacitor as shown in **Figure 9**, to harvest solar energy and store it [53]. By efficiency enhancement of the hybrid nanowire solar cells and a dual-functional titanium film serving as a conjunct electrode of the solar cell and supercapacitor, the integrated system is able to yield a total photoelectric conversion to storage efficiency of 10.5%, which is the record value in all the integrated solar energy conversion and storage system. This system may not only serve as a buffer that diminishes the solar power fluctuations from light intensity, but also pave its way toward cost-effective high-efficiency self-charging power unit. Finally, an integrated device based on ultrathin Si substrate is demonstrated to expand its feasibility and potential application in flexible energy conversion and storage devices.

Organic-inorganic hybrid solar cells based on n-type crystalline silicon and poly(3,4-ethylenedioxythiophene)-poly(styrenesulfonate) exhibited promising efficiency along with a low-cost fabrication process (**Figure 10**). Zhang et al. fabricated ultrathin flexible silicon substrates, with a thickness as low as tens of micrometers, which were employed to fabricate hybrid solar cells to reduce the use of silicon material [54]. To improve the light-trapping ability,

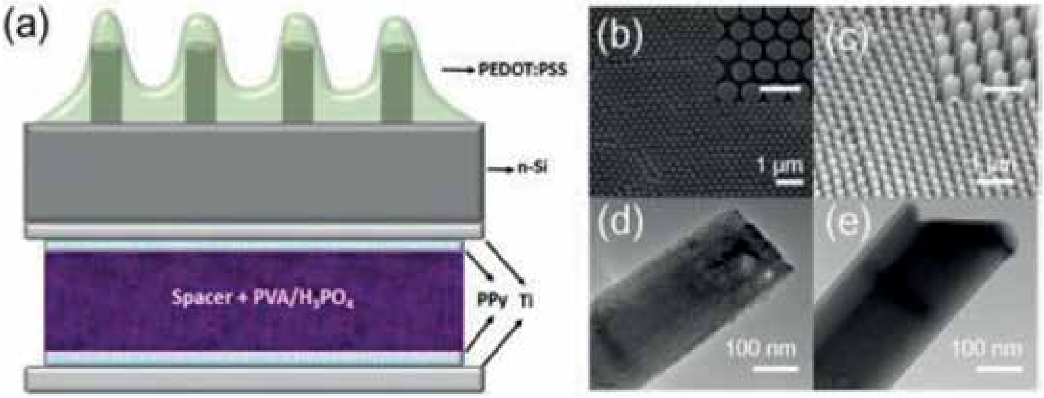

Figure 9. (a) Schematic of the integrated hybrid device containing a SiNW-based heterojunction solar cell and a polypyrrole-based supercapacitor. (b) SEM image of as-fabricated SiNW. (c) SEM image of SiNW after 2 h of PCl5 treatment. (d) TEM image of a single as-fabricated Si nanowire. (e) TEM image of a single Si nanowire after 10 min of methylation treatment. The scale bars are 500 nm in the insets of (b) and (c) [53].

nanostructures were built on the thin silicon substrates by a metal-assisted chemical etching method (MACE). However, nanostructured silicon resulted in a large amount of surface-defect states, causing detrimental charge recombination. Here, the surface was smoothed by solution-processed chemical treatment to reduce the surface/volume ratio of nanostructured silicon. Surface-charge recombination was dramatically suppressed after surface modification with a chemical, associated with improved minority charge carrier lifetime. As a result, a power conversion efficiency of 9.1% was achieved in the flexible hybrid silicon solar cells, with a substrate thickness as low as ~14 μm, indicating that interface engineering was essential to improve the hybrid junction quality and photovoltaic characteristics of the hybrid devices.

As shown in **Figure 10(b)**, the leakage current of the TMAH-treated nanostructured silicon devices is much lower than that of the untreated silicon devices, suggesting that the junction quality is improved. Furthermore, the J_{SC} of the hybrid devices based on different surface morphologies is consistent with the external quantum efficiency (EQE) spectra, as shown in **Figure 10(c)**. The device based on ~14-μm thick planar silicon without TMAH treatment gives a J_{SC} of 18.4 mA cm^{-2}, a V_{OC} of 0.56 V, and an FF of 0.75, achieving a PCE of 7.9%. The previously reported ultrathin planar silicon device with a thickness of 8.6 μm yields a PCE of 5.2% [55]. Here, the reduced J_{SC} for the device based on ~14-μm thick planar silicon is ascribed to the high light reflection of the planar silicon surfaces, which resulted in poor light absorption compared to that of a thicker device. In comparison with planar devices, nanostructured silicon solar cells exhibit a larger J_{SC} value, indicating that the incident light could be effectively absorbed by nanostructured silicon. The absorption spectra of the planar and nanostructured silicon with or without TMAH treatment are shown in **Figure 10(e)**. According to the absorption spectra, the nanostructured silicon exhibits an obviously better light absorption over a broad spectrum from the visible to the near-infrared range compared to that of planar silicon.

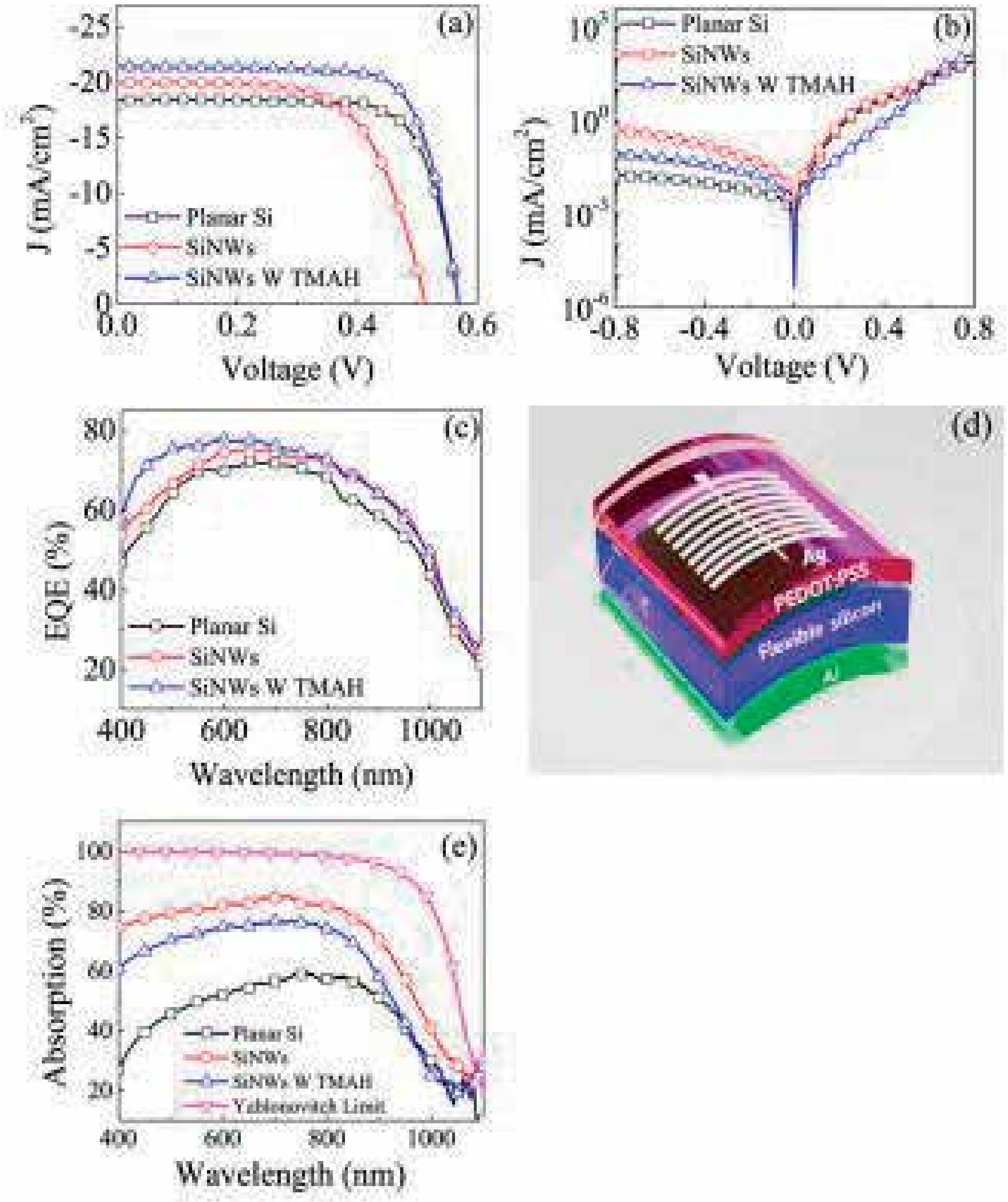

Figure 10. Electric-output characteristics of the PEDOT:PSS/Si devices under different surface conditions. (a) J–V curves under illumination at 100 mW cm^{-2}, (b) J–V curves in the dark, and (c) EQE spectra of devices based on silicon substrates with a planar surface (black), an as-prepared nanostructured silicon surface (red), and a TMAH-treated nanostructured silicon surface (blue). (d) Schematic device structure of the flexible PEDOT:PSS/Si hybrid solar cell. (e) Absorption spectra of silicon substrates with a planar surface, an as-prepared nanostructured silicon surface, a TMAH-treated nanostructured silicon surface, and upon Yablonovitch limit simulation [54].

4. Conclusion

In summary, facile silicon surface modification methods based on one or two MACE to synthesis PSiNWs were presented. The change in morphology based on HF or H_2O_2 effect was presented. Furthermore, this change also affects the optical properties specially the photoluminescence and compensates the poor light absorption of the planar silicon substrate. Several emerging strategies result in high-performance hybrid solar cells based on PSiNWs were presented. These strategies are based on the organic materials or/and the design of the solar cells or on the grid electrode as a contact. These findings could be potentially employed to further reduce the fabrication cost of silicon solar cells by reducing the consumption of silicon materials and increasing their efficiency.

Author details

Adel Najar[1]* and Amine El Moutaouakil[2]

*Address all correspondence to: adel.najar@uaeu.ac.ae

1 Department of Physics, College of Sciences, UAE University, UAE

2 Electrical Engineering Department, College of Engineering, UAE University, UAE

References

[1] Zhao XY, Wei CM, Yang L, Chou MY. Quantum confinement and electronic properties of silicon nanowires. Physical Review Letters. 2004;**92**:236805

[2] Cui Y, Lieber CM. Functional nanoscale electronic devices assembled using silicon nanowire building blocks. Science. 2001;**291**:851

[3] Lieber CM, Wang ZL, Nanowires F. MRS Bulletin. 2007;**32**:99

[4] Najar A, Charrier J, Ajlani H, Lorrain N, Haesaert S, Oueslati M, Haji L. Optical gain at 1.53 μm in Er $^{3+}$-Yb $^{3+}$ co-doped porous silicon waveguides. Materials Science and Engineering B. 2008;**146**:260

[5] Najar A, Lorrain N, Ajlani H, Charrier J, Oueslati M, Haji H. Er $^{3+}$ doping conditions of planar porous silicon waveguides. Applied Surface Science. 2009;**256**:581

[6] Najar A, Ajlani H, Charrier J, Lorrain N, Haesaert S, Oueslati M, Haji L. Optical study of erbium-doped-porous silicon based planar waveguides. Physica B: Condensed Matter. 2007;**396**:145

[7] Najar A, Charrier J, Lorrain N, Haji L, Oueslati M. Optical gain measurements in porous silicon planar waveguides codoped by erbium and ytterbium ions at 1.53 μm. Applied Physics Letters. 2007;**91**(12):121120-121120

[8] Najar A, Charrier J, Ajlani H, Lorrain N, Elhouichet H, Oueslati M, Haji L. Optical properties of erbium-doped porous silicon waveguides. Journal of Luminescence. 2006; **121**(2):245-248

[9] Najar A, Elhouichet H, Lorrain N. Oueslati Excitation mechanisms and localization sites of erbium-doped porous silicon M. Applied Surface Science. 2006;**252**(16):5808-5813

[10] Koyama H, Nakagawa T, Ozaki T, Koshida N. Post-anodization filtered illumination of porous silicon in HF solutions: An effective method to improve luminescence properties. Applied Physics Letters. 1994;**65**:1656

[11] Canham LT, Houlton MR, Leong WY, Pickering C, Keen JM. Atmospheric impregnation of porous silicon at room temperature. Journal of Applied Physics. 1991;**70**:422-431

[12] Huang Y, Duan X, Lieber CM. Nanowires for integrated multicolor nanophotonics. Small. 2005;**1**:142

[13] Bohr MT. Nanotechnology goals and challenges for electronic applications. IEEE Transactions on Nanotechnology. 2002;**1**:56

[14] Najar A, Jouiad M. Synthesis of InGaN nanowires via metal-assisted photochemical electroless etching for solar cell application. Solar Energy Materials and Solar Cells. 2017. DOI: 10.1016/j.solmat.2017.06.008

[15] Xia YN, Yang PD, Sun YG, Wu Y, Mayers N, Gates B, Yin Y, Kim F, Yan H. One-dimensional nanostructures: Synthesis, characterization, and applications. Advanced Materials. 2003;**15**:353

[16] Najar A, Gerland M, Jouiad M. Porosity-induced relaxation of strains in GaN layers studied by means of micro-indentation and optical spectroscopy. Journal of Applied Physics. 2012;**111**(9):093513-093513

[17] Slimane AB, Najar A, Elafandy R, San-Román-Alerigi D, Anjum D, Ng TK, Ooi BS. On the phenomenon of large photoluminescence. Red shift in GaN nanoparticles. Nanoscale Research Letters. 2013;**8**:342-348

[18] Najar A, Shafa M, Anjum D. Synthesis, optical properties and residual strain effect of GaN nanowires generated via metal-assisted photochemical electroless etching. RSC Advances. 2017;**7**(35):21697-21702

[19] Wagner RS, Ellis WC. Vapor-liquid-solid mechanism of single crystal growth. Applied Physics Letters. 1964;**4**:89-90

[20] Morales AM, Lieber CM. A laser ablation method for the synthesis of crystalline semiconductor nanowires. Science. 1998;**279**:208

[21] Zhang YF, Tang YH, Wang N, Yu DP, Lee CS, Bello I, Lee ST. Silicon nanowires prepared by laser ablation at high temperature. Applied Physics Letters. 1998;**72**:1835-1837

[22] Schubert L, Werner P, Zakharov ND, Gerth G, Kolb FM, Long L, Geosele U, Tan TY. Silicon nanowhiskers grown on 111 Si substrates by molecular-beam epitaxy. Applied Physics Letters. 2004;**84**:4968-4970

[23] Stelzner T, Pietsch M, Andrea G, Falk F, Ose E, Christiansen S. Silicon nanowire-based solar cells. Nanotechnology. 2008;**19**:295203

[24] Lu M, Li MK, Kong LB, Guo XY, Li HL. Silicon quantum-wires arrays synthesized by chemical vapor deposition and its micro-structural properties. Chemical Physics Letters. 2003;**374**:542-547

[25] Au FCK, Wong KW, Tang YH, Zhang YF, Bello I, Lee ST. Electron field emission from silicon nanowires. Applied Physics Letters. 1999;**75**:1700

[26] Yu DP, Lee CS, Bello I, Sun XS, Tang YH, Zhou GW, Bai ZG, Zhang Z, Feng SQ. Synthesis of nano-scale silicon wires by excimer laser ablation at high temperature. Solid State Communications. 1997;**105**:403

[27] Wang N, Tang YH, Zhang YF, Lee CS, Bello I, Lee ST. Si nanowires grown from silicon oxide. Chemical Physics Letters. 1999;**299**:237-242

[28] Juhasz R, Kylmeanen K, Galeckas A, Linnros J. Size-reduced silicon nanowires: Fabrication and electrical characterization. Materials Science and Engineering. 2005;**25**:733-737

[29] Hochbaum AI, Gargas D, Hwang YJ, Yang P. Single crystalline mesoporous silicon nanowires. Nano Letters. 2009;**9**:3550-3554

[30] Kumar D, Srivastava SK, Singh PK, Sood KN, Singh VN, Dilawar N, Husain M. Room temperature growth of wafer-scale silicon nanowire arrays and their Raman characteristics. Journal of Nanoparticle Research. 2010;**12**:2267-2276

[31] Srivastava SK, Kumar D, Singh PK, Kar M, Kumar V, Husain M. Excellent antireflection properties of vertical silicon nanowire arrays. Solar Energy Materials & Solar Cells. 2010;**94**:1506-1511

[32] Najar A, Charrier J, Pirasteh P, Sougrat R. Ultra-low reflection porous silicon nanowires for solar cell applications. Optics Express. 2012;**20**:16861-16870

[33] Najar A, Slimane A B, Hedhili MN, Anjum D, Sougrat R, Ng TK, Ooi BS. Effect of hydrofluoric acid concentration on the evolution of photoluminescence characteristics in porous silicon nanowires prepared by Ag-assisted electroless etching. Journal of Applied Physics. 2012;**112**:033502-033502

[34] Peng KQ, Yan YJ, Gao SP, Zhu J. Synthesis of large-area silicon nanowire arrays via self-assembling nanoelectrochemistry. Advanced Materials. 2002;**14**:1164

[35] Qiu T, Wu XL, Mei YF, Wan GJ, Chu PK, Siu GG. From Si nanotubes to nanowires: synthesis, characterization, and self-assembly. Journal of Crystal Growth. 2005;**277**:143-148

[36] Qu Y, Zhou H, Duan X. Porous silicon nanowires. Nanoscale. 2011;**3**:4060

[37] Zhang ML, Peng KP, Fan X, Jie JS, Zhang RQ, Lee ST, Wong NB. Preparation of large-area uniform silicon nanowires arrays through metal-assisted chemical etching. Journal of Physical Chemistry C. 2008;**112**:4444-4450

[38] Zhong X, Qu Y, Lin YC, Liao L, Duan X. Unveiling the formation pathway of single crystalline porous silicon nanowires. ACS Applied Materials & Interfaces. 2011;**3**:261-270

[39] To WK, Tsang CH, Li HH, Huang Z. Fabrication of n-type mesoporous silicon nanowires by one-step etching. Nano Letters. 2011;**11**:5252-5258

[40] Kooij ES, Butter K, Kelly J. Silicon etching in HNO_3HF solution: Charge balance for the oxidation reaction. Journal of Electrochemical and Solid-State Letters. 1999;**2**:178-180

[41] Turner DR. On the mechanism of chemically etching germanium and silicon. Journal of the Electrochemical Society. 1960;**107**:810-816

[42] Cullis AG, Canham LT, Calcott PD. The structural and luminescence properties of porous silicon. Journal of Applied Physics. 1997;**82**:909

[43] Lin L, Guo S, Sun X, Feng J, Wang Y. Synthesis and photoluminescence properties of porous silicon nanowire arrays. Nanoscale Research Letters. 2010;**5**:1822-1828

[44] Kontkiewicz AJ, Kontkiewicz AM, Siejka J, Sen S, Nowak G, Hoff AM, Sakthivel P, Ahmed K, Mukherjee P, Witanachchi S, Lagowski J. Evidence that blue luminescence of oxidized porous silicon originates from SiO_2. Applied Physics Letters. 1994;**65**:1436

[45] Zhao Y, Yang D, Sang W, Li D, Jiang M. Photoluminescence of oxidized porous silicon under UV-light illumination. Materials Science and Engineering B. 2005;**116**:95-98

[46] Bai ZG, Yu DP, Wang JJ, Zou YH, Qian W, Fu JS, Feng SQ, Xu J. You LP. Materials Science and Engineering B. 2000;**72**:117

[47] Lin LH, Sun XZ, Tao R, Li ZC, Feng JY, Zhang ZJ. Femtosecond inverse Faraday effect in magnetic ionic liquid [bmim]FeC_{14}. Journal of Applied Physics. 2011;**110**:073109

[48] Bashouti MY, Pietsch M, Brönstrup G, Sivakov V, Ristein J, Christiansen S. Heterojunction based hybrid silicon nanowire solar cell: Surface termination, photoelectron and photoemission spectroscopy study. Progress in Photovoltaics. 2014;**22**:1050-1061

[49] Dai X, Chen T, Cai H, Wen H, Sun Y. Improving performance of organic-silicon heterojunction solar cells based on textured surface via acid processing. ACS Applied Materials & Interfaces. 2016;**8**:14572-14577

[50] He J, Gao PQ, Liao MD, Yang X, Ying ZQ, Zhou SQ, Ye JC, Cui Y. Realization of 13.6% efficiency on 20 μm thick Si/organic hybrid heterojunction solar cells via advanced nanotexturing and surface recombination suppression. ACS Nano. 2015;**9**:6522-6531

[51] Kim E, Cho Y, Sohn A, Hwang H, Lee YU, Kim K, Park HH, Kim J, Wu JW, Kim DW. Mie resonance-modulated spatial distributions of photogenerated carriers in poly(3-hexylthiophene-2,5-diyl)/silicon nanopillars. Scientific Reports. 2016;**6**:29472

[52] Choi D, Choi A, Seo JH, Seo K. Embedded metal electrode for organic−inorganic hybrid nanowire solar cells, Han-Don Um. ACS Nano. 2017;**11**:6218-6224

[53] Liu R, Wang J, Sun T, Wang M, Wu C, Zou H, Song T, Zhang X, Lee ST, Wang ZL, Sun B. Silicon nanowire/polymer hybrid solar cell-supercapacitor: A self charging power unit with a total efficiency of 10.5%. Nano Letters. 2017;**17**:4240-4247

[54] Zhang J, Zhang Y, Song T, Shen X, Yu X, Lee ST, Sun B, Jia B. High-performance ultrathin organic–inorganic hybrid silicon solar cells via solution-processed interface modification. ACS Applied Materials & Interfaces. 2017;**9**:21723-21729

[55] Sharma M, Pudasaini PR, RuizZepeda F, Elam D, Ayon AA. Ultrathin, flexible organic–inorganic hybrid solar cells based on silicon nanowires and PEDOT:PSS. ACS Applied Materials & Interfaces. 2014;**6**:4356-4363

Chapter 10

Microstructure Engineering of Metal-Halide Perovskite Films for Efficient Solar Cells

Weidong Zhu, Jingjing Chang, Chunfu Zhang,
Jincheng Zhang and Yue Hao

Additional information is available at the end of the chapter

http://dx.doi.org/10.5772/intechopen.74225

Abstract

Photovoltaic (PV) devices with metal-halide perovskite films, namely perovskite solar cells, have become a rapidly rising star due to low cost of raw materials, simple solution processability, and swiftly increased power conversion efficiency (PCE). The PCEs so far certified have gone beyond 22% for perovskite solar cells and 23.6% for tandem devices with single crystalline silicon solar cells, which offer a promising PV technology for practical applications. In principle, performance of perovskite solar cells are largely dominated by the optoelectronic properties and stability of metal-halide perovskite films, which are determined by the microstructure features of the films in turns. In this chapter, we will describe the recently developed strategies on microstructure engineering of metal-halide perovskite films for efficient perovskite solar cells.

Keywords: metal-halide perovskites, polycrystalline film, microstructure engineering, power conversion efficiency, solar cells

1. Introduction

Photovoltaic (PV) devices with metal-halide perovskites that follow the formula of ABX_3 [$A = H_3NH_3$ (MA), $NH = CHNH_3$ (FA), or Cs; $B = Pb$, Sn; X = I, Br, and Cl] or their alloyed counterparts [1, 2], namely perovskite solar cells, have swiftly emerged as a focal point of PV community owing to their low-cost, easy and large-scale fabrication, swiftly improved power conversion efficiency (PCE) to over 22% from 3.8% in just few years [3], and feasibility of tandem with well-developed PV technologies [4]. Those combined merits basically come from exceptional optoelectronic features of metal-halide perovskite films such as high absorption coefficient, tunable bandgap, long and balanced carrier diffusions, ambipolar transport of charge carriers, tolerance of defects [5, 6], along with widely available raw materials and feasibility of film deposition via solution routes.

Critical to fabrication of efficient perovskite solar cells is deposition of high-quality metal-halide perovskite films with tailored microstructural features that mainly refer to surface coverage, grain size, texture, surface roughness, and so on [7, 8]. All of them are previously revealed to play extremely important roles for ultima device performance and even stability. For example, as for surface coverage of metal-halide perovskite films, Snaith et al. [9] revealed that the lowest average efficiency is observed for the lowest coverage of $MAPbI_{3-x}Cl_x$ film, and vice versa. In terms of grain size of metal-halide perovskite films, Huang et al. [10] demonstrated that solvent annealing route can effectively increase the grain size and crystallinity of $MAPbI_3$ films, which resulted in much improved material electronic property and device performance. Similarly, Ohkita et al. [11] showed that the cells exhibited improved PV parameters with increase of grain size of $MAPbI_3$ films. In particular, reduced trap-assisted recombination resulted from large-sized grains gave rise to high open-circuit voltage (V_{oc}) for the cells. In addition, Park et al. [12] declared that as $MAPbI_3$ grain size decreases, the photocurrent density-voltage (J-V) hysteresis of perovskite solar cells tended to be more obvious. On the part of texture of metal-halide perovskite films, Jo et al. [13] successfully fabricated $MAPbI_3$ films with two different crystal orientations with respect to the substrate by using two different organic precursors (MAI and MACl). They found that the PV performance is directly related to crystal orientation of $MAPbI_3$ due to anisotropy of charge transfer in the crystal, suggesting that control of crystal orientation of metal-halide perovskites is important to realize high-performance cells. With regard to surface roughness, Kwok et al. [14] prepared a bilayer-structured $MAPbI_3$ film, which is compose of a mesostructured underlayer and a dense upper layer. They revealed that higher V_{oc} of cell is directly related to smaller root mean squares (RMS) of $MAPbI_3$ upper layer. Overall, a metal-halide perovskite film with the desired microstructures of full surface coverage, large grain size, textured feature, and smooth surface, is highly desirable for efficient perovskite solar cells.

At this point, much research attention has been focused on microstructure engineering of metal-halide perovskite films. In the past year, there have been rapid progresses in this research field. Therefore, in this chapter we will focus our attention on the review of recently developed strategies on microstructure engineering of metal-halide perovskite films aiming to realize high-performance and stable perovskite solar cells. In particular, in the first section we begin with a general introduction to basic fundamentals of metal-halide perovskite materials that used as the absorbers for solar cells. In the second section, we come to the discussion of deposition technologies of metal halide perovskite films. And in the third section, we will discussion the recently developed strategies toward the microstructure engineering of metal-halide perovskite films by modifying the deposition technologies of metal halide perovskite films.

2. Basic fundamentals of metal-halide perovskites for solar cells

2.1. Crystal structures

The mineral perovskite named for Russian mineralogist Lev Perovski, possesses the chemical formula of $CaTiO_3$. Compounds with the same crystal structure, i.e., ABX_3 are called perovskites. For a cubic unit cell, eight corners of the cube are occupied by A-cations and a B-cation is resided in its body center. The B-cation is encircled by six X-anions that located at the face centers of the cube unit cell. The six X-anions and one B cation form an octahedral $[MX_6]^{4-}$ cluster. By changing the element types at A and/or B sites, we can obtain the perovskite variants with a variety of physical properties, such as semiconductive, superconductive, ferroelectric, antiferroelectric, etc. [16]. For the ones used for solar cells, the large cation at A site is commonly chosen to be organic cations such as methylammonium (MA, $CH_3NH_3^+$), formamidinium (FA, $HC(NH_2)_2^+$), phenylammonium (PhA, $C_2H_5NH_3^+$), or inorganic Cs^+ cation [17, 18], as shown in **Figure 1(a)**. A polar organic cation can yield a larger dielectric constant than an all inorganic system. However, organic cations are companied by poor stability of the compounds [19]. A large atom of Pb or Sn is generally settled down at B site, which then couples with halide X anions including Cl^-, Br^-, and I^- to form metal-halide perovskite. By designing the component ratios, a series of metal-halide perovskite variants can be realized, which thus suggests an interesting and effective way to develop new materials [20]. In addition, replacing the halide at X sites with BF^{4-}, PF^{6-}, or SCN^- can also engineer the materials' properties; especially in boosting their stability [17].

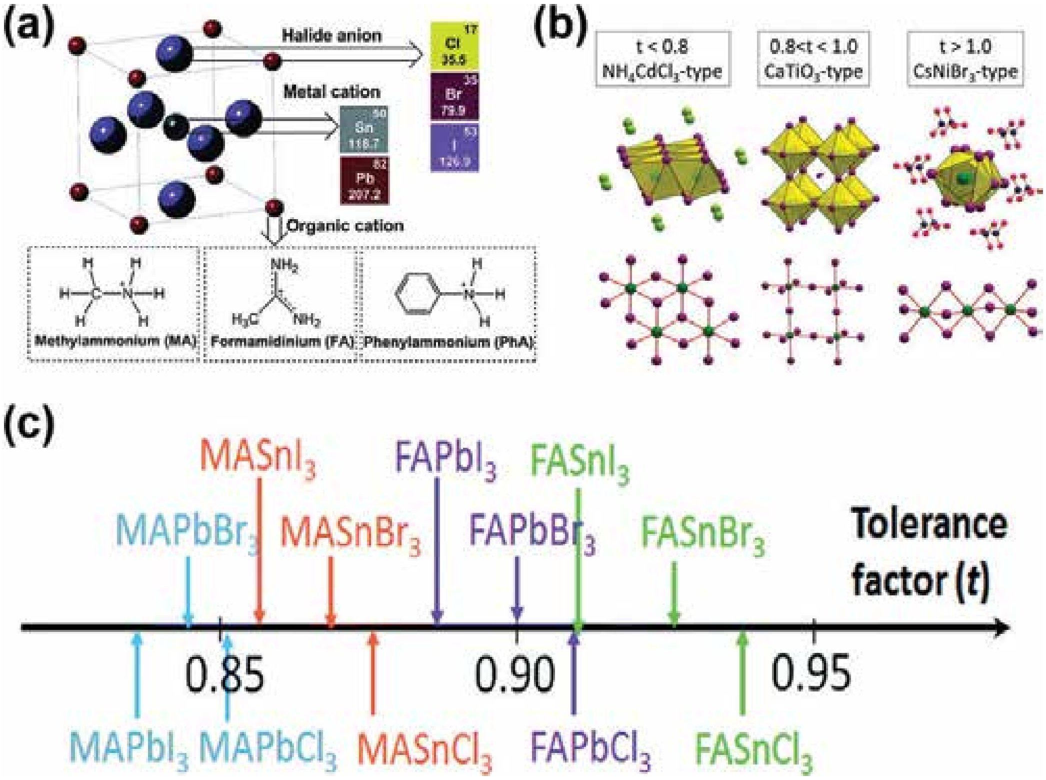

Figure 1. (a) Schematic crystal structure of metal-halide perovskites. Reproduced with permission from Ref. [17]. Copyright 2015, Royal Society of Chemistry. (b) Structural motifs for ABX_3 metal-halide perovskites as a function of the ionic radii of A^+, B^{2+}, and X^- ions expressed with a tentative tolerance factor value. Reproduced with permission from ref. [22]. Copyright 2015, American Chemical Society. (c) Tolerance factors (t) of a series of metal-halide perovskites. Reproduced with permission from Ref. [15]. Copyright 2015, Royal Society of Chemistry.

The structural formability and stability of metal-halide perovskites is guided by its geometric tolerance factor (t), $t = (r_A + r_X)/[\sqrt{2}(r_B + r_X)]$, where r_A, $r_{B,}$ and r_X are the effective ionic radii of A, B, and X, respectively [21]. As indicated in **Figure 1(b)**, for the ones with t close to 1, they prefers an ideal cubic structure, while they distorts into a low-symmetry structure, when t is smaller than 1. And, the ones with t value between 0.8 and 1.0 tend to adopt a cubic structure, and photo-inactive non-perovskite structures are formed when the value of t is larger (>1) or smaller (<0.8) [22]. **Figure 1(c)** gives the estimated t of a series of metal-halide perovskites [23]. We can see that all the values are in the range of 0.8–1, which is a universal feature of perovskite structure. Replacing Pb with Sn appears to be beneficial to increase t; yet it induces the serious decrease of the compound stability. This mainly comes from the fact that t is not the only determinant factor, and Pb is inerter to oxidization than Sn [6]. In addition, as for organic cation, it seems that both charge distribution and size dominant the crystal structure. Previous works revealed that MA and FA benefit to stabilized perovskite structure, while the others with similar size, such as $CH_3CH_2NH_3^+$, $(CH_3)_2NH_2^+$ are easily induce the formation of a non-perovskite structure [22].

At different temperatures, a metal-halide perovskite crystal usually exhibits α, β and γ phases, as schematized in **Figure 2** [24]. For example, the α to β phase transition for $MAPbI_3$ happens at 330 K, while the β to γ phase transition appears at 160 K. Noting that a non-perovskite δ phase was also found in some metal-halide perovskite variants such as $HC(NH_2)_2PbI_3$, $FAPbI_3$, $CsPbI_3$, and $CsSnI_3$. The B–X bond of δ phase is broken. So it cannot be derived from the α phase by B–X–B bond angle distortion [25].

2.2. Electronic structures

Electronic band structures of metal-halide perovskites were initially investigated by Koutselas et al. [26] using band structure calculations. Then, Umebayashi et al. [27] studied the electronic band structures of cubic phase metal-halide perovskites based on ultraviolet photoelectron spectroscopy and first principles density functional theory (DFT) band calculation. It has been revealed that valence band maximum (VBM) states of $MAPbX_3$ and $CsPbX_3$ (X = Cl, Br, I) crystals contain Pb 6p-I 5p σ-antibonding orbital, while conduction band minimum (CBM) states compose of Pb 6p-I 5 s σ anti-bonding and Pb 6p-I 5p π antibonding orbitals [27]. Yan et al. [28] conducted the calculations of band structure, partial charge density of VBM and CBM states and (partial) density of states (DOS) of α phase $MAPbI_3$. The results revealed that the direct bandgap locates at the R point. And, Pb has an occupied 6 s orbital below the top of valence bands. This lone pair of s electrons in $MAPbI_3$ maybe accounts for its unique optoelectronic properties. Further, partial charge density and DOS plots indicate that CBM largely compose of Pb p state, while VBM exhibits obvious Pb s and I p antibonding feature. This means that electronic structure of $MAPbI_3$ uniquely has the dual nature of ionic and covalent properties. In addition, the electronic states resulted from the organic cations are away from band edge. It means that organic cations have a negligible impact on basic electronic structures of $MAPbI_3$ [25].

2.3. Optoelectronic properties

2.3.1. Light absorption and bandgap

The feature of strong absorption over a wide range of spectrum is highly desired for absorber material of PV device, which is conductive to enlarge photocurrent, diminish the usage

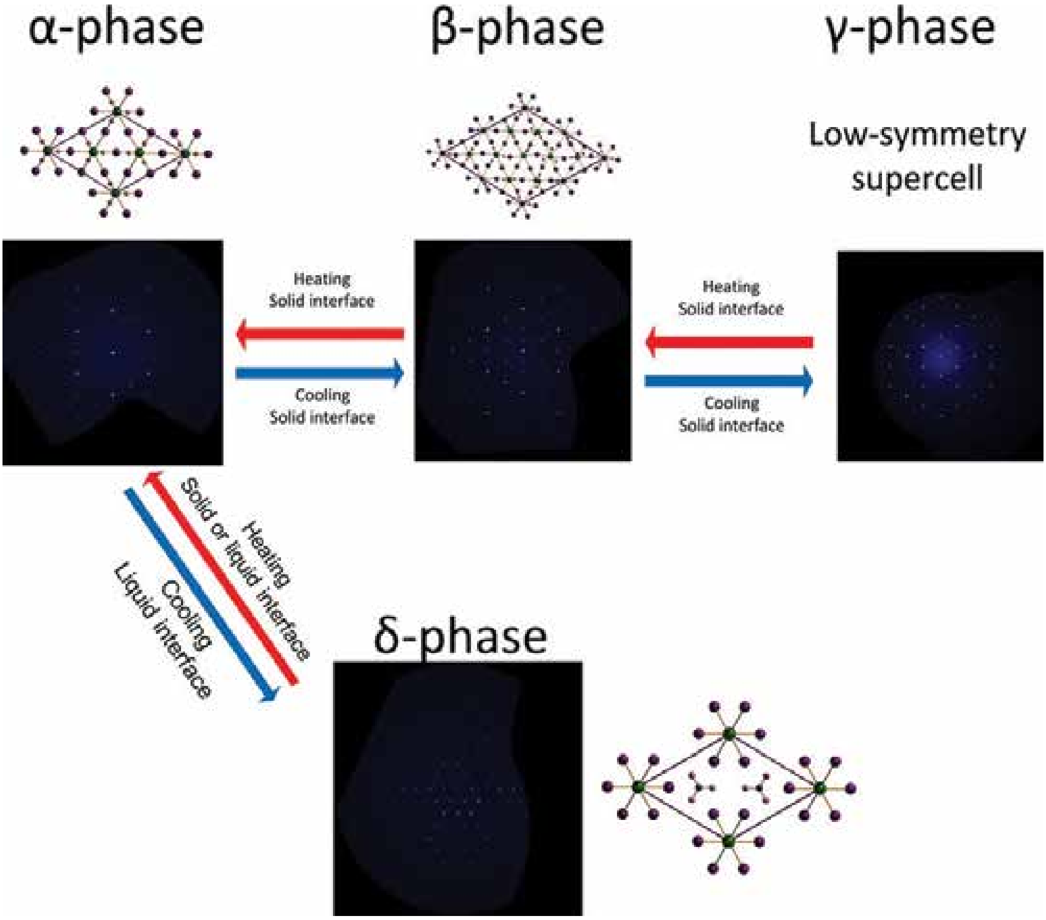

Figure 2. Graphical scheme of phase transitions of MA(Pb,Sn)X_3 materials. Precession images are drawn at [006] view. Reproduced with permission from Ref. [24]. Copyright 2013, American Chemical Society.

amount of raw material, and minimize the charge and energy loss during extraction to electrodes [6]. One highlighted property of metal-halide perovskite materials is their very high absorption coefficient along with sharp onset of absorption edge [2]. Moreover, most of metal-halide perovskite materials are direct bandgap semiconductors [28]. In terms of the most typical $MAPbI_3$, its absorption coefficient exceeds 3.0×10^4 cm^{-1} in the visible range, which means that it only needs 380 nm thin film to absorb 90% of the visible light [2]. In fact, the thickness of light absorption layer for most of perovskite solar cells is around 300–600 nm. In addition, $MAPbI_3$ film shows a very sharp absorption onset, which means the low density of deep states of it. The Urbach energy of $MAPbI_3$ film was estimated to as low as 15 meV, which is comparable to monocrystalline GaAs [29]. The sharp absorption onset of $MAPbI_3$ maybe contribute to the small offset between its optical bandgap (~1.55 eV) and V_{oc} of ultimate devices (~1.10 V) [6].

Another unique property of metal-halide perovskites is their bandgap tunability, which can be realized by substituting the atoms at A, B, or X sites. When MA was replaced with a slightly larger FA, the reduced bandgap from 1.55 to 1.48 eV was observed, corresponding to an absorption edge extended from 800 to 840 nm, as firstly reported by Eperon et al. [30]. And, the photocurrent of the cell with $FAPbI_3$ film can reach up to 23 mA cm^{-2}, because of extended light absorption range. While a smaller Cs^+ at A site gives rise to an increased bandgap of 1.73 eV [31]. For X site, after replacing I^- with Br^- or Cl^-, the bandgap increases to 2.30 eV for $MAPbBr_3$ or 3.12 eV for $MAPbCl_3$, respectively. **Figure 3(a–c)** shows the continuous bandgap variation of $FAPbI_yBr_{3-y}$ ($0 < y < 1$) films. Its absorption onset changes from 840 nm for $FAPbI_3$ to 550 nm for $FAPbBr_3$, corresponding the bandgap increases from 1.48 to 2.13 eV. For B site, a smaller cation size usually results in less bandgap. For example, the bandgap of $MAPbI_3$ decreases to 1.2 eV by replacing the Pb^+ with Sn^+ [24]. Similarly, the bandgap decreases from 1.67 eV for $CsPbI_3$ to 1.30 eV for $CsSnI_3$ and 1.08 eV for $CsGeI_3$ [24].

2.3.2. Long-range ambipolar charge transport

For most of semiconductors, the transport of electrons and holes is unbalanced, due to different effective masses (m_e^* and m_h^*). Surprisingly, numerous independent experimental studies have revealed that well-balanced electron and hole transport is established in metal-halide perovskites, namely ambipolar transport property. First principle calculation also indicates that this fact that electron effective mass ($m_e^* = 0.23\ m_0$) of this type materials is extremely similar to hole effective mass ($m_h^* = 0.29\ m_0$) [32]. Balanced ambipolar transport has an effect on bulk polarization during charge transport and collection; in turns affects PV parameters of perovskite solar cells. Moreover, metal-halide perovskites can convey both n-type and p-type properties when they are used in thin-film devices with different interfacial layers [22]. In addition, long carrier diffusion length of ~100 nm and ~1 μm were revealed

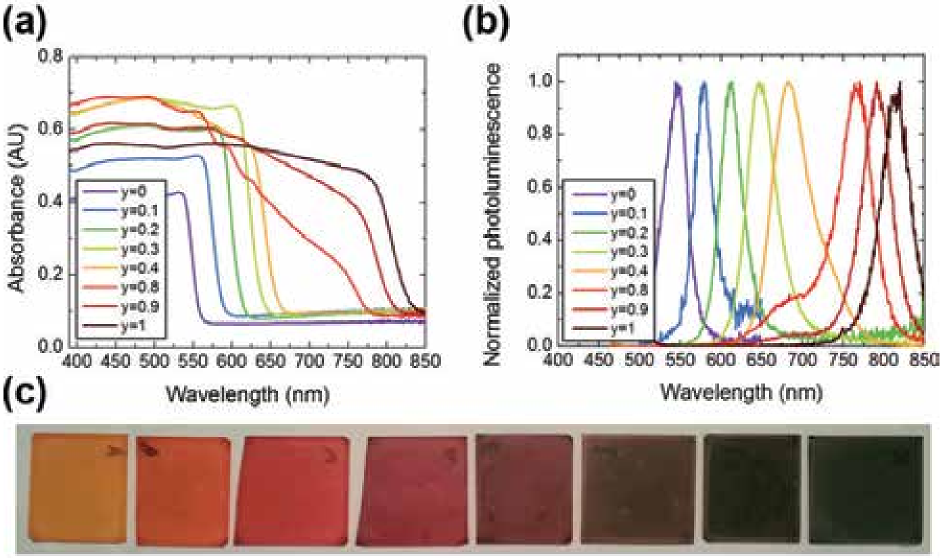

Figure 3. (a) UV-Vis absorbance spectra of $FAPbI_yBr_{3-y}$ metal-halide perovskite films with different y values. (b) Steady-state photoluminescence spectra for the corresponding films. (c) Photographs of the films with y increasing from 0 to 1 (left to right). Reproduced with permission from Ref. [30]. Copyright 2014, Royal Society of Chemistry.

for solution-processed $MAPbI_3$ and $MAPbI_{3-x}Cl_x$ films, which are much larger than that of organic semiconductors. Almost certainly, long diffusion length can bring reduced charge recombination and improved charge collection, thus excellent cell performance [18].

2.3.3. Exciton binding energy

The hybrid nature of metal-halide perovskite materials arise wonders whether incident photons generate free charges or bound excitons. So, the exciton binding energy of metal-halide perovskite materials has been intensively concerned [18]. In the 1990s, theoretical studies have revealed the exciton binding energy to be around 37 meV for $MAPbI_3$ [33]. This value is much lower than that of organic materials with the values ranged from 0.2 to 1 eV. The low binding energy together with long diffusion length maybe account for the high PECs of perovskite solar cells. The low binding energy of metal-halide perovskites is mainly related to their large dielectric constants, which give rise to strong dielectric screening effect [18]. Recently, Hu et al. [34] found that the dielectric constant $MAPbI_3$ is as high as ~32 under dark condition. And, the value can be greatly enhanced (~1000) under photoexcitation as investigated by Juarez-Perez et al. [35]. The high dielectric constant gives rise to strong dielectric screening effect, thus low exciton binding energy.

3. Film formation technologies

Up to now, various processing techniques have been developed to prepare metal-halide perovskite films, as summarized in **Figure 4**. They mainly include one-step spin-coating method, sequential solution deposition method, two-step spin-coating method, vacuum co-evaporation deposition method, sequential vacuum deposition method, and vapor-assisted solution deposition method [36].

The one-step spin-coating method involves spin-coating of a precursor solution containing PbX_2 with a certain amount of MAX firstly (X = I, Br, and Cl). Then, the metal-halide perovskites formed and grew during solvent evaporation. A post-annealing recipe with a temperature of ~100°C was usually required to remove residual solvents and complete crystallization. For this method, the film morphology and quality strongly depend on the processing conditions such as annealing temperature, solution concentration, precursor composition, solvent choice, etc. [36]. Although it is extremely simple, the one-step spin-coating method faces the difficulty to the deposition of pinhole-free metal-halide perovskite films. Solvent engineering is proved to be one of effective routes to overcome this obstacle. Spiccia et al. [37] proposed a fast deposition crystallization method to induce the crystallization of $MAPbI_3$ during spin-coating process. This method includes the spin-coating of $MAPbI_3$ precursor with N,N-dimethylformamide (DMF) as the solvent, followed by dropping anti-solvent such as toluene and chlorobenzene to complete the crystallization of $MAPbI_3$. The anti-solvent decreased the $MAPbI_3$ solubility in DMF solvent, and thereby promoting fast nucleation and crystallization [6]. Later, Jeon et al. [38] designed a mixed γ-butyrolactone and dimethyl sulfoxide (DMSO) as the processing solvent followed by toluene drop-casting. The difference is

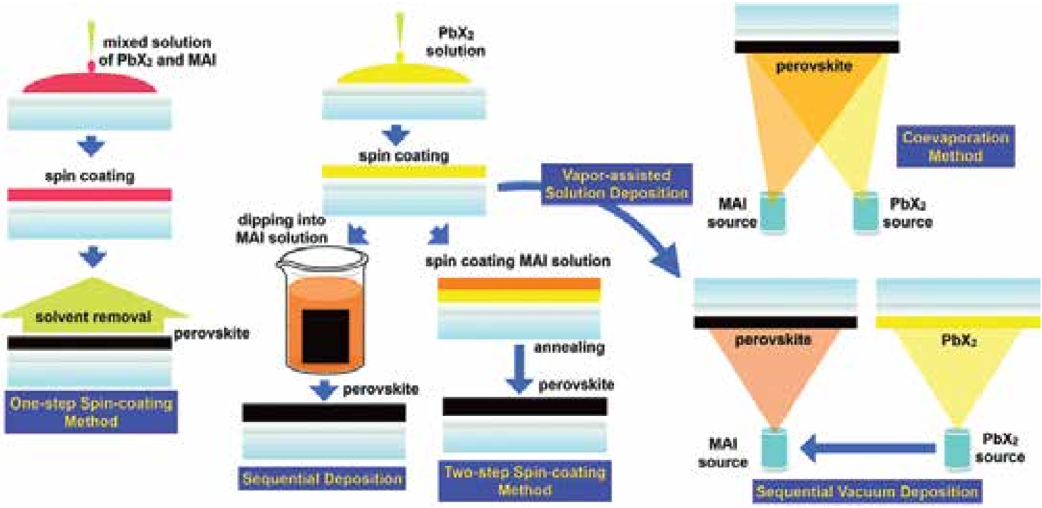

Figure 4. Illustrations of developed processing techniques for deposition of metal-halide perovskite films. Reproduced with permission from Ref. [36]. Copyright 2015, Royal Society of Chemistry.

that a dark brown $MAPbI_3$ film formed immediately after dropping of toluene solvent, while a transparent MAI-PbI_2-DMSO intermediate phase formed firstly after dropping of toluene using the mixed solvent. Both X-ray diffraction (XRD) and Fourier-transform infrared spectroscopy (FTIR) measurements verified the formation of intermediate phase. After being thermal annealed at 100°C for 10 min, intermediate phase film can transform to an extremely uniform and compact $MAPbI_3$ layer [6]. Similarly, Park et al. [39] further developed the intermediate phase route based on Lewis acid adduct of PbI_2, as shown in **Figure 5**. This method eventually resulted in an average PCE of 18.3% from 41 cells and the best value of 19.7%.

The sequential deposition procedure was firstly introduced by Grätzel et al. [40]. And in surprise, it yielded a high PCE of 15%. This method includes the spin-coating of a PbX_2 solution on substrate, followed by drying, and then dipping the substrate into an isopropanol (IPA) solution of MAX to accomplish the reaction in few minutes. Typically, the solutions are 1 M PbI_2 in DMF and MAI in IPA with relative low concentration from 0.004 to 0.006 M. After the dipping step, the residual MAI was rinsed out by IPA. With this method, the films' homogeneity can be dramatically improved and their morphology becomes more controllable than the one-step spin-coating method.

The two-step spin-coating method that is also known as interdiffusion method was proposed by Huang et al. [41]. It can be seen as the one derived from sequential deposition procedure. But, the difference is that metal-halide perovskite is formed by spin-coating an MAI layer on PbX_2 precursor film followed by thermal annealing at 100°C for a relative long time up to 2 h. This method is materials saving, and can synthesize more uniform films than sequential deposition.

Snaith et al. [42] firstly reported the vacuum co-evaporation deposited planar $MAPbI_{3-x}Cl_x$ perovskite solar cells by co-evaporating $PbCl_2$ and MAI in a vacuum thermal evaporation system. The PCEs with a narrow distribution and optimal one of 15.4% were observed in

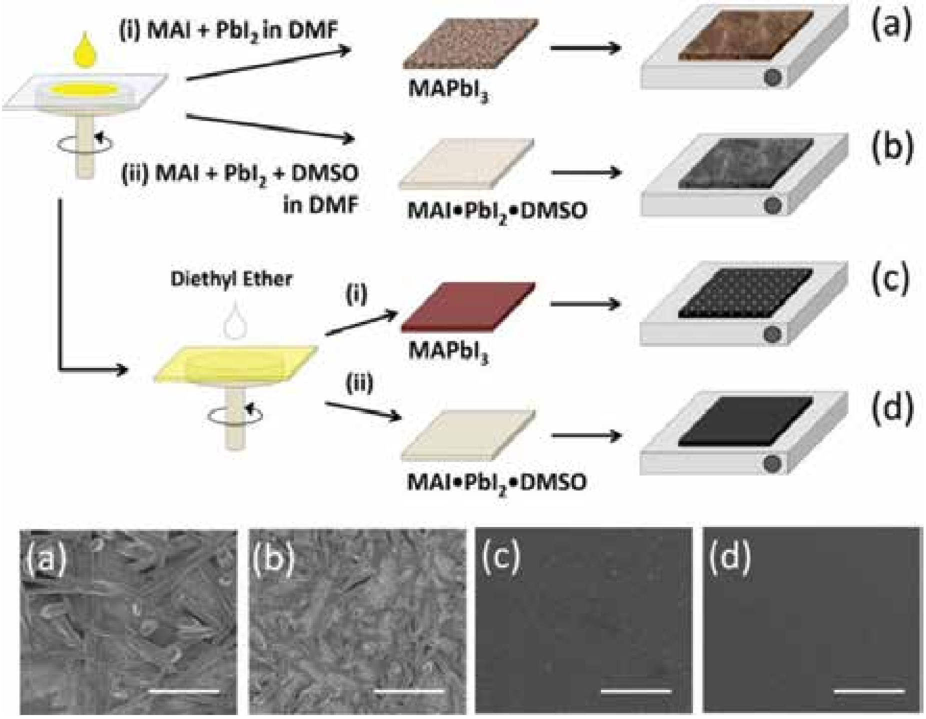

Figure 5. Schematic illustration of processing procedures for MAPbI$_3$ films deposition as well as the corresponding scanning electron microscopy (SEM) images. The MAPbI$_3$ films were deposited by one-step spin-coating of the DMF solution containing (a) MAI and PbI$_2$ or (b) MAI, PbI$_2$, and DMSO. Panels (c) and (d) were prepared by same solution as that in panels (a) and (b), but diethyl ether was dripped during the spinning process. Reproduced with permission from Ref. [39] . Copyright 2015, American Chemical Society.

contrast with that of one-step solution process. Due to its low control accuracy in precursor ratio, the sequential vacuum evaporation technology was further developed via depositing PbCl$_2$ and MAI layer by layer [43]. By heating the substrate during precursor evaporation, a pure-phase, homogeneous, and pinhole-free $CH_3NH_3PbI_{3-x}Cl_x$ film can be synthesized. However, the requirement of high vacuum degree of them inevitably increases the device cost, and thus partially restricts their practical applications.

Vapor-assisted solution deposition is firstly used by Yang et al. [44]. For it, PbI$_2$ film that was pre-deposited via spin-coating route reacted with MAI vapor under atmospheric pressure. The resultant MAPbI$_3$ film was revealed to be extremely smooth, and composed of microscale polycrystallites, delivering to a PCE of 12%.

4. Microstructure engineering of metal-halide perovskite films

The microstructural features of metal-halide perovskite films such as surface coverage, grain size, texture, surface roughness, and so on are previously revealed to play extremely vital roles for determining ultima device performances and even stability. In the past year, there have been rapid progresses in the research field of microstructure engineering of metal-halide perovskite films. In this section, we will focus our attention on the recently developed strategies on microstructure engineering of metal-halide perovskite films aiming to realize high-performance and stable perovskite solar cells.

4.1. Surface coverage engineering of metal-halide perovskite films

The reasons for ensuring surface coverage of metal-halide perovskite film in perovskite solar cells come from the following two reasons. On the one hand, if there are some regions without metal-halide perovskites padding, light will travel directly without absorption, which leads to decreased photocurrent in turns. On the other hand, any existed pinholes inevitably result in direct contact of electron transport layer with hole transport layer, thus resulting in the formation of shutting paths. They will form additional parallel resistors, causing declines in performance parameters of the cell.

The traditional one-step spin-coating method faces the difficulty to yield a uniform and full-coverage metal-halide perovskite film in large areas. Aiming to overcome this issue, some effective modifications have been reported. For example, as given in **Figure 6(a)**, Yu et al. [45] introduced a recrystallization process via DMF vapor fumigation to induce the self-repair of one-step deposited $MAPbI_3$ films with poor coverage and low crystallinity. By adjusting the cycle of recrystallization process, they found that $MAPbI_3$ films with dendritic structures spontaneously transformed to the uniform ones with full coverage and high crystallinity (**Figure 6(b–e)**). Solar cells with these modified $MAPbI_3$ films yielded reproducible average PCE of 10.25 ± 0.90% and the optimal one of 11.15%, which is both much higher than that of non-modified $MAPbI_3$ films (**Figure 6(f–d)**). In addition, the J-V hysteresis in the measurement of cell performance can also be effectively alleviated. The authors attributed this desired feature to improve the quality of $MAPbI_3$ films in the optimized devices.

Cui et al. [46] discovered that methylamine (CH_3NH_2) gas can trigger defect-healing of $MAPbI_3$ films via room-temperature ultrafast, reversible chemical reaction of $MAPbI_3$ with CH_3NH_2 gas. They revealed that healing of $MAPbI_3$ films can be ascribed to the formation and reconstruction of an intermediate $MAPbI_3{\cdot}xCH_3NH_2$ liquid phase during perovskite-gas interaction. $MAPbI_3$ film processed by one-step spin-coating method using DMF as solvent is composed of dendrite-like $MAPbI_3$ crystals. And voids with size up to several micrometers between them can be clearly found. After CH_3NH_2 induced defect-healing treatment, dendrite-like crystals and voids almost disappeared and a dense, smooth $MAPbI_3$ film has formed. And, AFM measurement further revealed that the healed film has a very dense and smooth surface, with a RMS roughness of ~6 nm. Benefiting from improved surface coverage of $MAPbI_3$ films by methylamine-induced defect-healing, obvious increase of PCE from 5.7 to 15.1% were realized for the cells. Afterwards, this interesting chemical reaction of CH_3NH_2 gas with metal-halide perovskite was investigated in detailed and extended for further uses such as reduction of intrinsic defect concentration of $MAPbI_3$ films [47], realization of solvent- and vacuum-free deposition of $MAPbI_3$ films [48], and so on.

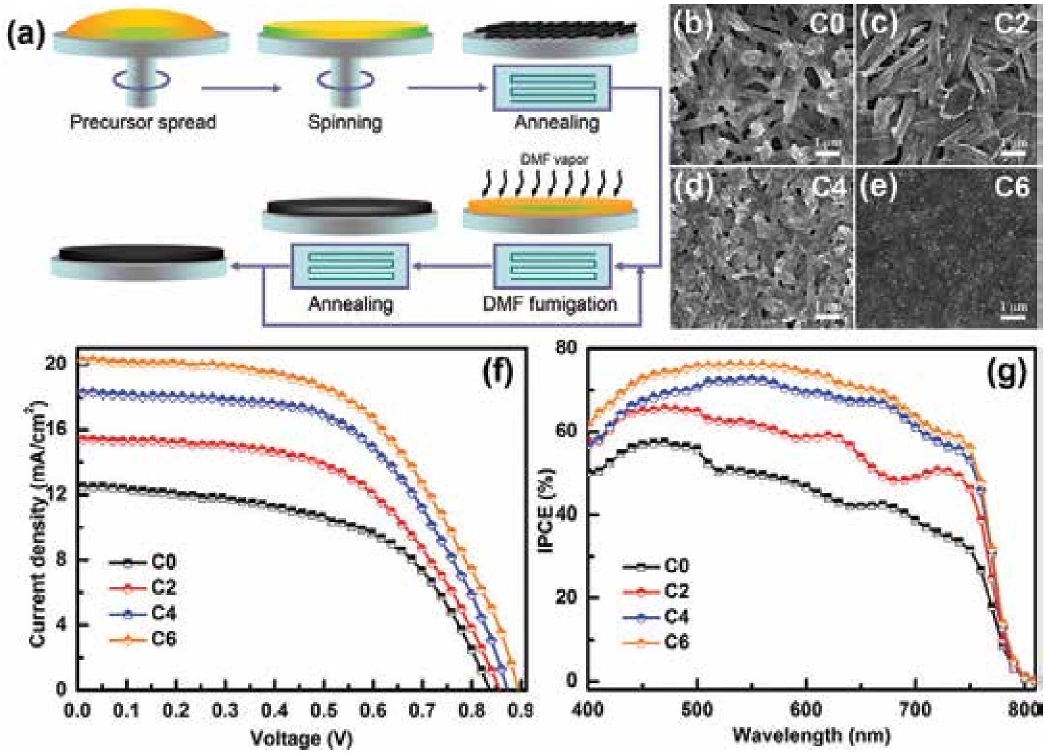

Figure 6. (a) Schematic processing procedure for $MAPbI_3$ film deposition (C0) and recrystallization *via* DMF vapor fumigation for 2 (C2), 4 (C4), and 6 (C6) cycles. (b–e) Surficial SEM images of samples C0, C2, C4, and C6. (f) J-V curves and (g) IPCE spectra of the devices based on samples of C0, C2, C4, and C6, respectively. Reproduced with permission from Ref. [45]. Copyright 2015, Royal Society of Chemistry.

4.2. Grain size engineering of metal-halide perovskite films

Increasing theoretical and experimental evidences indicate that, similar to well-developed thin-film PV devices such as CdTe and $Cu(InGa)Se_2$, primary energy loss in perovskite solar cells is also ascribed to non-radiative recombination of carriers at undesirable trap states. In general, for polycrystalline perovskite films trap states mainly come from crystal imperfections especially such as grain boundaries and intragranular defects [49, 50]. While number of grain boundaries is inversely proportional to average grain size for polycrystalline film, so numerous works have been focused on increasing grain size of metal-halide perovskite films by modifying deposition technologies of metal halide perovskite films.

For example, as shown in **Figure 7**, Yu et al. [49] demonstrated that a homogeneous cap-mediated crystallization with face-to-face configuration can control the crystallization kinetics of $MAPbI_3$ films in one-step spin-coating method. They found that homogeneous caps, especially the ones with low surface roughness, can effectively retard the nucleation rate, promote growth, and prevent composition loss of $MAPbI_3$ grains. Thus, pinhole-free $MAPbI_3$ films can be formed, which have many desirable features, such as greatly enlarged grains, significantly

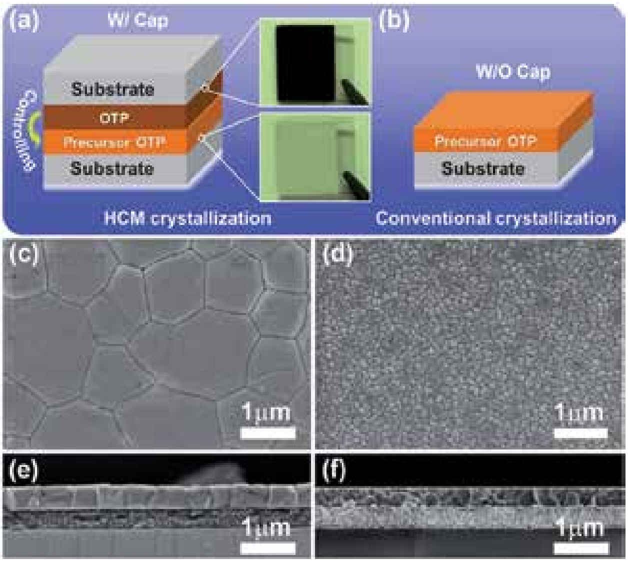

Figure 7. (a) Illustration of homogeneous cap-mediated crystallization configuration, where a crystallized $MAPbI_3$ on TiO_2/FTO substrate is placed face to face on precursor $MAPbI_3$ film. (b) Illustration of conventional crystallization configuration. Top-view and cross-sectional SEM images of $MAPbI_3$ films prepared by (c, e) homogeneous cap-mediated crystallization and (d, f) conventional crystallization, respectively. Reproduced with permission from Ref. [49]. Copyright 2016, Royal Society of Chemistry.

improved crystallinity, preferred (110) orientation, vertically aligned grain boundaries, and proper stoichiometry. As a result, planar-resultant heterojunction solar cells yielded a much enhanced average PCE of 17.87%. It should be noted that large fill factors (FFs) were observed in these efficient cells. In subsequent work, they revealed that PbI_2 heterogeneous cap can also realize $MAPbI_3$ films with large-sized grains [51]. Improved PCE was thus realized because of more efficient transport of charge carriers and decreased non-radiative recombination in corresponding devices. Overall, those works suggest a promising strategy to engineer grain size of metal-halide perovskite films.

In addition to crystallization process control, post-treatment strategies were also developed to engineer grain size of metal-halide perovskite films. For example, obvious grain coarsening via Ostwald ripening in one-step deposited $MAPbI_3$ film can be realized by post-synthesis high-temperature heating treatment assisted with additionally deposited CH_3NH_3I layer [50]. The grain coarsening via Ostwald ripening was revealed to be related to the heating treatment parameters (temperature and time). By optimizing them, the film with average grain size of ~2 μm, much increased crystallinity, and proper stoichiometry can be achieved. Due to those characteristics, defect states along with recombination centers were greatly reduced, and carrier transport and injection properties were much improved. So, efficiency of corresponding planar heterojunction solar cells can be boosted from 14.54 to 16.88%. Then, the same post-treatment recipe was used for thick $MAPbI_3$ films, and a same grain coarsening was observed in them. So post-treatment recipe gives the fact that thickening the absorb layer of cells to realize more sufficient absorption avoids serious aggravation of charge recombination. By further optimizing the thickness of coarsened $MAPbI_3$ films, highly efficient cells with relatively excellent reproducibility and the optimal efficiency of 19.24% were realized by Yu. et al. [50]. Afterward, a similar MABr treatment converts $MAPbI_3$ thin films to high-quality $MAPbI_{3-x}Br_x$ thin films following an Ostwald ripening process as reported by Zhao et al. [52]. But, they found that similar process is ineffective when replacing MABr with MAI. This phenomenon mainly comes from the fact that low-concentration MAI solution was used and low post-treatment temperature was adopted in their experiments. So, further investigations are needed to clarify those factors. More recently, Jen et al. [53] reported a simple pseudohalide-induced film retreatment technology as passivation for preformed $MAPbI_3$ film. They found that the retreatment process yields a controllable decomposition-to-recrystallization evolution of $MAPbI_3$ film. Corresponding, it remarkably enlarges grain size of the film in all directions, as well as improving crystallinity and hindering trap density.

4.3. Texture engineering of metal-halide perovskite films

As to polycrystalline films, orientation of crystal axis in each grain is another important microstructural feature that dominates their physical properties. Films with aligned crystal axes are so-called textured ones. They possess a single-crystal-like nature along crystal axis, so an enhancement in physical properties is expected for them. In general, ordinarily prepared polycrystalline films are composed of grains with random orientation. Methodology that is explored to develop texture to improve functional properties of polycrystalline films is known as texture engineering. Specifically, one-step deposited metal-halide perovskite films are similarly characterized with randomly oriented grains. Hence, texture engineering is of particular importance to modify their electrical and optical properties, and hence further improve the performance of ultimate cells.

Yan et al. [54] reported that reaction of $HPbI_3$ with low partial pressure MA gas can form a textured $MAPbI_3$ film with high crystallinity. The film exhibits much higher both thermal and moisture stability than the one prepared from MAI + PbI_2. Further investigation revealed that large Pb–N binding energy of ~80.04 kJ mol^{-1} results in a liquefied state after MA adhesion on $MAPbI_3$. And, a highly textured $MAPbI_3$ film is formed when excess MA expeditious are released. Cao et al. [55] found that MACl-containing precursor can yield $MAPbI_3$ film with strong (110) preferred orientation. The $MAPbI_3$ films were used for typical planar solar cells and delivered an impressive average efficiency of 16.63 ± 0.49% and champion efficiency of 17.22%. Yu et al. [56] demonstrated that face-down annealing of one-step deposited precursor films can enable the formation of (110) textured $MAPbI_3$ films consisting of high-crystallinity, well-ordered, micrometer-sized grains that span vertically the entire film thickness, as shown in **Figure 8**. Such microstructural features induced dramatically decreased nonradiative recombination sites as well as greatly improved transport property of charge carries in the films compared with that of the non-textured ones obtained by conventional annealing route. As a consequence, planar heterojunction perovskite solar cells with these textured $MAPbI_3$ films exhibit much improved PCE along with small hysteresis and excellent stability.

4.4. Surface roughness engineering of metal-halide perovskite films

Metal-halide perovskite film was usually sandwiched between electron-transporting layer and hole-transporting layer in perovskite solar cell. And, one of them has to be deposited

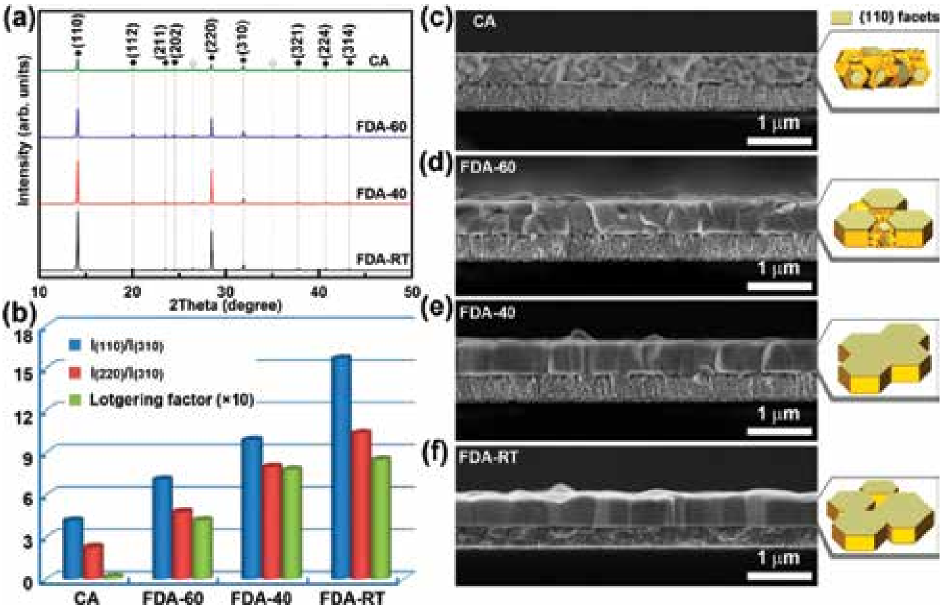

Figure 8. (a) XRD patterns of samples CA, FDA-60, FDA-40, and FDA-RT, respectively. (b) Corresponding histograms of XRD peak intensity ratios of (110) to (310) planes and (220) to (310) planes as well as calculated Lotgering factors. (c–f) cross-sectional SEM images of samples CA, FDA-60, FDA-40, and FDA-RT. Left inset describes the stereoshape model proposed for $MAPbI_3$ grains on TiO_2/FTO substrate. The facets are marked in brown for clarity. The samples with the preheating temperatures of room temperature (RT), 40, and 60°C were labeled as FDA-RT, FDA-40, and FDA-60, respectively. Reproduced with permission from Ref. [56]. Copyright 2017, American Chemical Society.

sequentially on metal-halide perovskite layer. So, surface roughness of metal-halide perovskite film has a significant impact on the cell's interface morphology. A roughened interface that resulted from rough metal-halide perovskite layer would strengthen internal light scattering [57]. And, a large interface area also benefits charge transport [14]. However, high surface roughness of metal-halide perovskite layer will increase short-circuiting possibility of device existing between silver electrode and metal-halide perovskite layer, in the case that electron-transporting layer or hole-transporting layer cannot fully cover the metal-halide perovskite film. In other words, a metal-halide perovskite layer with high roughness requires a thick electron-transporting layer or hole-transporting layer to eliminate short-circuiting. On the contrary, a thin one is preferred to ensure a reasonable FF. So, there is compromise in surface roughness of metal-halide perovskite film as far as cell performance is concerned, and some exploratory works have been undertaken. For example, one the one hand, Meng et al. [58] introduced a hot-pressing method that can transform $MAPbI_3$ film with rough surface to be a smooth one, and pinholes in original film can be cured effectively. This modified $MAPbI_3$ morphology is conductive to improve charge carrier transport and eliminate charge carrier recombination in perovskite solar cells. Moreover, much improved performances with high PCEs of 10.84 and 16.07% are thus realized in hole-transporting-layer-free and spiro-OMeTAD-based cells, respectively. Yu et al. [59] found that spray-assisted process instead of commonly used dipping process in a two-step spin-coating method can effectively reduce roughness of $MAPbI_3$ films. Experimental results demonstrated that the cells' average V_{oc} can be enhanced from 0.823±0.105 V to 0.940±0.008 V by spray-assisted process. It benefits from low leakage possibility between hole-transport layer and mesoporous TiO_2 layer when a smooth and pinhole-free $MAPbI_3$ has successfully formed. Finally, average PCEs of mesoporous cells could be promoted by 25% approximately. One the other hand, Chen et al. [60] reported a novel $MAPbI_3$ film with a dense under-layer and a porous upper-layer that was formed by using a thin mesoporous TiO_2 seeding layer and a gas-assisted crystallization method. This novel multitiered nanostructure allows for greatly improved light harvesting for wavelengths exceeding 500 nm, as well as a more effective interfacial charge separation for perovskite solar cells. The combination of these factors culminated in average PCEs over 15% and average short-circuit current density exceeded 22 mA cm^{-2}.

5. Conclusions

In summary, metal-halide perovskite films have many excellent optoelectronic properties such as high absorption coefficient, tunable bandgap, long and balanced carrier diffusions, ambipolar transport of charge carriers, tolerance of defects, along with capacity for film deposition via either solution or vacuum-based methods including one-step spin-coating method, sequential deposition method, two-step spin-coating method vacuum coevaporation deposition method, sequential vacuum deposition method, and vapor-assisted solution deposition method. Those desired features make them promising for high-performance and low-cost perovskite solar cells. The microstructural features that mainly refer to surface coverage, grain size, texture, surface roughness, and so on are vital in determining the performance of perovskite solar cells. Specifically, the ones with full surface coverage, large grain size, textured feature, and smooth surface, are highly desirable for efficient devices. Some important progresses in microstructure engineering of metal-halide perovskite films are described in this chapter, which will promote systematically understanding the role of microstructure engineering in the progress of perovskite solar cells.

Acknowledgements

This work was supported primarily by National Natural Science Foundation of China under Grant 61334002 and 61106063, and Class General Financial Grant from the China Postdoctoral Science Foundation (Grant No. 2016M602771).

Conflict of interest

The authors declare no competing financial interest.

Author details

Weidong Zhu*, Jingjing Chang, Chunfu Zhang*, Jincheng Zhang and Yue Hao

*Address all correspondence to: wdzhu@xidian.edu.cn and cfzhang@xidian.edu.cn

Wide Bandgap Semiconductor Technology Disciplines State Key Laboratory, School of Microelectronics, Xidian University, Xi'an, PR China

References

[1] Gao P, Gratzel M, Nazeeruddin MK. Organohalide lead perovskites for photovoltaic applications. Energy & Environmental Science. 2014;**7**(8):2448-2463. DOI: 10.1039/C4EE00942H

[2] Green MA, Ho-Baillie A, Snaith HJ. The emergence of perovskite solar cells. Nature Photonics. 2014;**8**:506-514. DOI: 10.1038/nphoton.2014.134

[3] Correa-Baena JP, Abate A, Saliba M, Tress W, Jesper Jacobsson T, Gratzel M, Hagfeldt A. The rapid evolution of highly efficient perovskite solar cells. Energy & Environmental Science. 2017;**10**(3):710-727. DOI: 10.1039/C6EE03397K

[4] Hörantner MT, Leijtens T, Ziffer ME, Eperon GE, Christoforo MG, McGehee MD, Snaith HJ. The potential of multijunction perovskite solar cells. ACS Energy Letters. 2017;**2**(10):2506-2513. DOI: 10.1021/acsenergylett.7b00647

[5] Yamada Y, Nakamura T, Endo M, Wakamiya A, Kanemitsu Y. Photocarrier recombination dynamics in perovskite $CH_3NH_3PbI_3$ for solar cell applications. Journal of the American Chemical Society. 2014;**136**(33):11610-11613. DOI: 10.1021/ja506624n

[6] Xiao Z, Yuan Y, Wang Q, Shao Y, Bai Y, Deng Y, Dong Q, Hu M, Bi C, Huang J. Thin-film semiconductor perspective of organometal trihalide perovskite materials for high-efficiency solar cells. Materials Science and Engineering Reports. 2016;**101**:1-38. DOI: 10.1016/j.mser.2015.12.002

[7] Park NG. Perovskite solar cells: An emerging photovoltaic technology. Materials Today. 2015;**18**(2):65-72. DOI: 10.1016/j.mattod.2014.07.007

[8] Huang F, Pascoe AR, Wu WQ, Ku Z, Peng Y, Zhong J, Caruso RA, Cheng YB. Effect of the microstructure of the functional layers on the efficiency of perovskite solar cells. Advanced Materials. 2017;**29**(20):1601715. DOI: 10.1002/adma.201601715

[9] Eperon GE, Burlakov VM, Docampo P, Goriely A, Snaith HJ. Morphological control for high performance, solution-processed planar heterojunction perovskite solar cells. Advanced Functional Materials. 2014;**24**(1):151-157. DOI: 10.1002/adfm.201302090

[10] Xiao Z, Dong Q, Bi C, Shao Y, Yuan Y, Huang J. Solvent annealing of perovskite-induced crystal growth for photovoltaic-device efficiency enhancement. Advanced Materials. 2014; **26**(37):6503-6509

[11] Kim HD, Ohkita H, Benten H, Ito S. Photovoltaic performance of perovskite solar cells with different grain sizes. Advanced Materials. 2016;**28**(5):917-922. DOI: 10.1002/adma.201401685

[12] Kim HS, Park NG. Parameters affecting I-V hysteresis of $CH_3NH_3PbI_3$ perovskite solar cells: Effects of perovskite crystal size and mesoporous TiO_2 layer. Journal of Physical Chemistry Letters 2015. 2014;**5**(17):2927-2934. DOI: 10.1021/jz501392m

[13] Bae S, Park JS, Han IK, Shin TJ, Jo WH. $CH_3NH_3PbI_3$ crystal orientation and photovoltaic performance of planar heterojunction perovskite solar cells. Solar Energy Materials & Solar Cells. 2017;**160**:77-84. DOI: 10.1016/j.solmat.2016.10.019

[14] Li G, Ching KL, Ho JYL, Wong M, Kwok HS. Identifying the optimum morphology in high-performance perovskite solar cells. Advanced Energy Materials. 2015;**5**(9):1401775. DOI: 10.1002/aenm.201401775

[15] Fan Z, Sun K, Wang J. Perovskites for photovoltaics: A combined review of organic-inorganic halide perovskites and ferroelectric oxide perovskites. Journal of Materials Chemistry A. 2015;**3**(37):18809-18828. DOI: 10.1039/c5ta04235f

[16] Cui J, Yuan H, Li J, Xu X, Shen Y, Lin H, Wang M. Recent progress in efficient hybrid lead halide perovskite solar cells. Science and Technology of Advanced Materials. 2015;**16**(3):036004. DOI: 10.1088/1468-6996/16/3/036004

[17] Zhang L, Liu X, Li J, McKechnie S. Interactions between molecules and perovskites in halide perovskite solar cells. Solar Energy Materials & Solar Cells. 2018;**175**:1-19. DOI: 10.1016/j.solmat.2017.09.038

[18] Hsiao YC, Wu T, Li M, Liu Q, Qin W, Hu B. Fundamental physics behind high-efficiency organo-metal halide perovskite solar cells. Journal of Materials Chemistry A. 2015;**3**(30):15372-15385. DOI: 10.1039/C5TA01376C

[19] Matthews PD, Lewis DJ, Brie PO. Updating the road map to metal-halide perovskites for photovoltaics. Journal of Materials Chemistry A. 2017;**5**(33):17135-17150. DOI: 10.1039/C7TA04544A

[20] Liyan Y, Alexander TB, David GL, Tao W. Recent progress and challenges of organo-metal halide perovskite solar cells. Reports on Progress in Physics. 2016;**79**(2):026501. DOI: 10.1088/0034-4885/79/2/026501

[21] Miura K, Funakubo H. Electronic structures of tetragonal ABX3: Role of the B-X coulomb repulsions for ferroelectricity and piezoelectricity. In: Barranco AP, editor. Advances in Ferroelectrics. Rijeka: InTech; 2012. pp. 1-24. DOI: 10.5772/52187

[22] Xiao JW, Liu L, Zhang D, De Marco N, Lee JW, Lin O, Chen Q, Yang Y. The emergence of the mixed perovskites and their applications as solar cells. Advanced Energy Materials. 2017;**7**(20):1700491. DOI: 10.1002/aenm.201700491

[23] Stoumpos CC, Kanatzidis MG. The renaissance of halide perovskites and their evolution as emerging semiconductors. Accounts of Chemical Research. 2015;**48**(10):2791-2802. DOI: 10.1021/acs.accounts.5b00229

[24] Stoumpos CC, Malliakas CD, Kanatzidis MG. Semiconducting tin and lead iodide perovskites with organic cations: Phase transitions, high mobilities, and near-infrared photoluminescent properties. Inorganic Chemistry. 2013;**52**(15):9019-9038. DOI: 10.1021/ic401215x

[25] Yin WJ, Yang JH, Kang J, Yan Y, Wei SH. Halide perovskite materials for solar cells: A theoretical review. Journal of Materials Chemistry A. 2015;**3**(17):8926-8942. DOI: 10.1039/C4TA05033A

[26] Koutselas IB, Ducasse L, Papavassiliou GC. Electronic properties of three- and low-dimensional semiconducting materials with Pb halide and Sn halide units. Journal of Physics: Condensed Matter. 1996;**8**(9):1217. DOI: 10.1088/0953-8984/8/9/012

[27] Umebayashi T, Asai K, Kondo T, Nakao A. Electronic structures of lead iodide based low-dimensional crystals. Physical Review B. 2003;**67**(15):155405. DOI: 10.1103/PhysRevB.67.155405

[28] Yin WJ, Shi T, Yan Y. Unique properties of halide perovskites as possible origins of the superior solar cell performance. Advanced Materials. 2014;**26**(27):4653-4658. DOI: 10.1002/adma.201306281

[29] De Wolf S, Holovsky J, Moon SJ, Löper P, Niesen B, Ledinsky M, Haug FJ, Yum JH, Ballif C. Organometallic halide perovskites: Sharp optical absorption edge and its relation to photovoltaic performance. Journal of Physical Chemistry Letters. 2014;**5**(6):1035-1039. DOI: 10.1021/jz500279b

[30] Eperon GE, Stranks SD, Menelaou C, Johnston MB, Herz LM, Snaith HJ. Formamidinium lead trihalide: A broadly tunable perovskite for efficient planar heterojunction solar cells. Energy & Environmental Science. 2014;**7**(3):982-988. DOI: 10.1039/c3ee43822h

[31] McMeekin DP, Sadoughi G, Rehman W, Eperon GE, Saliba M, Hörantner MT, Haghighirad A, Sakai N, Korte L, Rech B, Johnston MB, Herz LM, Snaith HJ. A mixed-cation lead mixed-halide perovskite absorber for tandem solar cells. Science. 2016;**351**(6269):151-155. DOI: 10.1126/science.aad5845

[32] Giorgi G, Fujisawa JI, Segawa H, Yamashita K. Small photocarrier effective masses featuring ambipolar transport in methylammonium lead iodide perovskite: A density functional analysis. Journal of Physical Chemistry Letters. 2013;**4**(24):4213-4216. DOI: 10.1021/jz4023865

[33] Hirasawa M, Ishihara T, Goto T, Uchida K, Miura N. Magnetoabsorption of the lowest exciton in perovskite-type compound $(CH_3NH_3)PbI_3$. Physica B: Condensed Matter. 1994;**201**:427-430. DOI: 10.1016/0921-4526(94)91130-4

[34] Hu M, Bi C, Yuan Y, Xiao Z, Dong Q, Shao Y, Huang J. Distinct exciton dissociation behavior of organolead trihalide perovskite and excitonic semiconductors studied in the same system. Small. 2015;**11**(18):2164-2169. DOI: 10.1002/smll.201402905

[35] Juarez-Perez EJ, Sanchez RS, Badia L, Garcia-Belmonte G, Kang YS, Mora-Sero I, Bisquert J. Photoinduced giant dielectric constant in lead halide perovskite solar cells. Journal of Physical Chemistry Letters. 2014;**5**(13):2390-2394. DOI: 10.1021/jz5011169

[36] Zheng L, Zhang D, Ma Y, Lu Z, Chen Z, Wang S, Xiao L, Gong Q. Morphology control of the perovskite films for efficient solar cells. Dalton Transactions. 2015;**44**(23):10582-10593. DOI: 10.1039/C4DT03869J

[37] Xiao M, Huang F, Huang W, Dkhissi Y, Zhu Y, Etheridge J, Gray-Weale A, Bach U, Cheng YB, Spiccia L. A fast deposition-crystallization procedure for highly efficient lead

iodide perovskite thin-film solar cells. Angewandte Chemie. 2014;**26**(37):10056-10061. DOI: 10.1002/ange.201405334

[38] Jeon NJ, Noh JH, Kim YC, Yang WS, Ryu S, Seok SI. Solvent engineering for high-performance inorganic–organic hybrid perovskite solar cells. Nature Materials. 2014;**13**:897. DOI: 10.1038/nmat4014

[39] Ahn N, Son DY, Jang IH, Kang SM, Choi M, Park NG. Highly reproducible perovskite solar cells with average efficiency of 18.3% and best efficiency of 19.7% fabricated via Lewis Base adduct of lead(II) iodide. Journal of the American Chemical Society. 2015; **137**(27):8696-8699. DOI: 10.1021/jacs.5b04930

[40] Burschka J, Pellet N, Moon SJ, Humphry-Baker R, Gao P, Nazeeruddin MK, Grätzel M. Sequential deposition as a route to high-performance perovskite-sensitized solar cells. Nature. 2013;**499**:316. DOI: 10.1038/nature12340

[41] Xiao Z, Bi C, Shao Y, Dong Q, Wang Q, Yuan Y, Wang C, Gao Y, Huang J. Efficient, high yield perovskite photovoltaic devices grown by interdiffusion of solution-processed precursor stacking layers. Energy & Environmental Science. 2014;**7**(8):2619-2623. DOI: 10.1039/c4ee01138d

[42] Liu M, Johnston MB, Snaith HJ. Efficient planar heterojunction perovskite solar cells by vapour deposition. Nature. 2013;**501**:395. DOI: 10.1038/nature12509

[43] Chen CW, Kang HW, Hsiao SY, Yang PF, Chiang KM, Lin HW. Efficient and uniform planar-type perovskite solar cells by simple sequential vacuum deposition. Advanced Materials. 2014;**26**(38):6647-6652. DOI: 10.1002/adma.201402461

[44] Chen Q, Zhou H, Hong Z, Luo S, Duan HS, Wang HH, Liu Y, Li G, Yang Y. Planar heterojunction perovskite solar cells via vapor-assisted solution process. Journal of the American Chemical Society. 2014;**136**(2):622-625. DOI: 10.1021/ja411509g

[45] Zhu W, Yu T, Li F, Bao C, Gao H, Yi Y, Yang J, Fu G, Zhou X, Zou Z. A facile, solvent vapor-fumigation-induced, self-repair recrystallization of $CH_3NH_3PbI_3$ films for high-performance perovskite solar cells. Nanoscale. 2015;**7**(12):5427-5434. DOI: 10.1039/c5nr00225g

[46] Zhou Z, Wang Z, Zhou Y, Pang S, Wang D, Xu H, Liu Z, Padture NP, Cui G. Methylamine-gas-induced defect-healing behavior of $CH_3NH_3PbI_3$ thin films for perovskite solar cells. Angewandte Chemie, International Edition. 2015;**54**(33):9705-9709. DOI: 10.1002/anie.201504379

[47] Liu Z, Hu J, Jiao H, Li L, Zheng G, Chen Y, Huang Y, Zhang Q, Shen C, Chen Q, Zhou H. Chemical reduction of intrinsic defects in thicker heterojunction planar perovskite solar cells. Advanced Materials. 2017;**29**(23):1606774. DOI: 10.1002/adma.201606774

[48] Chen H, Ye F, Tang W, He J, Yin M, Wang Y, Xie F, Bi E, Yang X, Grätzel M, Han L. A solvent- and vacuum-free route to large-area perovskite films for efficient solar modules. Nature. 2017;**550**:92. DOI: 10.1038/nature23877

[49] Zhu W, Bao C, Lv B, Li F, Yi Y, Wang Y, Yang J, Wang X, Yu T, Zou Z. Dramatically promoted crystallization control of organolead triiodide perovskite film by a homogeneous

cap for high efficiency planar-heterojunction solar cells. Journal of Materials Chemistry A. 2016;**4**(32):12535-12542. DOI: 10.1039/c6ta04332a

[50] Zhu W, Bao C, Wang Y, Li F, Zhou X, Yang J, Lv B, Wang X, Yu T, Zou Z. Coarsening of one-step deposited organolead triiodide perovskite films via Ostwald ripening for high efficiency planar-heterojunction solar cells. Dalton Transactions. 2016;**45**(18):7856-7865. DOI: 10.1039/C6DT00900J

[51] Wang Y, Li J, Li Q, Zhu W, Yu T, Chen X, Yin L, Zhou Y, Wang X, Zou Z. PbI_2 heterogeneous-cap-induced crystallization for an efficient $CH_3NH_3PbI_3$ layer in perovskite solar cells. Chemical Communications. 2017;**53**(36):5032-5035. DOI: 10.1039/C7CC01573A

[52] Yang M, Zhang T, Schulz P, Li Z, Li G, Kim DH, Guo N, Berry JJ, Zhu K, Zhao Y. Facile fabrication of large-grain $CH_3NH_3PbI_{3-x}Br_x$ films for high-efficiency solar cells via CH_3NH_3Br-selective Ostwald ripening. Nature Communications. 2016;**7**:12305. DOI: 10.1038/ncomms12305

[53] Dong H, Wu Z, Xi J, Xu X, Zuo L, Lei T, Zhao X, Zhang L, Hou X, Jen AKY. Pseudohalide-induced recrystallization engineering for $CH_3NH_3PbI_3$ film and its application in highly efficient inverted planar heterojunction perovskite solar cells. Advanced Functional Materials. DOI: 10.1002/adfm.201704836

[54] Long M, Zhang T, Zhu H, Li G, Wang F, Guo W, Chai Y, Chen W, Li Q, Wong KS, Xu J, Yan K. Textured $CH_3NH_3PbI_3$ thin film with enhanced stability for high performance perovskite solar cells. Nano Energy. 2017;**33**:485-496. DOI: 10.1016/j.nanoen.2017.02.002

[55] Fei C, Guo L, Li B, Zhang R, Fu H, Tian J, Cao G. Controlled growth of textured perovskite films towards high performance solar cells. Nano Energy. 2016;**27**:17-26. DOI: 10.1016/j.nanoen.2016.06.041

[56] Zhu W, Kang L, Yu T, Lv B, Wang Y, Chen X, Wang X, Zhou Y, Zou Z. Facile face-down annealing triggered remarkable texture development in $CH_3NH_3PbI_3$ films for high-performance perovskite solar cells. ACS Applied Materials & Interfaces. 2017;**9**(7):6104-6113. DOI: 10.1021/acsami.6b15563

[57] Zheng L, Ma Y, Chu S, Wang S, Qu B, Xiao L, Chen Z, Gong Q, Wu Z, Hou X. Improved light absorption and charge transport for perovskite solar cells with rough interfaces by sequential deposition. Nanoscale. 2014;**6**(14):8171-8176. DOI: 10.1039/C4NR01141D

[58] Xiao J, Yang Y, Xu X, Shi J, Zhu L, Lv S, Wu H, Luo Y, Li D, Meng Q. Pressure-assisted $CH_3NH_3PbI_3$ morphology reconstruction to improve the high performance of perovskite solar cells. Journal of Materials Chemistry A. 2015;**3**(10):5289-5293. DOI: 10.1039/C4TA06700B

[59] Li F, Bao C, Gao H, Zhu W, Yu T, Yang J, Fu G, Zhou X, Zou Z. A facile spray-assisted fabrication of homogenous flat $CH_3NH_3PbI_3$ films for high performance mesostructure perovskite solar cells. Materials Letters. 2015;**157**:38-41. DOI: 10.1016/j.matlet.2015.05.106

[60] Pascoe AR, Meyer S, Huang W, Li W, Benesperi I, Duffy NW, Spiccia L, Bach U, Cheng YB. Enhancing the optoelectronic performance of perovskite solar cells via a textured $CH_3NH_3PbI_3$ morphology. Advanced Functional Materials. 2016;**26**(8):1278-1285. DOI: 10.1002/adfm.201504190

Pathways Towards High-Stable, Low-Cost and Efficient Perovskite Solar Cells

Ahmed Mourtada Elseman, Sajid, Dong Wei,
Ahmed Esmail Shalan,
Mohamed Mohamed Rashad and Meicheng Li

Additional information is available at the end of the chapter

http://dx.doi.org/10.5772/intechopen.75195

Abstract

The power conversion efficiencies (PCEs) of perovskite solar cells (PSCs) have been reached the initial value when they emerged as dye sensitized solar cell (DSSC) in 2012. Immediately, the interests were drawn in this field worldwide. The researchers have improved the efficiency of PSCs up-to 22%, which was originally started from its initial value of 3.8%, just in 7 years. The rendering of long-term stabilization and effective cost have special importance for PSCs since the instability issue remained idle in spite of those recently increased efficiency values attained by various research groups. In this way, the better improvements of PSC may increase extraordinary exhibitions as compared to alternate solar cells like organic solar cell (OSC) or DSSC devices. This chapter begins with a general discussion on the requirement for an economical clean energy conversion device. In section 2, fundamental properties of PSC are fit together with their device architecture and working mechanism. In section 3 proceeds with a review on fundamental photovoltaic parameters joined by current-voltage hysteresis. Furthermore, the stability and cost issues will be discussed in Sections 4 and 5. In the end of this chapter, we are discussing the challenges and opportunities based on the chapter content.

Keywords: perovskite solar cells, working mechanism, photovoltaic, parameters, stability, low cost

1. Introduction

A huge number of researchers have been focused on the inventions in solar cell (SC) worldwide due to the feasible and effective electricity production from available free source of sunlight [1, 2].

There is no doubt that world's main source of energy is petroleum by 40%. The consumption of the petroleum accelerates very quickly due to energy needs of expanding industrial zones. It is relied upon to grow further unless an affordable novel clean energy technology becomes available.

Therefore, the government should take precautions against fuel consumptions by creating an environmental friendliness new energy sources and alternative energy themes. Clean energy is the best way of electricity due to ease of transformation in other energy forms herewith crucial for the human society. Accordingly, the cost of energy consumption have been made by electricity using machinery, for that, this directed the countries to consider the renewable energy transformers [3]. Consequently, numerous scientists from different foundations worldwide grew new sorts of alternative energy conversion devices in order to consolidate their capacity more [4]. The SCs are the most promising devices since solar energy is acknowledged to be almost infinite for human needs.

Nowadays, SCs are used in photovoltaic (PV) panels as new investments and meet the commercial energy requirements. Optimization the efficiency is necessary to satisfy those huge consumption needs. In **Figure 1**, researchers at National Renewable Energy Laboratory (NREL) in Golden, Colorado set the best efficiency for SCs reaching 32.6% under full-sun illumination. Thus, a majority of the investments forced to utilize silicon-based PV panels, which have high conversion rates. Whereas, the problem with expensive production processes that require a huge amount of water which will produce lots of pollutants to the environment.

On the other hand, organic solar cell (OSC) uses environmental friendly production procedures. In another meaning, many new usages of organic materials in electricity production are proposed and applied as favorable alternatives. These novel devices are essentially expected to own the low cost and at the same time high efficiency. In comparison with SCs,

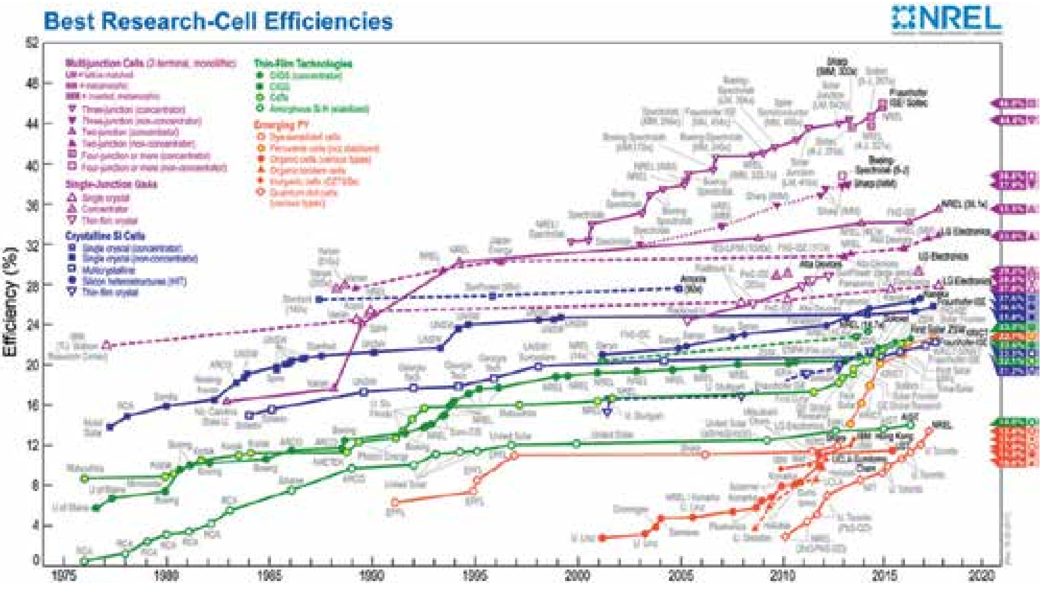

Figure 1. Reported timeline of solar cell energy conversion efficiencies (National Renewable Energy Laboratory), reprinted with permission from NREL [5].

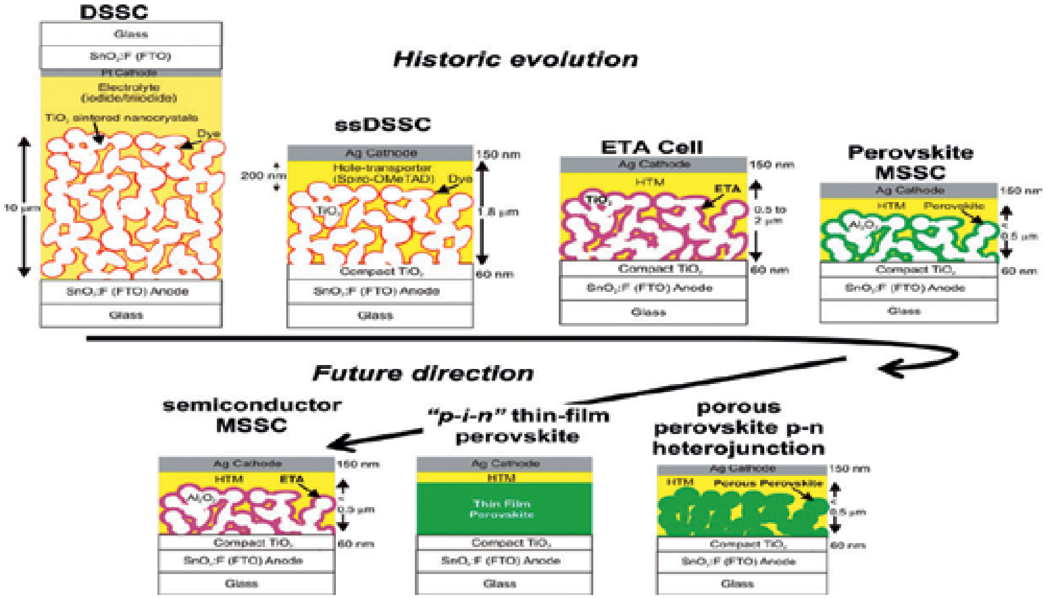

Figure 2. Historic evolution of the solar cell technology, starting from the electrolyte-based mesoscopic DSSC, the ssDSSC, the ETA cell to the MSSC perovskite absorber and the n-type TiO_2, reprinted with permission from ACS [17].

dye-sensitized solar cells (DSSCs) are commercially available in the market for a decade. However, these types of SCs are suffering from low efficiency, electrolyte degradation, and leaking encapsulation. In turn, to make a cutting-edge for this problem, experiments have been demonstrated a novel SC named perovskite solar cell (PSC) [6–11]. Consequently, this chapter will focus on PSC operational phenomena, device structure, photovoltaic parameters, and stability challenges [12, 13]. In **Figure 2**, the evolution of SC starting from the DSSC based electrolyte-based mesoscopic [14]. Then, ssDSSC where the electrolyte was replaced with an organic p-type whole conductor [15]. After that, the dye was replaced with an ETA semiconductor layer to give the ETA cell [16]. When the ETA was replaced by perovskite absorber and the n-type TiO_2 is replaced with a porous insulating scaffold to PSC. The development of the perovskite technology were elucidated as (a) porous perovskite distributed p-n heterojunction solar cells, where the Al_2O_3 is removed but the perovskite is directly structured to give a porous film subsequently filled in with a charge conductor, (b) thin-film p-i-n perovskite solar cells and the device introduce the structure as intrinsic thin perovskite film sandwiched between p and n type and finally (c) semiconductor MSSCs with solution-processed semiconductor, like SbS can be structured by the porous scaffold to deliver an MSSC.

2. Working mechanism and device architectures of PSCs

According to the operating principle of PSCs and the obtained information on the working mechanism, they are still insufficient for now [18, 19]. There are different approaches to figure out a suitable mechanism for the working principles of PSC. The principal mechanism of PSCs like (i) light absorption, (ii) charge separation, (iii) charge transport, and (iv) charge collection are essential to address because they are general SC parameters during conversion of sunlight into electricity.

In this regard, the choice of photon harvesters is the first step for the specification of the physical structure of an SC. Hence, investigation of PV parameters of perovskite has priority during the design engineering. This is optimum in terms of theoretical understanding for energy conversion mechanism [1, 20]. It is known that the structure of organic-inorganic halide exhibits both electron and whole transport properties together. Hence, PSCs can be engineered as *p-n* junction architecture or *p-i-n* junction structure. The two layouts can be described as a p-i-n junction if the light harvester or perovskite is an intrinsic semiconductor, whereas in p-n junction, the light harvester has *n*-type or *p*-type property. This junction is capable to carry electrons or holes to the perovskite harvester [1, 9–11, 21].

The typical structures of PSCs are engineered depending on two structures such as mesoporous and planar. **Figure 3** demonstrates the schematic architecture for both mesoporous and planar type PSCs. The first structure consists of a mesoporous type metal oxide layer like TiO_2 or Al_2O_3 accompanied by perovskite sensitizer. The second structure contains a perovskite film sandwiched between electron and hole transporting layers. Herein, the photo-generated charge carrier takes place in perovskite which further inject to the TiO_2 and finally collect at transparent conductive oxide glass [22–25].

In comparison, the two architectures follow the same charge transport rate. However, the mesoporous PSCs display higher recombination rates [26]. On the other hand, the planar PSCs are suitable for the field of flexible solar cells since they do not need high sintering temperature. The trends of generation and recombination of charge carrier in PSCs are depicted in **Figure 4**. The charge generation rate and charge movement take place from (1) to (3).

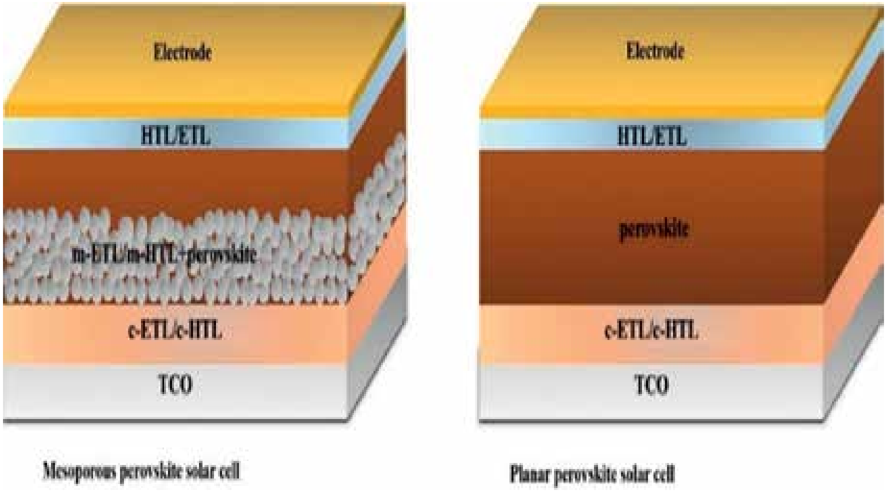

Figure 3. Schematic illustration of perovskite solar cells architectures, c-ETL; compact electron transporting layer, c-HTL; compact hole transport layer, m; mesoporous, TCO; transparent conductive oxide.

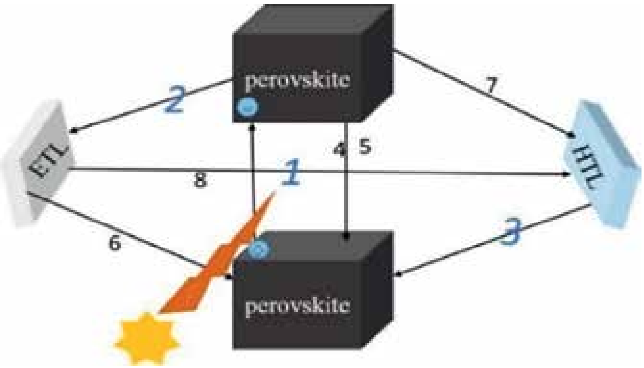

Figure 4. Trends of charge generation, charge transportation and recombination.

To manage efficient charge collection, these processes should be much faster than the recombination rate occurred from (4) to (8). This charge carrier and light management will further benefit high power conversion efficiency.

3. Paramount photovoltaic parameters of PSCs

3.1. Photocurrent density

Analyzing the device architecture of the PSC, it is very important to understand the factors that limit the photocurrents. The devices must minimize parasitic losses while the suitable thickness of photo-absorber such as organic-inorganic trihalide should have a better capability of incident photon harvesting. The enhancement in photocurrent density (J_{sc}) from 11 to 21 mA cm^{-2} has been achieved for the PSCs in 2 years [27, 28]. Later on, utilizing 1.6 eV energy band gap of perovskite materials in PSCs a J_{sc} of 22 mA cm^{-2} was obtained [29]. Researches are focused on understanding the photocurrent losses occurring in the PSCs. In this regard, internal quantum efficiency (IQE) has been confirmed as one of the major losses. Additionally, thin films in device stack such as FTO/TiO$_2$/spiro-OMeTAD/Au can cause reflection/transmission losses and parasitic absorption [30]. Crystallinity enhancement has been shown pleasurable to minimize IQE losses. Consequently, yielding photocurrents of 23 mA cm^{-2} [31]. Tuning the energy band gap via Tin (Sn) based perovskites; the photocurrent density has been improved from 25 to 26.9 mA cm^{-2} [32, 33]. However, the unstable Sn-based perovskites are crucial for their quantum efficiencies. This newly emerging field needs further insights to achieve the proposed theoretical photocurrents.

3.2. Open-circuit voltage

The enhancement of open-circuit voltage (V_{oc}) depends on the tunable energy band gap in PSCs. Thermodynamic limit of V_{oc} relates theoretical efficiency limit. The reciprocity between absorption and emission have been shown avoidable due to the radiative recombination, this returns to the V_{oc} limit of 1.33 V for $CH_3NH_3PbI_3$ (band gap ≈1.6 eV) [34]. The broad absorption edge reduces the maximum V_{oc} with almost no effect on J_{sc}. Therefore, a low density of Urbach tail accompanied by a sharp absorption edge is pleasurable for high performance as shown by many perovskite materials [35]. Any further loss is due to non-radiative recombination, which can be quantified by measuring the electroluminescence (EL) yield of the solar cell. Once it was possible to make pinhole-free films, the V_{oc} of PSCs exceeded 1 V [36]. This and the latest realization of solar cells without any charge transport layers [37] made clear that the perovskite itself is the source of the photovoltage generated by a splitting of the quasi-Fermi levels under illumination. Obviously, the charge carrier in the selective layers play a very important role. The surface recombination caused by imperfect charge carrier layers results in a reduce V_{oc}. There is no doubt that device engineering with suitable selective layers, optimize film morphology and perovskite composition lead to voltages ≥1.2 V [38]. Further improvement in V_{oc} needs in-depth understanding and reduce recombination rate due to impurities and interfaces.

3.3. Fill factor

The fill factor (FF) is connected to V_{oc} via recombination which gives maximum values of state of the art devices up to 82% [39]. There are some factors that affect the additional losses due to charge extraction depending on the electric field, voltage, external series resistances or shunt paths. The high charge mobility and large diffusion lengths in PSCs make it easy to gain high FF in a film of few 100 nm thickness [40]. However, the charge extraction occurs in resistive charge selective layers or recombination in the PSC itself could lead to low FF. In addition, the grain boundaries did not strongly affect V_{oc} and recombination but they can reduce the FF, even resulting in an anticorrelation of the FF and the film thickness. In another indication, grain boundaries constitute an obstacle for charge carrier. Plainly, the devices with p-i-n configuration have been shown the highest values of FF [41]. Increasing the FF further and approaching its theoretical limit of 91% (for $CH_3NH_3PbI_3$), needs to occur along with increasing the V_{oc} and will likely be the subject of future work by the PSCs community [20].

3.4. Current-voltage hysteresis

Performance parameters in PSCs cannot be discussed without addressing the hysteresis phenomenon. Scanning the current-voltage (*J-V*) characteristic curve of PSCs with back and forward voltage and vice versa will result in two different traces. This phenomenon makes the exact extraction of PCE from the *J-V* curve ambiguous. After its first reports, it turned into the subject of further examinations, demonstrating that it is a transient phenomenon which strongly depends on the scan rate [42, 43]. Numerous hypothetical and experimental studies elucidate that the PSC itself is responsible for the hysteresis processes that takes place on the timescales of seconds and larger. Further research efforts have demonstrated that the migration of ionic defects like iodine vacancies in the PSC is the most likely underlying process [44]. The documented details and rational results are still lacking and under investigation. Specifically, how articulated the hysteresis is, does rely not only on the slow process itself but also on its effect on photo-generated charge carrier via adjusting the recombination and charge extraction probabilities. However, the hysteresis is a result of complex processes which need thorough understanding of each phenomenon occurring in the whole solar cell.

Collectively, the performance of a PV cell can be determined by measuring the overall PCE from the ratio of maximum P_{out} in W m^{-2} to the input light irradiance (P_{in}) as represented in Eq. (1). Under the standard condition, the light intensity of P_{in} is 1000 W m^{-2}. The P_{out} of a cell is given by Eq. (2), where J_{mp} and V_{mp} refer to the current density and voltage at the maximum power. The FF is the ratio of P_{out} and the product of the maximum V_{oc} and J_{sc} (Eq. 3). The PCE or η relationship of Eq. (1) can be rewritten as Eq. (4), which is used to determine the cell performance.

$$\eta = \frac{P_{out}}{P_{in}} \tag{1}$$

$$P_{out} = V_{mp} \times J_{mp} \tag{2}$$

$$FF = \frac{P_{out}}{V_{OC} J_{SC}} \tag{3}$$

$$\eta = \frac{V_{OC} J_{SC}}{P_{in}} \tag{4}$$

4. Stability and cost challenges

Conventional solar cells have been emerged with efficiencies up to 25%. However, there are some shortcomings of these mature solar cells such as high-cost manufacturing, heavyweight, and rigidity. On the other hand, a relatively new PV technology based on PSCs has already achieved more than 22% efficiency. The vast chemical versatility and the low-cost processability of perovskite materials, the PSCs promise to lead the future of photovoltaic technology by offering cheap, lightweight and highly efficient solar cells. However, only highly expensive prototype organic HTMs have been displayed PCE over 20%. Furthermore, by uprightness of their ingredients, these HTMs unfavorably affect the long-term operational stability of the PSCs [45]. In this way, exploring cheap and stable HTMs that deliver similar high efficiencies is in great demand to empower large-scale implementation of PSCs. In the following sections we will discuss some of the promising possibilities with emphasis on inorganic HTMs.

5. Possible stable solutions

Regardless of the device architecture, the HTMs is one of the key components to fabricate highly efficient and stable PSCs. Small molecules, polymeric, carbon, and inorganic HTMs are four large families of HTMs used in PSCs. Here in, we will give an outline of the principal advantages/disadvantages for different HTMs, depicting the most recent representative results. There are many p-type semiconductor HTMs, which have been introduced with their corresponding device performance in several recent works [46–49]. Small molecules give the advantage of flexible processing from solution to evaporation joined by compatibility with pre-existing industrial lines designs for large-scale production of organic electronics. Moreover, optoelectronic properties of small molecules have the redox potential and tunable energy band gap which are generally simple to modify in order to adjust the molecular backbone to the particular perovskite [50, 51]. Chemical doping of the small molecule HTMs with Lithium salts, organic Lewis bases and metal-organic oxidants is an effective step to prepare highly efficient PSCs. Increase hole transporting capabilities (conductivity) while maintaining a low charge recombination at the interface with the perovskite is the most evident effect so far observed by doping the HTMs [52].

Carbon HTMs with nanotubes and nanopowder structure have been revealed as stable alternatives to the organics [25, 53, 54]. Carbon nanotubes as HTMs have been used to prepare highly efficient PSCs. However, the disadvantage associated with carbon nanotubes is expensive purification procedure to isolate the right semiconductor tubes. The highest recorded efficiency for a carbon nanotube is 15.5% [55]. On the other hand, carbon nanopowder offers one of the most economical HTM solutions, which is compatible with the large-scale production lines. However highly efficient PSCs prepared with nanopowder HTMs are still lacking. Although, inorganic HTMs have been explored as alternatives for long-term stability [56], but the deposition of inorganic HTMs as top contacts is complicated as the used processing solvents tend to be detrimental to the underlying perovskite layer [57]. Among various inorganic HTMs, copper thiocyanate (CuSCN) stands out as a stable, efficient and cheap candidate ($0.5/gr versus $500/gr for the commonly used spiro-OMeTAD). Recently, researchers at Michael Grätzel's lab have introduced two new concepts that overcome the major shortcomings of CuSCN-based PSCs. First, they developed a simple dynamic solution-based method for depositing highly conformal, 60-nm thick CuSCN layer that allows the fabrication of PSCs with stabilized PCE exceeding 20% [45] as depicted in **Figure 5**. Then, a thin passivation layer with reduced graphene oxide between the CuSCN and back electrode has been introduced to reduce the diffusion of gold contact. The new technique allows the PSCs to record excellent operational stability, retaining over 95% of their initial efficiency while operating at a maximum PCE for 1000 h under full-sun illumination at 60 °C. This exceeds even the stability of organic HTM-based PSCs that are recently dominated the field. These publications also discovered that the instability of the PSC originates from the degradation of CuSCN/gold contact during the solar cell's operation. These findings will pave the way for large-scale commercial deployment of this very promising new PV technology.

6. Summary

Effective photon harvesting in perovskite material has already delivered tangible results, contributing to SCs community [7]. The achievements in terms of long-term life-time of PSCs would see an economical photonics for future endeavor. Therefore, the innovation in PSC field engages a large amount of attention in the development of SCs that are reliable, highly efficient at converting sunlight to electricity and inexpensive to manufacture. Additionally, investigating the charge transport properties and improving device engineering methods

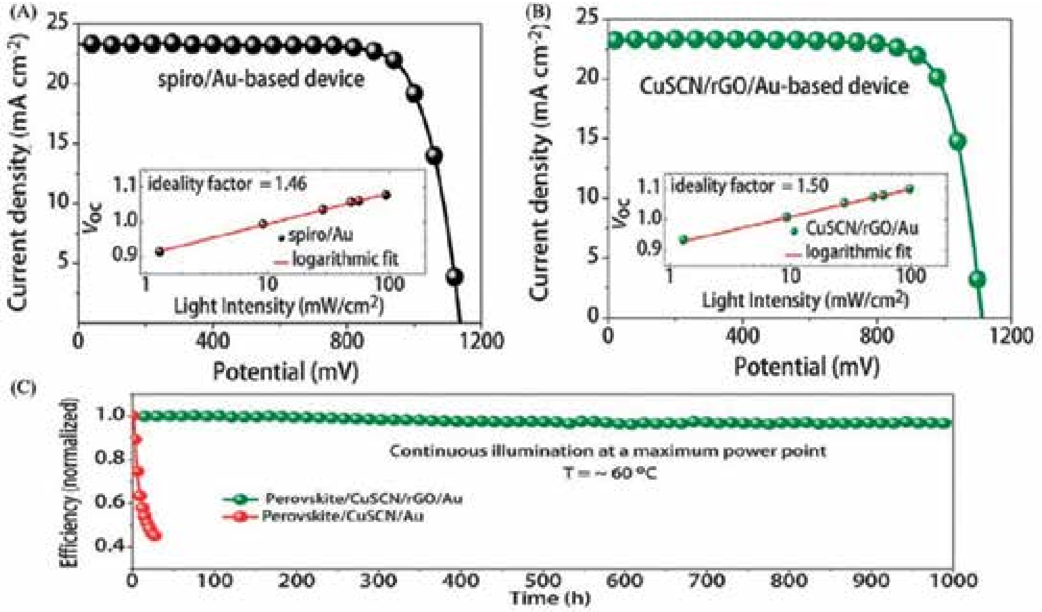

Figure 5. PV measurements of PSC based on spiro-OMeTAD and CuSCN HTM. (A) JV curve for the spiro-OMeTAD based device. (B) J-V curve for the CuSCN-based device. (C) Operational stability of an unencapsulated CuSCN-based device with and without a thin layer of reduced graphene oxide (rGO), *reprinted with permission from Science* [58].

are essential. In particular, the modification of used nano-materials has great influence. Moreover, the explanation of the photo-physical mechanism of solid-state SCs also plays an important role. However, the insufficient understanding of the working mechanism of PSCs will need further efforts. Therefore, explanation of the phenomenon on (i) light absorption, (ii) charge separation, (iii) charge transport, and (iv) charge collection are crucial during research to reveal a thorough understanding of PSCs mechanism. In addition, managing these working mechanism further contribute to the PV parameters such as photocurrent density, open-circuit voltage, FF and thus power conversion efficiency of the solar cell.

Furthermore, the HTM layer in the stack of PSC is one of the most important parts in terms of high efficiency and long-term stability. In this regard, PSCs based on inorganic HTMs with the efficiency of 20% has been shown. The incorporation of inorganic HTMs is promising with respect to their improved environmental sustainability. On the other hand, polymeric HTMs are thought to be favorable due to their high charge mobility with unique oxidation potential and preferred morphology [4, 59]. The third kind of HTMs is small molecules. Among these, spiro-OMeTAD has been the most used HTM in PSCs till now [60]; however, the tedious synthesis makes them very expensive. Therefore, commercial viability to PSCs will require us to synthesize and design novel small molecules. It is noteworthy that PSCs emerged rapidly with some uncertain phenomena associated with the device. The continuous investigation on current density and voltage characteristics of the PSCs would provide a good understanding point for the semiconducting behavior [61]. Collectively, improvement in the PSCs efficiency depends on deposition techniques and material composition [62]. In conclusion, solution-processed

PSCs are commercially valuable [63]. Moreover, inorganic HTMs found to be economically viable compared to organic HTMs. The commercialization of PSCs with inorganic HTMs is more flexible for future generated solar cells. It will also benefit the numerous scientists in the field that have been intensively searching for a material that could replace the currently used, prohibitively expensive organic hole-transporters.

Conflict of interest

The authors declare no conflict of interest.

Author details

Ahmed Mourtada Elseman[1], Sajid[2], Dong Wei[2], Ahmed Esmail Shalan[1],
Mohamed Mohamed Rashad[1] and Meicheng Li[2]*

*Address all correspondence to: mcli@ncepu.edu.cn

1 Electronic and Magnetic Materials Department, Advanced Materials Division, Central Metallurgical Research and Development Institute (CMRDI), Helwan, Cairo, Egypt

2 State Key Laboratory of Alternate Electrical Power, System with Renewable Energy Sources, School of Renewable Energy, North China Electric Power University, Beijing, China

References

[1] Jung HS, Park NG. Perovskite solar cells: From materials to devices. Small. 2015;**11**(1):10-25. DOI: 10.1002/smll.201402767

[2] Zhou Y, Zhu K. Perovskite solar cells shine in the “valley of the sun”. ACS Energy Letters. 2016;**1**(1):64-67. DOI: 10.1021/acsenergylett.6b00069

[3] Erickson LE. Reducing greenhouse gas emissions and improving air quality: Two global challenges. Environmental Progress & Sustainable Energy. 2017;**36**(4):982-988. DOI: 10.1002/ep.12665

[4] Green MA, Emery K, Hishikawa Y, Warta W, Dunlop ED. Solar cell efficiency tables (version 45). Progress in Photovoltaics: Research and Applications. 2015;**23**(1):1-9. DOI: 10.1002/pip.2573

[5] Nrel LK. Best Research-Cell Efficiencies. [57] MA Green, Corrigendum to Solar cell efficiency tables (version 46) Progress in Photovoltaics: Research and Applications. 2015;**23**(805812):1202

[6] Lotsch BV. New light on an old story: Perovskites go solar. Angewandte Chemie International Edition. 2014;**53**(3):635-637. DOI: 10.1002/anie.201309368

[7] Elseman AM, Shalan AE, Sajid S, Rashad MM, Hassan AM, Li M. Copper Substituted Lead Perovskites Materials Constructed with Different Halides for Working $(CH_3NH_3)_2CuX_4$ Based Perovskite Solar Cells from Experimental and Theoretical View. ACS applied materials & interfaces. 2018. DOI: 10.1021/acsami.8b00495

[8] Babayigit A, Ethirajan A, Muller M, Conings B. Toxicity of organometal halide perovskite solar cells. Nature Materials. 2016;**15**:247. DOI: 10.1038/nmat4572

[9] Elseman AM, Rashad MM, Hassan AM. Easily attainable, efficient solar cell with mass yield of nanorod single-crystalline organo-metal halide perovskite based on a ball milling technique. ACS Sustainable Chemistry & Engineering. 2016;**4**(9):4875-4886

[10] Rashad MM, Elseman AM, Hassan AM. Facile synthesis, characterization and structural evolution of nanorods single-crystalline $(C_4H_9NH_3)_2$ PbI 2 X 2 mixed halide organometal perovskite for solar cell application. Optik-International Journal for Light and Electron Optics. 2016;**127**(20):9775-9787

[11] Elseman A, Shalan A, Rashad M, Hassan A. Experimental and simulation study for impact of different halides on the performance of planar perovskite solar cells. Materials Science in Semiconductor Processing. 2017;**66**:176-185

[12] You J, Meng L, Song TB, et al. Improved air stability of perovskite solar cells via solution-processed metal oxide transport layers. Nature Nanotechnology. 2016;**11**(1):75-81. DOI: 10.1038/nnano.2015.230

[13] Shahbazi M, Wang H. Progress in research on the stability of organometal perovskite solar cells. Solar Energy. 2016;**123**(Supplement C):74-87. DOI: https://doi.org/10.1016/j.solener.2015.11.008

[14] O'regan B, Grätzel M. A low-cost, high-efficiency solar cell based on dye-sensitized colloidal TiO2 films. Nature. 1991;**353**(6346):737

[15] Murakoshi K, Kogure R, Wada Y, Yanagida S. Solid state dye-sensitized TiO_2 solar cell with polypyrrole as hole transport layer. Chemistry Letters. 1997;**26**(5):471-472

[16] Lévy-Clément C, Tena-Zaera R, Ryan MA, Katty A, Hodes G. CdSe-sensitized p-CuSCN/nanowire n-ZnO heterojunctions. Advanced Materials. 2005;**17**(12):1512-1515

[17] Snaith HJ. Perovskites: The emergence of a new era for low-cost, high-efficiency solar cells. The Journal of Physical Chemistry Letters. 2013;**4**(21):3623-3630

[18] Stranks SD, Eperon GE, Grancini G, et al. Electron-hole diffusion lengths exceeding 1 micrometer in an organometal trihalide perovskite absorber. Science. 2013;**342**(6156):341-344. DOI: 10.1126/science.1243982

[19] Xing G, Mathews N, Sun S, et al. Long-range balanced electron- and hole-transport lengths in organic-inorganic $CH_3NH_3PbI_3$. Science. 2013;**342**(6156):344-347. DOI: 10.1126/science.1243167

[20] Sajid AME, Jun J, Shangyi D, Hao H, Peng C, Dong W, Meicheng L. Novel hole transport layer of nickel oxide composite with carbon for high-performance perovskite solar cells. Chinese Physics B. 2018;**27**(1):17305-017305. DOI: 10.1088/1674-1056/27/1/017305

[21] Cui P, Wei D, Ji J, et al. Highly efficient Electron-selective layer free perovskite solar cells by constructing effective p-n heterojunction. Solar RRL. 2017;**1**(2):1600027-1600n/a. DOI: 10.1002/solr.201600027

[22] Cui P, Fu P, Wei D, et al. Reduced surface defects of organometallic perovskite by thermal annealing for highly efficient perovskite solar cells. RSC Advances. 2015;**5**(92):75622-75629. DOI: 10.1039/C5RA16669A

[23] Wei D, Ji J, Song D, et al. A TiO2 embedded structure for perovskite solar cells with anomalous grain growth and effective electron extraction. Journal of Materials Chemistry A. 2017;**5**(4):1406-1414. DOI: 10.1039/C6TA10418E

[24] Kim HS, Mora-Sero I, Gonzalez-Pedro V, et al. Mechanism of carrier accumulation in perovskite thin-absorber solar cells. Nature Communications. 2013;**4**(2242). DOI: 10.1038/ncomms3242

[25] Liu X-Y, Yu J-X, Li X-D, Liu G-C, Li X-F, Lee J-K. Effect of metal catalyst on the mechanism of hydrogen spillover in three-dimensional covalent-organic frameworks. Chinese Physics B. 2017;**26**(2):027302. DOI: 10.1088/1674-1056/26/2/027302

[26] Gonzalez-Pedro V, Juarez-Perez EJ, Arsyad WS, et al. General working principles of $CH_3NH_3PbX_3$ perovskite solar cells. Nano letters. 2014;**14**(2):888-893. DOI: 10.1021/nl404252e

[27] Lee MM, Teuscher J, Miyasaka T, Murakami TN, Snaith HJ. Efficient hybrid solar cells based on Meso-Superstructured organometal halide perovskites. Science. 2012;**338**(6107):643-647. DOI: 10.1126/science.1228604

[28] Liu M, Johnston MB, Snaith HJ. Efficient planar heterojunction perovskite solar cells by vapour deposition. Nature. 2013;**501**:395. DOI: 10.1038/nature12509

[29] Jeon NJ, Noh JH, Yang WS, et al. Compositional engineering of perovskite materials for high-performance solar cells. Nature. 2015;**517**:476. DOI: 10.1038/nature14133

[30] Ball JM, Stranks SD, Horantner MT, et al. Optical properties and limiting photocurrent of thin-film perovskite solar cells. Energy & Environmental Science. 2015;**8**(2):602-609. DOI: 10.1039/C4EE03224A

[31] Correa-Baena J-P, Anaya M, Lozano G, et al. Unbroken perovskite: Interplay of morphology, electro-optical properties, and ionic movement. Advanced Materials. 2016;**28**(25):5031-5037. DOI: 10.1002/adma.201600624

[32] Eperon GE, Leijtens T, Bush KA, et al. Perovskite-perovskite tandem photovoltaics with optimized band gaps. Science. 2016;**354**(6314):861-865. DOI: 10.1126/science.aaf9717

[33] Liao W, Zhao D, Yu Y, et al. Fabrication of efficient low-bandgap perovskite solar cells by combining Formamidinium tin iodide with Methylammonium lead iodide. Journal of the American Chemical Society. 2016;**138**(38):12360-12363. DOI: 10.1021/jacs.6b08337

[34] Tvingstedt K, Malinkiewicz O, Baumann A, et al. Radiative efficiency of lead iodide based perovskite solar cells. Scientific Reports. 2014;**4**:6071

[35] De Wolf S, Holovsky J, Moon S-J, et al. Organometallic halide perovskites: Sharp optical absorption edge and its relation to photovoltaic performance. The Journal of Physical Chemistry Letters. 2014;**5**(6):1035-1039

[36] Burschka J, Pellet N, Moon S-J, et al. Sequential deposition as a route to high-performance perovskite-sensitized solar cells. Nature. 2013;**499**(7458):316

[37] Liu D, Yang J, Kelly TL. Compact layer free perovskite solar cells with 13.5% efficiency. Journal of the American Chemical Society. 2014;**136**(49):17116-17122

[38] Jacobsson TJ, Correa-Baena J-P, Anaraki EH, et al. Unreacted PbI2 as a double-edged sword for enhancing the performance of perovskite solar cells. Journal of the American Chemical Society. 2016;**138**(32):10331-10343

[39] Marinova N, Tress W, Humphry-Baker R, et al. Light harvesting and charge recombination in $CH_3NH_3PbI_3$ perovskite solar cells studied by hole transport layer thickness variation. ACS Nano. 2015;**9**(4):4200-4209

[40] Wehrenfennig C, Eperon GE, Johnston MB, Snaith HJ, Herz LM. High charge carrier mobilities and lifetimes in organolead trihalide perovskites. Advanced Materials. 2014; **26**(10):1584-1589

[41] Pérez-del-Rey D, Forgács D, Hutter EM, et al. Strontium insertion in Methylammonium lead iodide: Long charge carrier lifetime and high fill-factor solar cells. Advanced Materials. 2016;**28**(44):9839-9845

[42] Tress W, Marinova N, Moehl T, Zakeeruddin S, Nazeeruddin MK, Grätzel M. Understanding the rate-dependent J–V hysteresis, slow time component, and aging in $CH_3NH_3PbI_3$ perovskite solar cells: The role of a compensated electric field. Energy & Environmental Science. 2015;**8**(3):995-1004

[43] Unger E, Hoke E, Bailie C, et al. Hysteresis and transient behavior in current–voltage measurements of hybrid-perovskite absorber solar cells. Energy & Environmental Science. 2014;**7**(11):3690-3698

[44] Yang S, Zheng YC, Hou Y, et al. Formation mechanism of freestanding $CH_3NH_3PbI_3$ functional crystals: In situ transformation vs dissolution–crystallization. Chemistry of Materials. 2014;**26**(23):6705-6710

[45] Arora N, Dar MI, Hinderhofer A, et al. Perovskite solar cells with CuSCN hole extraction layers yield stabilized efficiencies greater than 20%. Science. 2017:eaam5655

[46] Ameen S, Rub MA, Kosa SA, et al. Perovskite solar cells: Influence of hole transporting materials on power conversion efficiency. ChemSusChem. 2016;**9**(1):10-27. DOI: 10.1002/cssc.201501228

[47] Swetha T, Singh SP. Perovskite solar cells based on small molecule hole transporting materials. Journal of Materials Chemistry A. 2015;**3**(36):18329-18344. DOI: 10.1039/C5TA02507A

[48] Teh CH, Daik R, Lim EL, et al. A review of organic small molecule-based hole-transporting materials for meso-structured organic-inorganic perovskite solar cells. Journal of Materials Chemistry A. 2016;**4**(41):15788-15822. DOI: 10.1039/C6TA06987H

[49] Yu Z, Sun L. Recent Progress on Hole-Transporting Materials for Emerging Organometal Halide Perovskite Solar Cells. Advanced Energy Materials. 2015;**5**(12):1500213. DOI: 10.1002/aenm.201500213

[50] Jeon NJ, Lee HG, Kim YC, et al. O-Methoxy substituents in spiro-OMeTAD for efficient inorganic–organic hybrid perovskite solar cells. Journal of the American Chemical Society. 2014;**136**(22):7837-7840

[51] Malinauskas T, Tomkute-Luksiene D, Sens R, et al. Enhancing thermal stability and lifetime of solid-state dye-sensitized solar cells via molecular engineering of the hole-transporting material Spiro-OMeTAD. ACS Applied Materials & Interfaces. 2015;**7**(21):11107-11116. DOI: 10.1021/am5090385

[52] Abate A, Leijtens T, Pathak S, et al. Lithium salts as "redox active" p-type dopants for organic semiconductors and their impact in solid-state dye-sensitized solar cells. Physical Chemistry Chemical Physics. 2013;**15**(7):2572-2579. DOI: 10.1039/C2CP44397J

[53] Mei A, Li X, Liu L, et al. A hole-conductor–free, fully printable mesoscopic perovskite solar cell with high stability. Science. 2014;**345**(6194):295-298. DOI: 10.1126/science.1254763

[54] Gholipour S, Correa-Baena J-P, Domanski K, et al. Highly Efficient and Stable Perovskite Solar Cells based on a Low-Cost Carbon Cloth. Advanced Energy Materials. 2016;**6**(20):1601116. DOI: 10.1002/aenm.201601116

[55] Aitola K, Sveinbjornsson K, Correa-Baena J-P, et al. Carbon nanotube-based hybrid hole-transporting material and selective contact for high efficiency perovskite solar cells. Energy & Environmental Science. 2016;**9**(2):461-466. DOI: 10.1039/C5EE03394B

[56] Chen W, Wu Y, Yue Y, et al. Efficient and stable large-area perovskite solar cells with inorganic charge extraction layers. Science. 2015;**350**(6263):944-948. DOI: 10.1126/science.aad1015

[57] Qin P, Tanaka S, Ito S, et al. Inorganic hole conductor-based lead halide perovskite solar cells with 12.4% conversion efficiency. Nature Communications. 2014;**5**:3834. DOI: 10.1038/ncomms4834

[58] Arora N, Dar MI, Hinderhofer A, et al. Perovskite solar cells with CuSCN hole extraction layers yield stabilized efficiencies greater than 20%. Science. 2017. DOI: 10.1126/science.aam5655

[59] Jeon NJ, Noh JH, Kim YC, Yang WS, Ryu S, Seok SI. Solvent engineering for high-performance inorganic–organic hybrid perovskite solar cells. Nature Materials. 2014;**13**:897. DOI: 10.1038/nmat4014

[60] Yang S, Fu W, Zhang Z, Chen H, Li C-Z. Recent advances in perovskite solar cells: Efficiency, stability and lead-free perovskite. Journal of Materials Chemistry A. 2017;**5**(23):11462-11482. DOI: 10.1039/C7TA00366H

[61] Meloni S, Moehl T, Tress W, et al. Ionic polarization-induced current-voltage hysteresis in CH3NH3PbX3 perovskite solar cells. Nature Communications. 2016;**7**:10334. DOI: 10.1038/ncomms10334

[62] Back H, Kim J, Kim G, et al. Interfacial modification of hole transport layers for efficient large-area perovskite solar cells achieved via blade-coating. Solar Energy Materials and Solar Cells. 2016;**144**(Supplement C):309-315. DOI: https://doi.org/10.1016/j.solmat.2015.09.018

[63] Kaiyu Y, Fushan L, Jianhua Z, Chandrasekar Perumal V, Tailiang G. All-solution processed semi-transparent perovskite solar cells with silver nanowires electrode. Nanotechnology. 2016;**27**(9):095202

High-Quality Perovskite Film Preparations for Efficient Perovskite Solar Cells

Shangzheng Pang and Dazheng Chen

Additional information is available at the end of the chapter

http://dx.doi.org/10.5772/intechopen.75103

Abstract

Solar cells employing organolead halide perovskite films have caught tremendous attention, and their power conversion efficiencies were stunning from 3.9% to over 22% in only 6 years. Various research reports have shown that effective controls on perovskite crystallinity, homogeneity, and surface morphology are crucial to improving the power conversion efficiencies (PCE) of perovskite solar cells. Here, based on the typical one-step and two-step deposition methods, we would like to introduce the solvent treatment mechanisms of mixed-solvent-vapor annealing and polar solvent additive, investigate the growth mode and control means of perovskite films by physical characterizations, and discuss their effects on the photovoltaic performance improvements for perovskite solar cells.

Keywords: perovskite solar cell, one-step deposition, solvent annealing, two-step deposition, solvent additive

1. Introduction

Organolead halide perovskites are emerging materials with outstanding optoelectronic properties of high absorption coefficient, broad absorption, range, adjustable band gap, solution processing, and so on [1–6]. Employing this kind of material, solar cells have caught tremendous attention, and their power conversion efficiencies (PCEs) have dramatically increased from 3.8% to over 22% in only 6 years [1, 7–9]. This great progress mainly comes from the effective controls on perovskite crystallinity, homogeneity, and surface morphology, and many researchers have focused on the first-principles modeling molecular motion and dynamic crystal structure [10, 11], defect physics [12, 13], ionic conductivity [14], hysteresis characteristics [15], device structures and stability, and so on [16]. A high-quality perovskite film with low point defects and grain boundaries is necessary to obtain higher device PCEs.

This could greatly avoid the non-radiative recombination which could cause the loss of open-circuit voltage (*V*OC) and decreased carrier lifetime [17–19]. On the other hand, a high-quality perovskite should also have good charge transport properties and slow ionic transport so that the free carriers could be effectively collected by the electrode and the current hysteresis behavior in current–voltage sweep measurements could be effectively avoided. In order to achieve high-quality perovskite films, a lot of deposition categories have been developed, such as one-step solution method, two-step solution method, and vapor deposition method [20–22]. And, this chapter will describe two effective solvent treatment mechanisms in typical one-step and two-step solution methods to obtain perovskite film with high-quality and relatively high PCEs.

Firstly, the early presented one-step method has still been widely used due to the advantages of low cost, simple, and more compatible with the roll-to-roll process. It is well known that the annealing treatments are crucial in one-step method to transform PbI_2-MAI-DMSO intermediate phase [23] and deposit perovskite films, and the stand-alone solvent annealing or anti-solvent annealing has been proven to be efficient for improving the perovskite quality. Here, we would like to introduce a novel solvent-engineering method, namely, the mixed-solvent-vapor annealing in the one-step solution method. Generally, the $CH_3NH_3PbI_3$ possesses a poor solubility in anhydrous isopropanol, and the annealing in this vapor environment can result in a dense uniform and pinhole-free perovskite film. When a little polar aprotic DMF or DMSO vapor is mixed with the isopropanol vapor, after the mixed-solvent-vapor annealing process, the average grain size of $CH_3NH_3PbI_3$ crystals can be further increased, thus further enhanced short-circuit current density (*J*SC), suppressed reverse dark current, reduced recombination loss in PSCs, and improved device stability. All devices with planar heterojunction structure show the efficiency over 15%. What is more, by employing $CH_3NH_3I_3$-xClx perovskite precursor and interface modifying layer, the device PCE reaches around 19%.

Secondly, by incorporating a certain ratio of polar solvent such as N,N′-Dimethylformamide (DMF) into MAI/IPA precursor solution, we introduce a modified interdiffusion two-step sequential deposition method. As we all know, DMF could easily dissolve PbI_2 film while spin-coating MAI solution, and it has never been used in two-step method to fabricate perovskite film. Although DMF is a typical polar solvent for PbI_2 and perovskites, it has been found that a small ratio of DMF in the MAI solution could provide a beneficial atmosphere to promote MAI molecules diffusing into the bottom PbI_2 film and avoiding the PbI_2 residue, which is helpful to form perovskite with high quality. Simultaneously, it can also improve the surface morphology efficiently and enlarge the size of the perovskite crystal. Further, a PCE of 19.2% is achieved by the related planar heterojunction perovskite solar cells. And, this mechanism of polar solvent addition provides a facile way toward the high-quality perovskite film and high-performance devices.

As we all know, the performance of perovskite solar cells (PSCs) is strongly depending on the quality of perovskite layer. Here, based on the typical one-step and two-step deposition methods, we would like to introduce the solvent treatment mechanisms of mixed-solvent-vapor annealing and polar solvent additive to investigate the growth mode and control the means of perovskite films by physical characterizations and discuss their effects on the photovoltaic performance improvements for perovskite solar cells.

2. One-step method: prepared perovskite film

2.1. Film formation

The $CH_3NH_3PbI_3$ precursor solution was prepared by mixing 1.4 M PbI_2 and 1.35 M MAI dissolved in the co-solvent of DMSO:GBL (3:7 v/v) and stirred for 2 h at 70°C. The $CH_3NH_3I_3$-xClx precursor solution was prepared by mixing 1.26 M PbI_2, 0.14 M $PbCl_2$, and 1.35 M MAI was dissolved in the co-solvent of DMSO:GBL (3:7 v/v), and was stirred for 2 h at 70°C. The solution was then spin-coated onto the PEDOT:PSS layer with solvent-engineering method. Briefly, the spin-coating process was programmed to run at 1000 rpm for 15 s and then 5000 rpm for 25 s. When the spinning was at 37 s, 350 μl anhydrous toluene was injected onto the substrates. The perovskite films were solvent or thermally annealed on the hot plate at 100°C for 20 min. For the film treated with solvent annealing, the perovskite films were put on top of a hot plate and covered by a glass Petri dish. Around 40 μl of IPA, IPA:DMF (100:1 v/v) or IPA:DMSO (100:1 v/v) solvent was added around the substrates during the thermal annealing process, so that the solvent vapor could make contact with the perovskite films. More experimental details can be found in our previous work [24].

2.2. Results and discussion

The $CH_3NH_3PbI_3$ film morphologies and surface textures are investigated by atomic force microscopy (AFM) and scanning electron microscopy (SEM). As is shown in **Figure 1**, the root-mean-square (RMS) roughness value of the pristine $CH_3NH_3PbI_3$ film is 8.28 nm; this result is consistent with the report [23] by using the solvent-engineering method. Introducing the IPA vapor in the annealing process, the minimum RMS value of the $CH_3NH_3PbI_3$ film is achieved. The introduced liquid anhydrous isopropanol on the hot plate turns to gas rapidly in a confined space which produces a certain anti-solvent vapor pressure and retards the crystal formation of perovskite to improve the crystalline quality [25, 26]. When the polar aprotic solvents of DMSO and DMF are introduced in the IPA vapor annealing process, the RMS values increase to 10.51 and 9.04 nm, respectively. As we all know, $CH_3NH_3PbI_3$ is easily dissolved in DMSO and DMF, and a trace of DMSO or DMF introduced in the annealing process can induce a recrystallization process of $CH_3NH_3PbI_3$ leading to the change of the morphology and surface. The film quality can improve by precise control of the recrystallization process. However, an excessive polar aprotic solvent vapor will produce a negative effect and reduce the film quality. As discussed above, the DMSO vapor will be released by the PbI_2-MAI-DMSO intermediate phases. With extra DMSO introduced in the annealing process, the DMSO vapor will be excessive. This causes the largest RMS value in the perovskite film, which may be one of the reasons for the lower device performance than the IPA PSCs. Therefore, the introduced DMF is more suitable than DMSO, and the corresponding devices show a better performance.

It is shown in the SEM image (**Figure 2a**) that the pristine $CH_3NH_3PbI_3$ film has a small grain size in the range of 100–300 nm. Bright portions at the grain boundaries can be observed, which is likely to be less conductive PbI_2 as in the previous reports [23]. In addition, there are also spots of pinholes on the film surface. The charge transport and the photovoltaic performance [26] are strongly influenced by these defects. The average grain size of the $CH_3NH_3PbI_3$

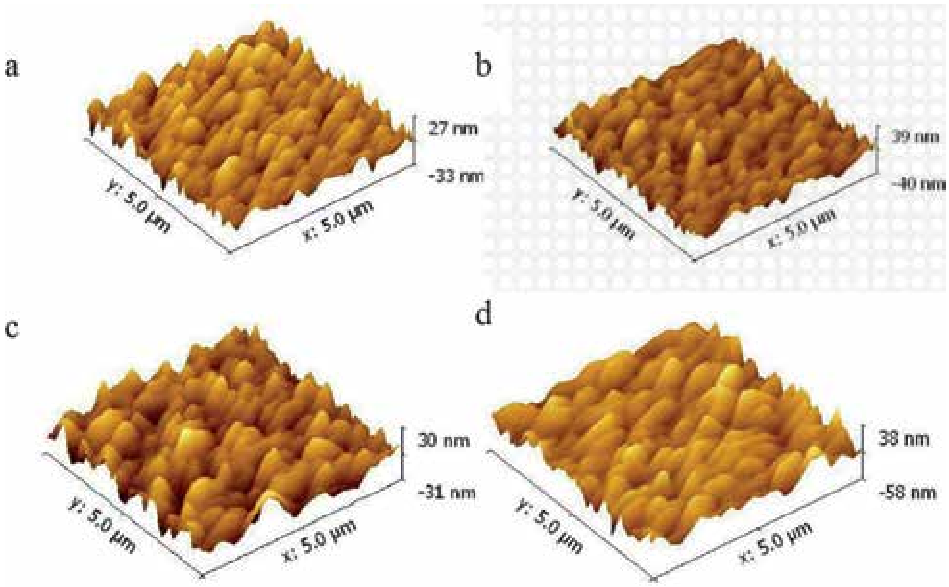

Figure 1. AFM images of perovskite films via (a) pristine, (b) IPA, (c) IPA/DMSO, and (d) IPA/DMF vapor annealing. The measured RMS values are (a) 8.28 nm, (b) 7.87 nm, (c) 10.51 nm, and (d) 9.04 nm (reprinted with the permission from [24], 2016, Elsevier).

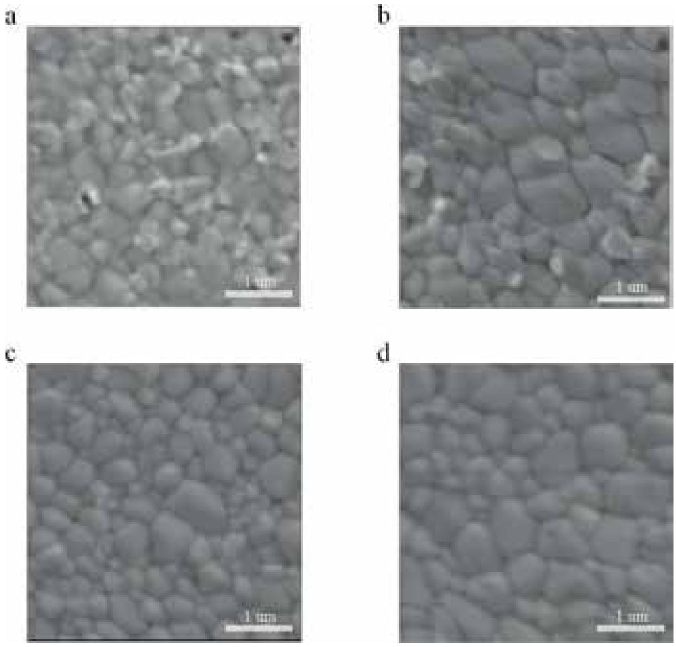

Figure 2. SEM images of perovskite films via (a) pristine, (b) IPA, (c) IPA/DMSO, and (d) IPA/DMF vapor annealing (reprinted with permission from [24], 2016, Elsevier).

has been increased with the obvious reduction of pinholes (**Figure 2b**) after treating the anhydrous IPA vapor in the annealing process. Then, the $CH_3NH_3PbI_3$ films become more compact and dense, and the pinholes disappear as shown in **Figure 2c** and **d** when the polar aprotic solvent of DMSO or DMF is further introduced in the annealing process. However, there is an obvious difference between the IPA/DMSO and IPA/DMF that resulted in perovskite films. The grain size of the IPA/DMF $CH_3NH_3PbI_3$ film is obviously larger than that of the IPA/DMSO $CH_3NH_3PbI_3$ film. The boundary defects and related recombination are reduced for the high crystalline, large grain size, and a small grain boundary area. This will benefit the charge transport and charge collection, which could be another reason for the better performance of IPA/DMF devices.

Figure 3 shows the XRD patterns of pristine, IPA, and IPA/DMF $CH_3NH_3PbI_3$ films. The formation of $CH_3NH_3PbI_3$ is proven by the diffraction peaks around 14.21, 28.51, and 31.88°, which are assigned to the (110), (220), and (310) lattice planes of the tetragonal perovskite structure, respectively. And, the improved crystallinity of the perovskite films annealed in IPA and IPA/DMF vapor has been confirmed by the stronger and sharper XRD diffraction peaks than that of pristine $CH_3NH_3PbI_3$. Significantly, the solvent annealing reduces the small peak at 12.8° belonging to PbI_2, which is in line with the previous SEM results. The $CH_3NH_3PbI_3$ film treated by the mixed IPA/DMF vapor shows stronger and sharper peaks, which reveals the higher crystallization. This again explains why the IPA-/DMF-treated devices acquire the best performance.

To fabricate perovskite solar cells, there are two typical device structures of mesoporous and conventional planar structure. Mesoporous device structures employing an n-type TiO_2

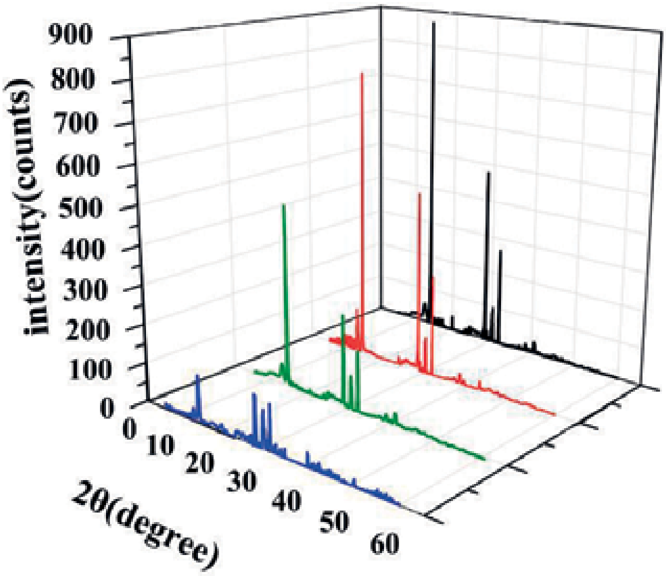

Figure 3. XRD patterns of CH3NH3PbI3 films with pristine (blue), IPA/DMSO vapor (green), IPA vapor (red), and IPA/DMF vapor (black) annealing (reprinted with the permission from [24], 2016, Elsevier).

layer as the bottom electron transport layer. A high-temperature (>450°C) sintering process for the TiO_2 scaffold, which is a great limitation on the substrate and increases the cost, is required. On the other hand, the conventional planar structures based on TiO_2 usually suffer from a large degree of J−V hysteresis. In 2013, Guo developed the first planar heterojunction perovskite solar cell with inverted structure design. The p-type layer was deposited before the perovskite film, while the n-type layer was deposited after the perovskite film [27]. This architecture was defined as p-i-n structure or inverted structure. Recent studies have shown that the inverted planar PSCs adopted in this study show negligible *J*−*V* hysteresis and promising device performance [28, 29]. Thus, the PSCs in this work adopt the inverted structure of ITO/PEDOT:PSS/$CH_3NH_3PbI_3$/PCBM/Ag (shown in **Figure 4(a)**), where the PCBM and PEDOT:PSS act as electron and hole transport layers, respectively.

The corresponding energy band diagram is illustrated in **Figure 4(b)**. PEDOT:PSS has the conduction band energy of around −3.0 eV and the valance band of around −5.2 eV, which suggests that holes from $CH_3NH_3PbI_3$ can be transported to PEDOT:PSS and collected by the anode, while electrons from $CH_3NH_3PbI_3$ can be blocked. In other words, this PEDOT:PSS acts as an electron-blocking layer and a hole extraction layer. At the same time, the PCBM layer plays the role of electron extraction layer, and it can effectively aid the electron transport to the cathode. Furthermore, it has been reported that PCBM can effectively passivate $CH_3NH_3PbI_3$ and minimize the *J*−*V* hysteresis [30]. This structure is expected to obtain better photovoltaic performance for perovskite solar cells.

The *J*–*V* characteristics of the fabricated $CH_3NH_3PbI_3$ PSCs are shown in **Figure 5(a)**, and their photovoltaic parameters are summarized in **Table 1**. The "pristine" represents the PSCs without the vapor treatment in the perovskite annealing process. The "IPA," "IPA/DMF (100:1 v/v)," and "IPA/DMSO (100:1 v/v)" represent the PSCs treated by corresponding vapors. It can be seen that the pristine PSCs exhibit an average PCE of 11.5%, with *J*SC = 17.1 ± 0.7 mA/cm^2, *V*OC = 0.96 ± 0.02 V, and FF = 70.1 ± 1.6%, and the best one shows a PCE of 12.2% with *J*SC = 18.1 mA/cm^2, *V*OC = 0.96 V, and FF = 70.1%. It is obvious that the PCE is mainly limited by the relatively low *J*SC, which is in line with the relatively low PCE for inverted planar PSCs [23]. However, by introducing the solvent vapor in the annealing process, the resulted PSCs show a significant improvement in

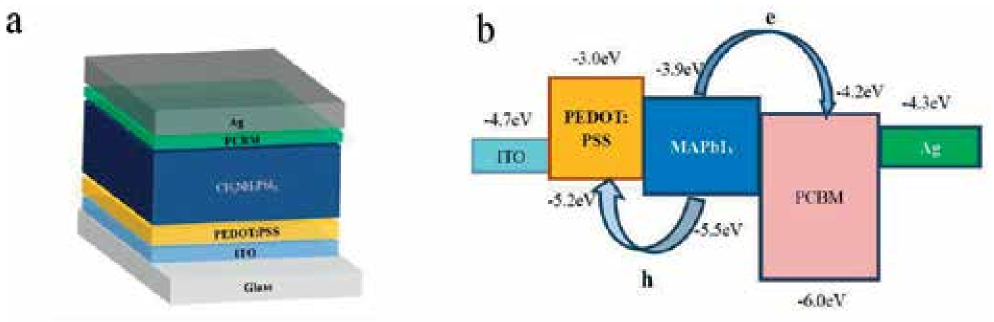

Figure 4. (a) Schematic structure of the devices in this study: ITO/PEDOT:PSS/$CH_3NH_3PbI_3$/PCBM/Ag. The thickness of each layer was not in scale with the real thickness for clarity. (b) Schematic illustration of energy band diagram of studied devices (reprinted with the permission from [24], 2016, Elsevier).

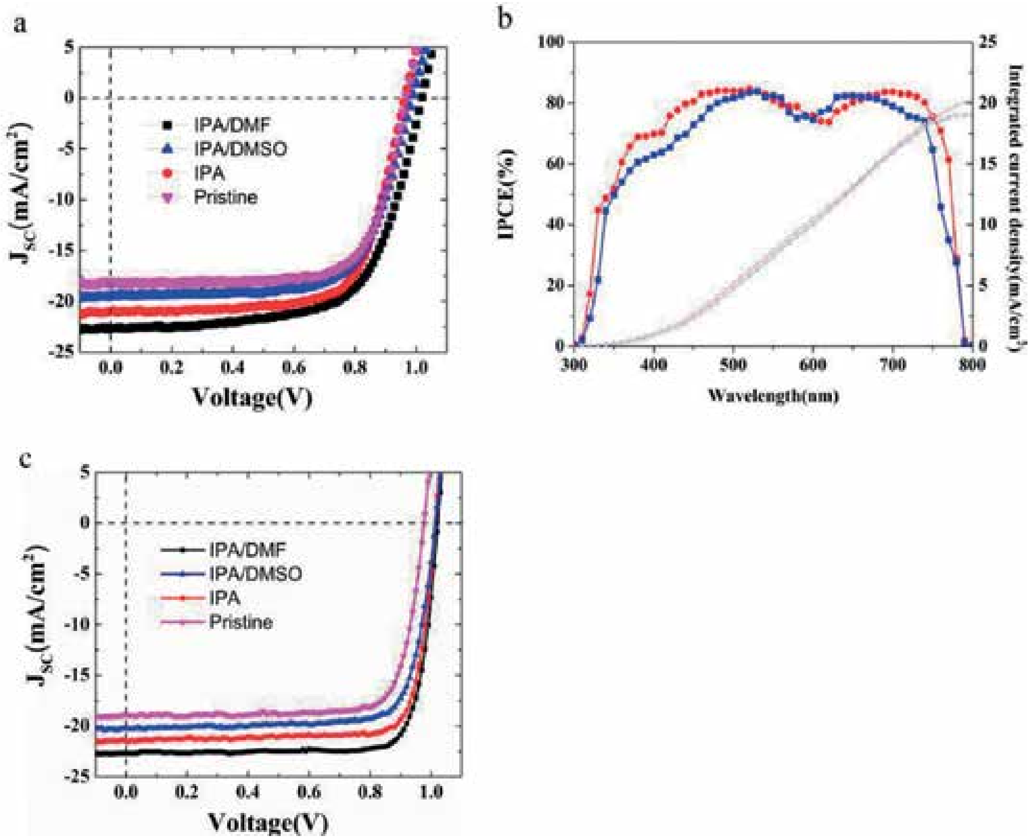

Figure 5. (a) *J–V* characteristics of $CH_3NH_3PbI_3$ PSCs without solvent annealing and with IPA, IPA/DMSO, or IPA/DMF solvent annealing under the simulated AM 1.5G illumination of 100 mW/cm^2. (b) IPCE curves and integrated current density of IPA PSCs (blue) and IPA/DMF PSCs (red). (c) *J–V* characteristics of $CH_3NH_3I_3$–xClx PSCs without solvent annealing and with IPA, IPA/DMSO, or IPA/DMF solvent annealing under the simulated AM 1.5G illumination of 100 mW/cm^2 (reprinted with the permission from [24], 2016, Elsevier).

performance (see **Figure 5b**). For the IPA PSCs, the greatly improved *J*SC of 19.8 ± 0.5 mA/cm^2 is obtained, as well as a slightly increased FF (70.4 ± 1.2) and *V*OC (0.98 ± 0.01 V); thus, the average PCE increased to 13.2% and the highest PCE of 14.2%(*J*SC = 20.9 mA/cm^2). It is suggested that the IPA vapor treatment can help enhance the $CH_3NH_3PbI_3$ crystallinity during the annealing process and thus improve the photovoltaic performance of PSCs. When the DMSO vapor is further introduced, the IPA/DMSO PSCs show an average PCE of 12.3% with *J*SC = 19.0 ± 0.7 mA/cm^2, *V*OC = 0.99 ± 0.01 V, and FF = 65.7 ± 1.8%, which is relatively inferior to the IPA PSCs. This is related to the PbI_2-MAI-DMSO intermediate phases and can be understood from the annealing process. Since the perovskite formation is reversible, the transform of PbI_2-MAI-DMSO intermediate phases will release extra DMSO vapor, combining with the introduced DMSO, and the excessive DMSO vapor would further affect the recrystallization of $CH_3NH_3PbI_3$ by shifting the reaction along the decomposition direction. However, when the IPA-/DMF-mixed vapor is adopted in the annealing process, the corresponding PSCs show an obviously improved *J*SC of 20.8 ± 0.6 mA/cm^2, *V*OC of 1.02 ± 0.01 V, and FF of 67.0 ± 1.5% and the PCE average values of 14.2%, and the

CH3NH3PbI3 PSCs	***V*OC (V)**	***JSC* mA/cm^2**	**FF (%)**	**PCE (%)**
Pristine	0.96 ± 0.02	17.14 ± 0.71	70.1 ± 1.6	11.5(12.2)
IPA	0.98 ± 0.01	19.85 ± 0.54	70.4 ± 1.2	13.2(14.7)
IPA/DMSO	0.99 ± 0.01	19.03 ± 0.73	65.7 ± 1.8	12.3(13.1)
IPA/DMF	1.02 ± 0.01	20.81 ± 0.56	67.0 ± 1.5	14.2(15.1)
CH3NH3I3-xClx PSCs	*V*OC (V)	*JSC* mA/cm^2	FF (%)	PCE (%)
Pristine	0.98 ± 0.01	19.00 ± 0.82	79.2 ± 0.6	14.0(14.3)
IPA	1.00 ± 0.01	20.83 ± 0.77	81.5 ± 0.5	17.3(18.1)
IPA/DMSO	1.00 ± 0.01	20.30 ± 0.58	78.0 ± 1.5	15.9(16.3)
IPA/DMF	1.02 ± 0.01	22.23 ± 0.50	80.6 ± 1.3	18.0(18.9)

The average results were based on ten devices.

Table 1. Photovoltaic parameters of $CH_3NH_3PbI_3$ and $CH_3NH_3I_3$-xClx PSCs under simulated AM 1.5G illumination (100 mW/cm^2) (reprinted with the permission from [24], 2016, Elsevier).

best one obtains a PCE of 15.1% and a *J*SC of 22.7 mA/cm^2. Compared with the PSCs with alone IPA vapor, it is clear that both *J*SC and *V*OC are strikingly enhanced for PSCs treated with IPA-/DMF-mixed vapor. In this work, the optimized ratio of IPA/DMF is 100:1(v/v), while the excessive DMF will be also destructive to the perovskite formations [24]. Additionally, the incident photo-to-electron conversion efficiency (IPCE) curves and the integrated current density are shown in **Figure 5b**. It is clear that the PSC treated with IPA-/DMF-mixed vapor shows a higher IPCE value at most wavelengths, as well as the largely integrated current density of 20.3 mA/cm^2, which is very close to the measured *J*SC in *J–V* characteristic.

To further improve the photovoltaic performance of inverted PSCs, the $CH_3NH_3I_3$-xClx precursor and BCP interface layer have been employed, and the resulted PSCs show a structure of ITO/PEDOT:PSS/$CH_3NH_3I_3$-xClx/PCBM/BCP/Ag. The measured photovoltaic parameters are summarized in **Table 1**. Without solvent annealing treatment, the pristine $CH_3NH_3I_3$-xClx device exhibits a relatively poor performance with *J*SC = 19.0 ± 0.82 mA/cm^2, *V*OC = 0.98 ± 0.01 V, and FF = 79.2 ± 0.6% and an average PCE of 14.0%. With anti-solvent vapor treatment in the annealing process, the performance of $CH_3NH_3I_3$-xClx device has been significantly improved compared with the pristine devices. For the IPA $CH_3NH_3I_3$-xClx PSCs, the *J*SC is greatly improved to 20.83 ± 0.77 mA/cm^2 with nearly unchanged *VOC* and FF. Thus, the average PCE of 17.3% and the highest PCE of 18.1% are achieved. Compared to the IPA $CH_3NH_3I_3$-xClx device, IPA/DMF $CH_3NH_3I_3$-xClx device shows a higher average PCE of 18.0% (the best device shows PCE of 18.9%) with *V*OC = 1.02 ± 0.01 V, *J*SC = 22.23 ± 0.50 mA/cm^2, and FF = 80.6 ± 1.3%.

Besides the efficiency of PSCs, the stability is another critical limitation for their commercial applications. The structural chemical stability of perovskite could be damaged by many factors such as interaction with moisture and oxygen especially at high temperatures. For the ITO/PEDOT:PSS/perovskite/PCBM/Ag structure, the hydrophilic and acidic nature of PEDOT:PSS is considered an unstable transport layer, also the possible oxidation of silver electrode. Here, we mainly discuss the device stability issue related to the perovskite layers. As we know, the stability of perovskite is related to its material nature [21], and also the preparation process and treatment have direct effects on the crystalline quality. For the un-encapsulated PSCs processed at different annealing conditions, we tested them in an ambient environment at 22°C with about 30% humidity. The degradation of key photovoltaic parameters of PCE, *J*SC, *V*OC, and FF are shown in **Figure 6**. After 8 days in air, the PCE of the pristine PSC kept 40% of the initial efficiency, with FF and *J*SC reduced to 59 and 70% of the original values. It should be noted that the device stability was significantly improved for the PSCs treated by IPA vapor and IPA/DMF mixed solvent vapor. And, the PCEs could keep 65 and 74% of the initial values after 8 days. This indicates the relationship of perovskite quality and device stability and provides a strategy to obtain high-efficient PSCs with good stability.

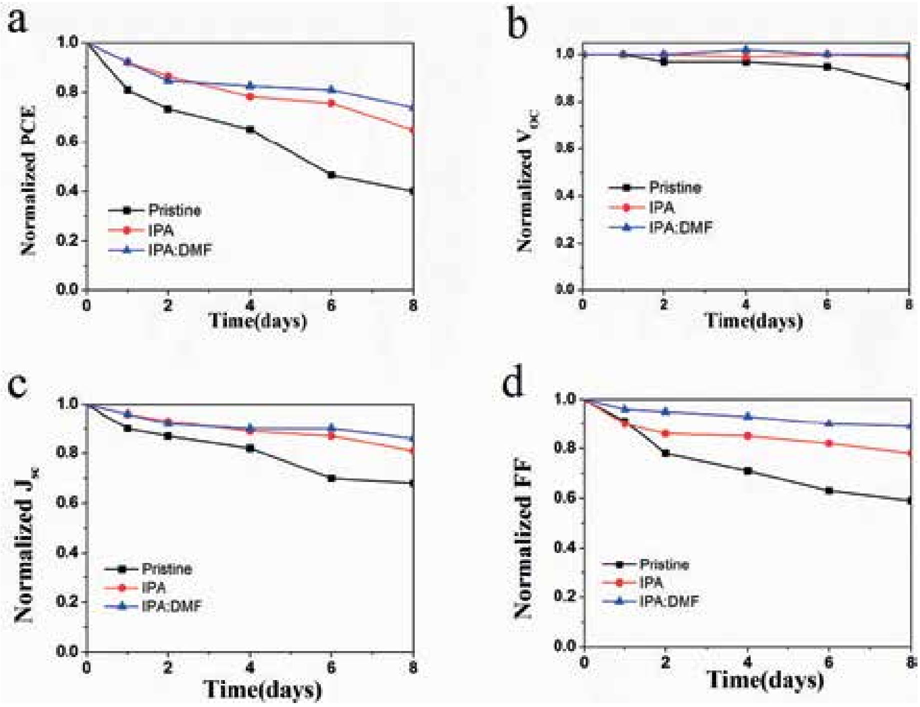

Figure 6. Stability of the devices with the structure of ITO/PEDOT:PSS/perovskite/PCBM/Ag: (a) normalized PCE, (b) normalized *V*OC, (c) normalized *J*SC, and (d) normalized FF (reprinted with the permission from [24], 2016, Elsevier).

3. Two-step method: Prepared perovskite film

3.1. Film formation

0.85 M PbI_2 and 0.15 M $PbCl_2$ were dissolved in the solvent of DMF and stirred for 2 h at 75°C. Forty milligrams of MAI were dissolved in the solvent of IPA with/without additionally 0.9 vol% DMF or GBL, respectively. Around 60ul PbX_2 precursor solution preheated to 75°C was transferred by pipettes to the ITO substrates. Briefly, the spin-coating process was programmed to run at 3000 rpm for 45 s, and a yellow transparent dense PbI_2 film was deposited. Then, MAI was spin-coated on top of the dried PbI_2 layer at room temperature at 3000 rpm for 45 s. All of the films were thermally annealed on the hot plate at 100°C for 10 min. And, the perovskite film is formed by interdiffusion process. **Figure 7** shows the photographs of perovskite films deposited by MAI/IPA and MAI/(IPA-0.9%DMF) solutions. It can be seen that the perovskite film shows a heterogeneous and whitish surface morphology if the pure MAI/IPA solution was used. And, the concentration variation of the MAI/IPA solution cannot reverse the situation. However, by introducing proper DMF (0.9%) solvent additive into the MAI/IPA solution, the dark brown perovskite film is obtained, and the optimized MAI concentration is 40 mg/L. To further know their difference, the morphology and crystalline quality of perovskite films were measured by scanning electron microscopy (SEM) and X-ray diffraction (XRD) tests, as well as their optical property by UV–visible spectrophotometer and photoluminescence spectra. More experimental details can be found in our previous work [36].

3.2. Results and discussion

Figure 8(a) and **(b)** displays the scanning electron microscopy (SEM) images of perovskite films. The perovskite film without DMF additive shows the small grain size and many pinholes between the grain boundaries (marked with the red circles). These defects increase recombination probability and severely hamper the charge transport and the device performance. However, when a small amount of DMF is added to MAI/IPA precursor, those pinholes among the grain boundaries are effectively eliminated in the resulted perovskite films, as shown in **Figure 8(b)**; also, the average grain size of perovskite is obviously increased.

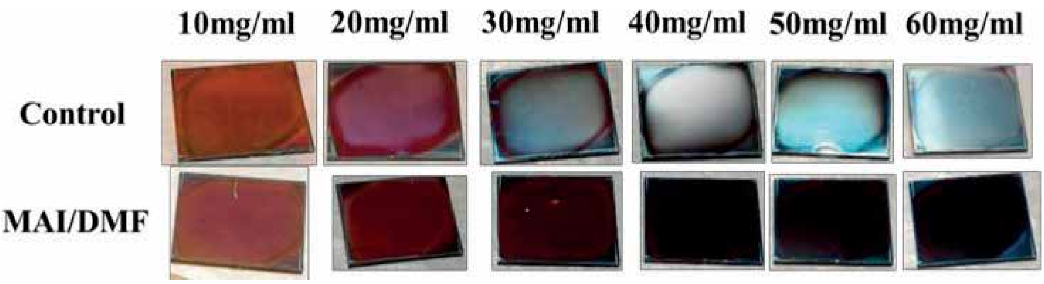

Figure 7. Photographs of perovskite films by spin-coating MAI/IPA solution (top) and MAI/(IPA-0.9%DMF) (bottom), respectively, with 10, 20, 30, 40, 50, and 60 mg/ml MAI concentrations (from left to right) (reprinted with the permission from [31], 2017, The Royal Society of Chemistry).

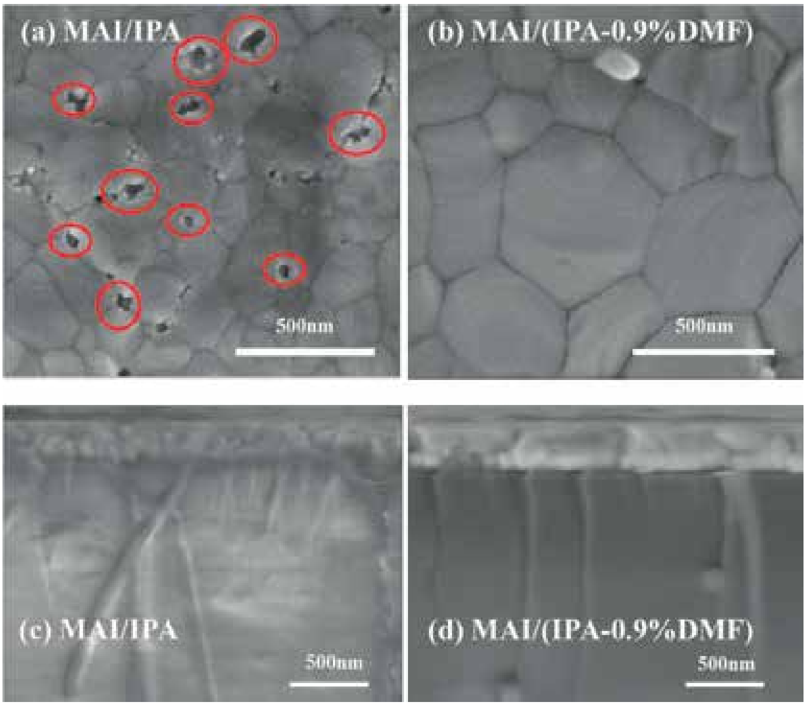

Figure 8. SEM images of perovskite films. Higher-magnification SEM image of the perovskite film without (a) and with (b) DMF additive, cross-sectional SEM image of the perovskite film without DMF additive (c) and with (d) DMF additive (reprinted with the permission from [31], 2017, the Royal Society of Chemistry).

Figure 8(c) and **(d)** displays the cross-sectional images of perovskite films deposited on glass substrate. While using MAI/IPA solution, the perovskite film shows the low-quality, incomplete-reaction PbI_2 and small grain size. However, by adding proper DMF into MAI precursor solution, a perovskite film with large grain size could be observed from **Figure 8(d)**. **Figure 9** shows the forming process of perovskite film by two-step deposition method. It is obvious that the controlled perovskite film seemed a bit low quality with the little crystal and more defects when the bare MAI/IPA solution were used. However, with proper DMF solvent additive doped into the MAI/IPA solution, the crystal quality of perovskite film could significantly be improved.

According to the high solubility of MAI and PbI_2 in DMF, we present a possible mechanism that [31] the small amount of DMF solvent provides a "wet" environment so that PbI_2 and MAI could react with each other and later a high-quality perovskite could be obtained after annealing. As we know, the DMF has a higher boiling point (152.8°C) that of IPA; thus, the presence time of DMF is relatively long during the 100°C annealing process. During the crystal growth process, the DMF additive could drive the MAI penetrating into the thick PbI_2 to form larger crystal grains by slowing down the perovskite crystallization rate, and a thick film with a pure phase since perovskite can be totally but very slowly dissolved in DMF, and the dissolving process depends on the amount of DMF. Moreover, proper DMF solvent vapor annealing could increase thin-film crystallinity, and crystalline domain size since the

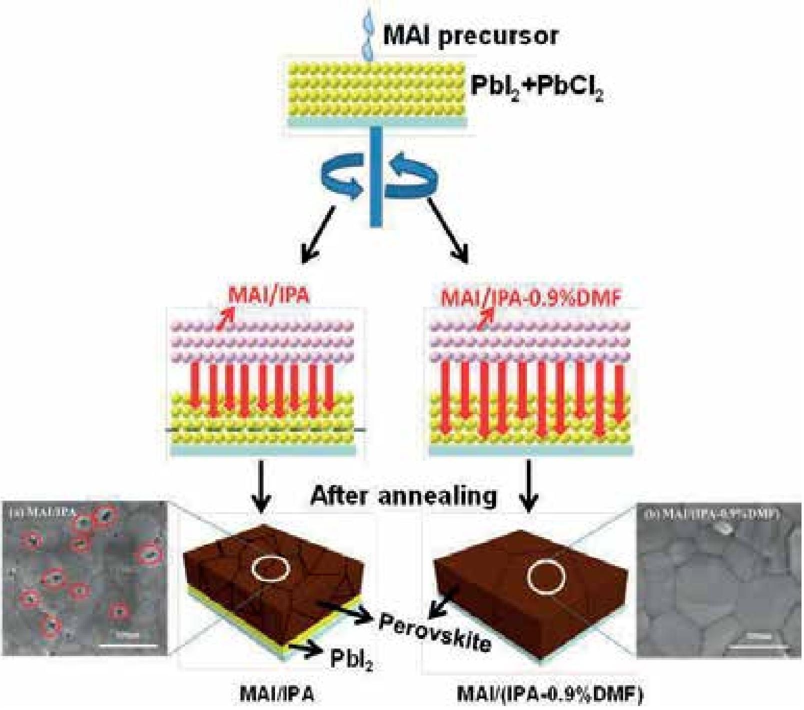

Figure 9. The schematic of interdiffusion procedure for preparing the uniform and dense perovskite film (reprinted with the permission from [31], 2017, the Royal Society of Chemistry).

DMF solvent could induce a second perovskite dissolution and recrystallization process. As a result, the large-size crystal grains and high-quality perovskite films are achieved, which can be partly supported by the SEM images. To verify this mechanism, the crystal quality, light absorption ability, and charge transport property are discussed as follows.

Figure 10(a) shows the XRD results of PbI_2, MAI, and perovskite films. As expected, the PbI_2 displays a characteristic diffraction peak at 2θ of 12.8°. And, the diffraction peaks of MAI at 2θ of 9.8, 19.65, and 29.65° are consistent with reported results. For the perovskite film without DMF additive, the diffraction peak at 12.8° means the PbI_2 residues in this film. However, when a 0.9 vol% DMF is added to MAI/IPA precursor, the PbI_2 diffraction peak disappears, and the peak intensity of perovskite is enhanced; both of them demonstrate the higher crystal quality of perovskite film. It is suggested that the presence of a small amount of DMF solvent could improve the complete conversion of PbI_2 to perovskite by promoting the reaction between PbI_2 and MAI. **Figure 10(b)** displays the steady-state PL spectra of the perovskite films on the glass or glass/ITO/PEDOT:PSS substrates. For the perovskite films on glass, the same peak position at 759 nm is observed; the PL peak intensity is enhanced after adding the DMF additive in MAI precursor, which demonstrates the improved perovskite film quality. Furthermore, for the perovskite/PEDOT:PSS/ITO/glass sample, the more obvious PL quenching in perovskite with DMF additive means the more efficient charge transfer from the perovskite to the PEDOT:PSS layer, which agrees the XRD discussion of the complete conversion of PbI_2 to perovskite. While

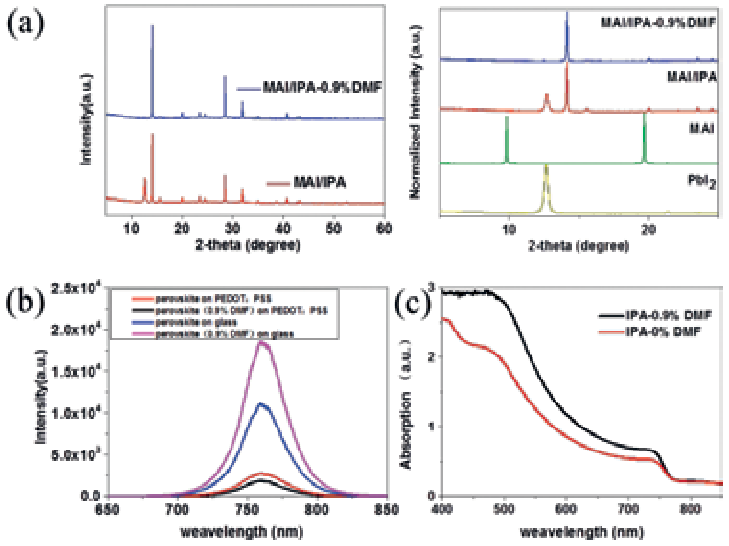

Figure 10. (a) XRD spectra of perovskite with MAI/IPA and MAI/IPA-0.9% DMF, respectively. (b) Normalized intensity of X-ray diffraction spectra of perovskite, PbI_2 and MAI, respectively. (c) Photoluminescence (PL) spectra at room temperature. Perovskite films grown on different substrates including glass or PEDOT:PSS. (d) Absorption spectra of the perovskite films, which were fabricated by spin-coating MAI/IPA and MAI/IPA-0.9%DMF on dried PbI_2 films (Reprinted with the permission from [31], 2017, the Royal Society of Chemistry).

for the perovskite without DMF additive, the low quenching efficiency can be attributed to the charge block effect of residual PbI_2 at perovskite/PEDOT:PSS interface. **Figure 10(c)** displays the absorption spectra of the perovskite films. It is clear that the light absorption in the perovskite film with 0.9% DMF additive is more efficient than the perovskite film without DMF additive at all absorption wavelength range. **Figure 11** exhibits the device structure of the perovskite solar cell and the corresponding energy diagram. In the device the highest occupied molecular orbital (HOMO) level and the lowest unoccupied molecular orbital (LUMO) level of PEDOT:PSS are 3.0 and 5.2 eV, respectively. So, the PEDOT:PSS layer plays the role of electron-blocking layer and hole transport layer. Correspondingly, the PCBM acts as hole-blocking layer and electron transport layer with the HOMO level of 4.0 eV and LUMO level of 6.2 eV. The BCP is used as the interface modification layer with the HOMO level of 7.0 eV. The Ag film and the ITO are chosen as the top and bottom electrodes.

Based on the high some batches of devices were fabricated, and **Figure 12(a)** displays typical *J*–*V* characteristics of the fabricated PSCs. Without DMF additive, the PSC exhibits a short- circuit current density (*J*SC) of 16.16 mA/cm^2, an open-circuit voltage (*V*OC) of 0.99 V, and a fill factor (*FF*) of 71.2% and a corresponding PCE of 11.4%. It is obvious that the low *J*SC and *FF* are the main factors limiting the PCE. Compared with the PSC without DMF additive, the PSC performance has been greatly improved as shown in **Figure 12(a)**, when the DMF is first introduced in the MAI solution. Consequently, *J*SC is greatly improved to 20.06 mA/cm^2, and *FF* is improved to 77.1% with a slightly increased *V*OC (1.00 V), which enhances the PCE to 15.5%. It can be inferred that the DMF solvent in the MAI solution can help to enhance the reaction between PbI_2 and MAI, improve the $MAPbI_3$ crystallinity and grain size, and improve the device

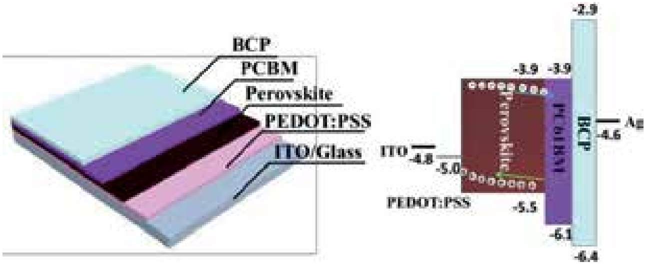

Figure 11. Device architecture of the perovskite solar cell (glass/ITO/PEDOT:PSS/perovskite/PC61BM/BCP/Ag) and the corresponding energy level diagram of corresponding materials used in the device (reprinted with the permission from [31], 2017, the Royal Society of Chemistry).

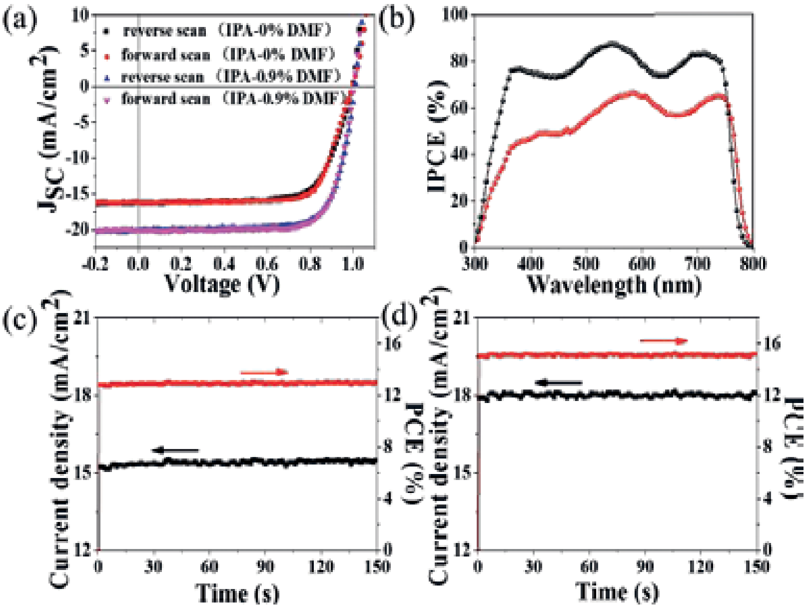

Figure 12. (a) *J–V* curves with different scanning directions at the condition of IPA and IPA- 0.9%DMF. Reverse (1.1 V → -0.2 V) and forward scan (−0.2 V → 1.1 V) measurement: the voltage step is 0.01 V. (b) IPCEs for the PSCs from MAI/IPA (red curves) and MAI/(IPA- 0.9%DMF)(black curves). Steady-state current density and PCE of the devices without (c) and with (d) DMF additive in MAI solution (Reprinted with the permission from [31], 2017, The Royal Society of Chemistry).

performance. The incident photo-to-electron conversion efficiency (IPCE) curves of the PSCs with/without DMF additive are shown in **Figure 12(b)**. The device with DMF additive shows a higher IPCE value than the device without the DMF additive, which is same as the improved efficiency of the device with DMF additive obtained from the *J–V* curve measurement.

As the photocurrent hysteresis behavior is a common issue in accurate characterization of device efficiency, the photocurrent hysteresis behaviors of PSCs with/without DMF additive were measured by changing the scanning directions (reverse scan (from a positive bias 1.1 V to a negative bias −0.2 V) and forward scan (from a negative bias −0.2 V to a positive bias 1.1 V)). **Figure 12(a)** displays the *J–V* characteristics of PSCs under different scan directions. Regardless of scan directions, highly consistent *J–V* curves and negligible photocurrent hysteresis are observed. This indicates the validity of our measured device performance. To further verify that the measured efficiency is reliable, we also measured steady-state outputs of current density and PCE. The measurements are set at the maximum power point for the steady-state PCE and *J* outputs. As shown in **Figure 12(c)**, the device without DMF additive also shows a stable current density, yielding a stabilized PCE of 11.4%. Meanwhile, the device with DMF additive also shows a stable current density, yielding a stabilized PCE of over 15% as shown in **Figure 12(d)**. This result further verifies the validity of our measured device performance.

Figure 13 displays the statistic results of the fabricated PSCs. Those statistic parameters clearly reveal that the DMF additive in the MAI solution could significantly enhance the photovoltaic performance of PSCs. It should be noted that the statistic results were based on 20 perovskite solar cell devices in several batches, which indicates that our experiments are reproducible. It confirms the validity of above discussion. Surprisingly, a champion device with a PCE of 19.2% is obtained during the optimization. The corresponding device exhibited the *J*SC = 23.4 mA/cm^2, *V*OC = 1.03 V, and *FF* = 79.6%, while a *J*SC = 16.3 mA/cm^2, *V*OC = 1.01 V, and *FF* = 74.7% belong to the champion cell without DMF, as displayed in **Figure 14**. At the same time, it should be noted that although the above discussion is on the device with DMF additive, devices with the GBL additive has the same trend, which shows that the method is a general method to enhance the PSC performance.

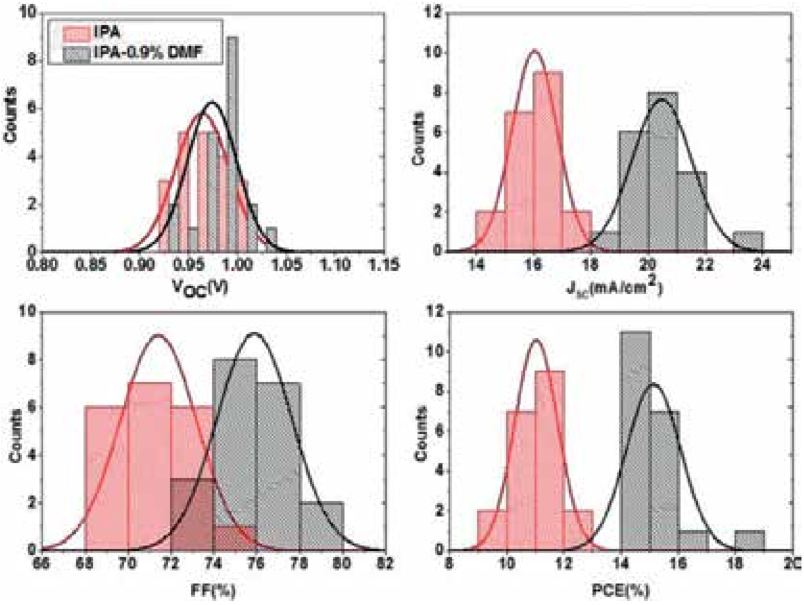

Figure 13. Comparison of histograms of photovoltaic parameters for the perovskite solar cells based on MAI/IPA (red) and MAI/(IPA-0.9%DMF) (black) condition. Data from 20 cells were used for the histogram (reprinted with the permission from [31], 2017, the Royal Society of Chemistry).

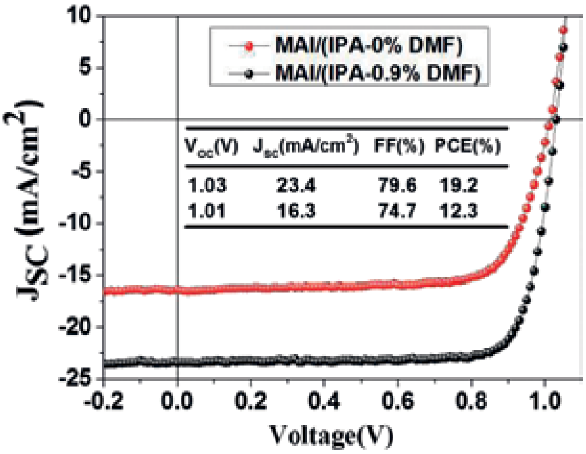

Figure 14. *J–V* curves for the best device (with or without 0.9%DMF) under standard AM1.5 simulated illumination (reprinted with the permission from [31], 2017, the Royal Society of Chemistry).

4. Conclusions

Organolead halide perovskites are emerging photovoltaic materials for next-generation solar cells. To obtain high-performance PSCs with good stability, the perovskite film with improved crystallinity, homogeneity, and surface morphology is of great importance. This chapter introduces the solvent treatment mechanisms of mixed-solvent-vapor annealing and polar solvent additive in the typical one-step and two-step perovskite deposition methods. These treatments effectively improve the perovskite film quality as well as the photovoltaic performance of planar PSCs with inverted structure. In details, compared to the alone IPA solvent annealing in one-step method, the introduction of a little polar aprotic solvent such as DMF is effective to improve the device performance. The XRD and SEM analysis demonstrates that the average grain size and crystallinity of perovskite film have been increased via IPA/DMF mixed solvent-vapor annealing (100:1, v/v). The PCE of the $CH_3NH_3PbIxCl_3$-x planar heterojunction solar cell increases from 14.0% of the pristine PSC to 17.3% of the IPA PSC and further to 18.0% of the IPA/DMF PSC and shows negligible $J - V$ hysteresis. In addition, the PSC stability is significantly improved treated by IPA/DMF mixed-solvent vapor. Our results show that the mixed-solvent-vapor annealing is a simple and promising method for PSCs and other photoelectric devices. For the interdiffusion of two- step sequential deposition, a small ratio of DMF solvent addicted into the MAI/IPA solution can help the complete conversion of PbI_2 into perovskite, which leads to the reduced pinholes, improved film morphology, increased grain sizes, enhanced film light absorption, and charge transport ability. The improved perovskite film quality is responsible for the enhancement of JSC and PCE for PSCs with inverted structure. Using this method, an optimized PCE as high as 19.2% was acquired for $CH_3NH_3PbIxCl_3$-x PSCs. In short, these two solvent treatment strategies could provide guidelines to further improve the perovskite quality and fabricate more efficient perovskite solar cells with good stability, which is essential to realize their commercialization in the future.

Acknowledgements

We thank the Natural Science Foundation of Shaanxi Province (2017JQ6014), Fundamental Research Funds for the Central Universities, and Class General Financial Grant from the China Postdoctoral Science Foundation (Grant No. 2016M602771).

Author details

Shangzheng Pang and Dazheng Chen*

*Address all correspondence to: dzchen@xidian.edu.cn

State Key Discipline Laboratory of Wide Band Gap Semiconductor Technology, School of Microelectronics, Xidian University, Xi’an, China

References

[1] Kojima A, Teshima K, Shirai Y, Miyasaka T. Organometal halide perovskites as visible-light sensitizers for photovoltaic cells. Journal of the American Chemical Society. 2009;**131**: 6050-6051. DOI: 10.1021/ja809598r

[2] Dong Q, Fang Y, Shao Y, Mulligan P, Qiu J, Cao L, Huang J. Electron-hole diffusion lengths > 175 μm in solution-grown CH3NH3PbI3 single crystals. Science. 2015;**347**:967-970. DOI: 10.1126/science.aaa5760

[3] Shi D, Adinolfi V, Comin R, Yuan M, Alarousu E, Buin A, Chen Y, Hoogland S, Rothenberger A, Katsiev K, Losovyj Y, Zhang X, Dowben P a, Mohammed OF, Sargent EH, Bakr OM. Low trap-state density and long carrier diffusion in organolead trihalide perovskite single crystals. Science (80-.). 2015;**347**:519-522. DOI: 10.1126/science.aaa2725

[4] Stranks SD, Eperon GE, Grancini G, Menelaou C, Alcocer MJP, Leijtens T, Herz LM, Petrozza A, Snaith HJ. Science. 2013;**342**:341-344

[5] Xing G, Mathews N, Sun S, Lim SS, Lam YM, Grätzel M, Mhaisalkar S, Sum TC. Electron-hole diffusion lengths exceeding 1 micrometer in an organometal trihalide perovskite absorber. Science (80-.). 2013;**342**:344-347. DOI: 10.1126/science.1243982

[6] Chang J, Zhu H, Li B, Isikgor F, Hao Y, Xu Q, Ouyang J. Boosting the performance of planar heterojunction perovskite solar cell by controlling the precursor purity of perovskite materials. Journal of Materials Chemistry A. 2016;**4**:887-893. DOI: 10.1039/c5ta08398b

[7] Jeon NJ, Noh JH, Yang WS, Kim YC, Ryu S, Seo J, Il Seok S. Compositional engineering of perovskite materials for high-performance solar cells. Nature. 2015;**517**:476. DOI: 10.1038/nature14133

[8] Yang WS, Noh JH, Jeon NJ, Kim YC, Ryu S, Seo J, Il Seok S. High-performance photovoltaic perovskite layers fabricated through intramolecular exchange. Science. 2015; **348**:1234. DOI: 10.1126/science.aaa9272

[9] Zhang W, Eperon GE, Snaith HJ. Metal halide perovskites for energy applications. Nature Energy. 2016;**1**:16048. DOI: 10.1038/NENERGY.2016.48

[10] Eames C, Frost JM, Barnes PRF, O'Regan BC, Walsh A, Islam MS. Ionic transport in hybrid lead iodide perovskite solar cells. Nature Communications. 2015;**6**:7497. DOI: 10.1038/ncomms8497

[11] Brivio F, Walker AB, Walsh A. Atomistic origins of high-performance in hybrid halide Perovskite solar cells J. Appl. Maternité. 2013;**1**, 042111. DOI: 10.1021/nl500390f

[12] Yin W, Shi T, Yan Y. Unique properties of halide perovskites as possible origins of the superior solar cell performance. Advanced Materials. 2014;**26**:4653. DOI: 10.1002/adma.201306281

[13] Yin WJ, Yang JH, Kang J, Yan Y, Wei SH. Halide perovskite materials for solar cells: A theoretical review. Journal of Materials Chemistry A. 2015;**3**:8926. DOI: 10.1039/c4ta05033a

[14] Chang J, Lin Z, Zhu H, Isikgor F, Xu QH, Zhang C, Hao Y, Ouyang J. Enhancing the photovoltaic performance of planar heterojunction perovskite solar cells by doping the perovskite layer with alkali metal ions. Journal of Materials Chemistry. A. 2016;**4**:16546.b. DOI: 10.1039/c6ta06851k

[15] Heo JH, Han HJ, Kim D, Ahnb TK, Im SH. Hysteresis-less inverted $CH_3NH_3PbI_3$ planar perovskite hybrid solar cells with 18.1% power conversion efficiency. Energy & Environmental Science. 2015;**8**:1602. DOI: 10.1039/c5ee00120j

[16] Wu CG, Chiang CH, Tseng ZL, Nazeeruddin MK, Hagfeldt A, Grätzel M. High efficiency stable inverted perovskite solar cells without current hysteresis. Energy & Environmental Science. 2015;**8**:2725. DOI: 10.1039/c5ee00645g

[17] Gang L et al. Pressure-induced Bandgap optimization in lead-based Perovskites with prolonged carrier lifetime and ambient Retainability. Advanced Functional Materials. 2017;**27**(3). DOI: 10.1002/adfm.201604208

[18] Ye Y et al. Top and bottom surfaces limit carrier lifetime in lead iodide perovskite films. Nature Energy. 2017): 16207;**2**. DOI: 10.1038/nenergy.2016.207

[19] Tianran C et al. Origin of long lifetime of band-edge charge carriers in organic– Inorganic lead iodide perovskites. Proceedings of the National Academy of Sciences. 2017:04421. DOI: 10.1021/acs.jpclett.5b01361

[20] Yang WS, Park BW, Jung EH, et al. Iodide management in formamidinium-lead- halide–based perovskite layers for efficient solar cells. Science. 2017;**356**(6345):1376-1379. DOI: 10.1126/science.aan2301

[21] Kim BS, Choi MH, Choi MS, Kim JJ. Composition-controlled organometal halide perovskite via CH 3 NH 3 I pressure in a vacuum co-deposition process. Journal of Materials Chemistry A. 2016;**4**:5663. DOI: 10.1039/C6TA00168H

[22] Bi C, Shao Y, Yuan Y, Xiao Z, Wang C, Gao Y, Huang J. Understanding the formation and evolution of interdiffusion grown organolead halide perovskite thin films by thermal annealing. Journal of Materials Chemistry A. 2014;**2**, 18508. DOI: 10.1039/C4TA04007D

[23] Park SM, Noh YJ, Jin SH, Na SI. Efficient planar heterojunction perovskite solar cells fabricated via roller-coating. Solar Energy Materials & Solar Cells. 2016;**155**:14. DOI: 10.1016/j.solmat.2016.04.059

[24] Sun X, Zhang C, Chang J, Yang H, Xi H, Lu G, Chen D, Lin Z, Lu X, Zhang J, Hao Y. Mixed-solvent-vapor annealing of perovskite for photovoltaic device efficiency enhancement. Nano Energy. 2016;**28**:417. DOI: 10.1016/j.nanoen.2016.08.055

[25] Eperon GE, Burlakov VM, Docampo P, Goriely A, Snaith HJ. Morphological control for high performance, solution-processed planar heterojunction perovskite solar cells. Advanced Functional Materials. 2014;**24**:151-157. DOI: 10.1002/adfm.201302090

[26] Yu Y et al. Ultrasmooth Perovskite film via mixed anti-solvent strategy with improved efficiency. ACS Applied Materials & Interfaces. 2017;**9**(4):3667-3676. DOI: 10.1021/acsami.6b14270

[27] Jeng JY, Chiang YF, Lee MH, Peng SR, Guo TF, Chen P, Wen TC. $CH_3NH_3PbI_3$ Perovskite/fullerene planar-heterojunction hybrid solar cells. Advanced Materials. 2013;**25**:3727-3732. DOI: 10.1002/adma.201301327

[28] Leijtens T, Eperon GE, Noel NK, Habisreutinger SN, Petrozza A, Snaith HJ. Stability of metal halide perovskite solar cells. Advanced Energy Materials. 2015;**5**. DOI: 10.1002/aenm.201500963

[29] Sun K, Chang J, Isikgor FH, Li P, Ouyang J. Efficiency enhancement of planar perovskite solar cells by adding zwitterion/LiF double interlayers for electron collection. Nanoscale. 2015;**7**:896-900. DOI: 10.1039/C4NR05975A

[30] Shao Y, Xiao Z, Bi C, Yuan Y, Huang J. Non-wetting surface-driven high-aspect-ratio crystalline grain growth for efficient hybrid perovskite solar cells. Nature Communications. 2015;**5**:5784-5784. DOI: 10.1038/ncomms8747

[31] Mo J, Zhang C, Chang J, Yang H, Xi H, Chen D, Lin Z, Lu G, Zhang J, Hao Y. Enhance planar perovskite solar cells efficiency via two-step deposition by using DMF as additive to optimize crystal growth behavior. Journal of Materials Chemistry A. 2017;**5**:13032-13038. DOI: 10.1039/C7TA01517H

Edited by Sadia Ameen,
M. Shaheer Akhtar and Hyung-Shik Shin

This book provides the fundamental understanding of the functioning of solar cellsand the materials for the effective utilization of energy resources. The main objective of writing this book is to create a comprehensive and easy-to-understand source of information on the advances in the rapidly growing research on solar cells.

Emerging Solar Energy Materials comprises 12 chapters written by the experts in the solar cell field and is organized with the intention to provide a big picture of the latest progress in the solar cell field and at the same time give an in-depth discussion on fundamentals of solar cells for interested audiences. In this book, each part opens with a new author’s essay highlighting their work for contribution toward solar energy.

Critical, cutting-edge subjects are addressed, including:
Photovoltaic device technology and energy applications
Functional solar energy materials
New concept in solar energy
Perovskite solar cells
Dye-sensitized solar cells
Organic solar cells
Thin-film solar cells

The book is written for a large and broad readership including researchers and university graduate students from diverse backgrounds such as chemistry, physics, materials science, and photovoltaic device technology. The book includes enough information on the basics to be used as a textbook undergraduate coursework in engineering and the sciences.

ISBN 978-1-83881-518-9

Published in London, UK

IntechOpen